Xi'an University of Technology

Faculty of Automation and Information Engineering

Program of Doctorate in Circuits and systems

Universidad de Alcalá

Escuela Politécnica Superior

Programa de Doctorado en Electrónica
Sistemas Electrónicos Avanzados, Sistemas Inteligentes

Research on the propagation efficiency of ultrasonic guided waves in the rail

Ph.D. Thesis

Author: Xiaoyuan Wei

Supervisors: Prof. Yuan Yang

Prof. Jesús Ureña Ureña

2020

Abstract

Ultrasonic guided waves (UGW) technique has the advantages of low detection frequency, long detection distance, strong anti-electromagnetic interference ability, and large coverage. Hence it has potential advantages in real-time detection of breakages in the rail. Based on the research background of UGW-based broken rail detection, this paper focuses on the characteristics optimization of piezoelectric ultrasonic transducers (PUTs) to improve the propagation efficiency of UGW in the rail. Due to the influence of energy attenuation, multimodal, dispersion, and on-site noise when the UGW propagates in the rail, the amplitude of the received UGW signal is low and the signal-to-noise ratio is poor. Therefore, this thesis mainly systematically studies the characteristics optimization of PUTs from the aspects of impedance matching, driving circuit optimization, and excitation signal optimization. The main work is as follows:

1. To deeply study of the electromechanical characteristics of longitudinal vibration sandwich piezoelectric ultrasonic transducer (referred to as PUTs), the PSpice equivalent circuit models of a piezoelectric ultrasonic transducer and the PSpice equivalent circuit model of a pitch-catch setup are established based on one-dimensional wave and transmission line theory. The PSpice model of the PUT and the PSpice model of the pitch-catch setup are analyzed from the time and frequency domains, respectively, and the accuracy of the built PSpice models is verified through some experiments. It is shown that the PSpice model of a PUT established above is highly scalable and can be combined with amplifiers, driving circuits, diodes.

2. With the aim of solving the problem of impedance mismatch between the piezoelectric ultrasonic transducer and the driving circuit and the rail surface, the effect of the impedance matching on the electromechanical properties of the piezoelectric ultrasonic transducer was studied from the electrical and acoustic ends, respectively. From the electrical side, the effects of different electrical impedance matching networks on the electromechanical characteristics of PUTs are studied in both time and frequency domains. It is shown that in the two LC impedance matching networks, the matching network formed by the series inductance and parallel capacitance is better. From the acoustic side, an experimental method is used to study the effect of acoustic impedance matching on the transient characteristics of PUTs. It is concluded that when the epoxy resin is doped with 10% tungsten powder and the coating thickness is 8 mm, the acoustic impedance matching effect is better.

3. To overcome the problems of the existing driving circuits that the excitation voltage is not high enough, the extra high voltage DC voltage is required and the impedance matching is not considered, this thesis proposed a high voltage pulse driving circuit based on the full-bridge topology. The driving circuit takes into account the suppression of overshoot and oscillation when the power MOSFET is turned off, and at the same time conducts the impedance matching and tailing absorption of the excitation signal for PUTs. The suppression of overshoot and oscillation adopts the RC snubber circuit, and the tailing absorption is accomplished by a bleeder resistor and a bidirectional thyristor. The correctness and effectiveness of the proposed high-voltage pulse driving circuit are verified through experiments. It was also found that the combined use of electrical impedance matching and absorption circuits can effectively improve

the energy conversion efficiency of PUTs.

4. To obtain the optimal performance of PUTs, the excitation signal of PUTs is optimized in terms of excitation signal frequency and excitation coding. First of all, to solve the problem of PUTs with having a resonance frequency shift after loading, this thesis proposes an optimal excitation frequency tracking method based on a digital band-pass tracking filtering. Then its correctness and stability are verified through some field experiments. Secondly, to improve the signal-to-noise ratio of the UGW signal, it is proposed to apply the Barker code excitation method to the broken rail detection, and use the pulse compression technique at the receiving end to realize the rapid recognition of the signal characteristics. Finally, for the case where the pulse-compressed signal produces undesirable peak sidelobes due to the effects of bandwidth, multipath, and noise, an adaptive peak detection algorithm based on the Hilbert transform combined with a digital bandpass tracking filter and a triangle filter. The accuracy and effectiveness of the above-mentioned Barker code excitation method and the adaptive peak detection algorithm are verified through experiments.

The study in this thesis presents a feasible solution for improving the propagation efficiency of UGW in the rails and at the same time provides theoretical guidance for the large-scale application of the real-time broken rail detection system based on UGW.

Keywords: Broken rail detection; Ultrasonic guided wave; piezoelectric ultrasonic transducer; Impedance matching; Driving circuits; Frequency tracking; Encoding excitation; Peak detection;

To my parents,
To my supervisors,
To everyone who gives me a lot of support

Acknowledgment

Time passes quickly like a white horse through a crevice, and doctoral studies are coming to an end. At the same time, the student career will also end, and a new journey of life will soon begin. In retrospect, there have been successes and joys and failures and pains along the way in learning, but the final result is still satisfactory. This stems from the companionship and understanding of parents and loved ones, the care and guidance of mentors, the care and support of good friends. On the occasion of the completion of my doctoral thesis, I would like to thank my mentors and good friends who have accompanied and helped me on the road of scientific research.

First of all, I would like to thank my supervisors, Prof. Yuan Yang at the Xi'an University of Technology and Prof. Jesús at the University of Alcala for their careful guidance and deep care. Their rigorous academic attitude, realistic work style, and serious and responsible attitude have all deeply influenced me and set a good learning example for me. A good bird chooses wood for its roost, I am lucky to have the two knowledgeable teachers. They have given me a lot of help and important opinions on the topic selection of my doctoral thesis, the design of the research plan, and the difficulties to overcome. Besides, they are always concerned with the overall progress of the thesis work and care for me both in my studies and in my life, which allows me to quietly work on my doctoral research.

Secondly, I would like to thank Prof. Jesús at the University of Alcala in Spain. With his caring and enthusiastic help, I can adapt quickly to life in a foreign country. He also helps me develop a detailed study plan, which is to motivate me to conduct my research quickly and in an orderly manner. Under his careful guidance, I have improved my English essay writing and have become more fluent in oral expression. Also, the successful completion of my doctoral thesis is possible under the guidance and assistance of Prof. Álvaro and Associate Prof. Maria Carmen.

Thirdly, I would like to thank the members of the research group at the Xi'an University of Technology, Dr. Lei Yuan, Dr. Wenqing Yao, Dr. Lei Zhang, Dr. Yang Wen, Dr. Mingjing Zhai, and master students including Yang Wang, Xiaochao Ding, Yanan Du, Haozhen Wang, Jiaxuan Yan, and Liu Cao for their support and selfless help in the theoretical research and experimental testing of my doctoral thesis. In particular, Dr. Yuan Lei has given me a lot of help in handling relevant procedures for studying abroad. The four masters Xiaochao Ding, Yanan Du, Haozhen Wang, and Jiaxuan Yan give me great support and assistance in the experimental testing and subsequent experimental data collation. I am grateful to Post Dr. David, Dr. Santiago, Dr. Pago, Dr. Khaoula, Dr. Elena, Dr. Rubén, as well as all the members of the research group at the University of Alcala for giving me both academic and life support during my stay period in Spain. Additionally, I would like to thank my friends Post Dr. Li Yang, Evani, and Bowen Xiao for helping me during my study abroad period, which makes my life enriched and less lonely.

Special thanks to my parents and my beloved Yulan zhou for their selfless care, unlimited understanding, and companionship during my doctoral studies. It is with their love that I can adjust my mentality quickly when my mood is low so that I can concentrate on completing the doctoral study tasks.

Besides, thanks to all the editors and reviewers in the dissertation submission for their

invaluable comments and suggestions. This helps me to continuously revise the research route of my doctoral topic, thus greatly improving the quality of my dissertation.

Finally, I would like to thank the experts and professors who took the time to review my thesis!

Contents

Index of Figures

1. Introduction

2. UGW Broken Rail Detection System and Related Theoretical Basis

3. Establishment of PSpice Model of SPUTs in Longitudinal Vibration

4. Research on the Effect of Impedance Matching on the Electromechanical Characteristics of PUTs

5. Research on the Optimization of Driving Circuits for PUTs

6. Research on the Optimization of Excitation Signals for PUTs

Index of Tables

5. Research on the Optimization of Driving Circuits for PUTs

6. Research on the Optimization of Excitation Signals for PUTs

List of Symbols

Name	Description
h	Thickness of the plate
tan	Tangent function
C_T	Transverse wave velocity
C_L	Longitudinal wave velocity
k	Wavenumber
c_g	Group velocity
c_p	Phase velocity
ω	Angular frequency
λ	Lame constant
μ	Lame constant
ρ	Density
∇	Operator of Hamilton
$\frac{\partial^2 u}{\partial t^2}$	Partial second derivative of displacement
$u(x,t)$	Displacement
t_i	Surface stress
σ_{ij}	Normal stress and shear stress
n_j	The Unit vector
d_{11}	Piezoelectric constant
d_{12}	Piezoelectric constant
d_{13}	Piezoelectric constant
d_{14}	Piezoelectric constant
d_{15}	Piezoelectric constant
d_{16}	Piezoelectric constant
d_{21}	Piezoelectric constant
d_{22}	Piezoelectric constant
d_{23}	Piezoelectric constant
d_{24}	Piezoelectric constant
d_{25}	Piezoelectric constant
d_{26}	Piezoelectric constant
d_{31}	Piezoelectric constant
d_{32}	Piezoelectric constant
d_{33}	Piezoelectric constant
d_{34}	Piezoelectric constant
d_{35}	Piezoelectric constant
d_{36}	Piezoelectric constant

Name	Description
f_{r}	Resonance frequency
s_{11}^{E}	Short circuit elastic compliance constant
l	The length of piezoelectric ceramic thin bar
f_{a}	Anti-resonance frequency
B	Piezoelectric material coefficients
s_{55}^{D}	Open circuit elastic compliance constant
$[M]$	Structural mass matrix
$[K]$	Elastic stiffness matrix
$[C]$	Structural damping matrix
$\{F\}$	External force
$\{\ddot{u}\}$	Structural acceleration
$\{\dot{u}\}$	Structural velocity
$\{u\}$	Structural displacement
exp( )	Exponential function
λ_i	*i*-th eigenvalue
ω_i	*i*-th natural frequency
ϕ_i	*i*-th eigenvalue vector
ω_d	Natural frequency under damping
ξ	The critical damping ratio
c	Vibration damping
c_0	Critical damping
j	Imaginary unit
C_0	Static capacitance
L_{m}	Dynamic inductance
C_{m}	Dynamic capacitance
R_{m}	Dynamic resistance
V	Voltage
I	Current
F_{L}	Force applied to the front surface
F_{B}	Force applied to the back surface
u_{L}	Particle velocity of the front surface
u_{B}	Particle velocity of the back surface
S_3	Strain
D_3	Electric displacement
T_3	Stress
c_{33}^{D}	Open circuit elastic stiffness constant
h_{33}	Piezoelectric constant
e_{33}	Piezoelectric stress constant
$\varepsilon_{33}^{\mathrm{S}}$	Clamped dielectric constant

Name	Description
ξ_3	Particle displacement
A	The cross-sectional area of piezoelectric ceramic disc
sin	Sine function
Z_0	Characteristic impedance
Z_{11}	Characteristic impedance
Z_{12}	Characteristic impedance
Z_{12}	Characteristic impedance
N	Ideal transformer ratio
Z_{R}	Acoustic impedance of the front end
Z_{L}	Acoustic impedance of the back end
Z_{TL}	Impedance of half-length lossless transmission line
Z_{TR}	Impedance of half-length lossless transmission line
X_1	Reactance
csc	Cosecant function
U_{s}	Equivalent voltage source
Z_{s}	Equivalent impedance of the active network
Z_1	Equivalent impedance of the load
X_{s}	Reactance
R_{s}	Resistance
R_1	Resistance
P	Transmission power
cos	Cosine function
Z	Acoustic impedance
Z_{m}	Acoustic impedance
Z_{m1}	Acoustic impedance
Z_{m2}	Acoustic impedance
T_{m}	Thickness of the matching layer
λ_{m}	Wavelength of sound wave
v_{m}	Acoustic velocity
v	Acoustic velocity
f_{s}	Mechanical resonance frequency
R	Resistance per unit length
L	Inductance per unit length
G	Conductance per unit length
C	Capacitance per unit length
Δz	Electrical transmission line length
$v(z,t)$	Node voltage
$i(z,t)$	Node current
α	Attenuation constant
β	Phase constant

Name	Description
$p(z,t)$	Sound pressure
$u(z,t)$	Particle velocity
k_c	Complex wavenumber
τ	Relaxation time
v_t	Acoustic velocity
E	Young's modulus
Z_{el}	Characteristic impedance
Z_a	Characteristic acoustic impedance
γ	Propagation constant
α_v	Attenuation coefficient from viscous losses
α_{tc}	Attenuation coefficient from thermal conduction
R_0	Dielectric loss resistance
$\tan\delta_e$	Dielectric loss factor
Q_e	Electrical quality factor
β_{33}^s	Dielectric isolation rate
Q_m	Mechanical quality factor
F	Resonance frequency
S	Cross-sectional area
NL	Transmission line normalized length
R_{air}	Air load
f_p	Parallel resonance frequency
$y(t)$	Hanning window modulated sinusoidal pulse signal
m_F	Mass of the front mass
m_B	Mass of the back mass
v_F	Surface vibration velocity of the front mass
v_B	Surface vibration velocity of the back mass
Y	Total admittance
B	Susceptance
f_m	Maximum admittance frequency
f_1	Half power point frequency
f_2	Half power point frequency
η_{P1}	Electro-acoustic power ratio
η_{G1}	Electro-acoustic gain ratio
η_v	Vibration velocity ratio
k_{effc}	Effective electromechanical coupling coefficient
R_{v1}	Alumina powder volume ratio
R_{v2}	Tungsten powder volume ratio
$f(t)$	Excitation signal
T	Excitation signal period

Name	Description
A_0	Initial amplitude
φ_0	Initial phase
arctan	Arctangent function
t_f	Current fall time
I_d	Drain current
V_{ds}	Drain-source voltage
C_{sn}	Capacitance of the turn-off snubber
R_{sn}	Resistance of the turn-off snubber
I_{rr}	Reverse recovery current of the integrated freewheeling diode
n_1	Primary turns of the pulse transformer
n_2	Second turns of the pulse transformer
Q_g	Gate charge
V_{gs}	Gate-source voltage
$V_{gs(th)}$	Gate turn-on voltage threshold
VCC	Bootstrap voltage
$H(\ )$	Transfer function
s	Laplace operator
Ω	Angular frequency
H_{OBP}	Bandpass output gain
$h(\tau)$	Window function
$W(t, f)$	Pseudo Wigner-Ville Distribution
$B[N]$	Barker sequence
ψ_{AA}	Auto-correlation function
$e[n]$	Transmitted signal
$v[n]$	Sample sequence of the carrier signal
$c[n]$	Oversampled Barker code sequence
T_N	Chip duration of Barker code
N_c	Cycles of the selected carrier
f_0	Frequency of excitation signal
$E^*(\omega)$	Complex conjugate of $E(\omega)$
k_1	Normalized amplitude constant
$h_1(t)$	Impulse response function of the matching filter
$d(t)$	Pulse compression signal
log( )	Logarithmic function
max( )	Maximum function
sgn( )	Symbolic function
$H[\ ]$	Output of HT
$F[\ ]$	Output of FFT
*	Convolution operator

Name	Description
$y[n]$	Received UGW signal
$d[n]$	Matched-filtered signal
$b[n]$	Output of the DBTF
$a[n]$	Normalized signal
$t[n]$	Output of the first-order forward differential filter
$s[n]$	Output of squaring transform
$m[n]$	Output of MA filter
N_{w}	Window width of MA filter
$t_{\mathrm{f}}[n]$	Output of the triangle filter
TP	Number of correctly detected peaks
FN	Number of missed peaks
FP	Number of false peaks

List of Abbreviation

GNSS	Global Navigation Satellite System
RCF	Rolling Contact Fatigue
AC	Alternating Current
EMAT	Electromagnetic Acoustic Transducers
SH	Shear Horizontal
UGW	Ultrasonic Guided Waves
3-D	Three Dimensional
SAFE	Semi-analytical Finite Element
PT	Piezoelectric Transducers
SNR	Signal-to-Noise Ratio
PUT	Piezoelectric Ultrasonic Transducers
SPUT	Sandwich Piezoelectric Ultrasonic Transducers
RFT	Resonance Frequency Tracking
PLL	Phase-Locked Loop
VCO	Voltage-Controlled Oscillator
PRF	Parallel Resonance Frequency
ZVS	Zero Voltage Switch
BPF	Bandpass filter
SHM	Structural Health Monitoring
EIM	Electrical Impedance Matching
AIM	Acoustic Impedance Matching
BVD	Butterworth-Van-Dyke
WT	Wavelet Transform
LFM	Linear Frequency Modulation
NDT	Non-Destructive Testing
HT	Hilbert Transform
MAF	Moving Average Filtering
DWT	Discrete Wavelet Transform
OEFT	Optimal Excitation Frequency Tracking
FE	Finite Element
WDTM	Wireless Data Transmission Module
LE	Length Extension
TE	Thickness Extension
PS	Planar Shear
TS	Thickness Shear
PSD	Power Spectrum Density
RC	Resistance Capacitance
AFTF	Automatic Frequency Tracking Filter
IFFT	Inverse Fast Fourier Transform
DFT	Discrete Fourier Transform

DC	Direct current
IIR	Infinite Impulse Response
DBTF	Digital Bandpass Tracking Filter
OEFT	Optimal Excitation Frequency Tracking
dB	Decibel
BW	Bandwidth
PWVD	Pseudo Wigner-Ville Distribution
WVD	Wigner-Ville Distribution
FM	Frequency Modulation
SLL	Sidelobe Level
MLW	Mainlobe Width
PSL	Peak Sidelobes Level
ST	Squaring Transform
MA	Moving Average
SET	Shannon Energy Transform
db1	First-order Daubechies Wavelet
Se	Sensitivity
+P	Positive Predictivity
Er	Error Rate
Acc	Accuracy

1 Introduction

1.1 Research Background and Significance

The railway is an important infrastructure of the country, and railway transportation occupies an important position in China's transportation system. At this stage of China's rapid economic development and the coexistence of various modes of transport, railway transport still occupies an extremely important position in China's national economic system, which is called “the artery of the national economy” [1]. In 2015, China adopted the “Belt and Road” strategy as the current highest national strategy, thus marking the development of railway transportation capacity as one of the national development strategies. The track, as the basis of the train's operation, is the part that directly bears the various loads of the locomotive vehicle. Under the repetitive action of the dynamic load on the locomotive vehicle, due to the material and construction of the rails, together with external factors such as line maintenance and climatic conditions, the rails produce various damages, including deformation, wear, cracks and even fractures. Especially in the seamless line section, the temperature change of the rail causes a large temperature force inside the rail. When the temperature is low, the rail bears a huge tensile force. At this time, if there are various defects in the rail, the rail is more likely to break, of which the breakage of rail welding seam is more common. According to statistics, the breakage of weld seam accounts for about 90% of the broken rails. After the occurrence of the broken, if the train is passing, it is very likely to cause the train derailment with a major traffic accident. On December 19, 2007, due to breakage of rails, a train derailment accident occurred in southern Pakistan, killing at least 58 people and injuring more than 120 people. On January 27, 2008, a passenger train in Turkey derailed in the western region owing to breakage of rails, resulting in 8 deaths and 21 injuries. On April 7, 2009, the 1164 train from Shaanxi Hancheng to Beijing West went to Yesanpo, Moshui County, Hebei Province, China, and the train derailed due to breakage of rails. Although there were no casualties, it caused traffic disruption on the Kyohara Line for more than 20 hours. This shows the importance of detecting rail damage for the safe operation of the train.

(a)

(b)

Fig. 1-1 National railway construction, (a) development plan, (c) high-speed railway

In recent years, China's high-speed railway has developed rapidly, as shown in Fig. 1-1 for China's railway construction plan. It is estimated that in 2020, the operating mileage of

high-speed railways in China will reach 18000 kilometers, the operating mileage of fast railways will reach 40000 kilometers, and the operating mileage of railways in the western region will reach more than 50000 kilometers [2-3]. Currently, the traditional rail breakage detection method can no longer fully meet the new requirements for detection accuracy, detection speed, and broken rail detection efficiency under the new situation. To meet the stable and safe running track conditions of high-speed trains, the requirement for online real-time monitoring of rail damage status is proposed. The current methods of detection of fracture for seamless railway have the problems of low detection efficiency, difficult installation, and maintenance, the inability to achieve full section coverage, and they can only identify the case of complete fracture. Therefore, the search for new inspection methods and the design and development of an online real-time monitoring system that can solve the deficiencies of existing inspection systems is important to eliminate the safety hazards of train operation and ensure the safe operation of the train.

1.2 Research Status at Home and Abroad

The detection level of broken rail in China has a certain gap compared with foreign countries. The methods currently used cannot achieve online real-time and accurate broken rail detection, and the false alarm rate is high. With the rapid development of high-speed railways, the existing methods have shown many deficiencies such as track occupancy, long inspection periods, low inspection efficiency, poor real-time, etc. Many new detection methods have emerged in recent years, however, most of these methods are still in the laboratory research phase and fewer are used in practice.

1.2.1 Research Status on Rail Fracture Detection Method

At present, the inspection of rail breakages in domestic and foreign mainly relies on hand-pushed flaw detection trolley, large rail flaw detection vehicles, and track circuits, as well as patrol workers for inspection [4]. The hand-pushed trolley based on the principle of ultrasonic detection, as shown in Fig. 1-2(a), can effectively detect rail fractures and nuclear injuries within the rail and can accurately determine the location of the damage. Nevertheless, the biggest disadvantage of this method is the long detection period, low detection efficiency, and longtime occupancy of the track, which is an offline detection method with poor real-time. Based on the principle of ultrasonic inspection, the high-speed rail flaw detection vehicle shown in Fig. 1-2(b) regularly inspects the track, with the advantages of fast inspection speed and high inspection accuracy, as well as damage analysis, data recording and playback. But it is expensive and the inspection is susceptible to the flatness and cleanliness of the rail surface. Likewise, it is also an offline inspection method with low real-time. The track circuit is a basic component of the railway signal system. It uses a section of rails in the operating line as a conductor to form a circuit, which can realize the functions of train occupancy detection and broken rail detection. The track circuit-based broken rail detection method is an in-line detection method that meets the requirements for real-time detection to the maximum extent possible. However, the track circuit belongs to high-voltage electrical equipment and is susceptible to the influence of electrical parameters and roadbed parameters, with a high false

alarm rate. Note that the track circuit cannot be installed in wet areas, making it difficult to cover the entire detection zone. Besides, with the rapid development of GNSS positioning technology, the positioning of trains can be achieved without the use of track circuitry, broken rail detection is only an additional function of the track circuit.

(a)

(b)

Fig. 1-2 The off-line detection equipment of rail flaw, (a) detection flaw trolley by hand push, (b) high-speed rail inspection vehicle

In addition to the above-mentioned mature detection methods, there are optical fiber detection, magnetic leakage detection, eddy current detection, machine vision detection, electromagnetic ultrasonic detection, ultrasonic phased array detection, laser-EMAT ultrasonic detection, some of which have been applied to rail damage detection. However, some of them are still in the laboratory research stage and have not been used on a large scale; the following will be introduced one by one.

- **Optical fiber detection**

Firstly, single-mode fiber is affixed to a rail web and the signal in the fiber is generated by a light source at the transmitting end and then received by an optical receiver at the receiving end. If the rail breaks, the optical fiber is also broken, resulting in that the optical receiver cannot receive the optical signal. At this time, the detection system determines that the detection interval is broken. For the application of optical fiber in the detection of broken rails, researchers at the University of Illinois conducted an in-depth study [5]. Optical fiber detection has proven to be a very reliable method for detecting broken rails, and it is suitable for short distances where electrical isolation and electromagnetic interference are difficult to achieve. But its biggest disadvantage is that the optical fiber is more difficult to install and maintain. Due to the higher requirements on the flatness of the rail surface, it is difficult to install. The fiber multiplexing technology after the rail breakage is very complicated and difficult to operate.

- **Magnetic leakage detection**

It is a non-destructive testing technique that identifies defects by detecting changes in the magnetic leakage field. After the ferromagnetic material is magnetized, the leakage magnetic field is formed on the structure surface due to the defects on this structure surface or near-surface, so the magnetic leakage detection is very sensitive to the damage of this part of the rail, which is suitable for the detection of rail surface damage [6-7]. However, the range of magnetic leakage detection is easily influenced by the thickness of the structure. When the structure is thick, the magnetic force decays rapidly and cannot penetrate the structure, resulting

in a large detection blind spot [8]. Also, when the detection speed is faster, the magnetic line density decreases which will seriously affect the detection accuracy of the system [9]. Due to the aforementioned shortcomings of magnetic leakage detection, it is often used as an auxiliary detection technique in the actual detection of rail damage.

- **Eddy current detection**

Eddy current detection is a detection method that uses the principle of electromagnetic induction to detect eddy current changes on the surface and near-surface of a conductive structure to determine whether there is damage in the surface and near of the structure surface. It does not require a tight fit of the AC solenoid to the structure, but rather a certain lifting distance, so the coupling agent is not required. And the detection is highly operable and easy to automate. Due to the influence of superficiality, eddy current detection technology is suitable for the detection of damage on or near the surface of structures, especially on the railhead [10]. In recent years, to compensate for the shortcomings of traditional piezoelectric ultrasound in the detection of surface and near-surface damage of rails, non-destructive testing researchers have attempted to use eddy current detection for the detection of rolling contact fatigue (RCF) cracks in the rails [11].

- **Machine vision detection**

It is based on a high-speed camera that captures images of the rails in real-time and analyzes the captured images against data from a previously established damage database to determine whether there is damage to the rails. In machine vision detection, the detection speed and the frame rate of the acquired image are two important factors that affect the detection accuracy. Currently, machine vision inspection is mainly used to detect rail head profiles, wear percentages, and surface damage such as rail RCF and rail corrugation defects, but it does not provide any information about internal rail defects [12-13]. Visual detection of cracks and flaking defects on the surface of rails was studied [14] by Ze Liu et al., Beijing Jiaotong University.

- **Electromagnetic ultrasonic detection**

Electromagnetic acoustic transducers (EMAT) can be excited and received in a conductor or magnetic material by the Lorentz force or magnetostrictive effect [15]. In general, it consists of a detection coil, an external magnetic field, and the structure under examination. Different types of ultrasound can be excited by designing the coil geometry, magnetic field direction, and different driving methods. The greatest advantage of EMAT is that it does not require coupling agents and pre-treatment of the surface of the examined part; it can be easily and flexibly excited to generate many types of ultrasound waves, such as lamb, SH, and surface waves [16-17]. EMAT can offer a wide range of applications in the field of non-destructive testing due to its non-contact, inspection efficiency, and design flexibility. The University of Warwick, University of Birmingham and the University of Bristol, UK, jointly conducted EMAT-related research that can be used for high-speed rail inspection. In China, the Harbin University of Technology and others also researched the EMAT-based rail inspection system [18].

- **Ultrasonic phased array detection**

Ultrasonic phased array technology is a new technology for non-destructive testing and evaluation of structural components, which uses a computer to control the ultrasonic excitation and reception of each small wafer in the phased array probe. At the same time, the different

time delays are applied to each wafer, resulting in strong acoustic interference on the wave-front of each wafer to obtain deflection and focus of the acoustic beam [19]. Therefore, for the inspection of rail weld seams, phased array inspection has a significant technical advantage over traditional ultrasonic. The greatest advantage of the ultrasonic phased array over the conventional ultrasonic pulse method is its flexible beam deflection and focusing performance. Foreign scholars are conducting research on the ultrasonic phase control array for rail detection [20-21]. In China, Nanchang University of Aeronautics and Astronautics also conducted research on the ultrasonic phased array detection method for rails [22]. However, ultrasonic phased array technology requires extensive data analysis and data processing is not as straightforward as traditional ultrasonic testing. As a consequence, there is currently no ultrasonic phased array system that can be used in a real sense for high-speed rail inspection.

- **Laser-EMAT ultrasonic detection**

Laser-EMAT is a combination of laser ultrasonic technology and EMAT, which uses laser pulses to achieve ultrasonic excitation and EMAT to receive ultrasonic signals. When a laser pulse hits the surface of a material, it generates ultrasonic waves through a thermal bombardment effect, which facilitates the generation of longitudinal, SH, lamb, and surface waves. Laser ultrasonic detection technology offers high temporal and spatial resolution due to the combination of the sensitivity of ultrasonic detection and the flexibility of the optical system [23]. Shandong Academy of Sciences Laser Institute in China has done a lot of work on rail damage detection by using laser-EMAT [24-26]. The Institute has developed a laser-EMAT-based method for determining RCF defects and waist cracks in steel rails, but it is still in the laboratory research stage.

According to the above-mentioned application and research on in-service rail nondestructive testing, to achieve efficient and reliable rail full-coverage testing, a combination of testing techniques is required. From the current development trend of non-destructive testing technologies, acoustic testing technology will be the future direction of development in the field of non-destructive testing of rails, especially some non-contact detection methods such as electromagnetic ultrasonic and laser ultrasonic.

1.2.2 Research Status on UGW Detection in the Rail

The theoretical study of guided waves originally derived, at the beginning of the last century, from the study of the problem of propagation of elastic waves in solid media in mechanics. The researchers first performed a theoretical study on the propagation characteristics of elastic waves in various waveguides, which went through several stages: propagation in infinite media, propagation in plates, propagation in cylinders, propagation in various pipes, and propagation in complex cross-sectional structures. Fig. 1-3 shows the ultrasonic wave propagation in the plate, where h indicates the plate thickness and z indicates the direction of ultrasonic wave propagation in the plate. From Fig. 1-3, it is found that ultrasonic waves are reflected and refracted many times at the upper and lower boundaries of the plate, and waveform conversion occurs. After propagation for a period of time, a “wave packet” is generated by superposition, that is, a guided wave mode in the plate. In the early 20th century, Rayleigh and Lamb studied the propagation of elastic waves in free-state isotropic plates and proposed the famous Rayleigh-Lamb frequency equation [27-28]:

$$\frac{tan(qh)}{tan(ph)} = -\frac{4k^2pq}{(q^2 - k^2)^2} \quad (1\text{-}1)$$

$$\frac{tan(qh)}{tan(ph)} = -\frac{(q^2 - k^2)^2}{4k^2pq} \quad (1\text{-}2)$$

where $p^2 = \omega^2/c_L^2 - k^2$, $q^2 = \omega^2/c_T^2 - k^2$; h indicates the thickness of the plate; C_T and C_L represent longitudinal and transverse wave velocities in the medium, respectively. The phase velocity and group velocity frequency dispersions of the resolved form in the plate are obtained by solving (1-1) and (1-2) equations.

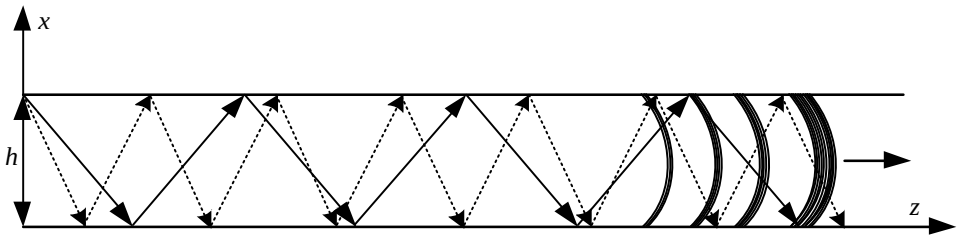

Fig. 1-3 The schematic diagram of ultrasonic guided waves propagating in the thin plate

On the basis of the study of waveguide theory in plates, waveguide theory was further developed. In 1923, Ghosh simulated the propagation process of axially propagating axisymmetric modes (longitudinal and torsional modes) in a pipeline [29] and derived the dispersion equation of the guided waves in the pipeline. Naghd et al. proposed the Timoshenko model [30] and studied the relationship between the wavenumber and frequency of the axisymmetric mode in the hollow cylindrical shell structure. In addition, the accuracy of plate and shell approximation theory was improved by modifying the conditions. Silk and Bainto conducted an in-depth study of the guided wave modes in the cylinder [31]. It is found that there are mainly three types of guided wave modes in the cylinder: axisymmetric longitudinal mode and torsional mode, and non-axisymmetric bending mode. Vogt T. et al. proposed a single (v, n) mode [32] when studying the guided wave scattering problem in some buried cylindrical structures, where $v > 1$, $v = 1$ corresponds to the original bending mode; v = 0 corresponds to the original longitudinal and torsional modes. The research on the theory of ultrasonic guided waves (UGW) in China has started relatively late, but extensive research has been actively carried out in related fields. Z.Q. Liu made a study on the guided wave theory [33-35], and gave some characteristics of the guided wave theory such as phase velocity, group velocity, and dispersion characteristics, and analyzed the common SH mode guided wave, guided wave in fine bars and lamb wave. D.A. Ta studied the propagation characteristics of UGW in pipelines [36] and analyzed the influence of UGW dispersion characteristics when the pipe inner diameter and wall thickness was changed. Based on the finite element theory, L.J. Yang et al. established a 3-D model of steel pipe [37], which simulated the propagation mode of the ultrasonic longitudinal guided wave L(0,2) in the steel pipe.

Compared to the studies on the detection of the plate and tubular structures by UGW, the theoretical study of the propagation of waveguides in shaped structures with complex cross-sections is late. The study of the dispersion characteristics of guided waves in waveguides

is an important basis for guided wave applications. This is due to the fact that the dispersion curve points out the mutually reinforcing interference region in all propagation paths, while various modalities with propagation capabilities are also available. Rail as a complex structure containing a variety of features, its dispersion characteristics cannot be obtained using analytical methods, resulting in the application of UGW in the rail detection research and development is slower. With the rapid development of computer technology and finite element analysis methods, a breakthrough has been made in the analysis of dispersion characteristics of such complex structures as rails. The existing methods for solving guided wave dispersion curves in complex structures include the finite element method [38-39], semi-analytical finite element (SAFE) method [40-41], boundary element method [42-43] and vibration modal analysis method [44]. The semi-analytical finite element method is recognized as the most effective and accurate method for solving dispersion characteristics and can be applied to any cross-sectional shape.

The method of UGW detection of railhead defects was studied by Rose J.L. and others [45-46], and it was found that when the excitation signal frequency is in the range of 40 kHz~80 kHz, it is more suitable for UGW propagation in the rail. Schwartz K. et al. studied the propagation characteristics of UGW in the rails [47] and investigated the interaction of ultrasonic waves with rails through experimental methods. It was shown that the longitudinal wave propagation in the rail has the smallest attenuation in a certain frequency range. Hayashi et al. utilized the SAFE method to solve for the dispersion characteristics of the guided waves in the rail [48], and at the same time combined with the dominant mode analysis method, the dominant mode was extracted from the bottom part of the rail and analyzed its wave structure. Fan Y. et al. investigated the propagation of ultrasonic surface waves and their interaction with railhead damage [49]. It is found that ultrasonic surface waves in the rail have the same propagation characteristics as Rayleigh waves in flat plates. Coccia S. et al. analyzed the dispersion characteristics of the guided wave in the railhead [50] and studied the guided wave modes generated in the railhead under both symmetric and asymmetric loading conditions. Bartoli I. et al. conducted a simulation study on the temperature stress in the rail [51]. Simultaneously, the SAFE method was used to study the effect of stress on the phase velocity and guided wave mode.

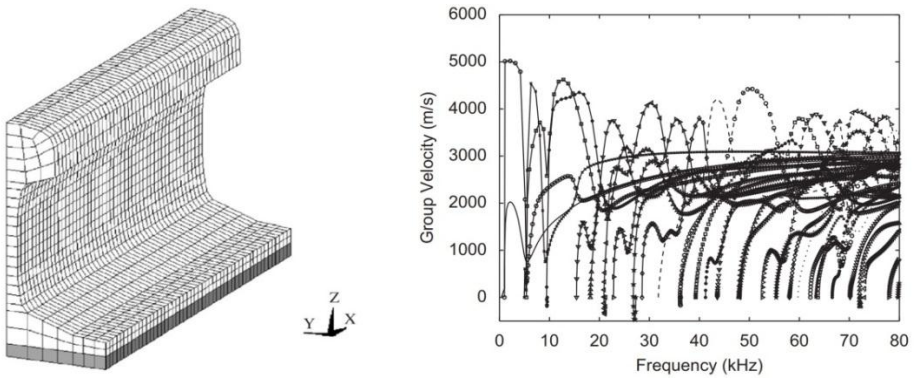

(a) (b)

Fig. 1-4 The finite element analysis of propagation characteristics for ultrasonic guided waves in rail, (a) half-rail model with rubber pads, (b) group velocity dispersion curve

Ryue J. et al. modeled the UIC60 rail with the help of finite element analysis software ANSYS

[52], and it was possible to model half of the rail due to its symmetry. Because the sleepers and ballast have a greater influence on the UGW signal with a frequency below 5 kHz, the propagation modeling of UGW signals with a higher frequency only needs to consider the influence of the rubber pad on the guided wave. The rubber pad is distributed as a continuous elastic base at the bottom of the rail, and the specific model is shown in Fig. 1-4. The simulation study found that the number of modes of the ultrasonic guide waves in the rail reached 63 at excitation signal frequencies up to 80 kHz. In the meantime, the propagation characteristics of UGW in the railhead, rail waist, and rail bottom were investigated.

Y.P. Zhang et al. first proposed a real-time rail break detection method based on the principle of ultrasonic guide wave detection [53], and the detection mechanism of the method was analyzed in depth. But the dispersion and multimodal characteristics of UGW signals in the rail were not analyzed. C. Lu et al. investigated the propagation characteristics and vertical vibration mode of the ultrasonic waves in the rail [54-55] and used the SAFE method to study the modal dispersion characteristics and wave structure of various vibration modes in the CHN60 rail. Then based on the ABAQUS software model, the scattering characteristics of the oblique cracks at different angles of the rail bottom were investigated in the horizontal and vertical vibration modes. X.N. Xu et al. used the SAFE method to analyze the dispersion characteristics of UGW in the rail [56], and analyzed the detection of temperature stress in the rail using the phase velocity parameter of UGW. L.Q. Zhu et al. proposed a seamless line integrity detection technology based on UGW and designed a functional prototype [57], and conducted actual line testing. Then SAFE element method was used to analyze the excitation frequency, mode, and vibration pattern to obtain UGW modes that were suitable for testing the rail integrity. J.J. Chang et al. used an air-coupled ultrasonic Rayleigh wave detection method [58] to evaluate the surface defects of railheads by the amplitude changes of the echo signals at different frequencies and defect depths. So far, there are relatively few rail damage detection systems based on UGW detection technology at home and abroad, especially the real-time online detection system. The British Welding Institute has developed the fourth generation of the guided wave-based detector TELETEST [59]. G-scanning detector based on UGW was developed by Imperial College London and the British UGW Railway company, for the detection of defects in the vertical distribution of rails and areas of hot welding of aluminum [60-61]. J.H. Hu et al. developed a detection system based on UGW for defects detection at the bottom of turnout rails [62]. Experimental tests have shown that the system was capable of detecting defects and cracks in more than 1% of the cross-sectional area at the bottom of the rails, independent of train traffic, with real-time online detection capabilities. The University of Warwick, UK, developed a railhead damage detection method based on electromagnetic ultrasonic detection technology [63]. VIGOR Company, Russia, successfully developed an EMAT-based offline rail defect detection system, which enabled a comprehensive inspection of the entire rail [64]. Tektrend designed an EMAT-based rail flaw detection vehicle [65]. Rose J.L. et al. proposed a method for the inspection of rails based on electromagnetic UGW technology [46]. Waveinsolids Company developed a long-range rail flaw detection vehicle based on electromagnetic UGW detection technology [66]. Y. Qiu et al. used EMAT for rail damage detection [67] and developed a hand-pushed rail flaw detection device. Burger F.A. et al. developed a real-time online detection system of UGW broken rail for seamless long-rail lines

[68-69], and the system structure was shown in Fig. 1-5.

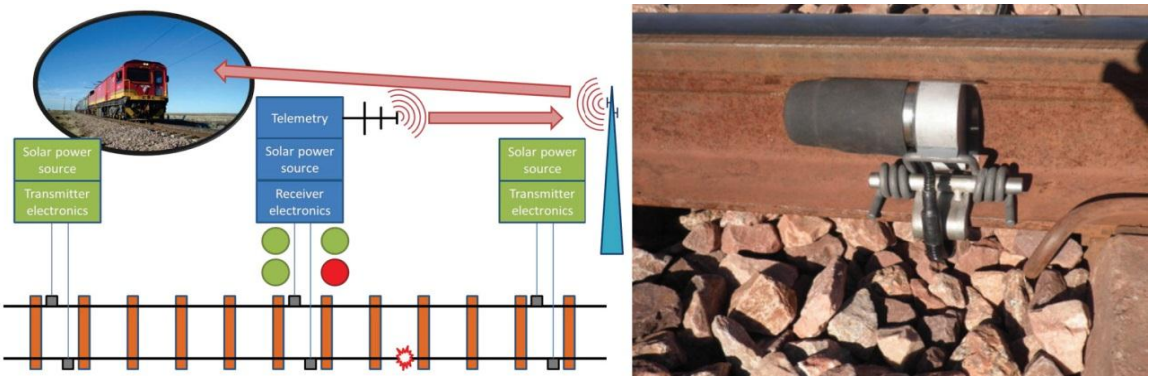

(a) (b)

Fig. 1-5 The broken rail detection system based on ultrasonic guided waves, (a) the schematic diagram of this system, (b) piezoelectric transducers mounted in rail web

The piezoelectric transducers (PT) are fixed with spring clips and mounted on the rail web, and the detection system has been installed on a heavy-duty freight line in South Africa, covering a detection interval of 840 km. Y. Yang from the Xi'an University of Technology took the lead in developing a real-time online detection system for rails based on UGW [70], filling the technology gap in China. At present, the detection system shown in Fig. 1-6 is installed on the Baocheng railway, Baoji City, China to achieve real-time online detection of rail damage covering the 64 km interval. It also uses PTs with high electroacoustic conversion efficiency to generate and receive UGW signals. In the detection system PTs are mounted on the rail web and fixed with epoxy resin and clamps.

(a) (b) (c)

Fig. 1-6 The real-time online rail detection system based on ultrasonic guided waves, (a) the internal display of signal processing device, (b) signal processing device and solar power supply module, (c) piezoelectric transducers mounted in rail web

In summary, it can be seen that there are relatively few real-time online inspection systems for rails based on UGW at home and abroad while existing inspection devices are primarily presented in three forms: hand-held, hand-pushed flaw detection trolleys, and large rail flaw detection vehicles. At present, the level of foreign rail damage detection technology is higher than that of China, especially in the real-time online detection of rails. The existing online real-time systems in China mainly highlights that there are still some key problems in

large-scale use and testing. Due to the complex on-site track environment, the transmission of UGW detection signals is unreliable, and the installation of PTs is inconvenient. Therefore, it is very urgent to study the propagation efficiency of UGW in the rail, to effectively improve the signal-to-noise ratio (SNR) of the received signal at the received end. Since the real-time online rail detection system based on UGW is an electro-mechanical-acoustic coupling system, this paper will conduct an in-depth study on PTs selection, impedance matching of PTs, the selection of excitation frequency and excitation pulse for PTs to improve the propagation efficiency of UGW in the rail. Commonly used UGW excitation and reception methods mainly include piezoelectric, electromagnetic, and laser pulse. The advantages and disadvantages of the three types of sensors are specifically listed in Tab. 1-1. According to Tab. 1-1, it is found that piezoelectric ultrasonic transducers (PUTs) are the most widely used and the current transducers used for UGW detection of rails are also mostly PUTs. Love P.W. developed a sandwich piezoelectric ultrasonic transducer (SPUT) for a rail integrity monitoring system [71], which was successfully applied to the monitoring system for a single detection interval of 2.5 km. Ramatlo D.A. et al. optimized the design of a SPUT for the excitation of UGW in the rails [72-73], which can be used for the damage detection of rail web. This illustrates the feasibility of using a SPUT for the excitation and reception of UGW in the rail inspection. Therefore, the SPUT is also used in this study to achieve the excitation and reception of UGW signals.

Tab. 1-1 Comparison of advantages and disadvantages of common transducer types

Transducer type	Advantages	Disadvantages
PUT	High energy conversion efficiency, high sensitivity, high SNR, low cost	Highly influenced by coupling conditions
EMAT	In-line fast detection, non-contact detection, excitation of almost all waveguide modes, good design	Low SNR, low energy conversion efficiency, only for the detection of conductive and ferromagnetic materials
LUT	Non-contact detection, high spatial-temporal resolution	High equipment cost, technical complexity, low SNR

1.2.3 Research Status on Characteristics Optimization of PUTs

The study of the UGW propagation efficiency in the rail can be divided into hardware optimization design and signal processing, specifically into the impedance matching of PUTs, the optimization of driving circuit and excitation signals of PUTs, and UGW signals processing.

- **The excitation frequency selection of PUTs**

PTs will produce shifts in their series and parallel resonance frequencies due to the acoustic load and environmental factors in detection applications [74-77]. Therefore, it is necessary to change the frequency of the pulse signal used to excite the PTs in real-time, otherwise, the energy transfer efficiency of PTs will be greatly reduced. At present, regarding the investigation of resonance frequency tracking (RFT), it has been proved that the RFT methods based on open-loop control have difficulties in maintaining the transducers operating at the optimal excitation frequency. Hence, these methods based on closed-loop control have attracted considerable attention. In the past few decades, vibration feedback oscillator had been used for RFT [78], but it led to tracking instability because the transducer was included in the

feedback path. The most widely used RFT method in industry is the phase-locked loop (PLL) method [79-83], which is based on the principle that PTs are resonant when the impedance phase is equal to zero. The phase difference of the voltage and the current applied to the transducer is used to control voltage-controlled oscillator (VCO), by which the driving frequency is adjusted to keep the zero phase difference. But the frequency tracking method based on PLL is only suitable for ultrasonic welding, ultrasonic cleaning, and ultrasonic machining, etc. PUTs are driven by the continuous-wave in the mentioned above applications. Maximum conductance tracking method proposed in [84] according to the phenomenon that the power transferred to the load achieves the peak at the largest admittance point. But the above system operated under 25 kHz, which limits its high-frequency applications. L.C. Cheng et al. [85] reported the parallel resonance frequency (PRF) tracing by utilizing the zero voltage switch (ZVS) technique. PRF tracking is based on a PT operating at a PRF, which allows for automatic power regulation when the load changes. Di et al. [86] implemented PRF tracing based on the online measuring for the static capacitance. H.J. Zhang et al. [87] proposed an automatic RFT method utilizing the relationships among the dynamic resistance, impedance phase, and resonance frequency of the PT. X. Liu et al. [88] proposed a tracking scheme based on a bandpass filter (BPF) oscillator, using the intrinsic resonance point of PTs through a sensing bridge. However, to achieve the maintenance of high power transmission efficiency, all of the above methods achieve automatic tracking of the resonant frequency at the transmitting end.

In particular, the pitch-catch mechanism is widely used in ultrasonic detection systems especially in SHM. It should be noted that PTs in ultrasonic detection applications typically operate in a pulsed wave mode, i.e., a pulsed string is used to excite PTs, which is quite different from other ultrasonic applications. For these applications such as ultrasonic welding, ultrasonic cleaning, and ultrasonic machining, the transmitting PTs normally operate at continuous wave mode, and their acoustic loads and ambient temperature change drastically. Hence, based on the frequency sweep tracking method, the power transmission efficiency of the transmitting PTs can greatly reduce. In long-range ultrasonic detection applications, the load and ambient temperature of PUTs change relatively slowly. Thus, frequency scan-based tracking methods are the most direct and effective. It should be noted that PTs have maximum gain at its resonance frequency while have maximum receiving gain at its parallel resonance frequency in ultrasonic detection systems. For improving power transmission efficiency in PTs, the frequency tracking at the receiving end has the following advantages:

a) The effect of ambient temperature variation on the detection frequency of the entire ultrasonic detection system is fully considered.
b) The effect of the entire detected structural part and the receiving PTs viewed as an acoustic load on the transmitting PTs is taken into account.
c) The receiving PTs can operate at the optimal working conditions and receive the maximum signal amplitude.

- **Impedance matching of PUTs**

In general, impedance matching of PTs mainly includes both electrical impedance matching (EIM) and acoustic impedance matching (AIM). To achieve high energy transfer efficiency, PTs usually operate at resonant frequencies, where the PT can be equivalent to a

capacitor and a resistance in parallel. At this time, its total impedance is capacitive. Due to the presence of capacitive reactance, the reactive power of PTs increases and the active power decreases, while the energy transfer efficiency of PTs will also be reduced. This requires the addition of an EIM circuit to effectively eliminate capacitive reactance and change resistance, thereby achieving efficient energy transmission. Besides, in ultrasonic testing applications, the difference in acoustic impedance between the vibration radiation surface of the ultrasonic transducer and the surface of the structure to be tested is large. Because ultrasonic waves are very likely to cause reflections at the structural-acoustic impedance discontinuities, the energy of incident waves will be greatly reduced. It is often necessary to fill a transition medium material between the two to achieve AIM, thereby reducing the acoustic impedance difference and reflected wave energy. Therefore, for impedance matching of PTs will be crucial for the improvement of the propagation efficiency of UGW in the structure.

Regarding the investigation of EIM for piezoelectric transducers, the published articles mainly focused on researching the electrical effect, such as bandwidth, the received amplitude, and the power of the acquired signal [89-92]. Also, the design of EIM networks for high-frequency transducers has attracted much attention. Lockwood G.R. et al. designed two-element transmission line matching circuits based on network theory [93], Moon J.Y. et al. proposed electrical matching networks based on filter structures [94], and Kim M.G. et al. presented an approach for the design of impedance matching network based on impedance analysis [95]. However, the effect of EIM networks on the electromechanical characteristics for piezoelectric ultrasonic transducers has received little attention. It is well known that the Butterworth-Van-Dyke (BVD) model is determined from an impedance analysis of piezoelectric transducers, but it cannot be used to directly investigate the electromechanical characteristics of piezoelectric transducers. Based on Mason’s equivalent circuit model of PTs, the effect of simple EIM networks, such as a shunt inductance, an inductance in series, on the electromechanical characteristics of SPUTs was investigated [96], but it is difficult the use of this method for parameter acquisition and combination with some other module circuits using this method. In summary, it can be found that there are few studies on the effect of EIM on the electromechanical characteristics of PTs, and only a single inductor is used to match PTs.

The matching layer design of PTs depends mainly on the application of the transducer. Ultrasonic transducer applications can be divided into two main categories: high-power and high-precision detection applications [97]. For high-precision testing applications, ultrasonic waves are required to have a short ring-down time and high bandwidth. For high-power applications, the highest possible ultrasonic power is obtained at the cost of bandwidth. However, for achieving a wide frequency band or maximum amplitude, this is closely related to the characteristics of the AIM layer. AIM between the transducer and the radiating medium is usually implemented using a quarter-wavelength or impedance gradient layer design theory [98]. At present, the research on AIM of PTs is mainly focused on the research of AIM of high-frequency PUTs in medical applications. It is reported that SiO2 aerogel is used as the AIM layer and the aerogel density in the range of 300 kg/m3~2000 kg/m3 can be used in ultrasound equipment [98], and the study showed that the energy transfer efficiency can be over 99% under certain conditions. The literature [99] compared and analyzed the homogeneous and composite matching layers, in which the homogeneous matching layer used tungsten-vinyl

complex, while the composite matching layer used tungsten-vinyl complex and polyurethane polymer. It is shown that the composite matching layer has a smaller insertion loss and the transducer is more sensitive. The rotary coating technique was used to prepare alumina-polymer nano-composite films with an acoustic impedance of 2.8 MRayls ~ 5.1 MRayls and attenuation rate of 15 dB/mm at a frequency of 40 MHz [100]. It was reported that the preparation of epoxy resin materials used light curing and their acoustic properties with acoustic impedance ranging was from 0.88 MRayls to 6.25 MRayls [101]. The influence of coupling interface layer thickness and shear modulus on the lamb wave generation of PTs was investigated in [102]. It was found that a thick coupling layer with low shear modulus is required for thinner piezoelectric transducers. For high-frequency medical ultrasound transducer, using RTV615 silicone rubber doped with different proportions of alumina powder to prepare matching layer material was reported in [103]. It was shown that the doped alumina powder has the best acoustic impedance matching characteristics at a volume fraction of 7.93%. Based on the quarter-wavelength theory, a combination of porous alumina and epoxy resin to design the matching layer was presented in [104]. It was shown that the designed matching layer can effectively increase the bandwidth with an insertion loss of -22.7 dB. The AIM materials were prepared by mixing different metal ions and grease [105] and it was shown that the AIM layer based on Li+ can effectively improve the detection sensitivity. To sum up, it can be found that the research on AIM of PTs mainly focuses on the material preparation of the matching layer and its acoustic properties, and concentrates on the design of the matching layer of high-frequency medical ultrasonic transducers. It is shown that there are fewer reports on the design of the matching layer of PUTs in detection applications.

- **Optimization design of driving circuits for PUTs**

Typically, the ultrasonic detection system consists of a transmitter, receiver, and PUT, as well as the object to be detected. The PUT is the core component of the ultrasonic inspection system, and its working condition will directly affect the reliability and accuracy of the inspection system. When the UGW signal is propagated over a long distance, its transmission loss is greater. For long-range UGW detection systems, to ensure that the amplitude of the received signal is sufficiently large, the output voltage peak-to-peak of the driving circuit is over 1000V. Therefore, the design of high-voltage and efficient PUT driving circuits is essential. Regarding the investigation of high voltage pulser for piezoelectric ultrasonic transducers, the published articles provide some topologies [106-107] such as a single-element structure (just using capacitor charge and discharge to form an instantaneous narrow pulse). Unfortunately, these topologies are only used for single pulse production and are not capable of generating long pulse trains. Based on the BVD model, it can be seen that piezoelectric ultrasonic transducers are mainly capacitive when they are operated at resonant frequencies. The capacitance of piezoelectric transducers can reach 3000pF, which will change the bandwidth of the pulser and also lead to reducing excitation efficiency. For this reason, the capacitance needs to be eliminated by some matching circuits [108]. Then a bipolar pulse generator that can produce long pulse trains was reported in [109]. It is shown that the output voltage pulse has lower unwanted DC and the low-frequency components can reduce leakage current. Besides, some topologies used P- and N-channel MOSFETs [110-114]. Combined with the pulse compression technique, they can operate up to 60 MHz and generate long pulse trains with a

maximum 240Vp-p excitation voltage. Svilainis L. et al. proposed a pulse generator based on the half-bridge topology for excitation of PUTs [115], which can generate voltage pulse with a peak-to-peak value of 500V but requires an extra DC high voltage. However, this excitation voltage is relatively low for PUTs used in long-range UGW detection systems. Svilainis L. et al. [116] designed a high-voltage pulse generator based on a half-bridge topology. It is capable of generating a pulse with a peak-to-peak voltage of 1000V, but it also requires an additional DC high voltage. In summary, it can be found that the current research on driving circuits of PTs is mainly focused on the driver design of high-frequency PUTs, while less attention is paid to the driving circuit of low frequency PUTs used in long-distance ultrasonic detection. Additionally, the peak-to-peak value of the pulse voltage generated by these driving circuits cannot meet the excitation requirements of PUTs in long-distance detection applications, and they rarely consider the EIM for PUTs.

- **Signal processing of UGW in the rail**

The SNR of the received signal is relatively low in practical applications due to the energy attenuation, dispersion, and multimodal effects of guided waves in long rails. In addition, the railway site environment is complex and variable and the UGW signal is influenced by environmental factors such as temperature, humidity, and rain. This leads to a further reduction in the SNR of the received signal and making signal feature identification more difficult. The UGW signal in the rails is limited by both time and frequency, with typical non-stable random signal characteristics. It is difficult to achieve good results with a single time domain or frequency domain processing. Scholars used the time-frequency analysis method based on wavelet transform (WT) to process the UGW signals in the rails [117-118]. It is shown that this method can improve the SNR of the signal and can be used for the separation of rail modals and defect detection. However, when interference signals with similar characteristics are received, it will lead to misjudgment. To reduce the impact of dispersion, scholars have proposed some methods of dispersion compensation. Wilcox P.D. [119] used the prior knowledge of the dispersion characteristics of guided waves to map guided wave signals from the time domain to the distance domain to achieve the dispersion compensation for guided wave signals. A UGW processing method based on compressed sensing was presented in [120] to accomplish the dispersion compensation of single-mode and multimodal guided waves. It should be noted that even if the dispersion effect of guided waves can be eliminated, the amplitude increase of the received signal is still limited. Initially, to effectively increase the SNR, the coded excitation technology was applied to some medical applications based on ultrasound detection. H. Zhang [121] used Barker code excitation to conduct UGW detection in long bones and it was found that Barker code can improve the SNR of the received signal by 6.64 dB. To improve the ultrasonic image quality, a new Barker coding excitation based on linear frequency modulation (LFM) carrier was proposed in [122]. Subsequently, coded excitation techniques were introduced to other ultrasonic detection applications. To achieve a high-resolution UGW response, M. Yucel et al. [123] comparatively analyzed the maximum length sequence and LFM excitation. P4 multiphase sequence used to encode the ultrasonic excitation signal was proposed in [124] for the non-destructive testing (NDT) system based on air-coupled PUTs. To easily identify the characteristics of high-voltage pulses in the track circuit, the effects of two coding excitations based on Kasami sequences and LS (Loosely Synchronized) coding was analyzed in

[125] and it was shown that Kasami sequences are better. However, both LFM signals and P4 multiphase sequences require complex hardware circuits; compared to Barker codes, Kasami sequences have higher autocorrelation distance sidelobe levels. Barker code has the lowest autocorrelation distance sidelobe level in all bi-phase codes with equaling length, and it only requires a single transmission and less hardware. Thence, the encoding excitation technique based on the Barker code used in the long rail broken detection system using UGW is utilized in this paper.

Generally, pulse compression can be achieved by a matched filter, weighted matched filter, and mismatched filter. To ensure a high SNR gain, pulse compression based on Barker codes is often implemented using a matched filter. Some sidelobe will appear in the output results of the matched filter, which is from the effects of UGW dispersion in the rail, effects of the used modulation techniques, bandwidth constraints, multi-path, and noise. Therefore, it is vital to adopt peaks detection approaches for the correct identification of maximum peaks. Existing research work shows that most peak detection systems are based on one or more fixed amplitude thresholds [126-127], but it will be more difficult to adjust this amplitude threshold when the energy of the detected signal changes continuously. To overcome this problem, the dynamic threshold was used in peak detection [128], which can adapt to the energy change of the received signal at different times and the influence of noise and other factors. There is an in-depth and systematic study on the identification of maximum values in the detection of ECG QRS wave groups in the medical field. An R peak detection method based on differential and dynamic threshold was proposed in [129]. M. S. Manikandan et al. [130] proposed a new R peak detector based on Shannon energy envelope, Hilbert transform (HT), and moving average filtering (MAF). Afterward, an automatic R-peak detection method based on WT and HT was presented in [131]. Besides, for track circuits based on coded transmissions, a new adaptive peak detection algorithm was proposed by discrete wavelet transform (DWT) and HT in [132]. However, these aforementioned algorithms either require some amplitude thresholds or have a high degree of complexity that does not meet the real-time requirements of the broken rail detection system based on UGW. Therefore, it is necessary to study the adaptive peak detection algorithm with high real-time performance.

1.3 Research Content and Structure of the Thesis

1.3.1 Main Research Contents and Chapter Arrangements

This thesis focuses on the problem of improving the propagation efficiency of UGW in rail. It mainly conducts in-depth research from the aspects of impedance matching, optimized design of driving circuits, optimization of excitation signals, and signal processing. The main content of this paper can be divided into the following seven chapters:

Chapter 1: Introduction

This chapter first introduces the research background and significance of the topic and elaborates on the current status of the existing rail damage detection. Subsequently, the problems faced by the broken rail real-time detection system based on UGW are brought out. It also illustrates the problems existing in the research of UGW propagation efficiency in the rail.

Chapter 2: UGW Broken Rail Detection System and Related Theoretical Basis

This chapter introduces the broken rail real-time detection system based on UGW and illustrates the related concepts of UGW and the vibration modes of PUTs. Furthermore, it focuses on the analysis methods and theories of PUTs, including one-dimensional wave and transmission line theory, equivalent circuit method, and finite element (FE) analysis method.

Chapter 3: Research on PSpice Model of SPUTs in Longitudinal Vibration

In this chapter, PSpice equivalent circuit models of SPUTs in longitudinal vibration and the pitch-catch setup are established, all based on the force-electricity analogy method, one-dimensional wave theory, and transmission line theory. This lays the foundation and provides theoretical guidance for the research on the electromechanical characteristics of PUTs.

Chapter 4: Research on the Effect of Impedance Matching on the Electromechanical Characteristics of PUTs

Based on the established PSpice model of longitudinal vibration SPUTs, this chapter focuses on the study of the effect of impedance matching on the electromechanical characteristics of SPUTs. The specific studies are mainly carried out from impedance analysis and time-domain transient analysis and the best matching network and acoustic matching layer materials are determined.

Chapter 5: Research on the Optimization of Driving Circuits for PUTs

This chapter optimizes the design of the driving circuit for PUTs from the aspects of circuit topologies, switching ripple absorption, EIM, and tailing absorption. Finally, the effectiveness and practicability of the proposed high voltage driving circuit are verified by some experiments.

Chapter 6: Research on the Optimization of Excitation Signals for PUTs

Based on the theory of digital tracking filter design, this chapter proposes to track the excitation frequency of a PUT from the receiving end. Based on the determination of the optimal excitation frequency, the optimal excitation pulse waveform and the number of pulse cycles are further determined in conjunction with the pulse compression technique. Besides, an adaptive peak detection algorithm is proposed.

Chapter 7: Summary and Future Works

This chapter begins with a summary of the work on the propagation efficiency of UGW in the rail. Then the shortcomings and deficiencies of the current broken rail real-time detection system based on UGW are described, as a base for giving future research works.

1.4 Conclusion

This chapter first introduces the research background and significance of the topic and elaborates on the current status of the existing rail damage detection. It also points out the shortcomings and drawbacks of the broken rail real-time detection system based on UGW. Besides, an overview of the main research contents of the thesis is presented and the research content of specific chapters is identified.

2 UGW Broken Rail Detection System and Related Theoretical Basis

The UGW detection technology has the advantages of low detection frequency, long-distance detection, and strong immunity to electromagnetic interference. However, when using the UGW detection technique, the dispersion and multimodal nature of the UGW leads to the characteristic complexity of the received signals. This chapter will specifically introduce a broken rail real-time detection system based on UGW and the related theoretical foundations. These provide a solid basis and theoretical guidance for the study of the propagation efficiency of UGW in the rail in the subsequent chapters of this document.

2.1 Broken Rail Real-time Detection System Based on UGW

The broken rail real-time detection system based on UGW shown in Fig. 2-1 consists of transmitter nodes, receiver nodes, communication equipment including wireless data transmission module (WDTM) and GPRS module, remote server, and terminals, power supply unit, and PUTs. The receiving node and the transmitting node are interactively arranged with 1km as the detection interval. The ultrasonic transducer is mounted on the rail web and the signal processing unit and power supply equipment are located next to the railway. Since there is no GPRS signal inside tunnels, WDTM modules are used to transmit the detection information in these scenarios employing a relay mode. The transmitting node sends the characteristic signal at a certain time interval. If the receiving node fails to receive the characteristic signal continuously, it will determine that a rail breakage occurs in the detection interval.

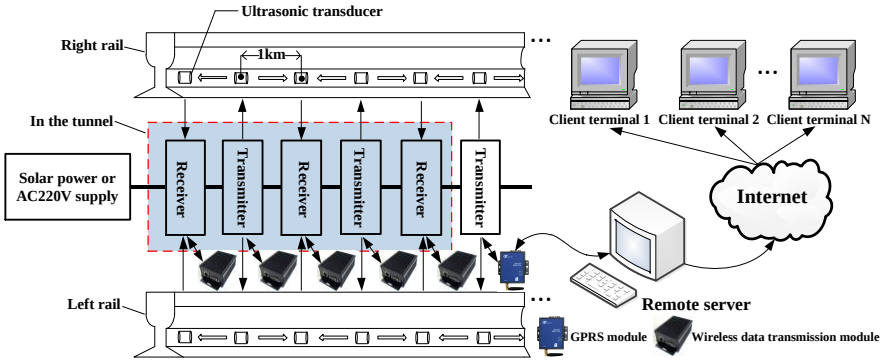

Fig. 2-1 Broken rail real-time detection system based on UGW

2.2 The Related Concepts of UGW

2.2.1 UGW

The propagation direction of elastic waves in the medium and the vibration direction of the sound source can be the same or different. Body waves refer to elastic waves propagating in an

infinitely uniform medium. According to the vibration direction, it can be divided into transverse waves and longitudinal waves, which respectively propagate forward at a certain speed without waveform coupling. The biggest difference between body waves and guided waves is that they are not affected by the boundary of the propagation structure. When ultrasonic waves propagate in the waveguide such as rails, bars, and pipes, multiple reflections, refractions, and transmissions will occur at the waveguide boundary or discontinuity, resulting in reflected waves, transmitted waves and refracted waves, which are coupled with each other to eventually form UGW.

2.2.2 Phase Velocity and Group Velocity

Phase velocity and group velocity are two important concepts that reflect the velocity of guided waves. The group velocity is the speed at which the envelope of the wave packet (or the maximum amplitude) propagates in the medium. It can also be considered as the speed at which the wave energy propagates along with the wave. The group velocity of guided waves can be calculated as follows [40]:

$$c_g = \frac{d\omega}{dk} \tag{2-1}$$

where ω represents angular frequency and k indicates wavenumber. The phase velocity reflects the propagation velocity of the fixed phase point on the guided wave along the propagation direction, and its calculation formula is as follows [40]:

$$c_p = \frac{\omega}{k} \tag{2-2}$$

Guided waves usually propagate in the form of wave packets, but for guided wave packets, it has certain energy in a certain frequency range. At the same time, these different frequency components propagate at different phase velocities, respectively, and the overall wave packet propagates forward at the group velocity. The relationship between group velocity and phase velocity is shown in Fig. 2-2, and the relationship between them can be expressed as [40]:

$$c_g = \frac{c_p^2}{c_p^2 - \omega \dfrac{dc_p}{d\omega}} \tag{2-3}$$

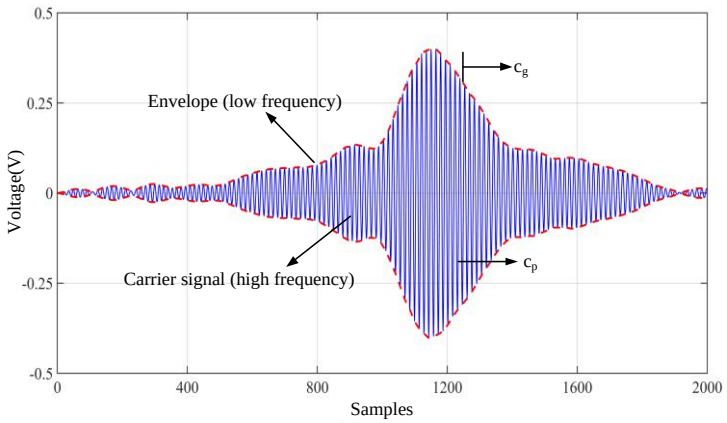

Fig. 2-2 The relationship between phase velocity and group velocity

From Fig. 2-2, the blue curve indicates the signal waveform and the red dotted line indicates the

signal envelope. The envelope has a lower frequency and the signal waveform has a higher frequency. The relationship between the two is like the relationship between a modulated signal and a carrier signal, where the signal waveform also contains waves with different frequency components. It should be noted that in dispersive media, phase velocities tend to be larger than group velocity values.

2.2.3 Multimodal and Dispersion Characteristics

The introduction of boundary conditions makes the waveguide multimodal and dispersive, which makes the process of solving the wave equation complex. The wave equation in an isotropic solid medium can be expressed as [133]:

$$(\lambda+2\mu)\nabla\nabla u-\mu\nabla\times\nabla\times u=\rho\frac{\partial^2 u}{\partial t^2} \tag{2-4}$$

where λ and μ are Lame constant, u indicates displacement. The stress and displacement boundary conditions can be expressed as

$$u(x,t)=u_0(x,t) \quad t_i=\sigma_{ij}n_j \tag{2-5}$$

Where t_i is surface stress, σ_{ij} represents normal stress and shear stress in various directions along the coordinate axis, n_j is the unit vector perpendicular to the direction of the media surface.

The dispersion characteristics are an important basis for studying the propagation characteristics of UGW. Due to the influence of the dispersion characteristics, the time-domain width of the UGW signal will become wider and the peak-to-peak value will gradually decrease, which will directly lead to the difficulty of analyzing and identifying the UGW signal. The dispersion characteristic curve of the guided wave is generally characterized by the dispersion characteristics of the phase velocity and the group velocity. Fig. 2-3 shows the dispersion curve of the guided wave in the CHN60 type rail.

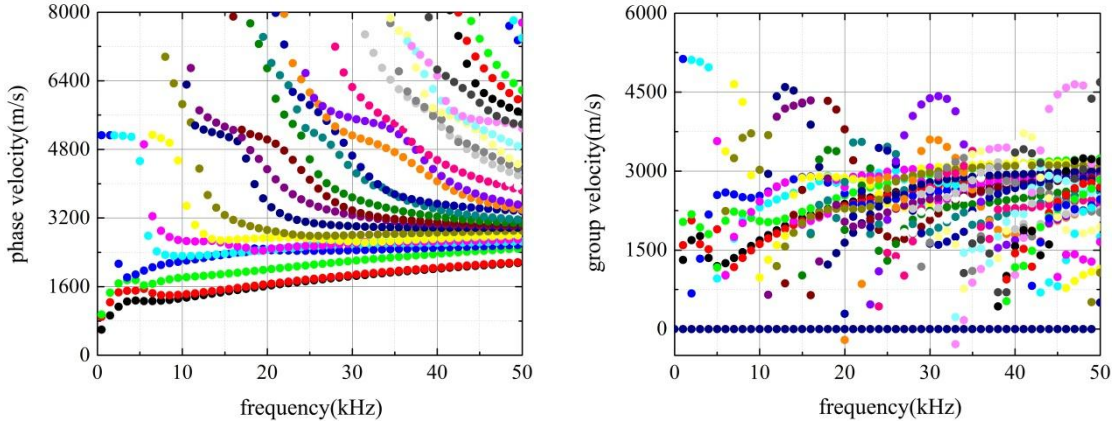

(a) (b)

Fig. 2-3 The dispersion curve of guided wave in rail, (a) phase velocity, (b) group velocity

From Fig. 2-3, it is found that as the excitation frequency of the guided wave increases, the number of modes of the guided wave increases. It can also be seen that at least two or more waveguide modes are generally present at a given excitation frequency, which propagates through the medium at different group speeds respectively. In particular, it should be noted that

the propagation characteristics of the guided wave are highly dependent on the shape of the waveguide. The more complex the waveguide cross-sectional characteristics, the greater the number of guided wave modes. Therefore, for a definite waveguide, the choice of excitation frequency is critical to the accuracy and reliability of UGW detection.

2.3 Common Vibration Modes of PUTs

The vibrations of piezoelectric ceramic vibrators can be divided into transverse effect vibrations and longitudinal effect vibrations. The difference between the two depends mainly on the excitation electric field of piezoelectric ceramic vibrators and the direction of elastic wave propagation. Under the transverse effect vibrating, the excitation electric field of the vibrator is perpendicular to the direction of propagation of the elastic wave, so the transverse effect vibrational mode of the piezoelectric ceramic is not subject to the electrical boundary conditions of the piezoelectric ceramic vibrator. Typical transverse effect vibration modes include the length-extension and width-extension vibration modes of rectangular piezoelectric ceramic vibrators, and the radial vibration modes of thin rings and thin discs. Under the longitudinal effect vibrating, the excitation electric field of the vibrator is parallel to the direction of propagation of the elastic wave, so the longitudinal effect vibration mode is bounded by the electrical boundary conditions of the piezoelectric ceramic vibrator. The longitudinal effect vibration modes are mainly the thickness vibration of thin plates, the longitudinal vibration of longitudinally polarized slender round bars, and the thickness-shear vibration mode of thin plates.

When the polarization direction is parallel to the direction of the exciting electric field, stretching vibrations are produced. But when the polarization direction is perpendicular to the electric field, shear vibrations are produced. Extension vibrations include both length-extension and thickness-extension vibrations, while shear vibrations include both plane shear and thickness-shear vibrations. Therefore, the vibration modes of piezoelectric ceramic vibrators mainly include length extension (LE), thickness extension (TE), planar shear (PS), and thickness-shear (TS) types, whose vibration schematics are shown in Fig. 2-4.

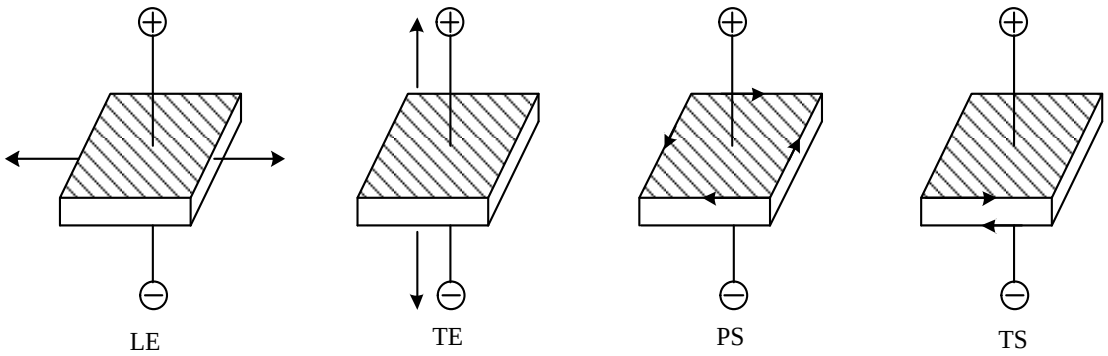

Fig. 2-4 The four types of vibration mode for piezoelectric ceramic

According to the relationship between the propagation direction of elastic waves and the vibration direction, the elastic waves generated by the piezoelectric effect can be divided into transverse and longitudinal waves. The relationship between the elastic waves and the piezoelectric effect is shown in Tab. 2-1.

Tab. 2-1 The relationship between the elastic wave and piezoelectric effect [134]

Elastic wave polarization axis direction	The elastic wave vibration direction	
	Longitudinal wave	Transverse wave
Longitudinal effect	TE d_{11}, d_{22}, d_{33}	TS d_{15}, d_{16}, d_{24}, d_{26}, d_{34}, d_{36}
Transverse effect	LE d_{12}, d_{13}, d_{21}, d_{23}, d_{31}, d_{32}	PS d_{14}, d_{25}, d_{36} 和 TS*

* For the TS vibration mode, longitudinal effects and lateral effects can exist simultaneously.

2.3.1 Extension Vibration

The extended vibration modes of piezoelectric ceramic vibrators mainly include length extension, radial extension, and thickness extension. The following is an example of the length extension vibration mode of piezoelectric ceramic thin long bars. As shown in Fig. 2-5 in the piezoelectric ceramic vibrator of thin long bars, the polarization direction of the vibrator and thickness direction are parallel to each other, while the electrode surface and thickness direction are perpendicular to each other, the two ends of the piezoelectric ceramic disc are in a mechanical free state. When an alternating electric field is applied, the thin long bar of piezoelectric ceramic will produce an extension vibration along its length. The vibration direction and the propagation direction of each of the particles in the vibration body are consistent with the extension direction of the length of the thin bars.

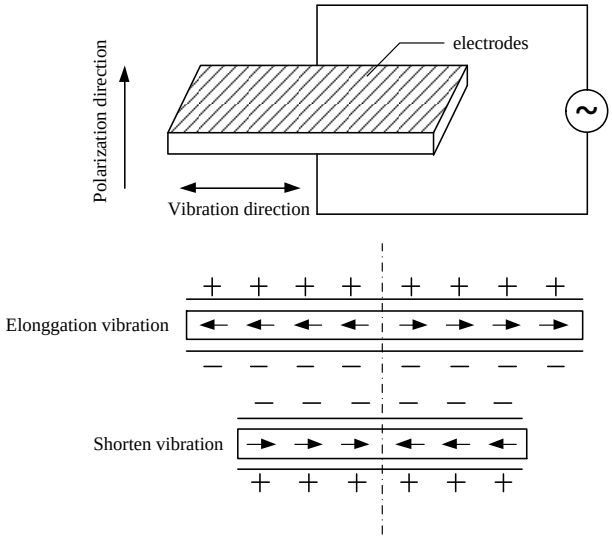

Fig. 2-5 The schematic diagram of stretching vibration in the length direction

The amplitude at the center of the piezoelectric thin bar is zero at the base frequency vibration, which is the node. The amplitude at both ends of the vibrator is the greatest, which is the antinode. Therefore, to avoid affecting the vibration of the vibrator, it must be fixed in the position of the node. In general, when the change frequency of the alternating electric field is equal to the resonant frequency, the piezoelectric ceramic vibrator will be in a resonant state. The relationship between the resonant frequency and the length of piezoelectric ceramic thin bars can be expressed as [134]

$$f_{\mathrm{r}}=\frac{1}{2l}\sqrt{\frac{1}{\rho s_{11}^{\mathrm{E}}}} \tag{2-6}$$

where l is the length of the piezoelectric ceramic thin bar, ρ is the material density of the piezoelectric ceramic and s_{11}^{E} is the short circuit elastic compliance constant.

According to equation (2-6), it is found that the resonant frequency of the LE vibration mode is inversely proportional to its length. It should be noted that the extension vibrations along with the thickness and width direction also exist in the piezoelectric ceramic thin bar, so the extension vibration resonance frequencies in the thickness and width direction are much larger than the resonance frequency of the piezoelectric ceramic vibrator along the length direction. Their interaction is very small and negligible. Generally, the resonant frequency of piezoelectric ceramic vibrators refers to the primary resonant frequency. However, piezoelectric ceramic vibrators produce high harmonics in addition to the primary harmonic frequency. For structures such as thin bars of piezoelectric ceramic with full electrodes, only an odd number of harmonic frequencies can be generated. The relationship between its odd resonant frequency and the fundamental frequency can be expressed as

$$f_{2n\text{-}1}=(2n-1)f_{\mathrm{r}} \tag{2-7}$$

where n takes a positive integer value and $n=1,\ 2,\ 3,\ldots$. In particular, the effective vibration frequency range of the LE vibration mode of the piezoelectric vibrator for thin bars is 15~200 kHz.

2.3.2 Shear Vibration in Thickness

For high-frequency applications, the TS vibration mode can be used in addition to the thickness vibration in the extension vibration mode. The main feature of this mode is that the electrode surface is parallel to the polarization direction. In the presence of an alternating electric field, the piezoelectric ceramic discs produce TS vibrations as shown in Fig. 2-6. In this Fig. 2-6, the polarization is in the third direction, and the applied electric field is in the first direction (i.e. the thickness direction). When the vibration occurs, the A_{13} plane produces a shear strain. The vibration direction is consistent with the third direction, but the wave propagation direction is consistent with the electric field direction, so this mode generates transverse waves.

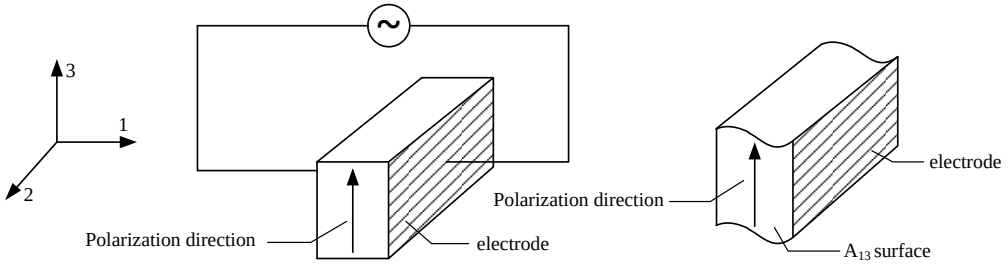

Fig. 2-6 The schematic diagram of shear vibration in the thickness direction

TS vibration can be divided into two categories. One is the polarization along the length or width of the piezoelectric ceramic vibrator. For this case, when an excitation electric field is applied in the thickness direction and the wave propagation direction is perpendicular to the polarization direction (i.e. width direction), TS wave is generated. Another is the polarization in

the thickness direction of the piezoelectric ceramic vibrator. In this case, when an excitation electric field is applied in the width or length direction and the wave propagation direction is parallel to the polarization direction (i.e. thickness direction), TS* wave is generated. The relationship between the anti-resonance frequency of TS vibration and the thickness of piezoelectric ceramics is given as [134]

$$f_a = \frac{1}{2t}\sqrt{\frac{1}{\rho s_{55}^{\mathrm{D}}}} \tag{2-8}$$

where t indicates the thickness of the piezoelectric ceramic disc, ρ is the material density of the piezoelectric ceramic and s_{55}^{D} represents the open circuit elastic compliance constant. According to equation (2-8), it can be concluded that the resonance frequency of the thickness-shear vibration mode is inversely proportional to its thickness.

2.3.3 Bending Vibration

For piezoelectric ceramic vibrators with more than two types of excitation electrodes, when the polarization direction is parallel to the direction of the electric field and the applied method is different, bending vibration will occur. Due to the vibration direction is perpendicular to the propagation direction of the elastic wave, so bending vibration is a transverse wave. Bending vibration can generally be divided into thickness bending and transverse bending. The following case is a specific example of a thickness bending vibration mode. In general, bending oscillations can be produced by bonding together two piezoelectric ceramic discs of equal thickness with electrodes on the back. When the two piezoelectric ceramic discs being bonded have opposite polarization directions, the excitation power supply should be connected in series. When the two piezoelectric ceramic discs have the same polarization direction, the excitation power supply should be connected in parallel. From Fig. 2-7, for series piezoelectric ceramic vibrators, when the upper electrode is positive, the lower electrode is negative, with the help of the reverse piezoelectric effect, the upper piezoelectric disc is elongated and the lower piezoelectric disc is shortened. At this time, a convex bending deformation is generated. When the positive and negative electrodes are swapped, the upper piezoelectric disc is shortened and the lower piezoelectric disc is elongated. At this time, a concave bending deformation can occur. If the applied electric field is an alternating electric field, a bending vibration appears.

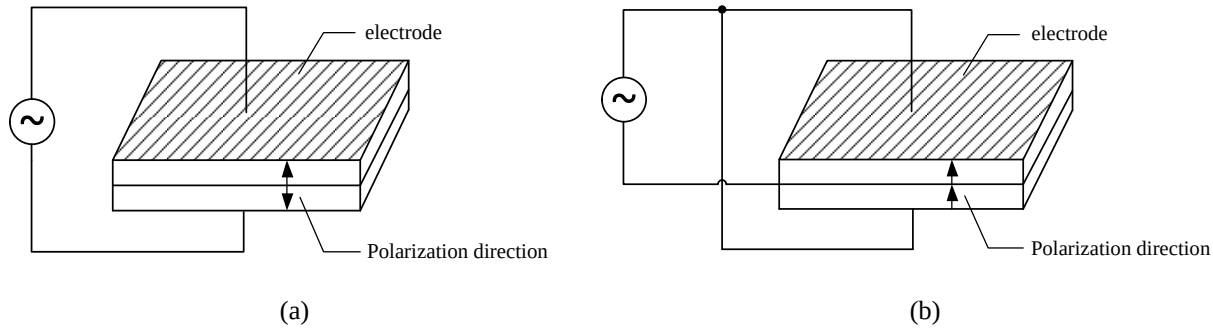

(a) (b)

Fig. 2-7 The piezoelectric ceramic vibrator of the thickness bending, (a) series type, (b) parallel type

When two piezoelectric ceramic bars with the same thickness and opposite polarization directions are bonded together, and an alternating voltage is applied to the adhesive disc, a bending vibration in the thickness direction appears. The relationship between the resonance

frequency and the length and thickness of the adhesive disc can be expressed as [134]

$$f_{\mathrm{r}} = B\frac{t}{l^2} \tag{2-9}$$

where the coefficient B is related to the properties of the piezoelectric ceramic material, t and l represent the thickness and length, respectively, of the piezoelectric ceramic disc. Besides, the bonding of two piezoelectric ceramic discs with opposite polarities to a thin metal disc can also produce bending vibration in the thickness direction. However, it should be noted that the thin metal disc and the adhesive have a great influence on the performance of the bending vibration component, so the thin metal disc is usually selected from a nickel-chromium-titanium alloy material with high stability.

2.4 Analysis Methods and Theory of PUTs

2.4.1 Modal Analysis and Harmonic Response Analysis Theory

Generally, if the long-term effect of the structure after loading is studied, static analysis is sufficient. However, if the loading process is short or the load is dynamic, then the dynamic analysis must be considered. In engineering applications, common types of dynamic analysis include modal analysis, harmonic response analysis, frequency spectrum analysis, and random vibration analysis. In these analyses, modal analysis is mainly used to study the vibration characteristics of structures and mechanical parts, i.e. natural frequency and vibration mode, and it is also an important basis for other analyses. For the Finite Element (FE) analysis of PUTs, modal analysis is often used to solve the vibration mode, and harmonic response analysis is used to obtain its admittance or impedance characteristics. Therefore, the focus here is on modal analysis and harmonic response analysis.

The biggest difference between dynamic and static analysis is that the inertial force is considered in the balanced equation, and the definition of internal force is different. The dynamic equilibrium equation is as follows [135]:

$$[M]\{\ddot{u}\}+[K]\{u\}+[C]\{\dot{u}\}-\{F\}=0 \tag{2-10}$$

where $[M]$ is the structural mass matrix, $[K]$ is the elastic stiffness matrix, $[C]$ is the structural damping matrix, $[F]$ is the external force applied on the structure; $\{u\}$ denotes the structural displacement, $\{\dot{u}\}$ is the structural velocity, $\{\ddot{u}\}$ is the structural acceleration.

Unlike static analysis, the internal forces in the dynamic analysis include not only structural deformation but also damping effects. The natural frequency can be obtained by analyzing the dynamic response of the structure under no load, and the balance equation can be expressed as

$$[M]\{\ddot{u}\}+[K]\{u\}+[C]\{\dot{u}\}=0 \tag{2-11}$$

For an undamping system, equation (2-11) can be rewritten as

$$[M]\{\ddot{u}\}+[K]\{u\}=0 \tag{2-12}$$

The solution of equation (2-12) can be expressed as

$$u = \phi \exp(i\omega t) \tag{2-13}$$

Substituting equation (2-13) into equation (2-12), the following eigenvalue equation is given as

$$[K]\{\phi_i\} = \lambda[M]\{\phi_i\} \tag{2-14}$$

where $\lambda = \omega^2$. If the number of eigenvalues of the system is *n*, then the degree of freedom of the FE model is *n*. λ_i represents the *i*-th eigenvalue and ω_i denotes the *i*-th natural frequency, ϕ_i indicates the corresponding eigenvector. It should be pointed out that the eigenvectors are also called modal or mode shapes, which represent the deformation state of the structure. Therefore, the natural frequency and mode of the structure can be obtained by solving the equation (2-14).

Generally in the FE analysis software, the natural frequency and mode shape are calculated for the undamping system, but most engineering applications need to consider structural damping. The natural frequency relationship under damping can express as

$$\omega_{\mathrm{d}} = \omega\sqrt{1-\xi^2} \tag{2-15}$$

where ω_d represents the natural frequency under damping, $\xi = c/c_0$ indicates the critical damping ratio, c denotes the vibration damping, c_0 indicates the critical damping. The common types of damping are direct modal damping, Rayleigh damping, and composite modal damping, which are illustrated as follows [135]:

- **Direct modal damping**

It can allow us the definition of the critical damping ratio ξ of each mode, and the value range is 1% ~ 10%.

- **Rayleigh damping**

Rayleigh damping assumes that the structural damping matrix is a linear combination of the structural mass matrix and the stiffness matrix, which is specifically expressed as follows:

$$C = \alpha M + \beta K \tag{2-16}$$

where α and β are constants. In general, this damping model is ineffective for large damping systems, i.e. systems with critical damping of more than 10%.

- **Composite damping**

A critical damping ratio can be defined for each material and corresponds to the damping of the entire structure. When multiple types of materials are present in the structure, it is more appropriate to characterize structural damping using composite damping.

Harmonic response analysis is a technique used to determine the steady-state response of a linear structure when subjected to one or more loads that vary in simple harmonic laws over time. The harmonic response analysis technique generally calculates only the steady-state forced vibration of a structure and it is a linear analysis technique. The generalized control equation is shown in equation (2-10) where the external force matrix $\{F\}$ and the displacement matrix $\{u\}$ are harmonic.

$$\{F\} = \left\{F_{\max} e^{j\psi}\right\} e^{j\omega t} = (\{F_1\} + j\{F_2\}) e^{j\omega t} \tag{2-17}$$

$$\{u\} = \left\{u_{\max} e^{j\psi}\right\} e^{j\omega t} = (\{u_1\} + j\{u_2\}) e^{j\omega t} \tag{2-18}$$

Substituting equations (2-17) and (2-18) into equation (2-10), the following eigenvalue equation

is given as:

$$(-\omega^2[M]+j\omega[C]+[K])(\{u_1\}+j\{u_2\})=(\{F_1\}+j\{F_2\}) \tag{2-19}$$

Harmonic response analysis of the structure can be performed according to equation (2-19). There are three common methods for solving simple harmonic motion equations: the complete method, the reduced method, and the modal superposition method. The complete method is the easiest method, by using a complete structural matrix, and allows asymmetric matrices. The reduction method uses a reduction matrix, which is faster than the complete method, but it needs the main degree of freedom, and gets an approximate mass matrix and damping matrix according to the main degree of freedom. The mode superposition method obtains each mode based on modal analysis and then calculates the sum of each mode multiplied by its coefficient, which is the fastest solution among the three methods.

2.4.2 Equivalent Circuit Method

According to the force-electricity analogy method, the mechanical vibration system is usually converted into a circuit system in the research field of ultrasonic transducers. The equivalent circuit method of the piezoelectric ceramic vibrator is to use electrical network terminology to represent the mechanical vibration characteristics of the piezoelectric elastic body and at the same time convert some mechanical quantities into electrical ones. This method is convenient for studying the transmission and reception characteristics of PTs and has direct physical significance. Hence, it is widely used in the design and research of PUTs. With the rapid development of computer technology, a lot of FE software has been developed, so that the FE method has also been applied to the research of PUTs. To adapt it for different uses, the equivalent circuit of the piezoelectric ceramic transducer has many forms. At present, commonly used models for establishing equivalent circuits mainly include the BVD model, Mason model [136], Redwood model [137], KLM model [138], and transmission line model [139]. These models will be illustrated in detail in the following sections.

A. BVD Model

As a simple and practical model, through the analysis and processing of the experimental results of the frequency response of the PT, the parameters of the electrical components in the equivalent circuit of the BVD model can be identified. Therefore, it is widely used in the modeling of PT equivalent circuits. From Fig. 2-8, the BVD model is mainly composed of series branches including dynamic inductance L_{m}, dynamic capacitance C_{m}, dynamic resistance R_{m}, and parallel branches consisting of static capacitance C_0.

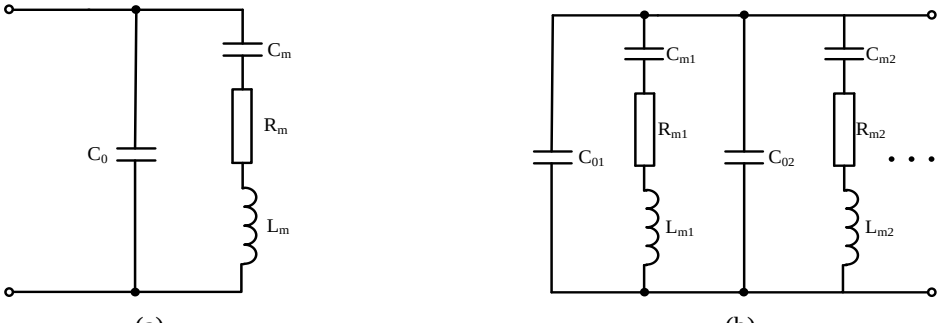

Fig. 2-8 BVD models of PUTs, (a) BVD model of a single frequency, (b) BVD model of multiple frequencies

It should be pointed out that the BVD model does not consider the electrical loss of the PT. It belongs to a lumped parameter equivalent circuit and is only valid near the single-mode series resonance frequency. Besides, some scholars have extended the BVD model of a single frequency to include multiple resonant frequencies of the transducer, and this extended model can model the PT equivalent circuit more effectively [140]. Nevertheless, for some complex vibration modes of piezoelectric ceramic vibrators, they are distributed parametric systems and the BVD model is no longer applicable.

B. Mason Model

The piezoelectric ceramic disc undergoes extension vibration in the thickness direction and its polarization direction and the thickness direction are the same, as shown in Fig. 2-9. Here, A indicates the area of electrodes, and t denotes the thickness of the piezoelectric ceramic disc, V represents the voltage applied to both ends of the ceramic disc. I is the current flowing through the piezoelectric ceramic disc, and F_{L} and F_{B} represent the forces applied to the front and back surfaces and u_{L} and u_{B} denote the particle velocity on the front and back surfaces, respectively. Especially, since the piezoelectric ceramic disc in thickness vibration can excite both the radial vibration base wave and the overtone, the diameter of the piezoelectric ceramic disc must be much larger than its thickness to avoid the interference of the thickness vibration base wave by the radial vibration high overtone. The piezoelectric ceramic disc boundary conditions are: strain S_3 and potential shift D_3 are non-zero. According to the above electrical and mechanical boundary conditions, the piezoelectric ceramic disc will be in thickness-extension vibration. Then the associated piezoelectric equation can be expressed as

$$T_3 = \mathrm{c}_{33}^{\mathrm{D}} S_3 - h_{33} D_3 \tag{2-20}$$

$$E_3 = -h_{33} S_3 + \frac{D_3}{\varepsilon_{33}^{\mathrm{S}}} \tag{2-21}$$

where c_{33}^{D} is the open circuit elastic stiffness constant, $h_{33} = e_{33} / \varepsilon_{33}^{\mathrm{S}}$ is the piezoelectric constant, and e_{33} is the piezoelectric stress constant and $\varepsilon_{33}^{\mathrm{S}}$ is the clamped dielectric constant.

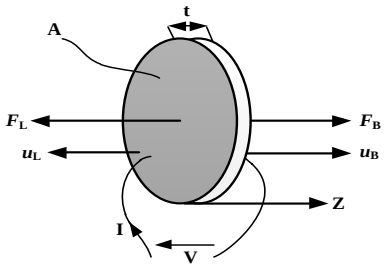

Fig. 2-9 The piezoelectric ceramic disc vibrating in the thickness direction

In general, piezoelectric materials are considered as good insulators. According to the electrostatic charging equation, the internal electric displacement D_3 of the piezoelectric ceramic disc is constant, so we can obtain

$$\frac{\partial D_3}{\partial z} = 0 \tag{2-22}$$

The stress equation of the piezoelectric ceramic disc is a function of the particle displacement

ξ_3 and the strain can be expressed as $S_3 = \partial\xi_3/\partial z$, so we can get:

$$\frac{\partial T_3}{\partial z} = \frac{\rho\partial^2\xi_3}{\partial t^2} \tag{2-23}$$

According to the above four equations, the plane wave equation can be expressed as:

$$\frac{\rho\partial^2\xi_3}{\partial t^2} = \frac{c_{33}^{D}\partial^2\xi_3}{\partial z^2} \tag{2-24}$$

By solving equation (2-24), the particle displacement ξ_3 can be expressed as:

$$\xi_3 = (C_1 e^{-j\beta z} + C_2 e^{j\beta z})e^{j\omega t} \tag{2-25}$$

Here, the two constants C_1 and C_2 can be determined according to the mechanical boundary conditions, and then the boundary conditions are specified as follows:

$$u_B = \frac{\partial\xi_3}{\partial t}\bigg|_{z=0}; \quad u_L = \frac{\partial\xi_3}{\partial t}\bigg|_{z=t} \tag{2-26}$$

$$F_B = -AT_3\bigg|_{z=0}; \quad F_L = -AT_3\bigg|_{z=t} \tag{2-27}$$

In addition, the voltage applied to both ends of the piezoelectric ceramic disc and the current flowing through it can be expressed as:

$$I = j\omega AD_3; \quad V = \int_0^t E_3 dz \tag{2-28}$$

The above equations are arranged into a matrix form as:

$$\begin{pmatrix} F_L \\ F_B \\ V \end{pmatrix} = \begin{pmatrix} Z_0 A/j\tan\beta t & Z_0 A/j\sin\beta t & h_{33}/j\omega \\ Z_0 A/j\sin\beta t & Z_0 A/j\tan\beta t & h_{33}/j\omega \\ h_{33}/j\omega & h_{33}/j\omega & 1/j\omega C_0 \end{pmatrix} \begin{pmatrix} u_L \\ u_B \\ I \end{pmatrix} \tag{2-29}$$

where $C_0 = A\varepsilon_{33}^{S}/t$ represents the clamped capacitance of the piezoelectric ceramic disc, $Z_0 = (\rho c_{33}^{D})^{1/2}$ is the characteristic acoustic impedance of the piezoelectric ceramic disc, and $\beta = \omega/(c_{33}^{D}/\rho)^{1/2}$ is the wavenumber.

According to the impedance analogy, the force analogy is voltage and the particle velocity analogy is current. Combined with the (2-29) equation, the Mason equivalent circuit model of the piezoelectric ceramic disc in thickness vibration can be obtained as shown in Fig. 2-10. It consists of a T-network and an ideal transformer. The T-network represents the propagation of sound waves in piezoelectric materials while the ideal transformer is used to achieve electrical coupling.

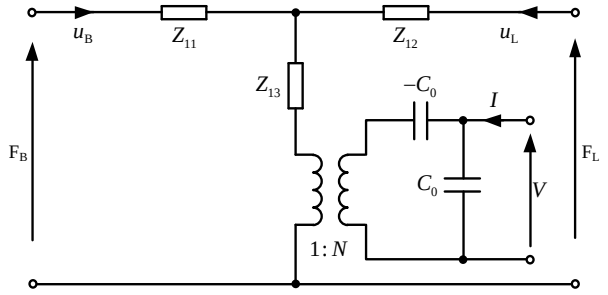

Fig. 2-10 The Mason model of piezoelectric ceramic disc vibrating in the thickness direction

From Fig. 2-10, it should be noted that the characteristic impedances $Z_{11} = Z_{12} = jAZ_0 \tan(\beta t/2)$, $Z_{13} = AZ_0 / j\sin(\beta t/2)$ and the ideal transformer ratio $N = h_{33}C_0$. Besides, the negative capacitance $-C_0$ and the ideal transformer are used to simulate the electromechanical coupling of piezoelectric ceramics. In essence, the Mason model is a six-terminal network that describes the electromechanical characteristics of piezoelectric ceramic vibrators, including two acoustic ports and one electrical port.

C. Redwood Model

The Redwood model was proposed by Redwood on the basis of the Mason equivalent circuit model in 1961. This is mainly to study the time-domain transient characteristics of piezoelectric ceramic transducers. The Redwood model of piezoelectric ceramics polarized in the thickness direction undergoing thickness vibration is shown in Fig. 2-11. It is essentially a six-terminal network, including two acoustic ports and one electrical port. The transmission line is used to simulate the propagation delay of sound waves.

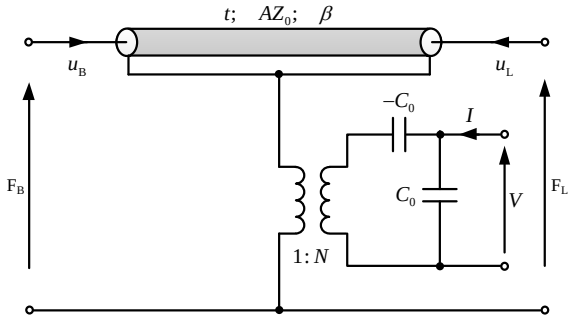

Fig. 2-11 The Redwood model of piezoelectric ceramic disk vibrating in the thickness direction

Likewise, the ideal transformers and the negative capacitance are used to achieve the electromechanical coupling of piezoelectric ceramics. Note that the turns ratio of the ideal transformer in the Redwood model is consistent with the Mason model. At this time, the circuit analysis program SPICE can be used to implement the Redwood equivalent circuit model, making the design and research of piezoelectric ceramic transducers more convenient.

D. KLM Model

The KLM model was also proposed in 1970 on the basis of the Mason equivalent circuit model. The KLM model of piezoelectric ceramic polarized in the thickness direction for thickness vibration is shown in Fig. 2-12. It also belongs to a six-terminal network in essence. The KLM model is proposed to solve the three problems of the Mason model: the existence of negative capacitance, the lack of a clear difference between the electrical part and the acoustic part, and the circuit complexity when combining multiple piezoelectric ceramics.

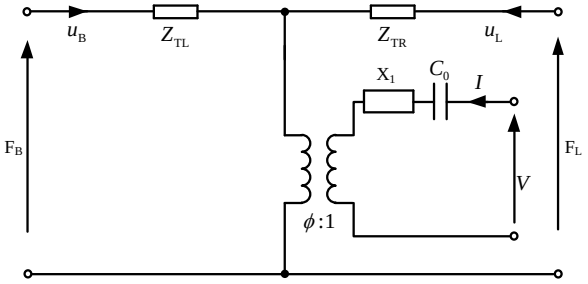

Fig. 2-12 The KLM model of piezoelectric ceramic disc vibrating in the thickness direction

Note that Z_{R} and Z_{L} represents the acoustic impedance of front and back ends for the piezoelectric ceramic transducer, Z_{TL} and Z_{TR} are the impedance when the lossless transmission line with characteristic impedance AZ_0 is half the length and X_1 is the reactance. The parameters of this lossless transmission line in the KLM equivalent circuit model are defined as

$$\mathrm{M}=\frac{h_{33}}{\omega AZ_0};\quad \mathrm{X}_1=jAZ_0\mathrm{M}^2\sin(\beta t/2);\quad \phi=\frac{1}{2\mathrm{M}}\csc(\beta t/2) \tag{2-30}$$

$$Z_{\mathrm{TL}}=AZ_0\left[\frac{Z_{\mathrm{L}}\cos(\beta t/2)+jAZ_0\sin(\beta t/2)}{AZ_0\cos(\beta t/2)+jZ_{\mathrm{L}}\sin(\beta t/2)}\right] \tag{2-31}$$

$$Z_{\mathrm{TR}}=AZ_0\left[\frac{Z_{\mathrm{R}}\cos(\beta t/2)+jAZ_0\sin(\beta t/2)}{AZ_0\cos(\beta t/2)+jZ_{\mathrm{R}}\sin(\beta t/2)}\right] \tag{2-32}$$

E. Transmission Line Model

The transmission line model was developed from the Redwood model, which was proposed by Leach in 1994. The biggest advantage of the model is that the ideal transformer is replaced by the controlled source model, and there is no negative capacitance in the entire equivalent circuit model. From Fig. 2-13, it is found that the entire model becomes more concise and easy to understand and it is easy to analyze using circuit analysis software.

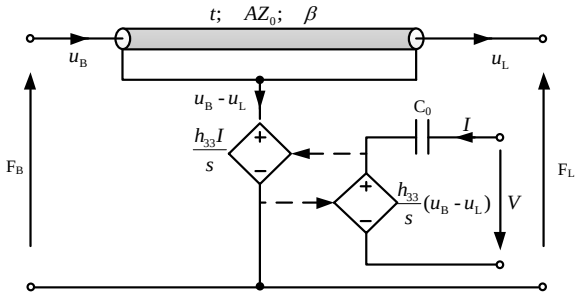

Fig. 2-13 The transmission line model of piezoelectric ceramic disk vibrating in the thickness direction

It is composed of the lossless transmission line, two controlled sources, and one capacitance. Here, the lossless transmission line is used to simulate the wave propagation in the piezoelectric ceramic disc while the two controlled sources are utilized to the electromechanical coupling of the piezoelectric ceramic disc. In Fig. 2-13, s denotes the Laplace transform operator, and the value of the capacitance C_0 is the same as that in the Mason model shown in Fig. 2-10. Puttter A. et al. [141] proposed the SPICE model of a lossy piezoelectric ceramic transducer in 1997, which improved the transmission line model. The mechanical and dielectric losses of piezoelectric ceramic transducers are taken into account in the SPICE model. Therefore, the PSpice model for SPUTs in longitudinal vibration will be established in this document based on the SPICE model of the lossy piezoelectric ceramic transducer.

2.4.3 FE Analysis Method

For the analysis of ultrasonic transducers, modal analysis and harmonic response analysis are generally used. Note that the specific analysis theory is given in subsection 2.4.1 in this thesis. Then the relationship between the resonance frequency and the impedance or admittance of the ultrasonic transducer with frequency is determined. The mainstream FE analysis software

includes ABAQUS, ANSYS, and COMSOL. The COMSOL software is more convenient for the modeling of ultrasonic transducers. It mainly involves structural mechanics, electrostatics modules, and multi-physics coupling. The calculation process of FE analysis is similar and the basic process is shown in Fig. 2-14. The results of the modal analysis of the SPUT with a resonance frequency of 35 kHz in longitudinal vibration by using COMSOL software are shown in Fig. 2-15. From Fig. 2-15, to ensure the accuracy of the calculation, the piezoelectric ceramic stack and other parts of the transducer use different meshing techniques. According to Fig. 2-15(c) and Fig. 2-15(d), it is found that the main vibration mode of the transducer is the longitudinal vibration, and the vibration displacement is the largest at the front mass, which is also consistent with the actual situation. The resonance frequency obtained is 36 kHz, and the error from the measured value is small. However, the FE analysis method has high requirements for computer hardware, and it is not conducive to combining the ultrasonic transducer model with other circuit modules.

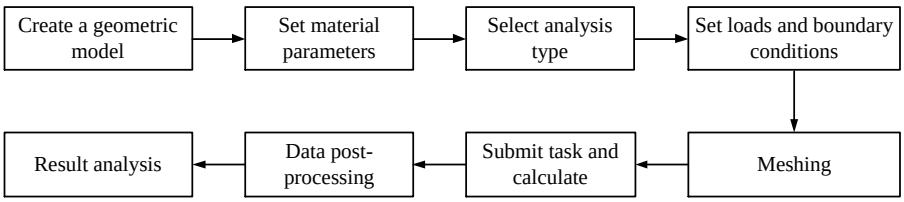

Fig. 2-14 The basic flow of finite element analysis and calculation

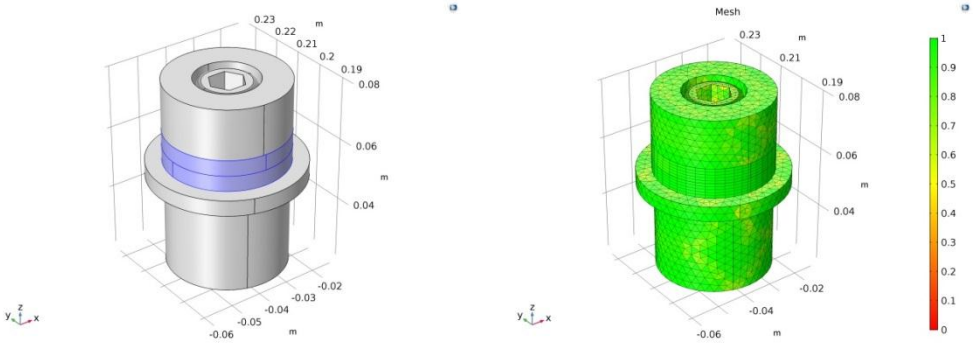

(a) (b)

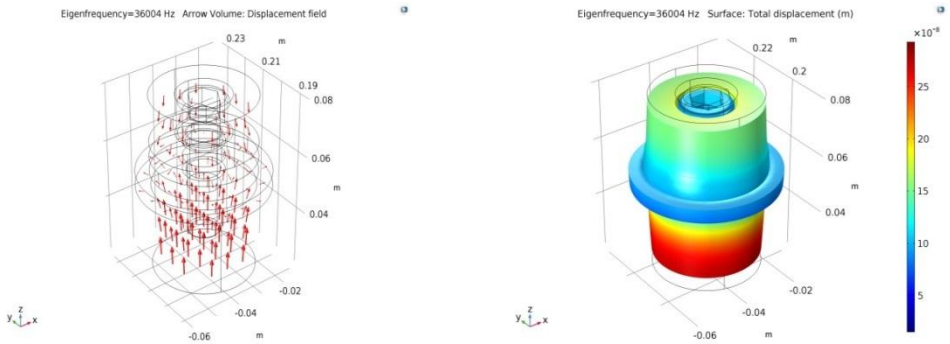

(c) (d)

Fig. 2-15 The finite element analysis of sandwiched piezoelectric ultrasonic transducers vibrating in the longitudinal direction, (a) the geometry structure, (b) mesh, (c) the vibration displacement vector, (d) the vibration displacement nephogram

2.5 Impedance Matching Theory of PTs

2.5.1 Electrical Impedance Matching of PTs

In general, the electrical matching of PUTs includes impedance transform, tuning, shaping, and filtering, which is expressed as follows.

- **Impedance transform**

According to AC circuit theory, the existence of an optimal load value for an ultrasonic excitation power supply enables the maximum electrical power output to the load. In practice, the electrical impedance of a PUT is not the same as the optimum load value of an ultrasonic excitation power supply. Therefore, to maximize the power of the PUT, an electrical matching circuit is necessary. Normally, a transformer or a series-parallel combination of inductances and capacitances is used to achieve the impedance transform.

- **Tuning**

PUTs generally work at the resonant frequency, and according to the resonant theory of PUTs, it can be seen that the PUT is capacitive near its resonance frequency. At this time, if the PUT is directly connected to the ultrasonic excitation power supply, it will produce large reactive power consumption or even affect the normal operation of the excitation power supply. For this reason, it is necessary to compensate for the capacitive impedance of the PUT, which is generally achieved through the inductive component.

- **Shaping and filtering**

To improve the power conversion efficiency of the circuit, ultrasonic excitation power supply often uses some switching devices such as power MOSFETs or IGBTs. However, the driving signals generated by these devices are square wave signals that contain many frequency components. Also, PUTs work at a single frequency, so the electrical matching circuit should also have the function of frequency-selective filtering, which is generally achieved by the combination of inductance and capacitance.

For the problem of power transmission of PUTs, it is necessary to study under what conditions the load can obtain the maximum power. In essence, this kind of problem comes down to the problem of power transmission from the active two-port network to the passive two-port network. The diagram of the energy transfer from an active network to a passive network is shown in Fig. 2-16. In Fig. 2-16, U_s is the equivalent voltage source, Z_s is the equivalent impedance of the active network, and Z_1 is the equivalent impedance of the load. These equivalent impedances can be expressed as

$$Z_s = R_s + jX_s, \quad Z_1 = R_1 + jX_1 \tag{2-33}$$

A. Variable load impedance Z_1

According to Fig. 2-16, the effective value of the current can be expressed as

$$I = \frac{U_s}{\sqrt{(R_s + R_1)^2 + (X_s + X_1)^2}} \tag{2-34}$$

From equation (2-34), the power obtained by the load can be given as

$$P = I^2 \cdot R_1 = \frac{R_1 U_s^2}{(R_s + R_1)^2 + (X_s + X_1)^2} \tag{2-35}$$

From equation (2-35), the maximum power value is obtained under $X_1 = -X_s$. Then equation (2-35) can be rewritten as

$$P = \frac{R_1 U_s^2}{(R_s + R_1)^2} \tag{2-36}$$

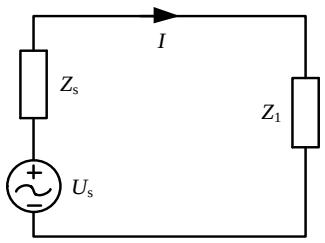

Fig. 2-16 The schematic diagram of energy transmission for active network and passive network

From equation (2-36), the following equation can be obtained:

$$\frac{dP}{dR_1} = \frac{(R_s + R_1)^2 U_s^2 - 2R_1(R_s + R_1)U_s^2}{(R_s + R_1)^4} = 0 \tag{2-37}$$

In light of equation (2-37), it is found that this extreme value condition is $R_1 = R_s$. Hence, the condition that the load gets the maximum power from the excitation power supply can be expressed as

$$Z_1 = R_1 + jX_1 = R_s - jX_s = Z_s^* \tag{2-38}$$

From equation (2-38), the load can get maximum power when the load impedance is equal to the complex conjugate of the impedance from the excitation power supply.

B. Variable load impedance $|Z_1|$ and unchanging impedance phase φ

Firstly, we assume that the load impedance can be expressed as:

$$Z_1 = |Z_1|\cos\varphi + j|Z_1|\sin\varphi \tag{2-39}$$

According to equation (2-39), the effective value of the current can be given as:

$$I = \frac{U_s}{\sqrt{(R_s + |Z_1|\cos\varphi)^2 + (X_s + |Z_1|\sin\varphi)^2}} \tag{2-40}$$

From equation (2-40), the power obtained by the load can be obtained as:

$$P = \frac{U_s^2 |Z_1|\cos\varphi}{(R_s + |Z_1|\cos\varphi)^2 + (X_s + |Z_1|\sin\varphi)^2} \tag{2-41}$$

According to equation (2-41), the following equation can be derived:

$$\frac{dP}{d|Z_1|}=\frac{U_s^2\cos\varphi\left[(R_s+|Z_1|\cos\varphi)^2+(X_s+|Z_1|\sin\varphi)^2\right]}{\left[(R_s+|Z_1|\cos\varphi)^2+(X_s+|Z_1|\sin\varphi)^2\right]^2}-\frac{2U_s^2|Z_1|\cos\varphi\left[(R_s+|Z_1|\cos\varphi)\cos\varphi+(X_s+|Z_1|\sin\varphi)\sin\varphi\right]}{\left[(R_s+|Z_1|\cos\varphi)^2+(X_s+|Z_1|\sin\varphi)^2\right]^2} \tag{2-42}$$

Letting equation (2-42) equal to zero, we can obtain:

$$|Z_1|^2=R_s^2+X_s^2\Rightarrow|Z_1|=\sqrt{R_s^2+X_s^2} \tag{2-43}$$

From equation (2-43), in this case, the load obtains maximum power when the modulus of load impedance is equal to the internal impedance of the excitation power supply. If the internal impedance of the excitation power supply is a pure resistance, the maximum power transmission condition is given as $|Z_1|=R_s$.

2.5.2 Acoustic Impedance Matching of PUTs

In ultrasonic testing applications, there is a serious mismatch between the acoustic impedance of the ultrasonic transducer used for testing and the acoustic impedance of the ultrasonic transducer material, which will cause a large amount of acoustic energy reflection at the interface and the sensitivity of the ultrasonic transducer greatly reduced. Therefore, it is common to use a material with the appropriate acoustic impedance as a transition medium (also called coupling agent) to resolve the acoustic impedance mismatch between the object to be tested and the ultrasonic transducer. The selection of the acoustic impedance value and application thickness of the coupling agent is based on the specifications described below. For ultrasonic detection applications, the acoustic impedance of the coupling agent should be between the ultrasonic transducer radiation surface and the acoustic load. Typically, to optimize the broadband response of a PUT, one or more layers of coupling agent are added between the radial surface of the PUT and the acoustic load. There are two main theoretical methods for calculating its acoustic impedance.

A. Traditional theory

The theory treats both piezoelectric elements and acoustic loads as semi-infinite. If the acoustic impedance of the piezoelectric component, coupling agent, and acoustic load are represented by Z_0, Z_m and Z_L, respectively, the acoustic impedance value is calculated for a single-layer coupling agent used to match [142].

$$Z_m=\sqrt{Z_0Z_L} \tag{2-44}$$

The acoustic impedance value for matching with a double layer coupling agent can be calculated as

$$Z_{m1}=Z_0^{3/4}Z_L^{1/4} \tag{2-45}$$

$$Z_{m2}=Z_0^{1/4}Z_L^{3/4} \tag{2-46}$$

where Z_{m1} represents the first layer coupling agent (near the radiating surface of the PUT) and Z_{m2} denotes the second layer coupling agent (near the acoustic load).

B. KLM model theory

The model is the same as the Mason model and it considers the piezoelectric element as half-wavelength thick. According to the transmission line theory, the acoustic impedance under single-layer matching is calculated as [143]:

$$Z_{\mathrm{m}} = Z_0^{1/3} Z_{\mathrm{L}}^{2/3} \tag{2-47}$$

Based on the above model theory, the acoustic impedance value can be calculated as follows, using double-layer coupling agent for matching:

$$Z_{\mathrm{m1}} = Z_0^{4/7} Z_{\mathrm{L}}^{3/7} \tag{2-48}$$

$$Z_{\mathrm{m2}} = Z_0^{1/7} Z_{\mathrm{L}}^{6/7} \tag{2-49}$$

It should be noted that according to the $\lambda/4$ transmission line theory in microwave applications, the thickness of the matching layer involved in the above acoustic impedance matching theory is calculated as

$$T_{\mathrm{m}} = \frac{\lambda_{\mathrm{m}}}{4} = \frac{v_{\mathrm{m}}}{f_s} \tag{2-50}$$

where T_{m} indicates the thickness of the matching layer, λ_{m} denotes the wavelength of the sound wave in the coupling agent material, and v_{m} represents the sound velocity in the coupling agent material. Additionally, it is noted that the acoustic impedance of the medium in the above theory is calculated as

$$Z = \rho v \tag{2-51}$$

where ρ indicates the material density and v denotes the sound velocity.

2.6 Conclusion

The broken rail real-time detection system based on UGW and the related theoretical foundations are illustrated in this chapter. For the theoretical foundations, two important velocity concepts (phase velocity and group velocity) of UGW, as well as the influence of multimodal and dispersive properties on detection, are introduced. Then, the common vibration modes and analytical theories and methods of PTs are introduced in detail, and the advantages of using equivalent circuit methods to study PTs are pointed out. Finally, the theory of impedance matching for PTs is presented, which mainly consists of EIM and AIM. This chapter provides theoretical guidance for the research work in the subsequent chapters.

3 Research on PSpice Model of SPUTs in Longitudinal Vibration

Currently, SPUTs are widely used because of their high power, high efficiency, low cost, and ease of manufacturing. The installation of PUTs used for railway testing must meet the installation specifications. Therefore, to facilitate installation and testing, this paper uses SPUTs in the longitudinal vibration. Besides, the UGW-based real-time broken rail detection system belongs to an electro-mechanical acoustic coupling system in essence. To further investigate the electromechanical characteristics of PUTs, an accurate and reliable analysis model of PUTs is required. Hence, this chapter focuses on the establishment of PSpice models of the SPUT in longitudinal vibration and the pitch-catch setup.

3.1 Establishment of PSpice Model of Single SPUT

3.1.1 The Structure of SPUTs

The SPUT in longitudinal vibration has the same overall structure as other types of SPUTs, except that the polarization direction and size of the piezoelectric ceramic disc are different. The three-dimensional structure of a SPUT in longitudinal vibration is shown in Fig. 3-1. It consists of a piezoelectric ceramic stack, front mass, back mass, metal electrodes, and the prestressed bolt. In general, the materials in SPUTs are divided into two categories, one is piezoelectric materials and the other is non-piezoelectric materials. Piezoelectric materials only refer to piezoelectric ceramic stack materials, and non-piezoelectric materials include front and back masses, electrodes, and prestressed bolt materials.

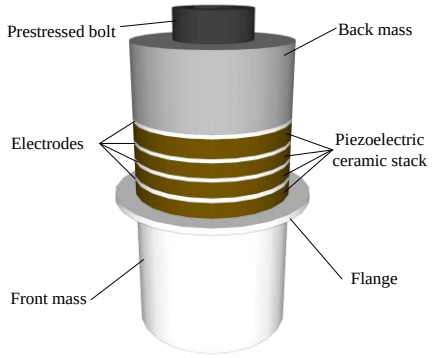

Fig. 3-1 Three-dimensional structure diagram of SPUT in the longitudinal vibration

In ultrasonic detection applications, the resonance and anti-resonance frequencies of SPUTs are focused on. In theory, the resonance and anti-resonance frequencies of the SPUT are mainly determined by the structural parameters of the piezoelectric ceramic stack, the front and back masses. The structural parameters of the rest parts have small influence on the above frequencies. Therefore, this paper focuses on the establishment of analytical models for the front and back masses and piezoelectric ceramic stack, to achieve the establishment of an analytical model of SPUTs. The structure of the SPUT shown in Fig. 3-1 is simplified as shown

in Fig. 3-2.

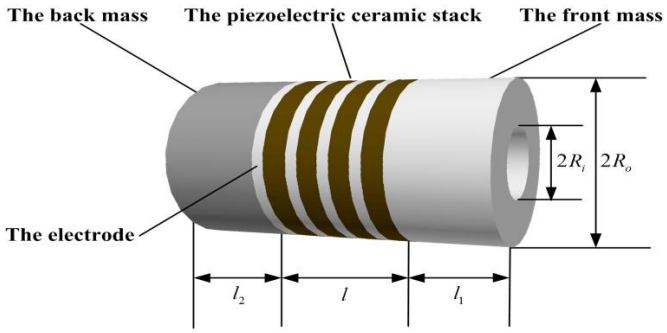

Fig. 3-2 Simplified structure diagram of a sandwich piezoelectric ultrasonic transducer

According to Fig. 3-2, it is found that the piezoelectric ceramic stack is composed of four piezoelectric ceramic rings with the same thickness and polarized direction. In Fig. 3-2, l_1 and l_2 represent the thickness of the front mass and back mass, respectively, l denotes the total thickness of electrodes and piezoelectric ceramic stack, $2R_i$ and $2R_o$ indicate the inner diameter and outer diameter, respectively.

3.1.2 Calculation of PSpice Model Parameters of SPUTs

To simplify the analysis about the vibration state of the SPUTs (refer to Fig. 3-1), some assumptions must be made as follows: (1) the diameter of the SPUT must be much less than its longitudinal length; (2) according to the network cascade theory, the piezoelectric ceramic stack can be regarded as a piezoelectric ceramic round stick poled along the axial direction when the thickness of the single piezoelectric ceramic ring is much less than its diameter; (3) the displacement and force are continuous on both sides of the connection surface for each component in SPUTs. Based on the above assumptions, the SPUT model is established to consider the longitudinal vibration of the piezoelectric ceramic ring without considering the radial vibration, thereby satisfying the one-dimensional wave theory. For the establishment of a SPUT model, this thesis will use the equivalent circuit method. This is mainly because the method uses electrical network terms to represent the mechanical vibration characteristics of piezoelectric elastomers based on the analogy of force and electricity. Simultaneously, some mechanical quantities are converted into electrical ones, and it has direct physical meaning, which is convenient for studying the transmission and reception characteristics of piezoelectric ultrasonic transducers.

A. Calculation of PSpice model parameters of piezoelectric ceramic rings in the longitudinal vibration

For the establishment of the PSpice model of a SPUT, the most critical thing is to establish an equivalent circuit model of the piezoelectric ceramic stack, because piezoelectric ceramics involve the conversion of electrical energy and acoustic energy at the same time. From Fig. 3-2, it is found that the piezoelectric ceramic stack consists of four same piezoelectric ceramic rings polarized in the thickness direction. Hence, a PSpice model of the piezoelectric ceramic ring is required. Firstly, according to the equivalent circuit lossy model of piezoelectric ceramic disc polarized in thickness direction which is established by Putter A, the PSpice model of lossy transmission line of the piezoelectric ceramic ring in the longitudinal vibration, as shown in Fig. 3-3(a). From Fig. 3-3(a), this PSpice model of the piezoelectric ceramic ring in the longitudinal vibration is primarily composed of two acoustic ports represented by B and F, one electrical

port denoted by E. It has specifically consisted of two controlled current sources indicated by F1 and F2, one controlled voltage source E, lossy transmission line T1, and resistance-capacitance elements. Note that to prevent the entire circuit from failing to converge and cause the calculation to fail, the resistance R_1 and the capacitance C_1 are used, and $R_1 = 1\,\mathrm{k\Omega}$, $C_1 = 1\,\mu\mathrm{F}$. The resistance R_1 provides a DC path to prevent the generation of floating ground. The top-layer model from Fig. 3-3(b) is established to facilitate the subsequent representation of the PSpice model of the entire SPUT. To accurately reflect the physical characteristics of the piezoelectric ceramic ring, the established PSpice model of the piezoelectric ceramic ring in the longitudinal vibration has considered the mechanical loss and dielectric loss. The lossy transmission line T1 can reflect the mechanical loss of piezoelectric ceramic and the resistance R_0 is used to represent the dielectric loss.

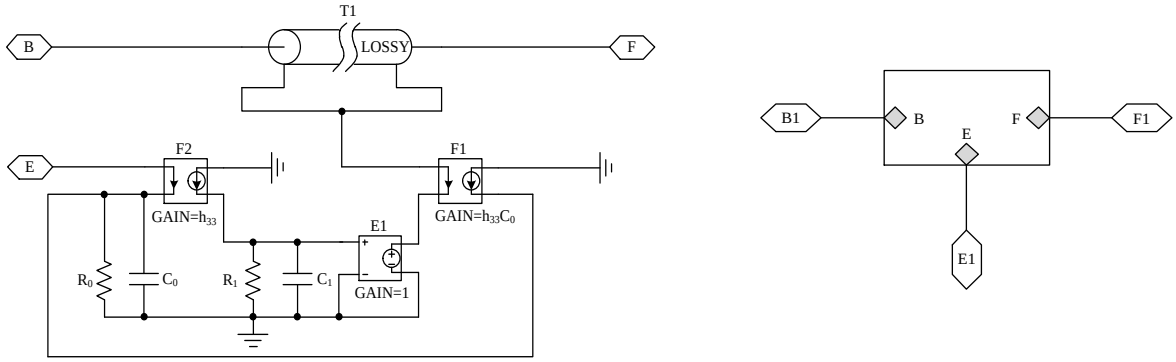

(a) (b)

Fig. 3-3 Loss transmission line PSpice model of the piezoelectric ceramic disk in thickness vibration, (a) bottom-layer model, (b) top-layer model

To obtain the parameters of lossy acoustic transmission line T1 shown in Fig. 3-3(a), the comparison of the wave propagation is carried out in electrical transmission lines and acoustical mediums. Considering a differential length Δz of a transmission line, as represented in Fig. 3-4, it can be illustrated by the parameters as follows [144]:

- R represents the resistance per unit length in $\Omega \cdot \mathrm{m}^{-1}$,
- L represents the inductance per unit length in $\mathrm{H} \cdot \mathrm{m}^{-1}$,
- G represents the conductance per unit length in $\mathrm{S} \cdot \mathrm{m}^{-1}$,
- C represents the capacitance per unit length in $\mathrm{F} \cdot \mathrm{m}^{-1}$.

Note that R and L are connected in series, G and C are connected in parallel.

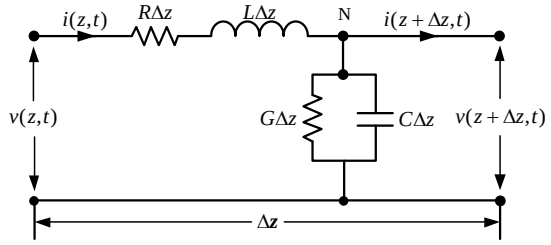

Fig. 3-4 The schematic diagram of the electrical transmission line under the length equaling to Δz

To obtain the above parameters, Kirchhoff's voltage law is used in the circuit of Fig. 3-4, that is:

$$v(z,t) - R\Delta z i(z,t) - L\Delta z \frac{\partial i(z,t)}{\partial t} - v(z+\Delta z,t) = 0 \tag{3-1}$$

which leads to

$$-\frac{v(z+\Delta z,t)-v(z,t)}{\Delta z}=Ri(z,t)+L\frac{\partial i(z,t)}{\partial t} \tag{3-2}$$

With the limit as $\Delta z\to 0$ equation (3-2) can be arranged as

$$-\frac{\partial v(z,t)}{\partial z}=Ri(z,t)+L\frac{\partial i(z,t)}{\partial t} \tag{3-3}$$

Similarly, by using Kirchhoff's law to the node N in Fig. 3-1, we can derive

$$i(z,t)-G\Delta z v(z,t)-C\Delta z\frac{\partial v(z+\Delta z,t)}{\partial t}-i(z+\Delta z,t)=0 \tag{3-4}$$

Then letting $\Delta z\to 0$, we can obtain

$$-\frac{\partial i(z,t)}{\partial z}=Gv(z,t)+C\frac{\partial v(z,t)}{\partial t} \tag{3-5}$$

We call equations (3-3) and (3-5) the general transmission-line equations, which are first-order partial differential equations based on $v(z,t)$ and $i(z,t)$.

For simplifying the pair partial differential equations, the time-harmonic cosine function is used and the voltage $v(z,t)$ and the current $i(z,t)$ can be expressed as:

$$v(z,t)=real\left[V(z)e^{j\omega t}\right] \tag{3-6}$$

$$i(z,t)=real\left[I(z)e^{j\omega t}\right] \tag{3-7}$$

where ω represents the angular frequency.

The general transmission line equations based on $V(z)$ and $I(z)$ can be obtained

$$-\frac{dV(z)}{dz}=(R+j\omega L)I(z) \tag{3-8}$$

$$-\frac{dI(z)}{dz}=(G+j\omega C)V(z) \tag{3-9}$$

Equations (3-8) and (3-9) are called time-harmonic transmission line equations which simplify to the following equations (3-10) and (3-11) under the lossless conditions ($R=0$, $G=0$).

$$-\frac{dV(z)}{dz}=j\omega LI(z) \tag{3-10}$$

$$-\frac{dI(z)}{dz}=j\omega CV(z) \tag{3-11}$$

To obtain the propagation constant and characteristic impedance of the transmission line, the time-harmonic transmission line equations are used. Through differentiating them concerning z, we can obtain:

$$\frac{d^2V(z)}{dz^2}-\gamma^2V(z)=0 \tag{3-12}$$

$$\frac{d^2I(z)}{dz^2}-\gamma^2I(z)=0 \tag{3-13}$$

where γ is called the propagation constant. It is composed of an attenuation constant α in $\mathrm{Np/m}$ and a phase constant β in $\mathrm{rad/m}$. It can be expressed as:

$$\gamma=\alpha+j\beta=\sqrt{(R+j\omega L)(G+j\omega C)} \tag{3-14}$$

The general solution of the differential equation (3-12) is denoted as:

$$V(x) = Ae^{-(\alpha+j\beta)z} + Be^{(\alpha+j\beta)z} \tag{3-15}$$

and equation (3-13) has the same form of solution. The time dependence for equation (3-16) can be got using multiplying by $e^{j\omega t}$.

$$v(x,t) = V(x)e^{j\omega t} = Ae^{-\alpha z}e^{j(\omega t-\beta z)} + Be^{\alpha z}e^{j(\omega t+\beta z)} \tag{3-16}$$

Equation (3-16) illustrates two traveling waves. One travels in the positive z direction with an amplitude A and it decays at a rate α, while the other travels in the opposite direction with an amplitude B and has the same decay-rate. The propagation of an acoustic wave is controlled by a pair of differential equations that have the same type as equations (3-12) and (3-13).

$$\frac{\partial^2 p(z,t)}{\partial^2 z} + k_c^2 p(z,t) = 0 \tag{3-17}$$

$$\frac{\partial^2 u(z,t)}{\partial^2 z} + k_c^2 u(z,t) = 0 \tag{3-18}$$

where $p(z,t)$ represents sound pressure and $u(z,t)$ indicates the particle velocity. Likewise, complex wavenumber k_c consists of attenuation constant α and wavenumber k. The complex wavenumber can be expressed as:

$$k_c = \frac{\omega}{v_t}\frac{1}{\sqrt{1+j\omega\tau}} \tag{3-19}$$

where τ is the relaxation time, $v_t = \sqrt{E/\rho}$ is the sound velocity and E indicates the Young's modulus.

The general solution for equation (3-17) is expressed as:

$$p(z,t) = Ae^{-\alpha z}e^{-j(\omega t-kz)} + Be^{\alpha z}e^{j(\omega t+kz)} \tag{3-20}$$

It is found that equation (3-20) has the same form that equation (3-16). In addition, equation (3-18) has the same general solution form that equation (3-17). Combined with equations (3-19) and (3-20), it can be derived that

$$\alpha = \frac{\omega}{v_t}\frac{1}{\sqrt{2}}\left[\frac{\sqrt{1+(\omega\tau)^2}-1}{\sqrt{1+(\omega\tau)^2}}\right]^{\frac{1}{2}} \tag{3-21}$$

$$k = \frac{\omega}{v_t}\frac{1}{\sqrt{2}}\left[\frac{\sqrt{1+(\omega\tau)^2}+1}{\sqrt{1+(\omega\tau)^2}}\right]^{\frac{1}{2}} \tag{3-22}$$

The characteristic impedance Z_{el} of the lossy acoustical medium is represented as

$$Z_{el} = \sqrt{\frac{R + j\omega L}{G + j\omega C}} \tag{3-23}$$

while the characteristic acoustic impedance Z_a of the lossy acoustic medium is represented as

$$Z_a = \rho v_t \sqrt{1 + j\omega\tau} \tag{3-24}$$

To approximate the characteristic impedance and propagation constant, the low order parts of equations (3-23) and (3-14) are reserved. They are rewritten as

$$Z_{el} \cong \sqrt{\frac{L}{C}}\left[1 + \frac{1}{2j\omega}\left(\frac{R}{L} - \frac{G}{C}\right)\right] \tag{3-25}$$

$$\gamma \cong \frac{1}{2}\sqrt{LC}\left(\frac{R}{L} + \frac{G}{C}\right) + j\omega\sqrt{LC} \tag{3-26}$$

Now we consider small but non-negligible losses, i.e. we suppose $R \ll \omega L$, $G \ll \omega C$ and $\omega\tau \ll 1$. Based on these assumptions, the second term of equation (3-25) is neglected, only keeping the $\sqrt{L/C}$ as the characteristic impedance. Likewise, according to equation (3-24), the acoustic characteristic impedance is derived as ρv_t. The wavenumber from equation (3-22) can be approximately expressed as ω / v_t. Besides, according to equation (3-26), the phase constant β can be obtained as $\omega\sqrt{LC}$.

To correlate the two theories, the impedance type analogy relationship is selected in which the mechanical force is denoted by the voltage and the current denotes particle velocity. The equivalence between the systems is:

$$Z_{el} \cong Z_a A = A\rho v_t \tag{3-27}$$

where A is the cross-sectional area for the acoustic beam.

The relationship of the low-loss characteristic impedance equation (3-27) is used to obtain the following expressions

$$L \equiv A\rho, \quad C \equiv \frac{1}{A\rho v_t^2} \tag{3-28}$$

Additionally, the real part of equation (3-26) represents the attenuation constant as follows

$$\alpha = \frac{1}{2}\sqrt{LC}\left(\frac{R}{L}\right) + \frac{1}{2}\sqrt{LC}\left(\frac{G}{C}\right) \tag{3-29}$$

Corresponding to equation (3-29), the classic theory relationship of acoustic attenuation is obtained as

$$\alpha_{classical} = \alpha_v + \alpha_{tc} \tag{3-30}$$

Where α_v denotes the attenuation coefficient resulting from viscous losses while α_{tc} is the attenuation coefficient deriving from the thermal conduction. According to equations (3-28), (3-29) and (3-30), it can be obtained that

$$R \equiv 2\rho v_t A\alpha_v, \quad G \equiv \frac{2\alpha_{tc}}{\rho v_t A} \tag{3-31}$$

Because of the low heat conductance of the materials used in the SPUT, the loss resulting from the thermal conductance can be neglected. Then letting the conductance $G=0$, we can get

$$\alpha = \alpha_v = \frac{R}{2}\sqrt{\frac{C}{L}} = \frac{\omega}{\omega}\frac{R}{2}\frac{1}{Lv_t} = \frac{\omega}{2v_t}\tan\delta_m \tag{3-32}$$

where $\tan\delta_m = 1/Q_m$ is the mechanical loss factor and Q_m is the mechanical quality factor. Substituting equation (3-32) into equation (3-31), we can get

$$R \equiv \omega L/Q_m = L\omega\tan\delta_m \tag{3-33}$$

Finally, the parameters of the acoustical lossy transmission line can be derived as:

$$L = A\rho, \quad C = \frac{1}{A\rho v_t^2}, \quad R = \frac{\omega L}{Q_m}, \quad G = 0 \tag{3-34}$$

The dielectric loss resistance R_0 and clamped capacitance C_0 can be calculated as [145]

$$R_0 = \frac{1}{C_0\tan\delta_e\omega} \tag{3-35}$$

$$C_0 = A/\beta_{33}^S t_1 \tag{3-36}$$

where $\tan\delta_e = 1/Q_e$ represents the dielectric loss factor, Q_e denotes the electrical quality factor, β_{33}^S indicates dielectric isolation rate, $A=\pi(R_o^2 - R_i^2)$ is the cross-sectional area of the piezoelectric ceramic ring, and t_1 is its thickness.

Tab. 3-1 Material parameters of piezoelectric ceramic PZT-4

Parameters	Value	Unit
Density ρ_1	7500	kg/m^3
Sound velocity v_t	4600	m/s
The area of the piezoelectric ceramic ring A	957.4e-6	m^2
The thickness of the piezoelectric ceramic ring t	5e-3	m
Mechanical quality factor Q_m	500	—
Dielectric loss factor $\tan\delta_e$	0.004	—
Dielectric isolation rate β_{33}^S	1.78e8	m/F
Piezoelectric constant h_{33}	27.12e8	V/m

In this paper, the input electric power of the SPUT is relatively small and it is in a discontinuous working state, and it is excited by a pulse signal, so PZT-4 is selected as the piezoelectric ceramic material. Because such materials have high piezoelectric constants and electromechanical coupling coefficients, PUTs can achieve high electromechanical conversion efficiency. Tab. 3-1 shows the material parameters of the piezoelectric ceramic PZT-4. Now,

combining with the material parameters in Tab. 3-1 and equations (3-34), (3-35), and (3-36), the PSpice model parameters of the piezoelectric ceramic ring in the longitudinal vibration are obtained.

B. Calculation of PSpice model parameters of front and rear metal covers and metal electrodes

The equivalent circuit parameters of the front and back masses in the SPUT are calculated. Since the mechanical loss of the metal material used in the SPUT has little effect on the resonance and anti-resonance frequencies of the SPUT and the length of the metal material is short, hence this paper uses a lossless transmission line to model the front and back masses, the metal electrodes. The PSpice model of the lossless transmission line is shown in Fig. 3-5, which mainly includes three parameters: resonance frequency *F*, transmission line normalized length *NL*, and characteristic impedance Z_0. The specific calculation is given as [146]

$$F = \frac{NL}{l} v_t \tag{3-37}$$

$$Z_0 = \rho v_t S \tag{3-38}$$

where v_t indicates the acoustic velocity, *S* represents the cross-sectional area, *l* indicates the length of the transmission line and *NL*=0.25. To obtain a large displacement amplitude ratio of the front and back masses and improve the forward radiation capability of SPUT, the front metal mass generally uses light metals such as aluminum alloys, aluminum-magnesium alloys. The back metal mass uses heavy metals such as steel, copper while the metal electrodes use copper or steel materials. It should be noted that in this study, the front metal mass of the SPUT is made of aluminum alloy, the back metal mass is made of 45 # steel, and the metal electrode is made of copper. The specific parameters are described in Tab. 3-2. According to equations (3-37), (3-38) and the material parameters from Tab. 3-2, the calculation of equivalent circuit parameters of front and back masses, metal electrodes is conducted.

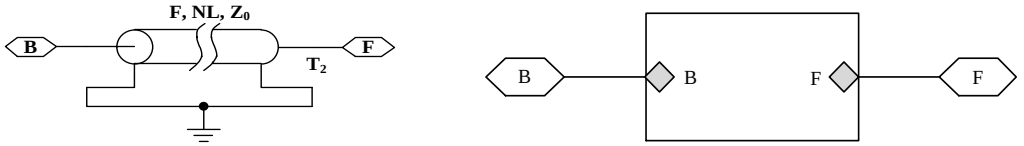

(a) (b)

Fig. 3-5 PSpice model of the lossless transmission line, (a) bottom-layer model, (b) top-layer model

Tab. 3-2 The metal material parameters of SPUTs

Materials	45# steel	Aluminum alloy	Copper
Density ρ, kg/m^3	7800	2700	8900
Sound velocity v_t, m/s	5262	5037	3718
Cross-sectional area S, m^2	1134.1e-6	1075.2e-6	1134.1e-6
Thickness l, m	45e-3	43e-6	0.5e-3

C. PSpice model of longitudinal vibration piezoelectric ceramic stack

From Fig. 3-2, the piezoelectric ceramic stack is composed of four same piezoelectric ceramic rings polarized in the thickness direction and their connection relationship is shown in Fig. 3-6. According to Fig. 3-6, the polarization directions of two adjacent ceramic rings are

opposite, which makes the longitudinal vibration of each ceramic ring superimposed in phase. At the same time, this ensures the coordinated vibration of the piezoelectric ceramic stack. Note that the number of piezoelectric ceramic rings is even which is to ensure the front and back masses connecting with electrodes of the same polarity. In addition, for the sake of safety, the front and back masses of the PT are generally connected to the negative end of the excitation power supply.

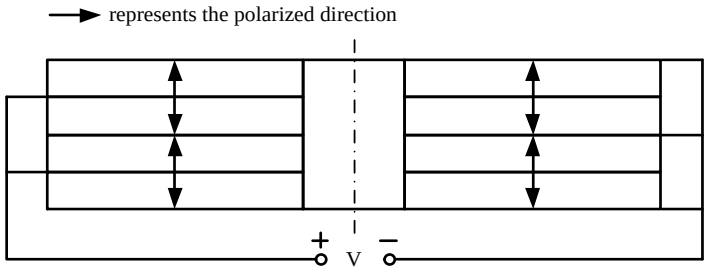

Fig. 3-6 The piezoelectric ceramic stack composed of four piezoelectric ceramic rings with the same thickness and polarized direction

The piezoelectric rings located in the piezoelectric ceramic stack are connected mechanically in series while they belong to the parallel relationship in the electrical terminals. According to the cascade theory and Fig. 3-3 (b), the PSpice equivalent circuit model of the piezoelectric ceramic stack with metal electrodes can be obtained as shown in Fig. 3-7. From Fig. 3-7, T3, T4, T5, and T6 indicate metal electrode discs; P1, P2, P3, and P4 indicate lossy piezoelectric ceramic rings.

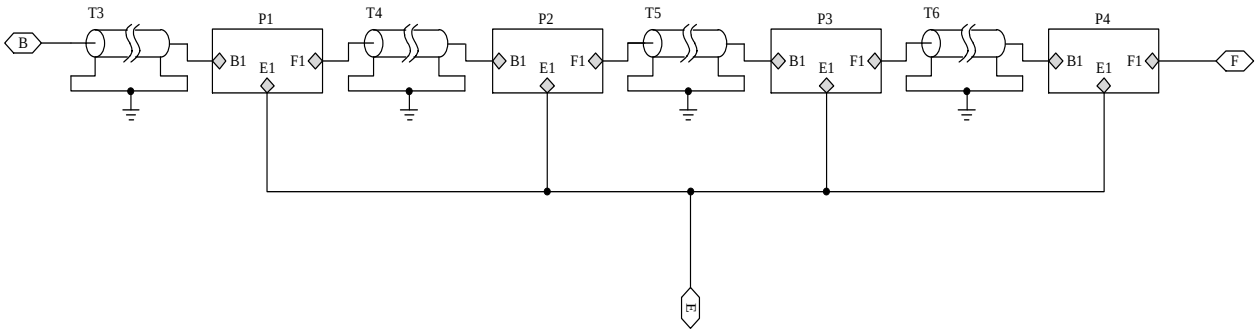

Fig. 3-7 PSpice circuit model of a piezoelectric ceramic stack in longitudinal vibration

The number of metal electrodes and piezoelectric ceramic rings corresponds to the actual transducer. Note that B, E, and F have the same meaning as B, E, and F in Fig. 3-3 (a). Also, to facilitate the connection of the various modules in the SPUT, the equivalent circuit model of the piezoelectric ceramic stack shown in Fig. 3-7 can also be represented by the top model shown in Fig. 3-3 (b). In summary, for the PSpice modeling of SPUTs in the longitudinal vibration of different structural sizes, only the piezoelectric ceramic material parameters shown in Tab. 3-1 and the related metal materials shown in Tab. 3-2 are required.

3.1.3 PSpice models of Single SPUT and the Pitch-catch Setup

Since there is no conversion of electrical energy between the front and back metal masses and the piezoelectric ceramic stack, they can be connected in series. Based on the PSpice equivalent circuit model of the piezoelectric ceramic stack in the longitudinal vibration shown in Fig. 3-7 and the PSpice model of the lossless transmission line shown in Fig. 3-5 (b), the

PSpice model of SPUTs in the longitudinal vibration can be realized according to the cascade theory, as shown in Fig. 3-8. The model considers only the modeling of the front and back masses, the piezoelectric ceramic stack (in fact it considers the adhesive layer between the front and back masses and the piezoelectric ceramic stack), the metal electrodes and the air load.

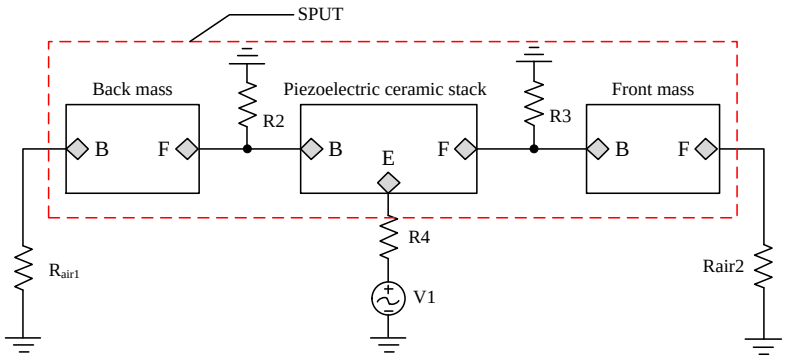

Fig. 3-8 PSpice model of SPUTs in the longitudinal vibration

The resistances $R2$ and $R3$ are used to represent the adhesive layer mentioned above and their values are $R2$=$R3$=1.2 MΩ. In addition, the resistance R4 represents the internal resistance of the AC voltage source $V1$ and $R4$=50 Ω. The radiating surface and back of the SPUT are in direct contact with air, so the resistances R_{air1} and R_{air2} are used to simulate the air load and they can be calculated as:

$$R_{air1}=R_{air2}=\rho_{air}v_{air}A_1 \tag{3-39}$$

where $v_{air}=340$ m/s represents the acoustic speed in the air, $A_1=1134.1e-6$ m^2 denotes the cross-sectional area of the contacting air, and $\rho_{air}=1.23$ kg/m^3 indicates the air density. Based on the established PSpice model of SPUTs in the longitudinal vibration, by applying different excitations, the electromechanical characteristics and time-domain transient characteristics of PUTs can be easily analyzed.

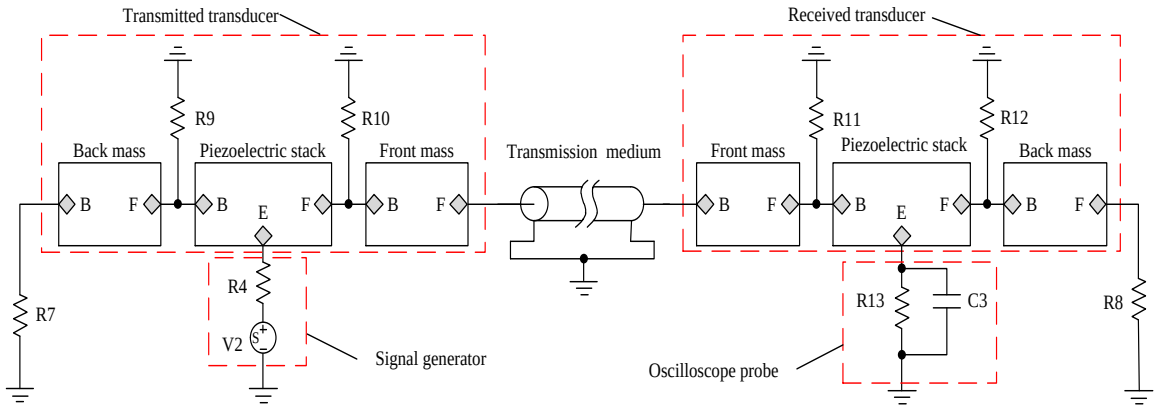

Fig. 3-9 PSpice equivalent circuit model of a pitch-catch setup

Then the PSpice equivalent circuit model based on the pitch-catch mechanism is shown in Fig. 3-9. It primarily includes one transmitter used to produce an ultrasonic wave signal, one receiver used to receive the ultrasonic wave signal, transmission medium, signal generator, and oscilloscope. Note that the loss of the transmission medium is neglected in the PSpice model, so the transmission medium is simulated by using the lossless transmission line shown in Fig. 3-5. From Fig. 3-9, the oscilloscope probe is accomplished by the resistance $R13$ and the capacitance $C3$, and $R13=10$ MΩ, $C3$=3.9 pF. The resistance $R4$ is the internal resistance of

signal source $V2$ and $R4 = 50\ \Omega$. Besides, the resistances $R7$ and $R8$ represent the air load of the back mass with values $R7 = R8$=0.472 Ω. The resistances $R9$, $R10$, and $R11$, $R12$ are used to model the bonded layer and their values are $R9 = R10 = R11 = R12 = 1\ \mathrm{M}\Omega$. For the PSpice equivalent circuit model of the pitch-catch setup, the impedance analysis and transient analysis in time domain are conducted only by adding different signals at the source $V2$. The impedance analysis uses the 1 V AC voltage source while the transient analysis in time domain utilizes an amplitude-adjustable signal source.

3.2 PSpice Model Verification of SPUTs

3.2.1 PSpice Model of Single SPUT

Based on the PSpice model of the SPUT shown in Fig. 3-8, the voltage and the current flowing through the resistance R4 are obtained by using the voltage and current probes, respectively. The impedance, resistance, reactance, and impedance phase of PUTs are specifically expressed as follows:

$$Z \equiv V(R4:2)/I(R4) = R + \mathrm{j}X \tag{3-40}$$

$$R \equiv \mathrm{R}(V(R4:2)/I(R4)) \tag{3-41}$$

$$X \equiv \mathrm{IMG}(V(R4:2)/I(R4)) \tag{3-42}$$

$$Phase \equiv \mathrm{P}(V(R4:2)/I(R4)) \tag{3-43}$$

where Z represents the impedance, R indicates the resistance, X denotes the reactance, *Phase* is the impedance phase, $V(R4{:}2)$ indicates the voltage of the second pin of the resistance $R4$ to ground, and $I(R4)$ denotes the current flowing through the resistance $R4$.

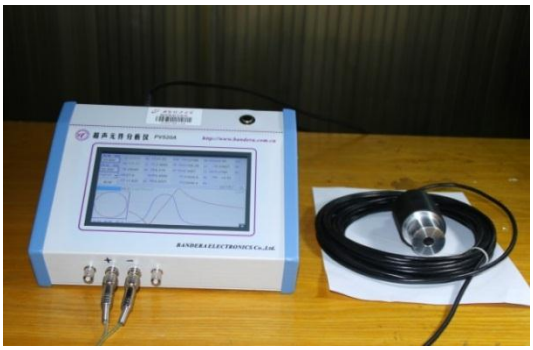

Fig. 3-10 A test platform based on impedance analyzer PV520A of SPUTs

When the PUT works at the resonance frequency, the impedance is the smallest, but when it operates at the anti-resonance frequency, the impedance is the largest. Therefore, the two resonance frequencies can be obtained by analyzing the impedance characteristics of the PUT. By adding an AC signal with a voltage of 1 V to the excitation source *V1* in the PSpice model of the SPUT shown in Fig. 3-8, the impedance analysis can be performed. Then according to equations (3-40), (3-41), (3-42), (3-43), the impedance, resistance, reactance and impedance phase of the PUT can be obtained. Besides, to verify the correctness of the simulation results, some SPUTs with the same size and parameters as the SPUT used in the simulation model have

been manufactured. Based on the impedance analyzer PV520A (BEIJING BAND ERA CO., LTD., Beijing, China), an impedance test platform as shown in Fig. 3-10 has been built and the SPUT in the longitudinal vibration has been tested.

The simulated and measured results of the impedance analysis of SPUTs are shown in Fig. 3-11 where it is found that for the impedance, resistance, and reactance of the PUT, the experimental results and simulation results are in good agreement, especially the parameter of resistance. Regarding the impedance phase, the experimental results and simulation results have the same trend, but there is a large gap between the maximum values of the two. According to Fig. 3-11(a), the test and simulated resonant frequency and anti-resonant frequency can be obtained and listed in Tab. 3-3. From Tab. 3-3, the difference between the simulation result and the test result of the resonance frequency is larger, and the difference between the simulation result and the experimental result of the anti-resonance frequency is smaller. In general, the experimental results and simulation results have good consistency. For this reason, the correctness of the established PSpice model of SPUTs in longitudinal vibration is verified.

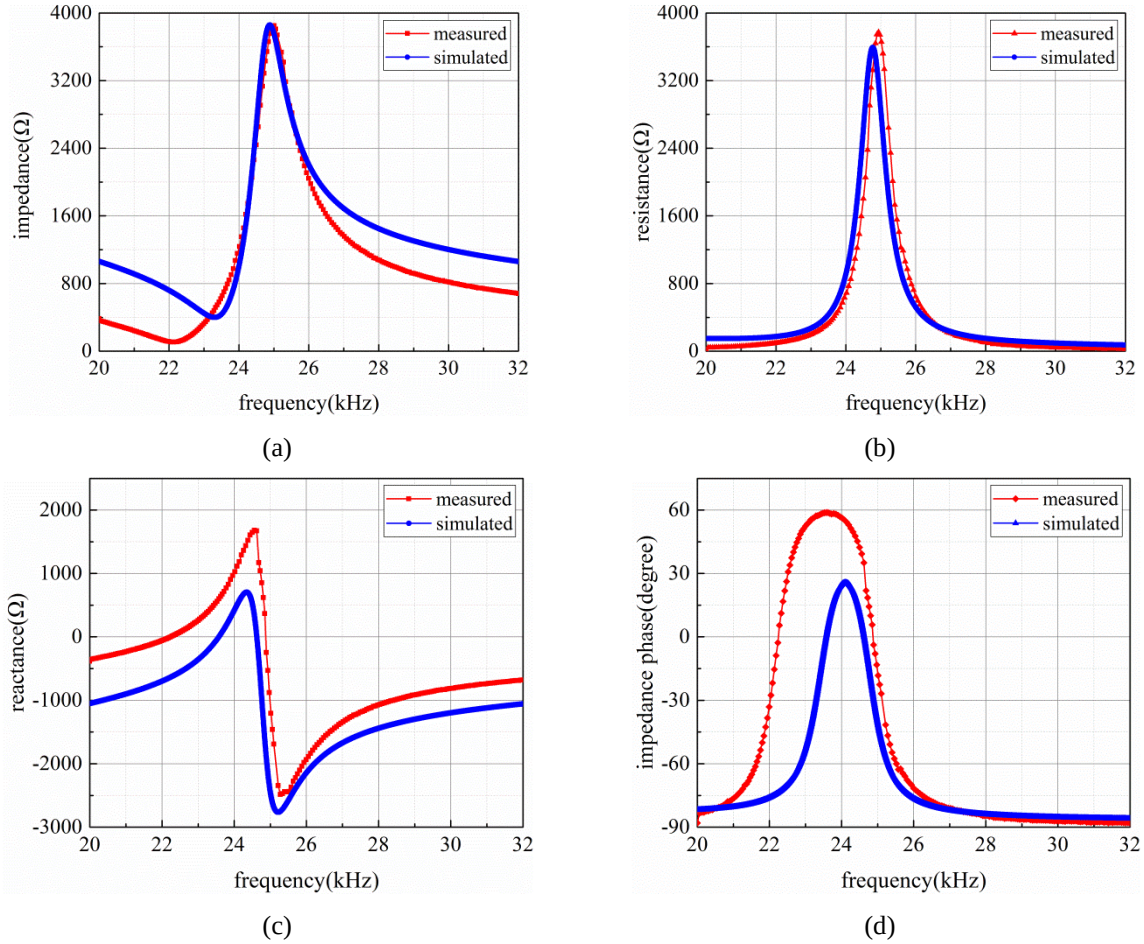

Fig. 3-11 Impedance analysis results, (a) impedance, (b) resistance, (c) reactance, (d) impedance phase

Tab. 3-3 The measured and simulated resonance frequencies and anti-resonance frequencies for a SPUT

Parameters	Simulated f_t	Measured f_m	Relative error $\Delta\%$
Resonance frequency f_s(kHz)	23.309	22.2	4.99
Anti-resonance frequency f_p(kHz)	24.885	25.1	0.86

Several factors can explain the frequency differences in Tab. 3-3. Firstly, the standard physical parameters of the piezoelectric ceramic rings, the metal masses, and the metal electrodes are applied in simulation; to a certain extent, they are different from the truthful physical parameters. Secondly, it must be met in the theoretical analysis condition that the length of the SPUT has to be much more than its diameter so that the vibration of the SPUT can be approximated as the longitudinal vibration of an extended composite round bar. However, it is not possible in practical cases. Thirdly, based on the above analysis, the prestressed bolt and the epoxy resin used for sealing the sandwiched transducer are ignored in the proposed PSpice model. Here, it should be pointed out that the prestressed bolt affects the electrical impedance, resulting in some frequency error. Also, the sealing epoxy resin can lead to some frequency error because it changes the vibrator length. For the practical transducers, these should not be neglected.

To study the vibration velocity ratio of the front and back masses of the SPUT, with the PSpice model of the SPUT in the longitudinal vibration shown in Fig. 3-8, the SPUT is excited with the Hanning window modulated sinusoidal pulse signal. The mathematical expression of this signal is given as:

$$y(t) = 0.5 * \left[1 - \cos(\frac{2\pi ft}{N})\right] * \sin(2\pi ft) \tag{3-44}$$

where N represent the pulse cycles, t is the time, and f denotes the signal frequency. In general, to make the front mass of the SPUT radiate more energy, the front mass is made of light metal and the back mass is made of heavy metal. Then the law of conservation of momentum is given as:

$$m_F v_F = m_B v_B \tag{3-45}$$

$$\frac{v_F}{v_B} = \frac{m_B}{m_F} \tag{3-46}$$

where m_F and m_B represent the mass of the front and back masses, respectively, v_F and v_B denote the surface vibration velocities of the front and back masses. From equation (3-46), it is found that the vibration velocity is inversely proportional to the mass.

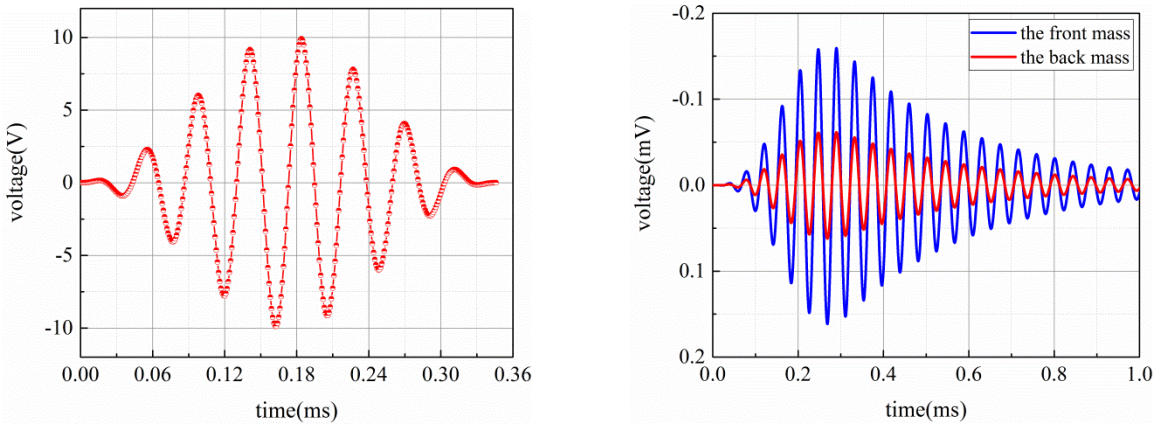

(a) (b)

Fig. 3-12 Transient analysis of a sandwiched piezoelectric transducer, (a) Hanning-window modulated sinusoidal pulse signal, (b) vibration velocity analysis of front and back masses

The 8-cycle sinusoidal pulse signal modulated by the Hanning window as shown in Fig. 3-12(a) is applied to the SPUT. Then the simulated results show that the vibration speeds of the front and back masses are shown in Fig. 3-12(b). According to Fig. 3-12(b), the vibration velocity ratio of the front and back masses is obtained as:

$$\frac{v_F}{v_B} = \frac{0.32}{0.12} \approx 2.7:1 \tag{3-47}$$

From the perspective of theory, when the front and back masses are made of hard aluminum and 45 # steel, the vibration velocity ratio of the front and back masses is 3:1. The simulation results are consistent with the theoretical analysis, further verifying the accuracy of the established PSpice model of SPUTs.

3.2.2 PSpice Model of the Pitch-catch Setup

In the ultrasonic testing system, the pitch-catch mechanism is often used, i.e. one end transmits a signal, and the other end receives a signal, to judge whether there are abnormal conditions in the detection interval according to the characteristics of the received signal. Therefore, based on the PSpice model of the pitch-catch setup, the impedance and transient characteristics in time domain are analyzed. Firstly, a 1 V AC voltage source is applied to the PSpice equivalent circuit model of the pitch-catch setup to conduct the impedance analysis. The transmission medium uses aluminum rods with a diameter of 37 mm and lengths of 20 mm and 100 mm, respectively.

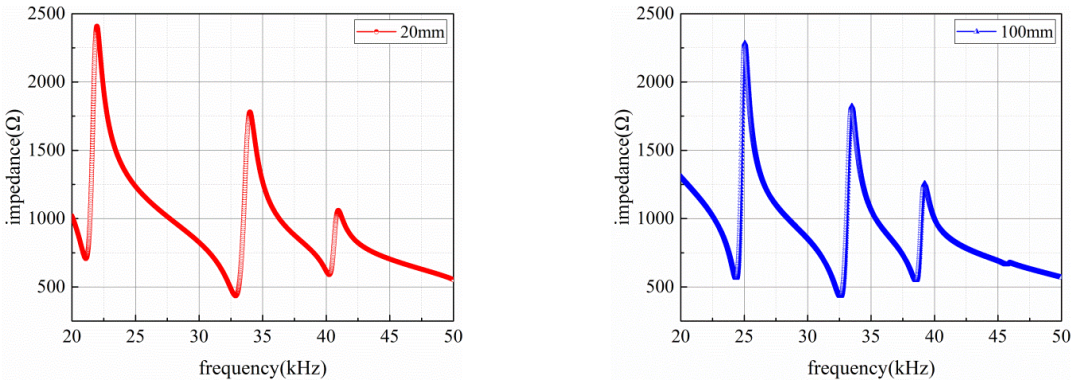

(a) (b)

Fig. 3-13 Impedance analysis of a pitch-catch setup under different lengths medium, (a) 20 mm, (b) 100 mm

The voltage and current flowing through the resistance R4 are obtained through voltage and current probes, respectively. According to equation (3-40), the impedance of the PSpice model of the pitch-catch setup can be calculated and the results are shown in Fig. 3-13. From Fig. 3-13, it is found that compared to the single SPUT, the pitch-catch setup generates multiple resonant modes and the number of resonant modes increases as the length of transmission medium increases. Combining Fig. 3-13(a) and Fig. 3-13(b), three resonant modes appear when the transmission medium length is 20 mm, while they increase to four resonance modes when the transmission medium length is 100 mm. The resonance frequency and anti-resonance frequency corresponding to the main resonant mode are reduced. The main resonance frequencies for the two lengths considered are 21.098 kHz and 24.363 kHz, respectively.

Secondly, based on the PSpice model of the pitch-catch setup from Fig. 3-9, the transient analysis is carried out and the sinusoidal pulse signal modulated by the Hanning window is also chosen as the excitation signal. The detailed analysis scheme is given as:

- The length of the transmission medium is 20 mm and the excitation signal frequencies are 23.309 and 21.098 in kHz, respectively.
- The length of the transmission medium is 100 mm and the excitation signal frequencies are 23.309 and 24.363 in kHz, respectively.

Then, to verify the accuracy of the simulated results, the pitch-catch experimental platform has been built, as shown in Fig. 3-14. It consists of the arbitrary/functional generator used to generate the excitation signal, the oscilloscope used to record the voltage signal and SPUTs used to transmit and receive the ultrasonic wave signal and the aluminum rods used to transmit the ultrasonic wave signal. Moreover, to make the transducer and the transmission medium fit tightly, glycerin is used as an acoustic agent. Under the condition of the different length transmission medium, the simulated and experimental results of the voltage signal received by the transducer are compared, as shown in Fig. 3-15 and Fig. 3-16.

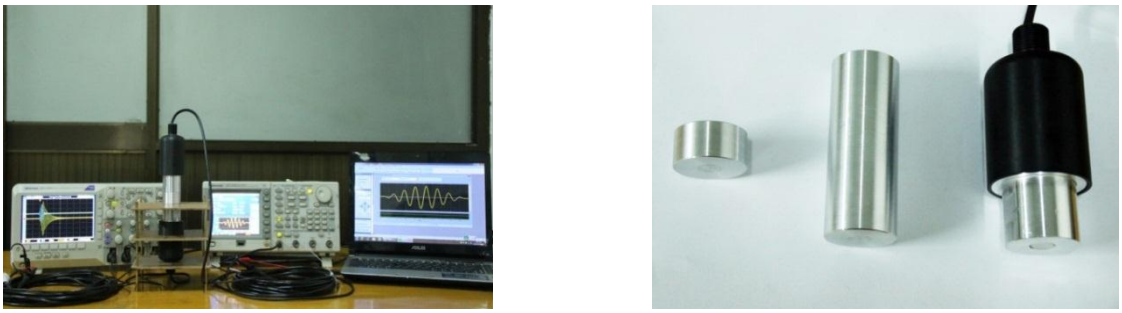

(a) (b)

Fig. 3-14 Transient test in time domain, (a) experimental platform, (b) different lengths aluminum bars and SPUTs

According to Fig. 3-15 and Fig. 3-16, it can be found that the simulated results have good consistency with the experimental ones. Besides, it can be concluded that the optimal excitation frequency for the pitch-catch setup is not necessarily the resonance frequency for the SPUT, because the last resonance frequency was obtained under the condition of no load. In the pitch-catch setup, the transmission medium and the receiving transducer are both the acoustic loads of the transmitting transducer, so the resonance frequency and anti-resonance frequency of the transducer are shifted and multiple resonance modes are generated. Generally, the resonance frequency and anti-resonance frequency of the primary resonance mode are used in practical applications.

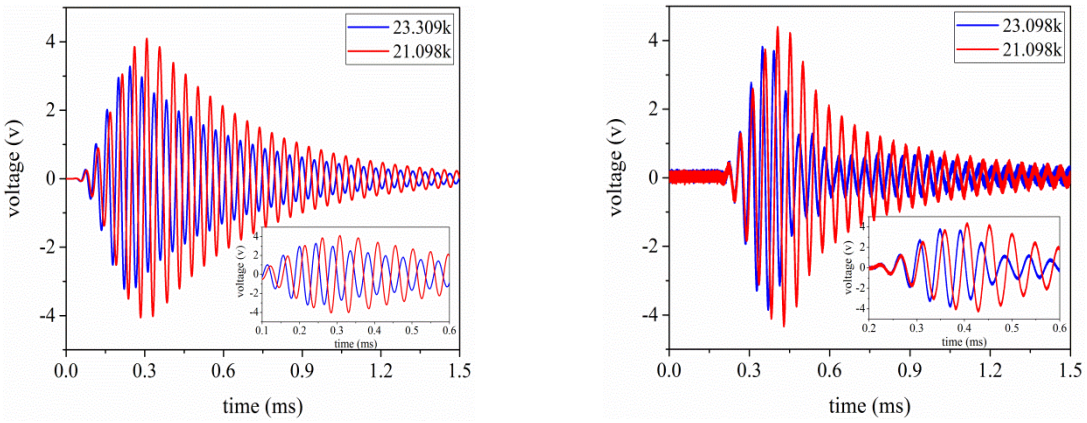

(a) (b)

Fig. 3-15 Transient analysis of a pitch-catch setup under the length of medium equaling 20 mm, (a) simulated results, (b) measured results

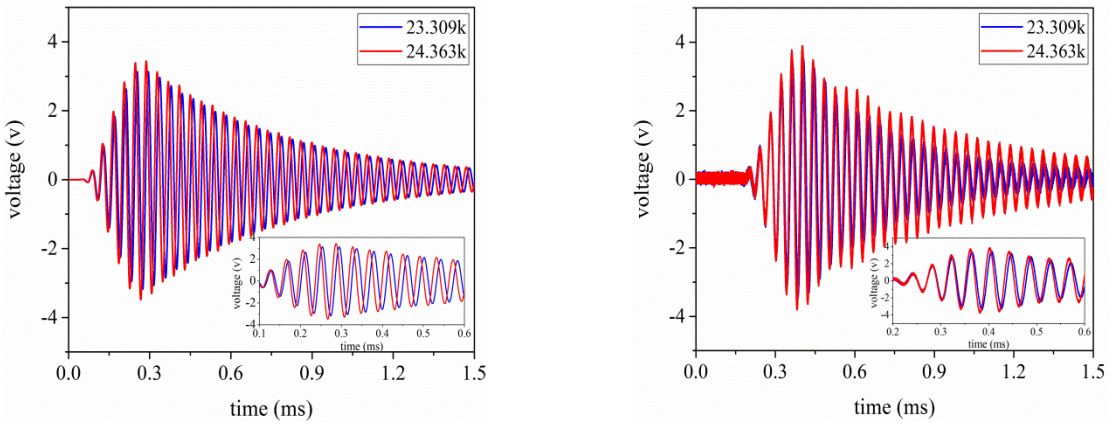

(a) (b)

Fig. 3-16 Transient analysis of a pitch-catch setup under the length of medium equaling 100 mm, (a) simulated results, (b) measured results

Tab. 3-4 The measured and simulated voltage values under the length of the transmission medium having 20 mm

Excitation frequency（kHz）	Simulated voltage（V）	Measured voltage（V）	Relative error Δ_1%
23.309	6.65	7.76	14.3
21.098	8.16	8.88	8.1

Tab. 3-5 The measured and simulated voltage values under the length of the transmission medium having 100 mm

Excitation frequency（kHz）	Simulated voltage（V）	Measured voltage（V）	Relative error Δ_2%
23.309	6.32	6.96	9.2
24.363	6.92	7.76	10.8

In addition, from Fig. 3-15 and Fig. 3-16, the simulated and measured results of the voltage signal received by the SPUT under the same transmission medium length and different excitation frequencies are listed in Tab. 3-4 and Tab. 3-5. According to Tab. 3-4 and Tab. 3-5, it is found that there is a relatively large difference between the measured and simulated results for the voltage signal received by the transducer. The main reasons for this difference are: the trial transducer cannot guarantee that the two transducers are the same; the standard material parameters of the transmission medium used in the simulation are different from the actual material parameters; the frequency difference and the effect of prestressed bolts also lead to large amplitude difference of the received signal.

3.3 Conclusion

To better study the electromechanical characteristics of SPUTs in the longitudinal vibration, based on the one-dimensional wave and transmission line theory, the PSpice equivalent circuit model of SPUTs and the PSpice equivalent circuit model of the pitch-catch setup are established. From the perspective of time and frequency domains, the PSpice models mentioned above are analyzed and their accuracies are verified by some experiments. The established PSpice equivalent circuit model of SPUTs is highly scalable and can be easily combined with

module circuits such as driving circuits, filters, and amplifiers. Thus, it provides a solid basis and theoretical guidance for the study of the content of subsequent chapters.

4 Research on the Effect of Impedance Matching on the Electromechanical Characteristics of PUTs

Due to the problem of impedance mismatch in the detection application of PUTs, the efficiency of energy conversion and energy transmission of PUTs are low. Hence, firstly, based on the established PSpice lossy equivalent circuit model of SPUTs, the effect of EIM on the electromechanical characteristics of SPUTs in the longitudinal vibration is investigated in time and frequency domains. Secondly, based on the experimental analysis method at the acoustic end, the effect of AIM on the transient characteristics of SPUTs in the longitudinal vibration is studied from time and frequency domains.

4.1 Research on the Effect of EIM on the Electromechanical Characteristics of PUTs

PUT is a device that converts ultrasonic frequency electrical energy into mechanical vibration. In general, a PUT with a single vibration mode near its resonance frequency can be approximated by an equivalent circuit as shown in Fig. 4-1 (a). This equivalent circuit consists of a mechanical branch including dynamic resistance R_{m}, dynamic capacitance C_{m}, and dynamic inductance L_{m}; and also an electrical branch composed of static capacitance C_0 and dielectric loss resistance R_0. Based on the above equivalent circuit, the total admittance of the PUT can be expressed as [147]

$$Y = G + jB = \left[\frac{1}{R_0} + \frac{R_{\mathrm{m}}\omega^2 C_{\mathrm{m}}^2}{(1-\omega^2 L_{\mathrm{m}} C_{\mathrm{m}})^2 + R_{\mathrm{m}}^2 \omega^2 C_{\mathrm{m}}^2} \right] + j\left[C_0\omega + \frac{(1-\omega^2 L_{\mathrm{m}} C_{\mathrm{m}})\omega C_m}{(1-\omega^2 L_{\mathrm{m}} C_{\mathrm{m}})^2 + R_{\mathrm{m}}^2 \omega^2 C_{\mathrm{m}}^2} \right] \tag{4-1}$$

where ω denotes the angular frequency of the excitation signal for PUTs, G indicates the conductance, and B represents the susceptance. According to equation (4-1), the conductance and the susceptance of the PT can be obtained as

$$G = \frac{1}{R_0} + \frac{R_{\mathrm{m}}\omega^2 C_{\mathrm{m}}^2}{(1-\omega^2 L_{\mathrm{m}} C_{\mathrm{m}})^2 + R_{\mathrm{m}}^2 \omega^2 C_{\mathrm{m}}^2} \tag{4-2}$$

$$B = C_0\omega + \frac{(1-\omega^2 L_{\mathrm{m}} C_{\mathrm{m}})\omega C_m}{(1-\omega^2 L_{\mathrm{m}} C_{\mathrm{m}})^2 + R_{\mathrm{m}}^2 \omega^2 C_{\mathrm{m}}^2} \tag{4-3}$$

Combining equations (4-2) and (4-3), the conductive trace equation can be expressed as

$$(G - \frac{1}{R_0} - \frac{1}{2R_{\mathrm{m}}})^2 + (B - \omega C_0)^2 = (\frac{1}{2R_{\mathrm{m}}})^2 \tag{4-4}$$

From equation (4-4), it is found that the conductive trace of the PUT near the resonant

frequency can be represented as a circle as shown in Fig. 4-1(b). The center of this circle is $(1/R_0+1/2R_m, \omega C_0)$ and the radius is $1/2R_m$. Note that in Fig. 4-1(a), the value of the dielectric loss resistance is much larger than other parallel elements, so the dielectric loss resistance is generally ignored in this equivalent circuit.

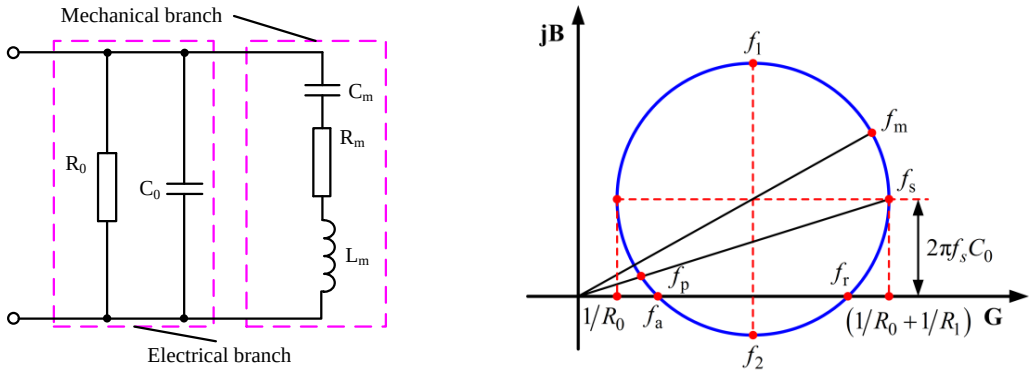

(a) (b)

Fig. 4-1 The equivalence of PUTs near resonance frequency, (a) the equivalent circuit, (b) the admittance circle

From Fig. 4-1(b), the specific description of the marked frequency points is given as: f_s is the mechanical resonance frequency (the frequency point that has the maximum conductance), f_p is the parallel resonance frequency, f_r is the resonance frequency under zero impedance phase, f_a is the anti-resonance frequency under zero impedance phase, f_m represents the maximum admittance frequency and, finally, f_1 and f_2 denote the half-power point frequency. Compared to the anti-resonance frequency, the resonance frequency is closer to the mechanical resonance frequency. The mechanical resonance frequency is also called series resonance frequency and it can be expressed as

$$f_s = \frac{1}{2\pi\sqrt{L_m C_m}} \tag{4-5}$$

The best emission performance of PUTs can only be obtained at $f_s = f_m = f_r$, because the total impedance in this case is the smallest and only resistive. However, due to the existence of the static capacitance C_0, the entire admittance circle is shifted upward by $2\pi f_s C_0$ along the direction of the susceptance axis. This will cause the above frequency relationship to be unsatisfactory, and as the excitation frequency increases, the above three frequencies will differ greatly. To eliminate the influence of the static capacitance, inductive components such as inductances are usually used to compensate for the capacitive reactance. Also, PUTs work with different damping conditions and the radius of the conduction circle varies; the greater the damping, the smaller the radius of the conduction circle and vice versa. If the sum of the dynamic resistance and the load resistance in the mechanical branch circuit is represented by a resistance, it is possible to use the admittance circle to obtain the relationship of the change in the admittance of the PT due to the load change. When the damping of the piezoelectric transducer is unchanged, the radius of the admittance circle will become smaller as the load increases, and vice versa.

Generally, an ultrasonic wave transmitter usually can be simplified, as shown in Fig. 4-2. It is composed of an ultrasonic excitation source, EIM network, and ultrasonic transducer. According to the impedance matching theory, the maximum power transmission of ultrasonic transducers can be obtained, when the input and output impedances of an EIM network (Z_{in} and

Z_{out}) are just equal to the complex conjugates of the electrical impedances of the excitation source (Z_s) and a piezoelectric ultrasonic transducer (Z_t) at the resonance frequency, respectively.

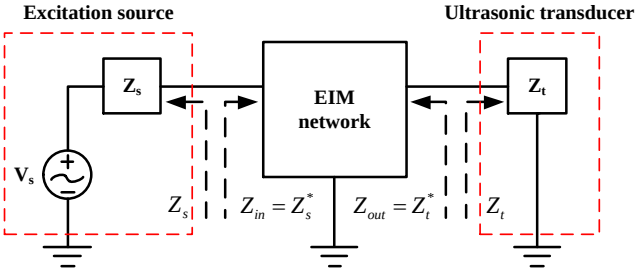

Fig. 4-2 A simplified configuration of an ultrasonic transmitter

It is well-known that the impedance has resistive and reactive components. It can be expressed as:

$$Z_s(\omega) = R_s(\omega) + jX_s(\omega) \tag{4-6}$$

$$Z_t(\omega) = R_t(\omega) + jX_t(\omega) \tag{4-7}$$

where j represents the imaginary unit and ω denotes angular frequency. For an optimal electrical impedance matching network, the input and output electrical impedance of the EIM network can be written as

$$Z_{in}(\omega) = Z_s^*(\omega) = R_s(\omega) - jX_s(\omega) \tag{4-8}$$

$$Z_{out}(\omega) = Z_t^*(\omega) = R_t(\omega) - jX_t(\omega) \tag{4-9}$$

Here, Z_s^* and Z_t^* are the complex conjugates of Z_s and Z_t, respectively.

4.1.1 PSpice Model of PUTs with EIM Network

The PSpice model of a SPUT with an EIM network and the PSpice model of the pitch-catch setup are shown in Fig. 4-3 and Fig. 4-4, respectively. According to these Figures, the impedance matching network is located between the ultrasonic excitation source and the SPUT. The device parameter values in the model are consistent with the device parameters in the aforementioned model.

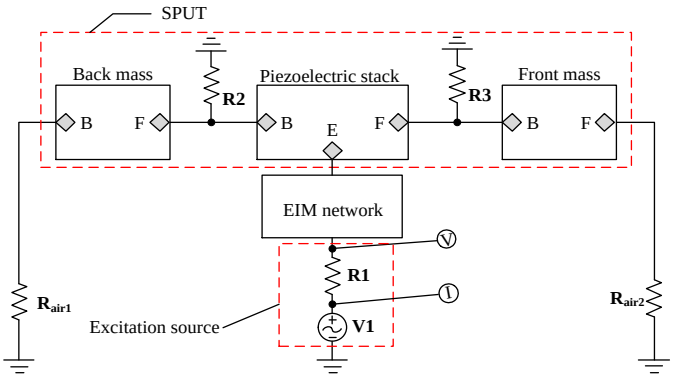

Fig. 4-3 The PSpice model of single SPUT with EIM networks

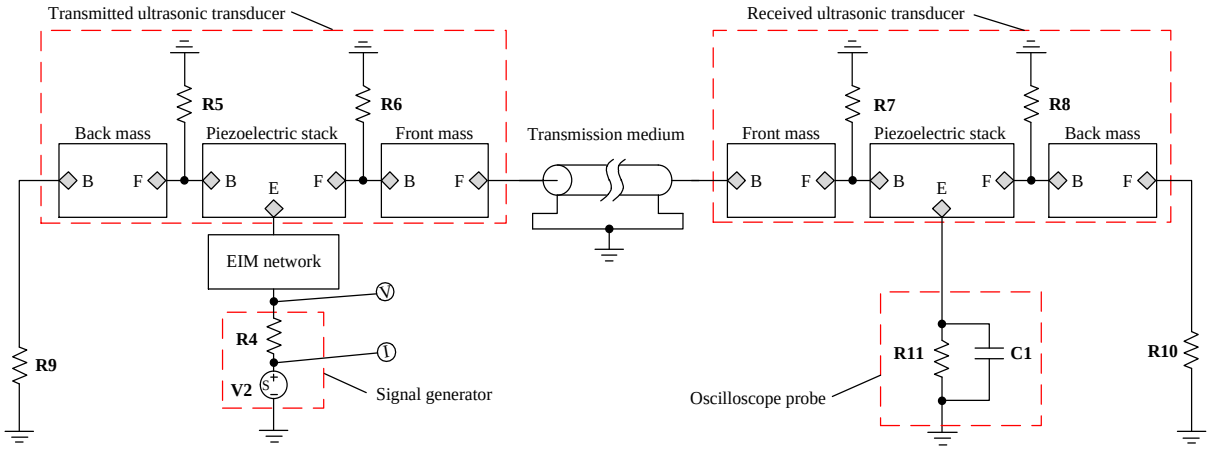

Fig. 4-4 The PSpice model of the pitch-catch setup with EIM networks

Many important electromechanical characteristics parameters such as input impedance and phase, resistance, reactance, and electroacoustic power ratio, gain ratio, and vibration velocity ratio of PUTs can be derived according to the above PSpice models from Fig. 4-3 and Fig. 4-4. These parameters are defined as

$$Z_i = \frac{V(R1:2)}{I(R1)}, \quad Z_{\mathrm{is}} = \frac{V(R4:2)}{I(R4)} \tag{4-10}$$

where Z_{i} and Z_{is} represent the input impedance of PTs and the pitch-catch setup, respectively. $V(R1:2)$ and $V(R4:2)$ denote the voltage across resistances $R1$ and $R4$, $I(R1)$ and $I(R4)$ indicate the current of through resistances $R1$ and $R4$. According to equation (4-10), the resistance and the reactance can be expressed as

$$R_{\mathrm{i}} = \mathrm{Re}\left[Z_{\mathrm{i}}\right], \quad X_{\mathrm{i}} = \mathrm{Im}\left[Z_{\mathrm{i}}\right] \tag{4-11}$$

$$R_{\mathrm{is}} = \mathrm{Re}\left[Z_{\mathrm{is}}\right], \quad X_{\mathrm{is}} = \mathrm{Im}\left[Z_{\mathrm{is}}\right] \tag{4-12}$$

where R_{i} and X_{i} represent the input impedance and reactance of PTs, R_{is} and X_{is} denote the input impedance and reactance of the pitch-catch setup.

According to Fig. 4-3, the electro-acoustic power and gain ratio for single SPUT can be derived as

$$\eta_{P1} = \frac{P_1 + P_2}{P_{i1}}, \quad \eta_{G1} = \frac{V_2}{V_1} \tag{4-13}$$

where η_{P1} and η_{G1} represent the electro-acoustic power ratio and the electro-acoustic gain ratio, respectively. P_1 and P_2 indicate the consumed powers of resistances R_{air1} and R_{air2}, respectively, and P_{i1} denotes the input electrical power. V_1 and V_2 are the excitation voltage and the radiated acoustic pressure from the front mass, respectively.

The vibration velocity ratio between the front mass and the back mass is expressed as:

$$\eta_v = \frac{V_{P-P}(R_{air2})}{V_{P-P}(R_{air1})} \tag{4-14}$$

where $V_{P-P}(R_{air1})$ and $V_{P-P}(R_{air2})$ represent the vibration velocities of the front mass and the back mass, respectively. From Fig. 4-4, the electro-acoustic power and gain ratio for the

pitch-catch setup can be obtained as:

$$\eta_{P2}=\frac{P_3+P_4+P_5}{P_{i2}},\ \ \eta_{G2}=\frac{V_4}{V_3} \tag{4-15}$$

where η_{P2} and η_{G2} are the electro-acoustic power and gain ratio, respectively. P_3 and P_4 indicate the radiated powers from the front and back metal masses, respectively. P_4 is the received power, while P_{i2} is the input electrical power. Also, V_3 and V_4 are the excitation voltage and the received voltage, respectively. Besides, the effective electromechanical coupling coefficient k_{effc} can be obtained as:

$$k_{effc}=\sqrt{1-(f_s/f_p)^2} \tag{4-16}$$

where f_s and f_p are resonance and anti-resonance frequencies, respectively. Note that the effective electromechanical coupling coefficient k_{effc} depends on many factors, such as the materials, the dimensions and structures, and the electrical and mechanical loads.

4.1.2 Selection and Parameters Calculation of Matching Networks

Currently, matching networks mainly include series inductance, parallel inductance, and the combination of inductance and capacitance. The effect of the EIM on the electromechanical characteristics of PUTs is studied based on two matching networks. The two matching networks include I type (series capacitance and parallel inductance) and II type (series inductance and parallel capacitance), as shown in Fig. 4-5.

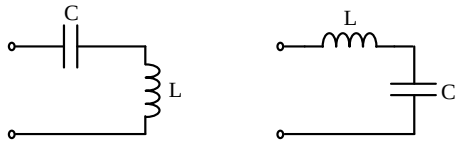

Fig. 4-5 Impedance matching networks

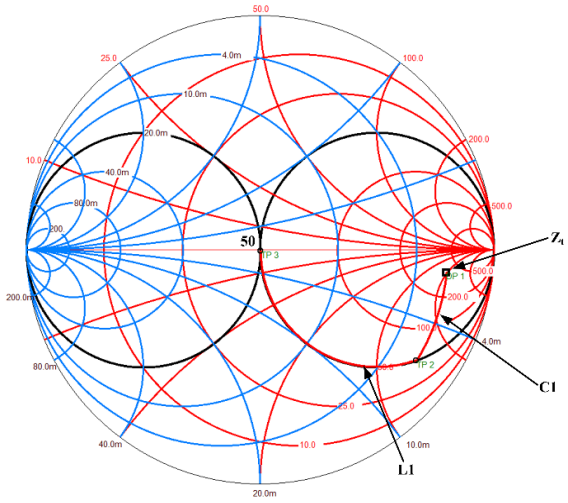

Fig. 4-6 Smith chart

The parameters of EIM networks are conveniently obtained using the Smith chart tool (Smith V3.10 is designed by Prof. Fritz Dellsperger and Michel Band, Bern University of Applied Sciences, Bern, Switzerland.). In the case of matching single SPUT, the load impedance is the

input electrical impedance, which is likely to be seen at the far right end of the Smith chart as shown in Fig. 4-6. In general, the source impedance is usually $50\,\Omega$, which is located at the center of the Smith chart. The EIM matching network is used, therefore, to move the load impedance to the $50\,\Omega$ impedance point through adding capacitances or inductances in series or parallel. Especially, note that an inductance in parallel moves the impedance point along the constant conductance curves, while a capacitance in series moves the impedance point along the constant resistance curves. Similarly, a capacitance in parallel moves the impedance point along the constant conductance curves, however, an inductance in series moves the impedance point along the constant resistance curves.

4.1.3 Impedance Analysis

The impedance analysis is performed based on Fig. 4-3 and Fig. 4-4 under no matching conditions. The specific analysis results are listed in Tab. 4-1. From which, the parameters of the two matching networks shown in Fig. 4-6 with the help of the Smith chart are calculated; the calculation results are listed in Tab. 4-2. Since the theoretically calculated inductance and capacitance parameters do not have corresponding real product specifications, the data in Tab. 4-2 take the specification values that are closest to the theoretically calculated results. According to the PSpice equivalent circuit models of SPUTs and the pitch-catch setup shown in Fig. 4-3 and Fig. 4-4, the important electromechanical characteristic parameters such as the impedance, impedance phase, electro-acoustic power ratio, and electro-acoustic gain ratio are obtained through AC analysis. The impedance analysis results of PUTs under different EIM networks are given in Fig. 4-8 and Fig. 4-9.

Tab. 4-1 The electrical impedance at resonance and anti-resonance frequencies of the single SPUT and the pitch-catch setup

Parameters	f_s (kHz)	f_p (kHz)	Z (Ω)
Single SPUT	23.309	24.885	351.362-j186.203
The pitch-catch setup	24.363	25.050	388.592-j407.495

Tab. 4-2 Impedance matching network parameters of single SPUT and the pitch-catch setup

Impedance matching network	Single SPUT		The pitch-catch setup	
	L (mH)	C (nF)	L (mH)	C (nF)
I type	1.0	47	1.2	33
II type	1.0	33	1.5	22

For verifying the accuracy of the analysis results, an experimental platform has been built. It is composed of an impedance analyzer (PV520A made by BEIJING BAND ERA CO., LTD, Beijing, China) and a single SPUT with EIM circuits, as shown in Fig. 4-7. Fig. 4-8(a-c) shows the simulated results of the input impedance, resistance, and reactance while Fig. 4-8(d-f) shows the corresponding measured ones. Note that the frequencies corresponding to the minimum and maximum impedance values are resonance and anti-resonance frequencies, respectively.

(a) (b)

Fig. 4-7 Impedance test of SPUTs, (a) test diagram, (b) Physical diagram of the test platform

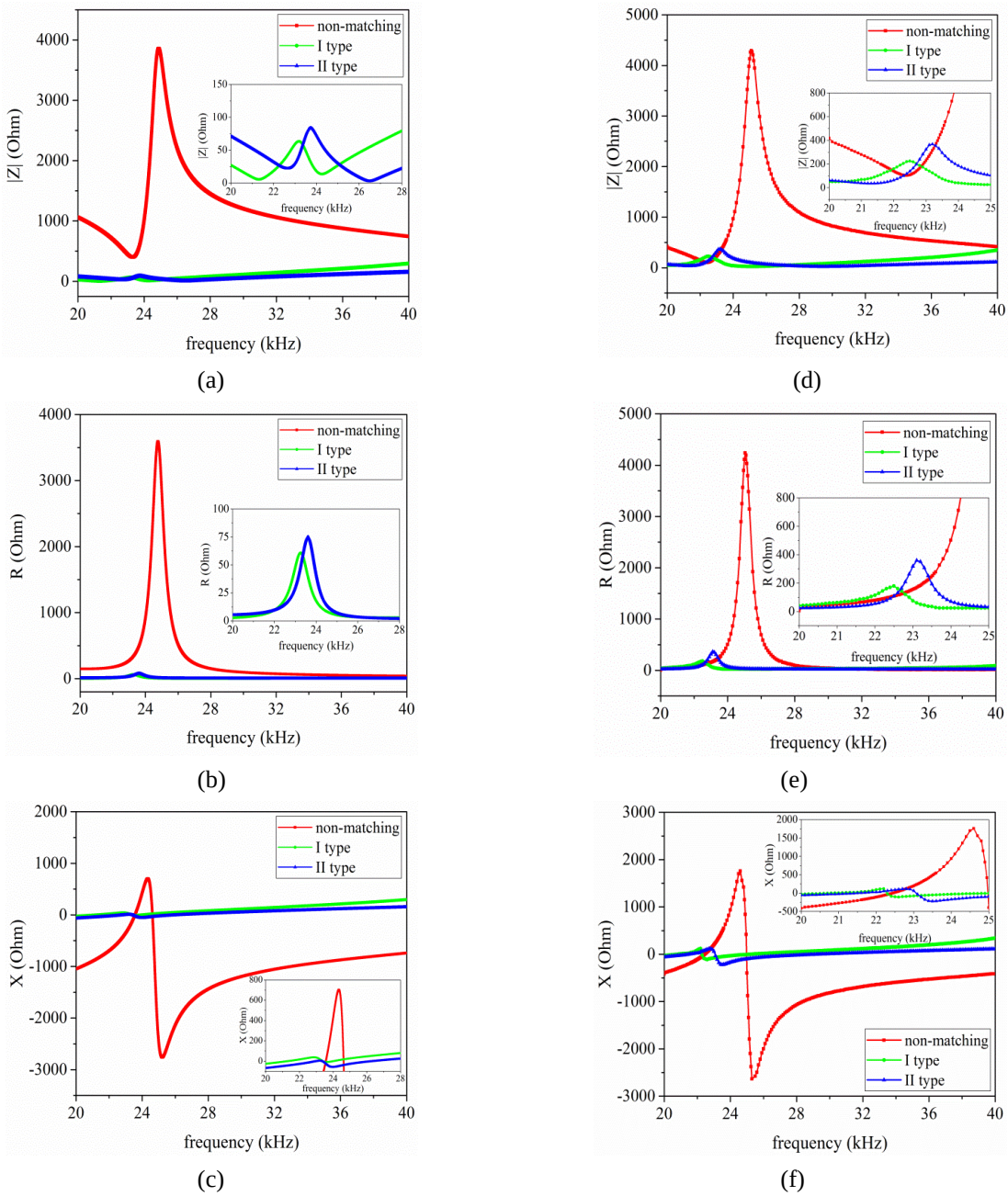

(a) (d)

(b) (e)

(c) (f)

Fig. 4-8 Impedance analyses of SPUTs for different EIM networks, (a-c) simulated results, (d-f) measured results

From Fig. 4-8(a-c), it can be found that when I and II type EIM networks are connected with the sandwiched piezoelectric ultrasonic transducer, the resonance and anti-resonance

frequencies are decreased. Simultaneously, the electrical impedance reaches $50\,\Omega$ and the reactance is close to zero at the resonance frequency. Comparing I type with II type EIM networks, the former makes the resonance and anti-resonance frequencies more substantial decrease. From Fig. 4-8(d-f), it is shown that when I and II type EIM networks are used, the measured impedance, resistance, and reactance are greatly decreased in the whole frequency range of $20\,\text{kHz}\sim40\,\text{kHz}$. To sum up, the measured results have good consistency with the simulated analysis ones. According to Fig. 4-8(a) and Fig. 4-8(d), the resonance frequency and anti-resonance frequency and effective electromechanical coupling coefficient are listed in Tab. 4-3.

Tab. 4-3 Measured and simulated resonance, anti-resonance frequencies and the effective electromechanical coupling coefficient

Impedance matching networks	f_s (kHz)	f_p (kHz)	f_{ms} (kHz)	f_{mp} (kHz)	k_{effc}	k_{meffc}
Non-matching	23.3	24.9	22.5	25.0	0.35	0.44
I type	21.2	23.2	20.0	22.5	0.41	0.46
II type	22.6	23.9	21.3	23.2	0.31	0.40

In Tab. 4-3, f_s, f_p and k_{effc}, f_{ms}, f_{mp} and k_{meffc} indicate the simulated and measured results of series resonance frequency, parallel resonance frequency, and the effective electromechanical coupling coefficient. From Tab. 4-3, it can be seen that when I and II type EIM networks are used, the former makes the effective electromechanical coupling coefficient increase, while the latter makes it decrease. It is shown that the theoretically analyzed results are in good agreement with the measured ones. The frequency differences of the simulated and measured results can be due to the following factors. Firstly, the used PSpice model of sandwiched piezoelectric ultrasonic transducers is not exactly the same as the manufactured transducers. Secondly, it is well known that the manufactured transducers are different, owing to fabrication error and materials difference, etc. Thirdly, due to the limitation of the values of commercial off-the-shelf components, the calculated values of inductors and capacitors in EIM networks are different from the values of the components used in the experimental platform.

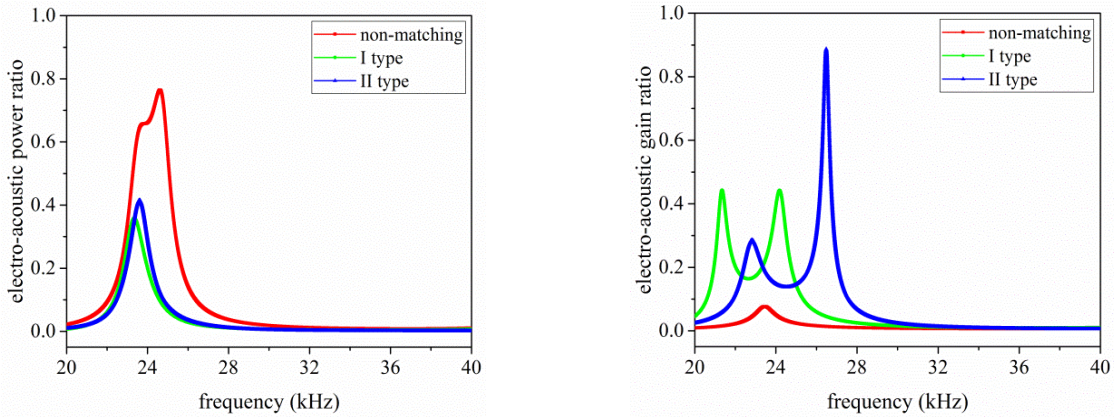

(a) (b)

Fig. 4-9 The electro-acoustic characteristics of SPUTs with EIM network, (a) electro-acoustic power ratio, and (b) electro-acoustic gain ratio

In addition, Fig. 4-9 illustrates the relationship between electro-acoustic power and gain ratio and operational frequency, respectively. From Fig. 4-9, when I and II type EIM networks

are used, the electro-acoustic power ratio is decreased, while the electro-acoustic gain ratio is increased at resonance and anti-resonance frequencies. When compared I type with II type EIM networks, it can be found that the latter makes the electro-acoustic power ratio more substantially decrease at the resonance frequency, while the former makes it more substantially decrease at anti-resonance frequency; the latter makes the electro-acoustic gain ratio more substantially increase at the resonance frequency, and the former makes it more substantial increase at anti-resonance frequency. In summary, it can be concluded that the electro-acoustic power ratio has a maximum value near the anti-resonance frequency, while the electro-acoustic gain ratio has a maximum value near the resonance frequency.

The impedance analysis results of the pitch-catch setup under different EIM networks are shown in Fig. 4-10. In light of Fig. 4-10(a-c), it can be seen that the PUTs produces multiple resonant modes under having an acoustic load. It is pointed out that the analysis below focuses on the first resonant mode. When I and II type EIM networks are connected, the resonance and anti-resonance frequencies are decreased. Comparing I type with II type EIM networks, the former makes the resonance and anti-resonance frequencies more substantially decrease. Fig. 4-10(d-f) describes the variation relationship between electro-acoustic power and gain ratio, the phase of input electrical impedance, and the working frequency, respectively. From Fig. 4-10(d) and Fig. 4-10(e), when I and II type EIM networks are connected, the electro-acoustic power ratio is decreased but the electro-acoustic gain ratio is increased at resonance and anti-resonance frequencies.

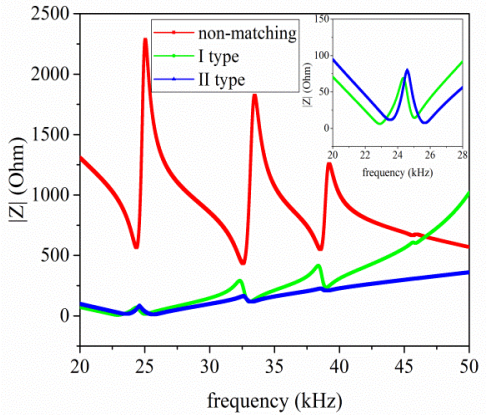

(a)

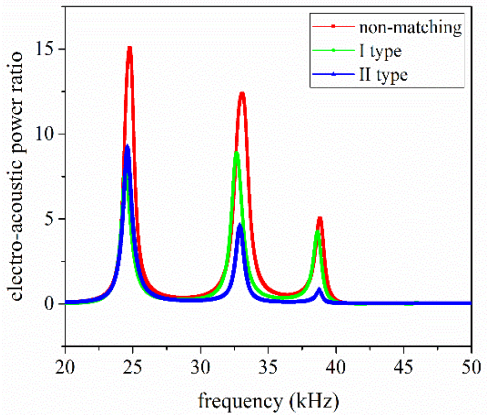

(d)

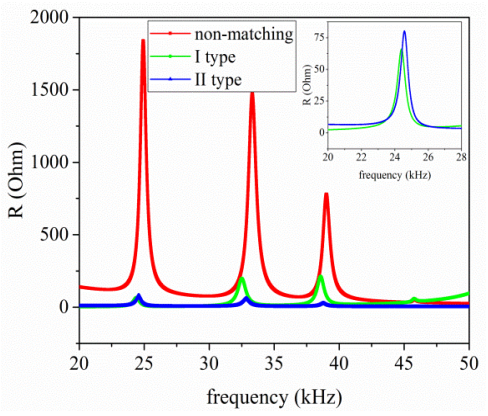

(b)

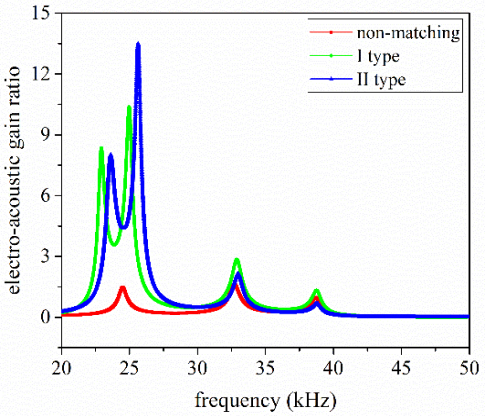

(e)

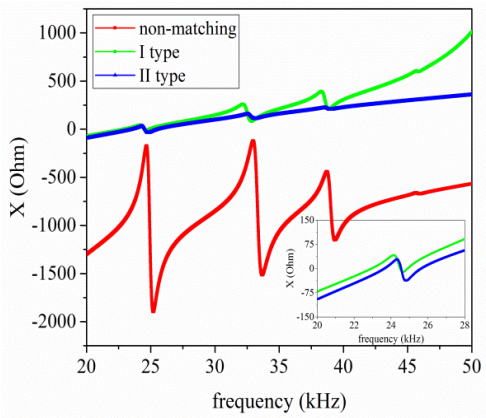

(c)

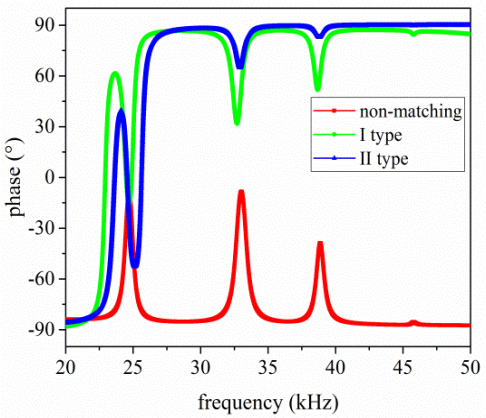

(f)

Fig. 4-10 The impedance analysis results of the pitch-catch setup with EIM networks, (a) impedance; (b) resistance, (c) reactance, (d) electro-acoustic power ratio, (e) electro-acoustic gain ratio, and (f) phase

Comparing I type with II type EIM networks, the latter makes electro-acoustic power ratio more substantially decrease at the resonance frequency, while the former makes it more substantially decrease at anti-resonance frequency; the latter makes the electro-acoustic gain ratio more substantially increase at the resonance frequency, while the former makes it more substantially increase at anti-resonance frequency. Then, according to Fig. 4-10(f), it can be found that when II type EIM network is connected, the phase of the input electrical impedance is near to zero degrees.

4.1.4 Time Domain Transient Analysis

To further investigate the effect of EIM networks on the electromechanical characteristics of SPUTs, based on the PSpice equivalent circuit models shown in Fig. 4-3 and Fig. 4-4, the transient characteristics in time domain of SPUTs and the pitch-catch setup are analyzed. Fig. 4-11 describes the vibration velocities of the front and back masses. According to Fig. 4-11, the vibration velocity and vibration speed ratio are listed in Tab. 4-4. From Tab. 4-4, it can be easily seen that when I and II type EIM networks are connected, the vibration velocities of the front and back masses are increased by more than twice; the vibration velocity ratio is almost unchanged. Comparing I type with II type EIM networks, the latter makes the vibration velocities of the front and back masses more substantially increase.

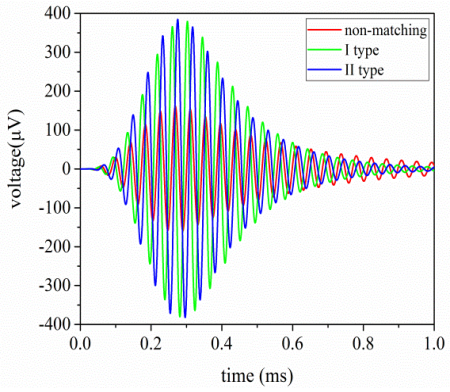

(a)

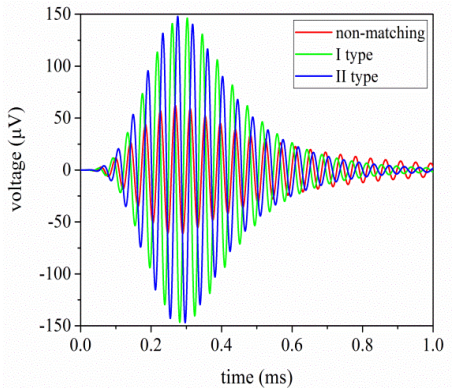

(b)

Fig. 4-11 The vibration velocity of the single SPUT with EIM networks, (a) the vibration velocity of the front mass, (b) the vibration velocity of the back mass

Tab. 4-4 The vibration velocity of the front mass and vibration velocity ratio for single sandwiched piezoelectric ultrasonic transducer

Parameters	Non-matching	I type	II type
Vibration velocity (μV)	322.8	758	769.2
Vibration velocity ratio η_v	2.604	2.592	2.603

A pitch-catch setup experimental platform has been built to verify the accuracy of the analysis results, as shown in Fig. 4-12. It is primarily composed of two SPUTs, a digital oscilloscope, an arbitrary waveform generator, a personal computer, and some inductances and capacitances. The excitation signal selects 5 cycle sine pulse modulated by the Hanning window with an excitation voltage of 20 V. The transient analysis in time domain of the pitch-catch setup is conducted under different matching situations. The analysis results are shown in Fig. 4-13, where it can be seen that when I and II type EIM networks are used, the oscillation of the received voltage signal is reduced; the latter makes the oscillation more substantial decrease. The received voltages of measured and simulated cases are listed in Tab. 4-5.

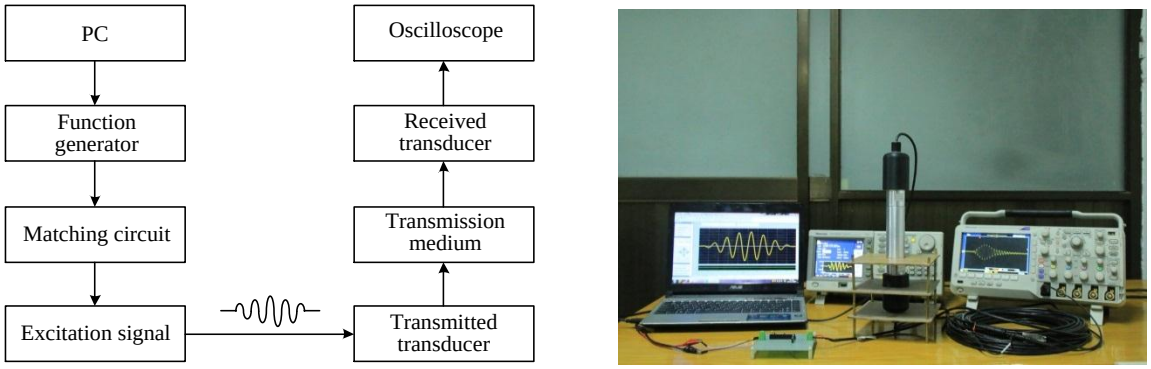

(a) (b)

Fig. 4-12 The transient test of the pitch-catch setup with EIM networks, (a) the test platform diagram, (b) physical picture of the test platform

Tab. 4-5 Simulation and test results of the received voltage of a pitch-catch setup

Parameters	V_s (V)	V_m (V)	Δ_1%
Non-matching	7.25	7.67	5.5
I type	20.7	21.4	3.4
II type	23.5	23.9	1.7

In Tab. 4-5, V_s and V_m are the simulated and the measured voltage values that are derived from the received ultrasonic transducer, respectively, and $\Delta_1 = |V_s - V_m| / V_m$ is the relative error. In light of Tab. 4-5, when I and II type EIM networks are connected, the received voltages of the sandwiched piezoelectric ultrasonic transducer are increased more than twice. Comparing I type with II type EIM networks, the latter makes the received voltage more substantially increase, which has good consistency with the transient analysis results of the single SPUT. It is shown that the measured results are in good agreement with the simulated ones. Several factors can well illustrate the differences in the received voltages in Tab. 4-5.

Firstly, the used PSpice model of the SPUT is not exactly the same as the manufactured transducers. Secondly, due to the effect of frequency differences for the used transducer, this can lead to some amplitude differences.

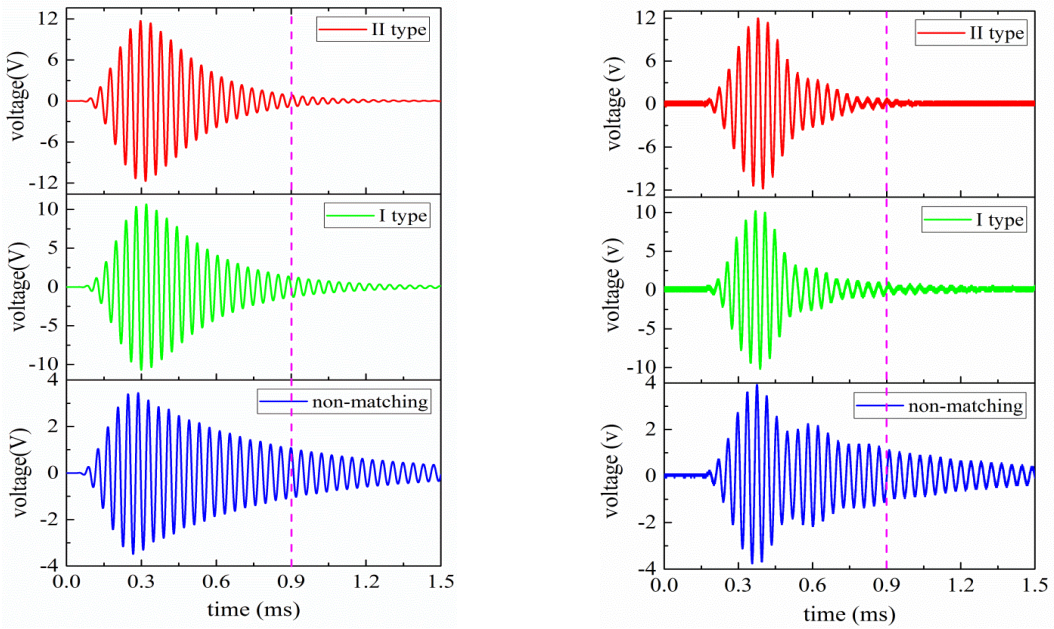

(a) (b)

Fig. 4-13 The transient analysis results of the pitch-catch setup with EIM networks, (a) simulated results, (b) measured results

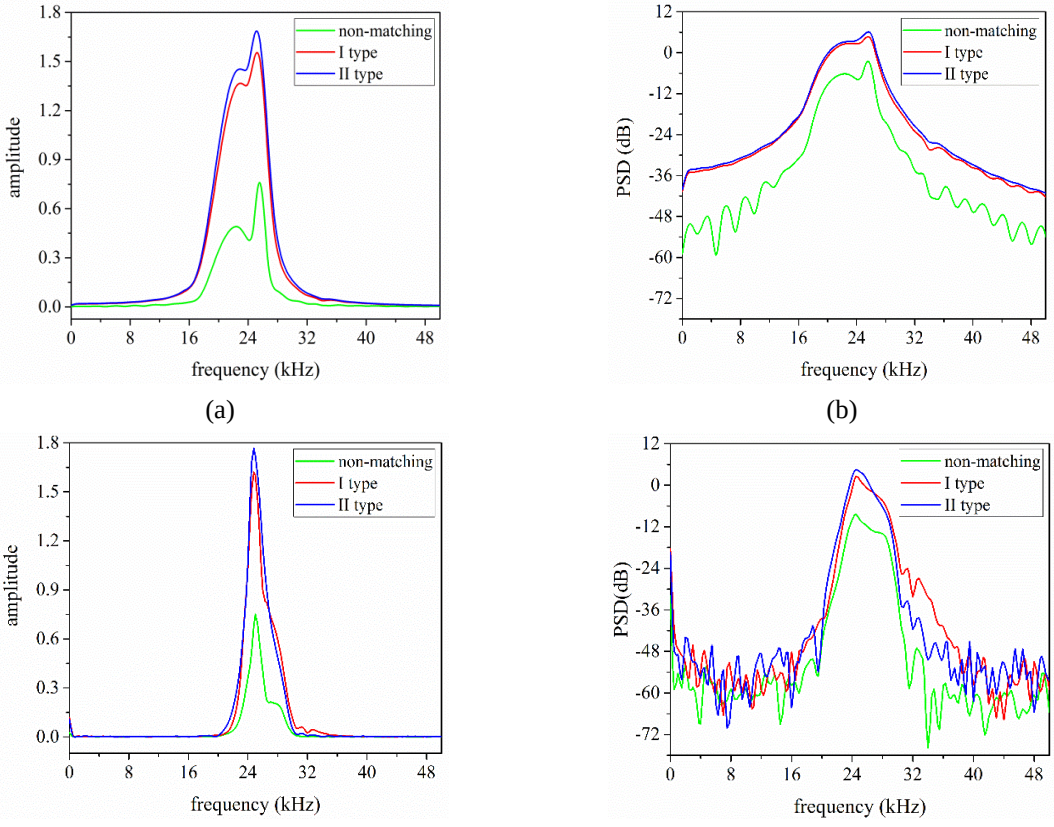

(a) (b)

(c) (d)

Fig. 4-14 The analysis of frequency spectrum and PSD, (a-c) simulated results, (c-d) measured results

To further investigate the effect of EIM networks on the SPUTs, the analyses of the frequency spectrum and power spectrum density (PSD) for the received voltage signals are

performed and the analyzed results are shown in Fig. 4-14. Fig. 4-14(a-b) illustrates the simulated frequency spectrum and PSD results, and Fig. 4-14(c-d) describes the corresponding measured ones. According to Fig. 4-14, it can be concluded that when I and II type EIM networks are connected, the received signal amplitude at the resonance frequency in frequency spectrum is increased more than twice; the latter makes the amplitude largely increase.

Tab. 4-6 The analysis results of the frequency spectrum and PSD for the pitch-catch setup

Impedance matching networks	A_s	A_m	PSD_s (dB)	PSD_m (dB)	Δ_2%	Δ_3%
Non-matching	0.43	0.52	-7.91	-8.37	17.3	5.5
I type	1.45	1.53	2.72	2.6	5.2	4.6
II type	1.58	1.67	4.25	4.51	5.4	5.8

The specific frequency and power spectrum analysis results for the pitch-catch setup are listed in Tab. 4-6. In this table, A_s and A_m are the simulated and measured signal amplitude at the resonance frequency in the frequency spectrum, respectively, and $\Delta_2 = |A_s - A_m| / A_m$ is the relative error. Then, PSD_s and PSD_m are the simulated and measured power spectral density at the resonance frequency, respectively, and again $\Delta_3 = |PSD_s - PSD_m| / PSD_m$ represents the relative error. According to Tab. 4-6, it can be seen that when I and II type EIM networks are used, the PSD is largely increased and the latter makes it more substantially increase. The differences between the simulated and measured results in Tab. 4-6 can be explained by the following factors. Firstly, the used PSpice model of single SPUT is not exactly the same as the real manufactured transducers. Secondly, due to the effect of frequency difference for the used transducer, this can lead to some differences in the frequency spectrum amplitude and PSD.

4.2 Research on the Effect of AIM on the Electromechanical Characteristics of PUTs

The ultrasonic wave has an important characteristic, i.e. when it propagates to the interface of the acoustic impedance discontinuity it causes that most of the energy is reflected, and only a small amount of energy is incident and continues propagating forward. If the incident angle and reflection angle are known, the energy distribution can be calculated according to the Snell's law. However, when the ultrasonic wave enters the rail, it undergoes multiple boundary reflections, refractions, and other couplings to form UGW signals and the situation become very complex. Therefore, the specific distribution of UGW signal energy is not discussed in this section. This section aims to solve the problem of impedance discontinuity between the PUT and the surface of the rail web so that the incidence efficiency of ultrasonic waves and the amplitude of the received UGW signal are improved.

4.2.1 Selection and Preparation of Acoustic Coupling Agent

Generally, the acoustic matching layer materials (also called acoustic coupling agents) are water, motor oil, white Vaseline, SiO_2 aerogel, tungsten-vinyl composite, and epoxy resin;

among which water and white petrolatum are very good acoustic coupling agents. Because the PUT in the broken rail detection system based on UGW has to be installed on the rail web of the in-service rail for a long time to collect the real-time rail status information, considering the firmness of the installation and the problem of acoustic impedance matching for PUTs, epoxy resin is a good choice. Also, the radiating surface of the PUT used in this document uses hard aluminum and the material of the rail is mostly manganese steel, so the acoustic impedance difference between the two materials is very large. Therefore, epoxy resin is used as the base material, and a certain proportion of alumina powder or tungsten powder is added to the mixed epoxy resin material to prepare the matching layer material. The selected materials are mainly epoxy resin E-51, epoxy resin amine curing agent W93, alumina powder (particle size 10 in micrometer), and tungsten powder (particle size 10 in micrometer). The specific process of sample preparation is:

- Preparation of base resin: Epoxy resin E-51 and amine curing agent W93 are mixed according to the mass ratio of 4: 1, and then stir well until a homogeneous mixture is formed.
- Add filler: Taking a certain amount of matrix resin into the paper cup, then the alumina powder in batches is added and then stirs evenly. To prevent the agglomeration of metal powder during stirring, it is carefully stirred to ensure that the metal powder is evenly dispersed in the base material.

The acoustic properties of pure epoxy resin, the acoustic properties of samples prepared by mixing alumina powder and epoxy resin, and the acoustic properties of samples prepared by mixing tungsten powder and epoxy resin are shown in Tab. 4-7, Tab. 4-8 and Tab. 4-9. Especially, note that the parameters in the above tables are all from the literature [148].

Tab. 4-7 Acoustic properties of pure epoxy resin samples

Type of curing agent	Density (kg/m^3)	Acoustic velocity (m/s)	Acoustic impedance (MRay1)	Acoustic attenuation (dB/cm.MHz)
Amine curing agent W93	1190	2727	3.25	3.58

Tab. 4-8 Acoustic properties of samples prepared by mixing alumina powder with epoxy resin

Alumina powder volume ratio	Density (kg/m^3)	Acoustic velocity (m/s)	Acoustic impedance (MRay1)	Acoustic attenuation (dB/cm.MHz)
*R*v1=5%	1329	2719	3.61	7.58
*R*v1=10%	1459	2708	3.95	8.77
*R*v1=20%	1733	2882	4.99	6.39

Tab. 4-9 Acoustic properties of samples prepared by mixing tungsten powder with epoxy resin

Tungsten powder volume ratio	Density (kg/m^3)	Acoustic velocity (m/s)	Acoustic impedance (MRay1)	Acoustic attenuation (dB/cm.MHz)
*R*v2=5%	1870	2713	4.06	8.01
*R*v2=10%	2530	2054	5.21	5.79

4.2.2 Time Domain Transient Analysis

The section investigates the effect of AIM of PUTs on the transient characteristics in time domain. Specifically, different AIM layer materials prepared as indicated in Section 4.2.1 will be used in combination with experiments for analysis.

An experimental platform has been built, as shown in Fig. 4-15. It consists of an arbitrary waveform generator, a digital oscilloscope, two SPUTs, and the transmission medium. Note that PUT 1# is responsible for transmitting ultrasonic signals while PUT 2# is responsible for receiving ultrasonic signals. To simplify the experiment, steel rods of the same material are used instead of rails, and the transmission medium uses a steel rod with a diameter of 37 mm and a length of 100 mm. White vaseline is evenly applied between the radiation surface of the PUT 2# and the surface of the steel rod to ensure that the two are in close contact. The excitation signal adopts 8-cycle and 16-cycle sinusoidal pulse signals, whose frequency and peak-to-peak voltage are 35 kHz and 20 V, respectively. Based on the above excitation conditions of PUTs, this section analyses the received signal in time domain under the use of the following three matching layer materials: pure epoxy resin and epoxy resin mixed with different proportions of alumina powder, epoxy resin mixed with tungsten powder in different proportions. According to the equation (2-50), Tab. 4-7, Tab. 4-8 and Tab. 4-9, the matching layer thickness of the 0.1 times wavelength is 7.7 mm. Therefore, for pure epoxy resin, Tm=1 mm, 4 mm, 5 mm, and 7 mm are used while the thickness of the matching layer of the latter two situations is Tm=8 mm for specific analysis.

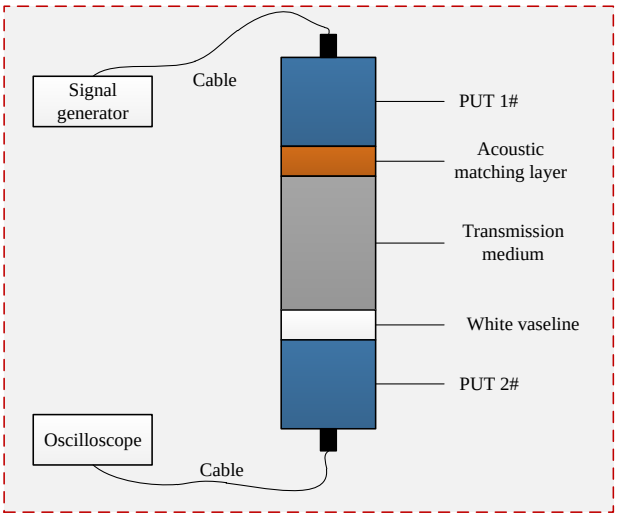

Fig. 4-15 Experimental platform of acoustic impedance matching of piezoelectric ultrasonic transducers

In the first place, using 8-cycle and 16-cycle sinusoidal pulses to excite PUTs respectively, the epoxy resin matching layer of four thicknesses is analyzed based on the experimental platform shown in Fig. 4-15. The specific results are shown in Fig. 4-16. From Fig. 4-16, it is found that as the thickness of the matching layer increases, the waveform of the received signal becomes smoother. Compared with the 8-cycle sinusoidal pulse excitation, the 16-cycle sinusoidal pulse excitation makes the first wave and the second wave of the received signal overlap less. According to Fig. 4-16, the peak-to-peak value of the received signal at different excitation cycles and the thickness of the epoxy layer can be obtained and listed in Tab. 4-10. From this table, the peak-to-peak value of the received signal is the largest when Tm=5 mm, it

is closed to the largest when *T*m=4 mm, and it is the smallest when *T*m=7 mm. It can be preliminarily determined that under using epoxy resin for acoustic matching, the thickness of the matching layer is preferably 5 mm, followed by 4 mm, and the thickness of the two matching layers is far less than the quarter wavelength thickness.

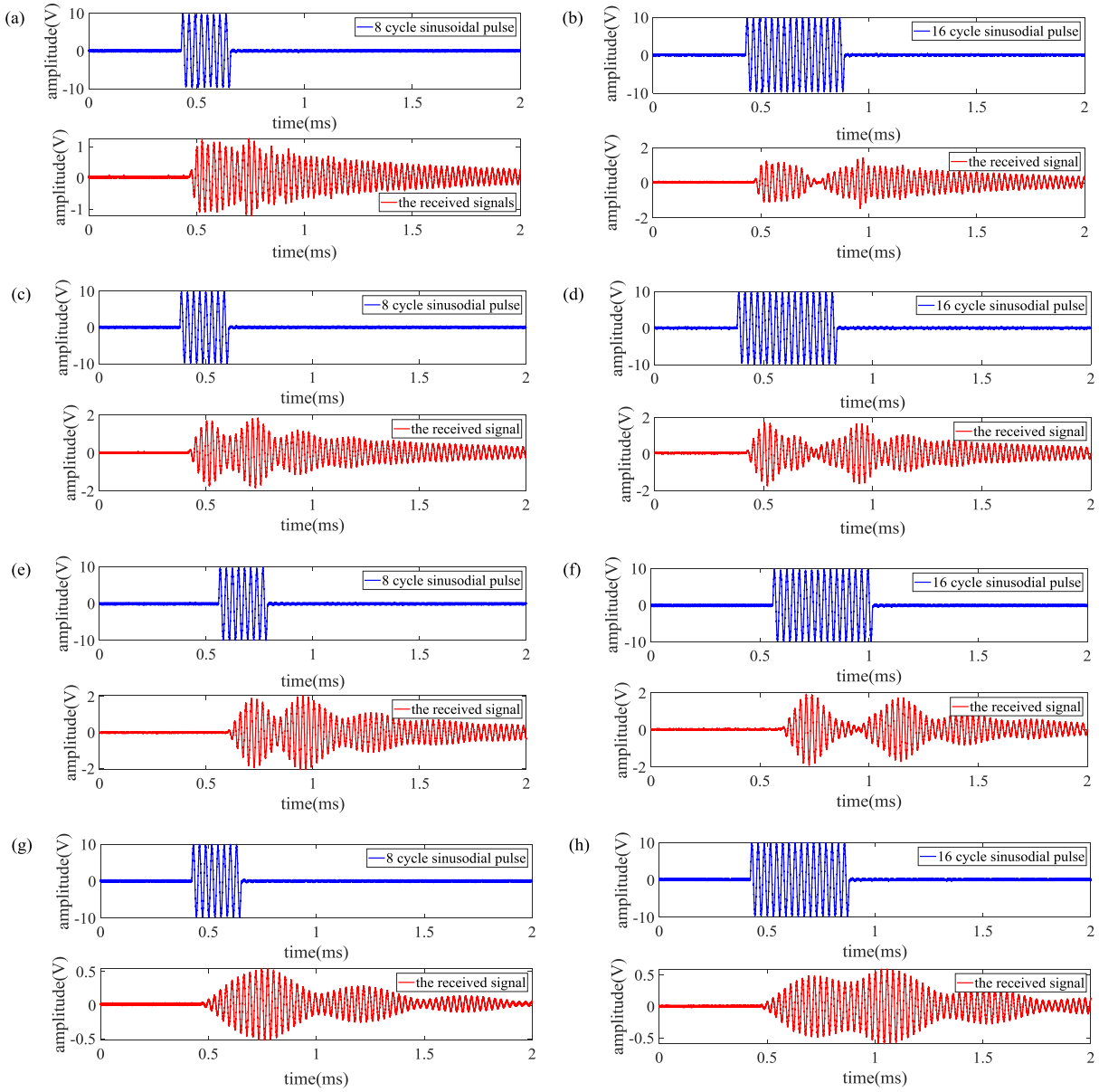

Fig. 4-16 The analysis of received signals under different excitation cycles and layer thickness of epoxy resin, (a) (b) *T*m=1 mm, (c) (d) *T*m=4 mm, (e) (f) *T*m=5 mm, (g) (h) *T*m=7 mm

Tab. 4-10 Peak-to-peak values of the received signal under different excitation cycles and layer thickness of the epoxy resin

Parameters	The thickness of the matching layer			
	*T*m=1 mm	*T*m=4 mm	*T*m=5 mm	*T*m=7 mm
8 cycle	2.48V	3.72V	4.04V	1.06V
16 cycle	2.88V	3.48V	3.80V	1.08V

In the second place, based on three different proportions of alumina powder (*R*v1=5%,

*R*v1=10%, and *R*v1=20%), the corresponding received signals are analyzed, as shown in Fig. 4-17. From Fig. 4-17, it is found that as the proportion of alumina powder incorporated increases, the received signal waveform also becomes smoother. Compared with the 8-cycle sinusoidal pulse excitation signal, the 16-cycle sinusoidal pulse excitation signal makes the first wave and second wave of the received signals overlap less. According to Fig. 4-16, the peak-to-peak value of the received signal is obtained and listed in Tab. 4-11 when different excitation cycle numbers and different proportions of aluminum powder are added.

Tab. 4-11 Peak-to peak of the received signal under different excitation cycles and different proportion of aluminum oxide powder

Parameters	Alumina powder volume ratio		
	*R*v1=5%	*R*v1=10%	*R*v1=20%
8 cycle	1.62V	1.72V	1.32V
16 cycle	1.64V	1.76V	1.32V

From Tab. 4-11, it can be seen that when the ratio of alumina powder is *R*v1=10%, the peak-to-peak value of the received signal is the largest, it is the second after the largest when *R*v1=5%, and it is the smallest when *R*v1=20%.

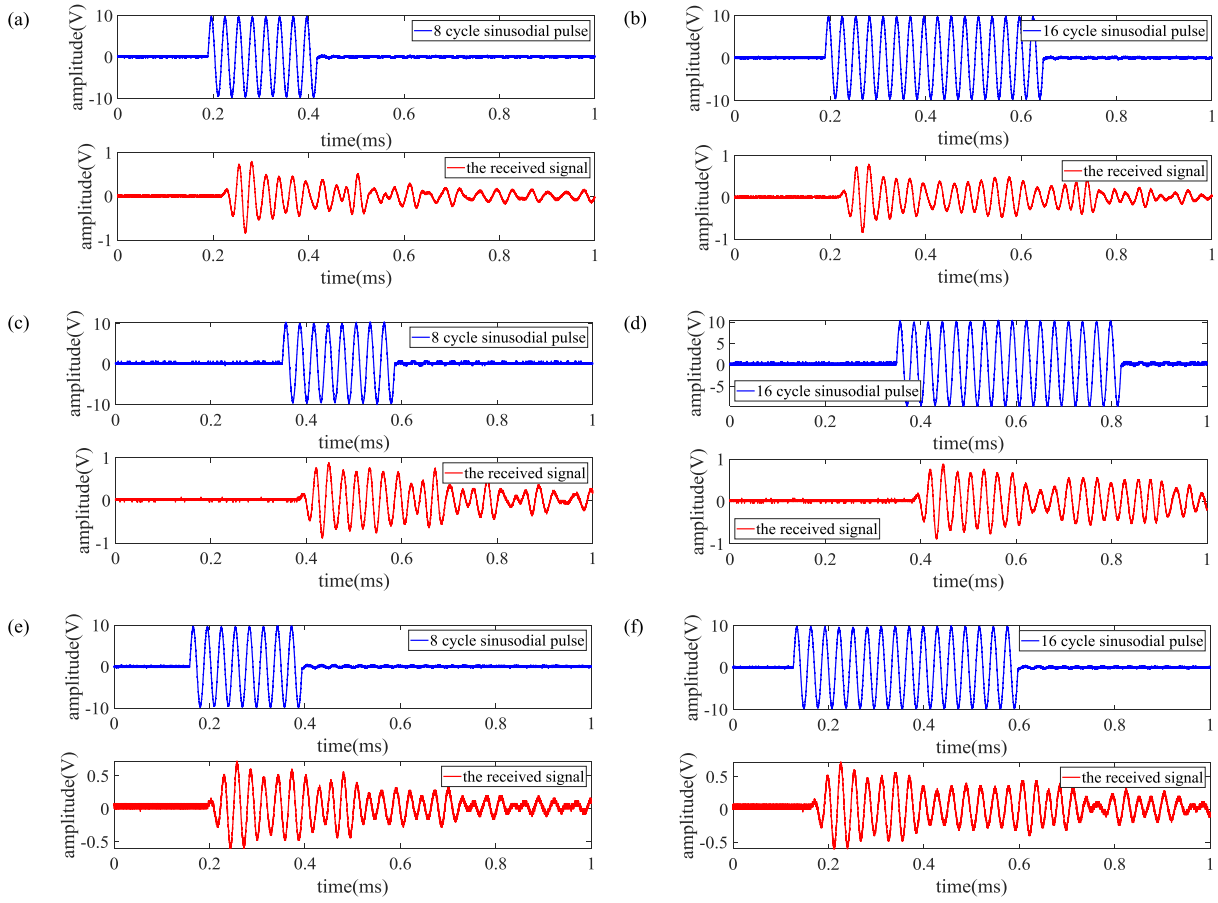

Fig. 4-17 The analysis of the received signals under different excitation cycles and different proportion of aluminum oxide powder, (a) (b) *R*v1=5%, (c) (d) *R*v1=10%, (e) (f) *R*v1=20%

Finally, using 8-cycle and 16-cycle sinusoidal pulses to excite PUTs, the received signals

are analyzed for three different proportions of tungsten powder (*R*v2=0%, *R*v2=5%, and *R*v2=10%), as shown in Fig. 4-18. From Fig. 4-18, it is found that compared with pure epoxy resin and mixed with different proportions of alumina powder, the received signal is smoother under the use of the mixed one with different proportions of tungsten powder. As the incorporation ratio of tungsten powder increases, the first and second waves of the received signal do not overlap at all when the excitation signal cycle is 16. Besides, according to Fig. 4-18, when different excitation cycle numbers and different proportions of tungsten powder are added, the peak and peak values of the received signals are listed in Tab. 4-12.

Tab. 4-12 Peak-to peak of the received signal under different excitation cycles and different proportion of tungsten powder

Parameters	Tungsten powder volume ratio		
	*R*v2=0%	*R*v2=5%	*R*v2=10%
8 cycle	2.60V	3.68V	3.68V
16 cycle	3.08V	3.28V	3.64V

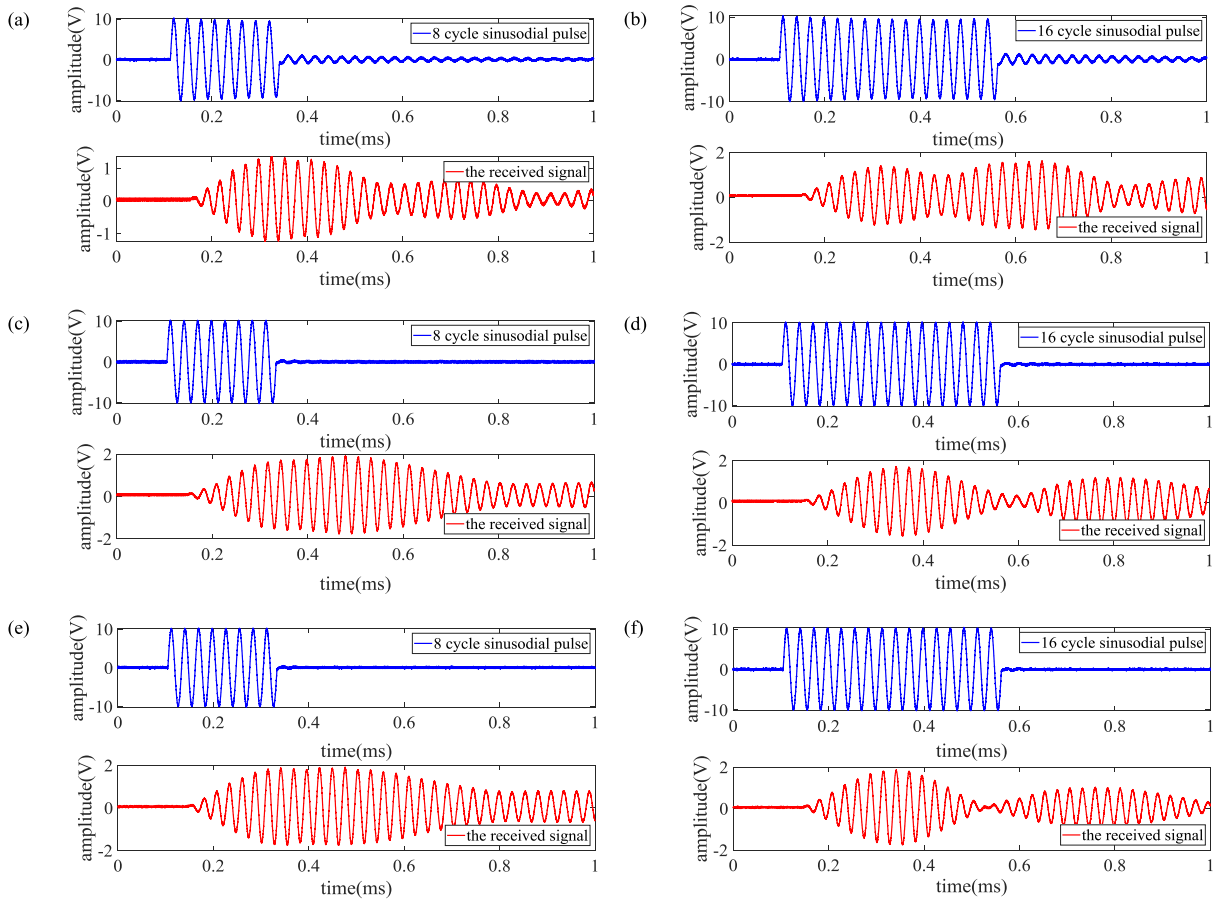

Fig. 4-18 The analysis of the received signals under different excitation cycles and different proportion of tungsten powder, (a) (b) *R*v2=0%, (c) (d) *R*v2=5%, (e) (f) Rv2=10%

In the light of Tab. 4-12, when the excitation cycle is 8, the peak-to-peak values of the received signals are equal and maximum under the incorporation proportion of tungsten powder of *R*v2=5% and 10%. However, when the excitation cycle is 16, the peak-to-peak value of the received signal is the largest under the incorporation proportion of tungsten powder of

*R*v2=10%. Therefore, the matching effect is the best when the incorporation proportion of tungsten powder is Rv2 = 10%.

4.2.3 Frequency Domain Analysis

To further determine which of the above matching situations is more effective, this section focuses on analyzing the spectrum of the received signal under different matching situations. Because the excitation signal frequency is 35 kHz, the frequency range of spectrum analysis is 25 kHz ~ 50 kHz. Firstly, under the different number of excitation cycles and the thickness of the epoxy resin layer, the frequency spectrums of the received signals are analyzed, as shown in Fig. 4-19. From Fig. 4-19, it is found that compared with the 8-cycle sinusoidal pulse excitation signal, the spectral energy leakage of the received signal is serious and then the 16-cycle sinusoidal pulse excitation is used with the energy mainly distributed around 35 kHz and 40 kHz. According to Fig. 4-19, the maximum amplitude and corresponding frequency of the received signal spectrum at different excitation cycles and the thickness of the epoxy layer are listed in Tab. 4-13. From Tab. 4-13, it is shown that when the excitation cycle is 8, and the matching layer thickness *T*m=5 mm, the received signal spectrum amplitude is the largest. However, when the excitation cycle is 16, and the matching layer thickness *T*m=4mm, the received signal spectrum amplitude is the largest. In the above two cases, the frequencies corresponding to the maximum amplitude of the spectrum are 37.70 kHz and 37.90 kHz, which are around 38 kHz. Hence, the matching effect is best when the thickness of the matching layer is *T*m=5mm.

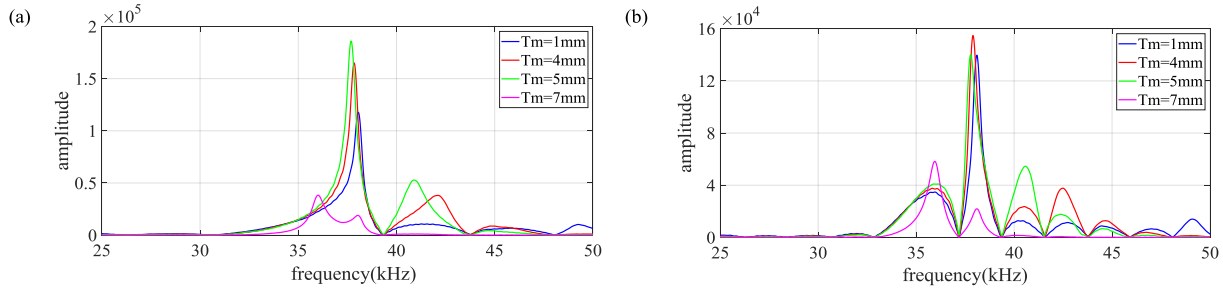

Fig. 4-19 Frequency spectrum analyses of the received signals under different excitation cycles and layer thickness of epoxy resin, (a) 8 cycle, (b) 16 cycle

Tab. 4-13 Frequency spectrum maximum values and corresponding frequencies of the received signal under different excitation cycles and layer thickness of the epoxy resin

Parameters	The thickness of the matching layer			
	*T*m=1 mm	*T*m=4 mm	*T*m=5 mm	*T*m=7 mm
8 cycle	117800	165100	186000	38330
16 cycle	139800	154800	140100	58310
8 cycle	38.05 kHz	37.85 kHz	37.70 kHz	36.01 kHz
16 cycle	38.10 kHz	37.90 kHz	37.77 kHz	35.95 kHz

Secondly, under different excitation cycle numbers and different proportions of alumina powder, the frequency spectrum of the received signal is performed, as shown in Fig. 4-20. Also, it can be seen that compared to the 8-cycle excitation, the received signal spectrum energy

leakage is large and under the 16-cycle excitation the energy is mainly distributed around 37 kHz. In the light of Fig. 4-20, under different excitation cycles and different proportions of alumina powder, the maximum value of the received signal spectrum and the corresponding frequency are listed in Tab. 4-14.

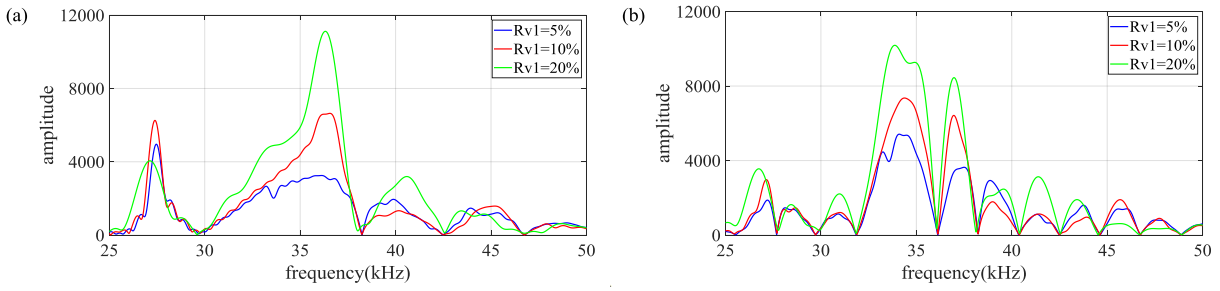

Fig. 4-20 Frequency spectrum analyses of the received signals under different excitation cycles and different proportion of aluminum oxide powder, (a) 8 cycle, (b) 16 cycle

From Tab. 4-14, it is found that under the incorporation proportion of aluminum powder *R*v1=5%, the received signal spectrum amplitude is the largest. The received signal spectrum amplitude is the next largest when the incorporation proportion of aluminum powder *R*v1=10%. When *R*v1=5% and the number of excitation cycles are 8 and 16, the frequencies corresponding to the maximum amplitude of the frequency spectrum are 36.30 kHz and 33.84 kHz, respectively. Thus, the matching effect is the best when the alumina powder is mixed with *R*v1=5%.

Tab. 4-14 Frequency spectrum maximum values and corresponding frequencies of the received signals under different excitation cycles and different proportion of aluminum oxide powder

Parameters	Alumina powder volume ratio		
	*R*v1=5%	*R*v1=10%	*R*v1=20%
8 cycle	11110	6641	3250
16 cycle	10180	7357	5411
8 cycle	36.30kHz	36.56kHz	36.10kHz
16 cycle	33.84kHz	34.38kHz	34.07kHz

Finally, under different excitation cycle numbers and different proportions of tungsten powder, the frequency spectrum of the received signal is analyzed, as shown in Fig. 4-21. From Fig. 4-21, compared with the above two matching cases, when the tungsten powder with different proportions is mixed, the received signal spectrum leakage is small and the energy is mainly concentrated in the frequency range of 35 kHz ~ 40 kHz. According to Fig. 4-21, under different excitation cycle numbers and different proportions of tungsten powder, the maximum frequency spectrum and corresponding frequency of the received signal are obtained and listed in Tab. 4-15. In the light of Tab. 4-15, when the excitation cycle is 8 and the incorporation proportion of tungsten powder *R*v2=10%, the maximum value of the received signal spectrum is maximum. However, when the excitation cycle is 16 and the incorporation proportion of tungsten powder is *R*v2=5% and Rv2=10%, the maximum value of the received signal spectrum is similar. Therefore, the matching effect is the best when the incorporation proportion

of tungsten powder is *R*v2=10%. Combining Fig. 4-19, Fig. 4-20 and Fig. 4-21, it is shown that the excitation signal frequency is 35 kHz, but the frequency corresponding to the maximum value of the frequency spectrum is not around 35 kHz. This is mainly because its resonance frequency will shift when the PUT is with load.

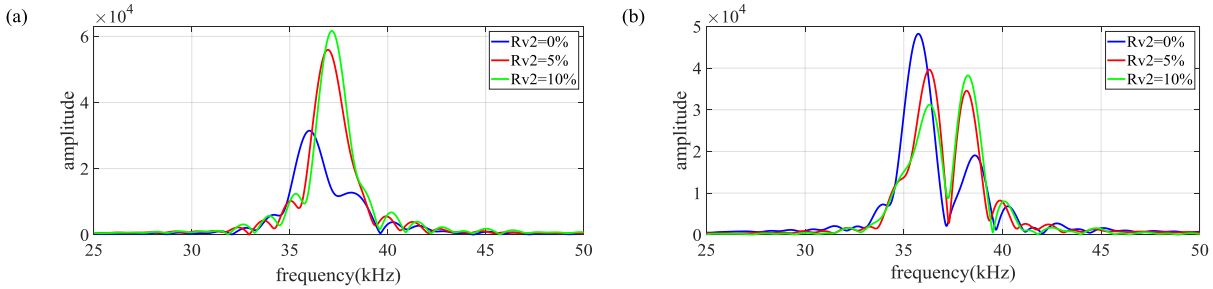

Fig. 4-21 Frequency spectrum analyses of the received signals under different excitation cycles and different proportion of tungsten powder, (a) 8 cycle, (b) 16 cycle

Tab. 4-15 Frequency spectrum maximum values and corresponding frequencies of the received signals under different excitation cycles and different proportion of tungsten powder

Parameters	Tungsten powder volume ratio		
	*R*v2=0%	*R*v2=5%	*R*v2=10%
8 cycle	31460	55970	61640
16 cycle	48240	39590	38250
8 cycle	35.99 kHz	36.94 kHz	37.15 kHz
16 cycle	35.75 kHz	36.32 kHz	38.25 kHz

4.3 Conclusion

Given the problem that PUTs are capacitive under operating near the resonance frequency and there is an impedance discontinuity with the structure to be detected during the detection, the effect of impedance matching on the electromechanical characteristics of PUTs is investigated, all that based on the established PSpice model of SPUTs. It is shown that the LC matching network composed of series inductance and parallel capacitance can effectively eliminate the capacitive impedance of the PUT and accomplish the variable resistance, which makes PUTs more matched with the driving circuit. Then the acoustic impedance matching based on the experimental method is studied. It is found that the matching effect is the best when the epoxy resin thickness is 5 mm; the matching effect is optimal when the alumina powder mixing ratio of *R*v1=5% and the coating thickness is 8 mm; the best matching effect is obtained when the incorporation proportion of tungsten powder of *R*v2=10% and the coating thickness is 8 mm. Comparing the above three situations, the optimal matching effect is obtained when the incorporation proportion of tungsten powder is *R*v2=10% and the coating thickness is 8 mm.

5 Research on the Optimization of Driving Circuits for PUTs

For ultrasonic detection systems, PUTs usually work in the pulse mode, and the driving circuit of PUTs is an important part of the ultrasonic detection system. In particular, for long-distance rail detection systems based on UGW, the driving circuit of PUTs needs to generate several thousands of volts of high voltage pulses to excite them. At the same time, it is necessary to improve the emission efficiency of the PUT to ensure that the amplitude of the received signal is large enough to facilitate the identification of the signal characteristics. Therefore, the study of the optimization of the driving circuit of PUTs is crucial.

5.1 Analysis of Driving Circuit of PUTs

5.1.1 Vibration Analysis of PUTs

According to the vibration principle of piezoelectric ceramic, it is known that piezoelectric ceramic disks perform the forced vibration with damping owing to the effect of elastic force and resistance. Suppose a 5-cycle pulse signal is applied to a piezoelectric ceramic sheet, which can be expressed as

$$f\left(t\right)=\mathrm{H}\cos\left(\omega_1 t\right),\ t\in\left[0,5\mathrm{T}\right] \tag{5-1}$$

where T represents the excitation signal period, ω_1 denotes the excitation signal angular frequency. Then the vibration equation of piezoelectric ceramic disk can be obtained as [149]

$$\frac{d^2y}{dt^2}+2\beta\frac{dy}{dt}+\omega_0^2 y=f\left(t\right) \tag{5-2}$$

where β is the damping factor, ω_0 is the resonance frequency of piezoelectric ceramic disk and y represents the vibration displacement.

By solving equation (5-5), the vibration displacement can be derived as

$$y=\begin{cases}\mathrm{A}_0e^{-\beta t}\cos\left(\sqrt{\omega_0^2-\beta^2}t+\varphi_0\right)+\mathrm{A}\cos\left(\omega_1 t+\varphi\right),t\in\left[0,5\mathrm{T}\right]\\ \mathrm{A}_1e^{-\beta t}\cos\left(\sqrt{\omega_0^2-\beta^2}t+\varphi_1\right),t\in\left[5\mathrm{T},+\infty\right)\end{cases} \tag{5-3}$$

where A_0 and φ_0 are initial amplitude and phase, respectively; A_1 and φ_1 are separately amplitude and phase at $t=5T$; A and φ are amplitude and phase of the forced vibration. The parameters mentioned above can be expressed as

$$\mathrm{A}=\frac{\mathrm{H}}{\sqrt{\left(\omega_0^2-\omega_1^2\right)+4\beta^2\omega_1^2}} \tag{5-4}$$

$$\varphi=\arctan\frac{-2\beta\omega_1}{\omega_0^2-\omega_1^2} \tag{5-5}$$

$$A_0 = \frac{A\cos\varphi}{\cos\varphi_0} \tag{5-6}$$

$$\varphi_0 = \arctan\frac{-\omega_1\tan\varphi}{\beta\sqrt{\omega_0^2-\beta^2}} \tag{5-7}$$

From equations (5-4) and (5-5), piezoelectric ceramic disks can achieve the forced vibration of maximum amplitude and the phase for forced vibration $\varphi \approx \pi/2$ when excitation angular frequency ω_0 exactly equal to ω_1. The amplitude for damping vibration A_0 approximately equals zero from equation (5-6). Therefore it is illustrated that the effect of damping vibration on the amplitude of forced vibration is minimum during the stimulation of the excitation signal. Then from equation (5-3), it can be obtained that the amplitude of damping vibration at $t = 5T$ can be represented as

$$A_1 = \sqrt{y_0^2 + \frac{\left(v_0^2+\beta y_0^2\right)^2}{\omega_0^2-\beta^2}} \tag{5-8}$$

where y_0 is the vibration displacement and v_0 is the vibration velocity. Note that the angular frequency for damping vibration ω_d is less than the resonance frequency ω_0 and $\omega_d = \sqrt{\omega_0^2 - \beta^2}$.

To further analyze the damping oscillation, the PUT is excited by the 5-cycle high voltage pulse signal. The voltage waveform across the piezoelectric ultrasonic transducer is shown in Fig. 5-1. The voltage waveform can be divided into two stages: stage I (forced vibration with damping) and stage II (damping vibration). Fig. 5-1(b) and Fig. 5-1(c) describe the frequency spectrum analysis results of stage I and stage II, respectively. According to these Figures, it can be found that the damping vibration frequency is less than the forced vibration frequency. In general, the resonance frequency of PUTs is chosen as the excitation frequency to achieve high power transmission. The damping vibration can lead to difficulty in distinguishing echoes, producing the detecting blind zone, which can seriously impact the use of the pulse-echo method for the damage localization.

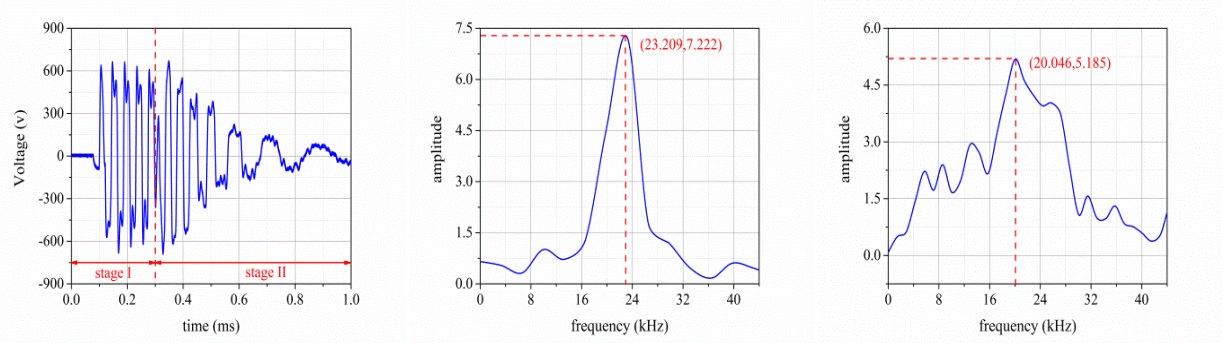

(a) (b) (c)

Fig. 5-1 The analysis of the voltage waveform for PUTs, (a) experimental waveform, (b) stage I frequency spectrum, (c) stage II frequency spectrum

Hence, the damping vibration must be decreased or eliminated. Based on the wave superposition principle, to generate a wave with zero vibration displacement and velocity at

each point, the two waves must meet the following conditions: ① they have the same amplitude and vibration frequency; ② the phase difference is π. Therefore, to reduce the complexity of the excitation signal, this paper intends to use an absorption circuit composed of a bleeder resistor and a bidirectional thyristor in series to absorb the excitation signal tailing of PUTs.

5.1.2 Power MOSFET Absorption Circuit

The switching characteristics of the power MOSFETs show extensive voltage overshoot and ringing especially during turn off, which is due to the effect of parasitic parameters such as drain inductance, source inductance, gate-source capacitance, and drain-source capacitance. For decreasing this parasitic oscillation with reduction of the switching losses, the turn-off snubber circuit is highly required. The turn-off snubber circuit is implemented by using RC (Resistance Capacitance) snubber. The capacitance of the turn-off snubber can be calculated by using the following relationship [150]:

$$C_{\mathrm{sn}} = \frac{I_{\mathrm{d}} \cdot t_{\mathrm{f}}}{2 \cdot V_{\mathrm{ds}}} \tag{5-9}$$

where I_{d} is the drain current, t_{f} is the current fall time and V_{ds} is the drain-to-source voltage. When $I_{\mathrm{d}} = 10\ \mathrm{A}$, $V_{\mathrm{ds}} = 24\ \mathrm{V}$ and $t_{\mathrm{f}} = 30\ \mathrm{ns}$, according to equation (5-9), the capacitance $C_{\mathrm{sn}} = 6.25\mathrm{nF}$. The resistance of the turn-off snubber should be chosen by obeying the relationship that the peak current through it is less than the reverse recovery current of the integrated freewheeling diode during turn on. Then the turn-off snubber resistance can be given as [150]:

$$R_{\mathrm{sn}} = \frac{V_{\mathrm{ds}}}{I_{\mathrm{rr}}} \tag{5-10}$$

where I_{rr} is the reverse recovery current of the integrated freewheeling diode. From equation (5-10), the turn-off snubber resistance can be obtained as $R_{\mathrm{sn}} = 1.41\ \Omega$ when the reverse recovery current is 17 A.

5.1.3 EIM of PUTs

PUTs usually work at a mechanical resonance frequency (also called series resonance frequency), according to Fig. 5-2 (a), it can be seen that PUTs are capacitive. To improve the power transmission efficiency of PUTs, the EIM is required. Fig. 5-2 (b) shows the impedance matching network when the PUT works at the resonance frequency. The matching network uses the combination of series inductance and parallel capacitance. Due to the fact that the designed full-bridge driving circuit contains a pulse transformer, the effect of this pulse transformer on the impedance matching of PUTs also needs to be considered. According to Fig. 5-2 (a), the input impedance of the PUT, as well as the resonance and anti-resonance frequencies can be expressed as follows:

$$Z=\frac{\left(\frac{1}{\mathrm{j}\omega C_{\mathrm{m}}}+R_{\mathrm{m}}+\mathrm{j}\omega L_{\mathrm{m}}\right)\left(\frac{1}{\mathrm{j}\omega C_{\mathrm{m}}}\right)}{\left(\frac{1}{\mathrm{j}\omega C_{\mathrm{m}}}+R_{\mathrm{m}}+\mathrm{j}\omega L_{\mathrm{m}}\right)+\frac{1}{\mathrm{j}\omega C_{\mathrm{m}}}}=\frac{\left(\omega^2 C_{\mathrm{m}}L_{\mathrm{m}}-1\right)-\mathrm{j}\omega C_{\mathrm{m}}R_{m}}{\omega^2 C_0 C_{\mathrm{m}}R_{\mathrm{m}}+\mathrm{j}\left[\omega^3 C_0 C_{\mathrm{m}}L_{\mathrm{m}}-\omega\left(C_0+C_{\mathrm{m}}\right)\right]} \tag{5-11}$$

$$\omega_{\mathrm{s}}=\sqrt{\frac{1}{L_{\mathrm{m}}C_{\mathrm{m}}}},\quad \omega_{\mathrm{p}}=\sqrt{\frac{C_0+C_{\mathrm{m}}}{L_{\mathrm{m}}C_0C_{\mathrm{m}}}} \tag{5-12}$$

where j is the imaginary unit, ω is the operating angular frequency, ω_{s} and ω_{p} are the resonance and anti-resonance frequencies, respectively.

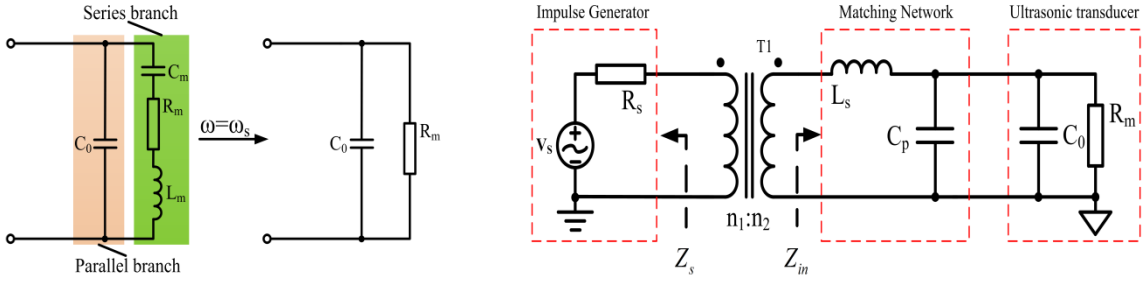

(a) (b)

Fig. 5-2 The design of electrical impedance matching for ultrasonic transducer, (a) BVD equivalent circuit model, (b) EIM network

The connection relations of an impulse generator, an EIM network, and an ultrasonic transducer are described as shown in Fig. 5-2 (b). In this Figure, Z_{s} is the input electrical impedance of the impulse generator and Z_{in} is the input electrical impedance of the EIM network and ultrasonic transducer. The input impedances Z_{s} and Z_{in} can be expressed as:

$$Z_{\mathrm{s}}=R_{\mathrm{s}}+\mathrm{j}X_{\mathrm{s}} \tag{5-13}$$

$$\begin{aligned}Z_{\mathrm{in}}=R_{\mathrm{in}}+\mathrm{j}X_{\mathrm{in}}&=\mathrm{j}\omega_{\mathrm{s}}L_{\mathrm{s}}+\frac{R_{\mathrm{m}}}{1+\mathrm{j}\omega_{\mathrm{s}}R_{\mathrm{m}}\left(C_{\mathrm{p}}+C_0\right)}\\&=\frac{R_{\mathrm{m}}}{1+\omega_{\mathrm{s}}^2R_{\mathrm{m}}^2\left(C_{\mathrm{p}}+C_0\right)^2}+\mathrm{j}\left[\omega_{\mathrm{s}}L_{\mathrm{s}}-\frac{\omega_{\mathrm{s}}R_{\mathrm{m}}^2\left(C_{\mathrm{p}}+C_0\right)}{1+\omega_{\mathrm{s}}^2R_{\mathrm{m}}^2\left(C_{\mathrm{p}}+C_0\right)^2}\right]\end{aligned} \tag{5-14}$$

Note that the input electrical impedance of the impulse generator is only one resistance in general. According to EIM theory, the maximum power transmission of ultrasonic transducers can be achieved when the following conditions are satisfied

$$X_{\mathrm{in}}=0\Rightarrow L_{\mathrm{s}}=\frac{R_{\mathrm{m}}^2\left(C_{\mathrm{p}}+C_0\right)}{1+\omega_{\mathrm{s}}^2R_{\mathrm{m}}^2\left(C_{\mathrm{p}}+C_0\right)^2} \tag{5-15}$$

$$R_{\mathrm{in}}=\frac{R_{\mathrm{m}}}{1+\omega_{\mathrm{s}}^2R_{\mathrm{m}}^2\left(C_{\mathrm{p}}+C_0\right)^2} \tag{5-16}$$

$$R_{\mathrm{s}}=\left(\frac{n_1}{n_2}\right)^2\cdot R_{\mathrm{in}}=\left(\frac{n_1}{n_2}\right)^2\cdot\frac{R_{\mathrm{m}}}{1+\omega_{\mathrm{s}}^2R_{\mathrm{m}}^2\left(C_{\mathrm{p}}+C_0\right)^2} \tag{5-17}$$

where n_1 and n_2 represent the primary and secondary turns of the pulse transformer T1.

5.1.4 Driving Circuit Topology of PUTs

The topologies used in drivers for PUTs mainly include one active element, half-bridge, and push-pull, as shown in Fig. 5-3. The driver with only one active element from Fig. 5-3(a) can generate a steep negative step at the output, which is widely used in spike and single pulse applications. The half-bridge driver from Fig. 5-3(b) can reduce power consumption in pulser itself especially under light loads, which is due to additional MOSFET used to return to zero. However, the above two topologies cannot generate a bipolar pulse train. The push-pull driver from Fig. 5-3(c) has galvanic output isolation and can produce bipolar pulse using only one power supply. But it has the disadvantage that the MOSFETs are operated at twice the power supply voltage.

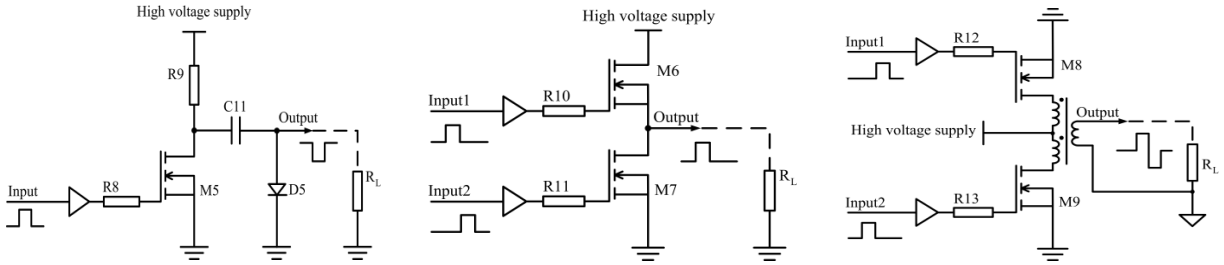

Fig. 5-3 The topologies for drivers, (a) one active element, (b) half-bridge, (c) push-pull

Besides, the conventional pulser for SPUTs from Fig. 5-4 has a simple structure and can generate bipolar pulse trains, but it has relatively high withstand voltage for power MOSFET and its conversion efficiency still needs to be improved. Here, T1 is a pulse transformer used to promote the excitation voltage. Additionally, in comparison with other topologies of driving circuits, the power MOSFETs in full bridge topology requires a lower withstanding voltage. Therefore, the full-bridge topology is chosen here to optimize the driving circuit of SPUTs used in long rail detection.

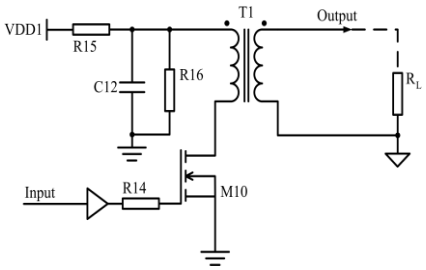

Fig. 5-4 The conventional driving circuit for PUTs

5.2 Full-bridge High Voltage Driving Circuit

5.2.1 The Overall Scheme of Driving Circuits

Based on the theoretical analysis of subsection 5.1, to achieve high-efficiency driving of PUTs to improve their emission efficiency, this thesis optimizes the driving circuit of PUTs

based on the full-bridge driving topology. The driving circuit fully considers the overshoot and oscillation generated when the power MOSFET is turned off, the EIM of the PUT, and the tailing absorption of the excitation signal. Then the schematic diagram of the driving circuit is shown in Fig. 5-5. It mainly includes the power supply circuit, the full-bridge circuit, an RC snubber circuit, a tailing snubber circuit, and the EIM circuit. Note that there is no need of applying any external DC high voltage. The bus voltage VDD1 is 24 V~36 V, and the output voltage of the full-bridge is boosted through a pulse transformer, thereby generating a high voltage pulse signal for exciting the PUT.

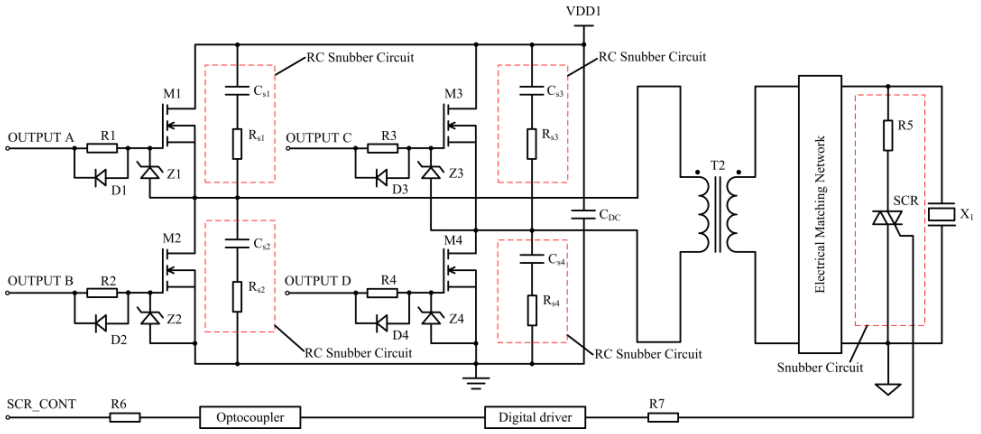

Fig. 5-5 The designed high-voltage driving circuit based on full-bridge

There are particular devices in the circuit: *Z*1, *Z*2, *Z*3, and *Z*4 are Zener diodes used to protect the gates of the four MOSFETs of the full-bridge circuit; *R*1, *R*2, *R*3, and *R*4 are gate limit current resistances to prevent that an excessive current can damage the gates of the MOSFETs; *D*1, *D*2, *D*3, and *D*4 are used to accelerate the turn-off of the four MOSFETs (to extract stored charge in the gate capacitance during turn-off), thereby reducing the turn-off losses of the MOSFETs; and C_{DC} is the DC bus support capacitance used to eliminate the fluctuation of the bus voltage. The tailing absorption circuit can be implemented by the bleeder resistance R5 and bidirectional thyristor SCR (BTA16-800B, STMicroelectronics Inc.) in series which are connected to both ends of the PUTs. The thyristor SCR is opened at the moment of the excitation signal ending, which can lead to the elimination of damping vibration. The EIM uses a matching network composed of series inductance and parallel capacitance and takes into account the effect of the coil inductance of the pulse transformer to realize the efficient matching of the piezoelectric ultrasonic transducer.

5.2.2 The Driving Scheme of Power MOSFETs

Considering that the broken rail detection system based on UGW will be used to the status monitoring of the rail in service, the system is supplied by solar power, so the entire system design follows the guideline of low power design. For the driving circuit of PUTs, the selection of the power MOSFETs needs to consider the on-resistance of the MOSFET, fast switching, drain-source breakdown voltage V_{DSS}, and the maximum drain current I_D. Also, the bus voltage VDD1 of the full-bridge driving circuit of PUTs is 24 V~36 V. According to the above parameters of the MOSFET, this work selects as the power MOSFET the IRLU3410PbF produced by International Rectifier (IR). Its maximum drain current I_D is 17 A and the drain-source on-resistance is only 0.105 Ohms. The drain-source breakdown voltage V_{DSS} is

100V that is much higher than the highest bus voltage of the driving circuit, which can meet the requirements of the driving circuit.

In general, the voltage and current of the control signal generated by the MCU are too small to drive the power MOSFETs, so the voltage and current of the control signal need to be amplified by the driving circuit. The full-bridge circuit can be divided into two parts, the high side, and the low side, where the high and low side contains two power MOSFETs, respectively. As shown in Fig. 5-5, the gate control signal of the low side power MOSFETs (*M*2 and *M*4) can be co-grounded and it can be connected to the ground of the entire driving circuit bus voltage while the gate control signal of the high side MOSFETs (*M*1 and *M*3) cannot be co-grounded and it is floating ground. To overcome this problem, there are two driving schemes used to select, as follows:

Scheme 1: Using the driver IC IXDF604SIA, since each IC can drive two power MOSFETs, it is sufficient to use three driving chips IXDF604SIA for the full-bridge driving circuit. Among them, two are used for driving high-side power MOSFETs, and one is used for driving low-side power MOSFETs. Besides, for the driving of high-side power MOSFETs, two isolated power supplies are required to provide power for the two IXDI604SIA.

Scheme 2: Using the driver IC IR2110S, since each IC can drive two power MOSFETs, only two driving chips IR2110S are needed for the full-bridge driving circuit. It is should be noted that two additional isolated power supplies are not required. Besides, there is a bootstrap circuit inside the IR2110S, which just needs to add a bootstrap capacitor and a fast recovery diode.

Comparing Scheme 1 and Scheme 2, it is found that Scheme 1 requires three driving ICs and two isolated power supplies, so the overall cost is too high. Hence, the power MOSFETs driving in the full-bridge driving circuit designed in this thesis adopts Scheme 2. Then the driving circuit diagram and control signal waveforms are shown in Fig. 5-6. According to Fig. 5-6(a), the isolated power supply in the driving circuit of the high-side power MOSFET mainly depends on the bootstrap capacitor *C*7 and the bootstrap diode *D*5. The bootstrap circuit composed of the two components can provide sufficient gate charge to ensure normally turn-on of the MOSFET. Therefore, the choice of the bootstrap capacitance and diodes is particularly important. According to the gate characteristics of the power MOSFET, it must be provided with sufficient gate charge in a very short time to ensure its conduction.

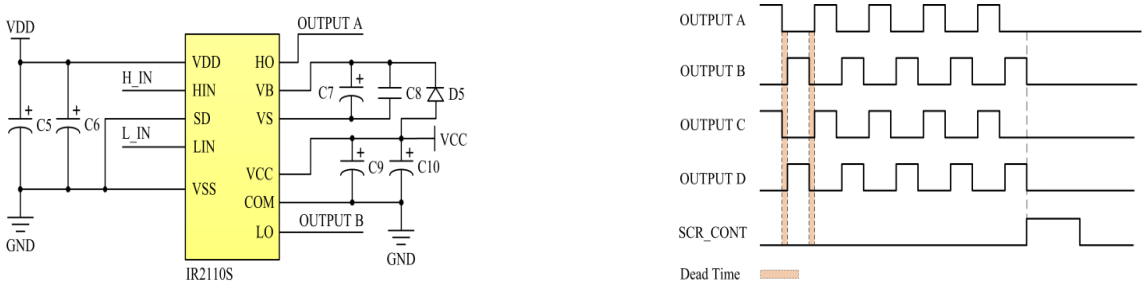

(a) (b)

Fig. 5-6 The design of the control signals, (a) IR2110S driver, (b) control signal waveform

From the query of the electrical characteristics table of the power MOSFET (IRLU3410), the gate-source voltage is 10 V when it is turned on, and the gate turn-on threshold voltage $V_{gs(th)}$ is 1.0~2.0 V. The total charge required by the gate when fully turned on Q_g is 34 nC and the

bootstrap voltage VCC is 15 V. The specific calculation of the bootstrap capacitance is given as [151]:

$$C7 > 2Q_{\mathrm{g}}\left(VCC - V_{\mathrm{gs}} - 0.5V_{\mathrm{gs(th)}}\right) \tag{5-18}$$

Substituting the electrical parameters of the power MOSFET into equation (5-18), the bootstrap capacitor $C7$=15 nF can be obtained. Considering that a certain design margin is required, the value of $C7$ is 100 nF. It should be noted that if the value of the bootstrap capacitance is too large, it will lead to longer conduction time and more losses. Also, the bootstrap diode is a very important bootstrap device. Note that the bootstrap diode can block the high voltage on the DC bus and the current it bears is the product of the gate charge and the switching frequency. At the same time, to reduce the charge loss, it is necessary to select a fast recovery or ultrafast recovery diode with a small reverse leakage current as a bootstrap diode. Likewise, there is a certain margin in the design. The bootstrap diode selected is the ultra-fast recovery diode MUR140, whose maximum recovery time T_{rr} is only 50 ns, and the peak reverse voltage V_{RRM} is 400 V that is much higher than the DC bus voltage VDD1, and its maximum reverse leakage current I_{RM} is 0.005 mA (T_{A}=25 ℃). From Fig. 5-6(b), for the four power MOSFETs in the full-bridge topology, only two driving signals with opposite phases need to be provided. To prevent the two power MOSFETs of the same bridge arm from passing through and causing the power MOSFET to burn down, a certain dead time is considered for the design of the two driving signals. When the driving signal of the power MOSFET is just over, the bidirectional thyristor drive signal controls its conduction, thereby realizing the fast tailing absorption of the excitation signal of the PUT.

5.2.3 Power and Driving Circuits Implementation

Since the broken rail real-time detection system based on UGW works outdoors, so the power supply usually uses solar power or AC 220V. For economic and safety considerations, more solar power is used to convert solar energy into electrical energy and store it in lead-acid batteries or special gel batteries. The power supply in the designed full-bridge driving circuit is mainly used to supply power for the driver chips IR2110S, IXDI604SIA, and the DC bus. The driver chip IR2110S needs 5 V and 15 V while the driving chip IXDI604SIA needs an isolated power supply of 15 V, and the DC bus voltage range is 24 V~36 V. The specific implementation and power distribution are shown in Fig. 5-7.

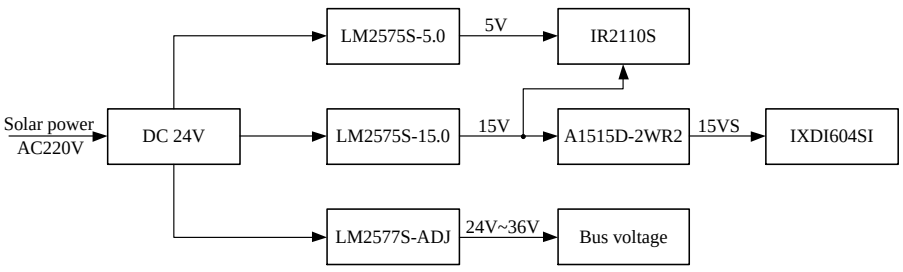

Fig. 5-7 Power supply design and power supply configuration block diagram

The power module mainly uses the switching power supply LM2575S-5.0, LM2575S-15.0, LM2577S-ADJ produced by National Semiconductor, and the 15V isolated power supply A1515D-2WR2 produced by MORNSUN, China. Because the design topologies of the power

chips LM2575S-5.0 and LM2575S-15.0 are the same, only the 15 V power supply design circuit diagram is given as shown in Fig. 5-8, where the power symbol BAT represents the battery power supply voltage.

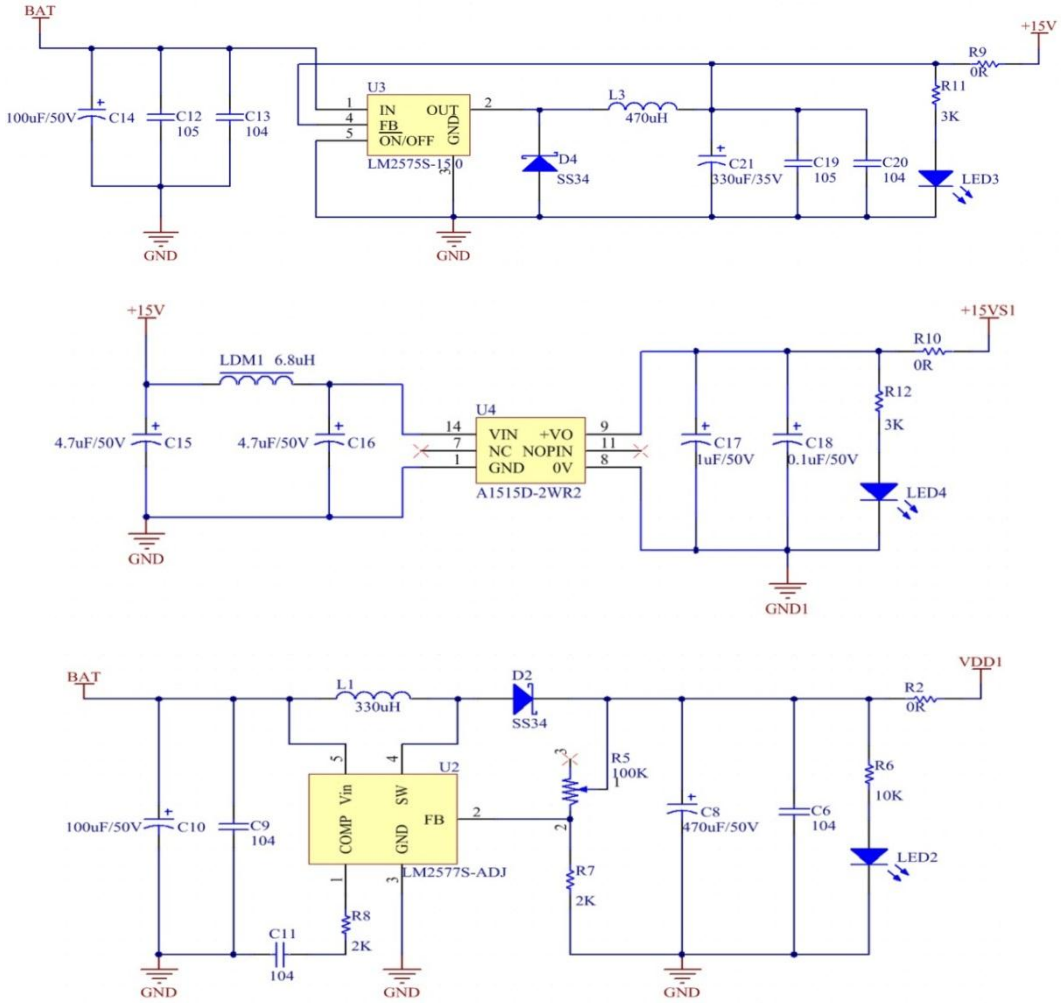

Fig. 5-8 Power supply design circuit schematic diagram

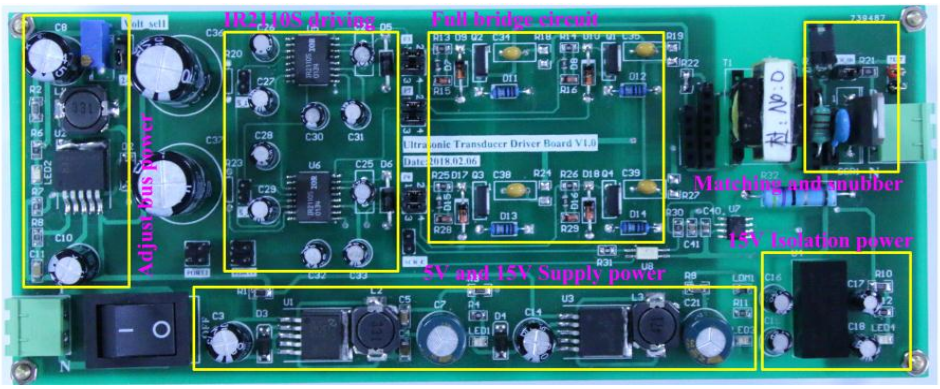

Fig. 5-9 The designed high-voltage driving circuit board based on full-bridge

It should be noted that, for the LM series switching power supplies produced by National Semiconductor Corporation, only a simple configuration can be used. Generally, input capacitance, output capacitance, Schottky diode, and power inductance are needed. The reverse recovery voltage of the Schottky diode should be 1.25 times the maximum output voltage of the power supply, and the current should be 1.25 times the maximum load current. The withstand

voltage of the output capacitance should be 1.5 times the maximum output voltage of the power supply. An electrolytic capacitance with a small equivalent series resistance is selected and the power inductance value is determined according to the maximum output voltage of the power supply and the maximum load current. To facilitate the testing of the proposed full-bridge high-voltage drive circuit, the PCB board is shown in Fig. 5-9. It is found that the proposed driving circuit board mainly involves bus voltage regulation module, IR2110S driving circuit module, full-bridge circuit module, matching and tailing absorption circuit module, 5 V and 15 V power supply module, 15 V isolated power module.

5.3 Comparative Analysis with Traditional Driving Circuits

Firstly, the effect of the excitation signal duty cycle on the output voltage of the proposed driving circuit is analyzed. Secondly, based on the test platforms of single PUT and the pitch-catch setup, the proposed full-bridge driving circuit is compared with the traditional driving circuit. The PUT used in the study is a SPUT in longitudinal vibration with a resonance frequency of 29.29 kHz, and the parameters of the lumped parameter equivalent circuit model can be obtained by conducting impedance analysis based on the impedance analyzer PV520A, as shown in Tab. 5-1.

Tab. 5-1 Equivalent parameters of a sandwiched piezoelectric ultrasonic transducer

Parameters	Values
f_s(kHz)	29.290
C_0(nF)	5.988
C_m(nF)	0.412
L_m(mH)	71.720
R_m(Ω)	779.340

To study the effect of the duty cycle of the excitation signal on the output voltage of the proposed full-bridge driving circuit, the PUT was loaded by using an 8-cycle square wave pulse signal with a frequency of 29.29 kHz. Additionally, the DC bus voltage VDD1 is 24 V and the change range in the duty cycle is 14% ~ 49% by using the step size of 5%. Then the analysis of the output voltage signal in time and frequency domains is performed and the detailed analysis results are shown in Fig. 5-10.

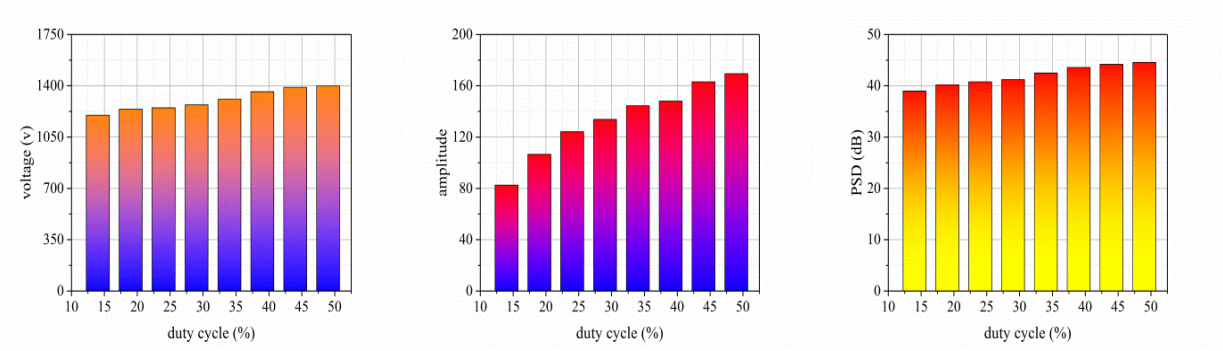

(a) (b) (c)

Fig. 5-10 The effect of duty cycle on the output voltage, (a) voltage, (b) frequency spectrum, (c) PSD

From Fig. 5-10, as the duty cycle gradually increases, the peak-to-peak value of output voltage, frequency spectrum amplitude, and PSD also gradually increase. In addition, it is found that when the duty cycle is 49%, the maximum amplitudes of the peak-to-peak value of output voltage, frequency spectrum, and PSD are obtained. From the two aspects of the output voltage of the driver and the voltage received by the transducer, the comparative analysis of the proposed full-bridge driver and the traditional driver (also called the pulse generator) is carried out.

5.3.1 The Output Voltage Comparison of Driving Circuits

To compare the output voltage of the pulsers, a test platform of the single SPUT has been built as shown in Fig. 5-11. The test platform mainly consists of an ARM control board, a driving board, and the SPUT, a high voltage probe, and an oscilloscope (Tektronix DPO2024B). Here, the driving signals are an 8-cycle square wave pulse with a central frequency of 29.29 kHz, the DC bus voltage VDD1 is 24 V and the duty cycle is 49%. The output voltages of the two pulse generators are analyzed in time and frequency domains, including discrete Fourier analysis and PSD analysis. The specific analysis results are shown in Fig. 5-12. First of all, according to Fig. 5-12, the tail amplitude of the output voltage waveform of the proposed driver is larger, and the entire waveform is relatively smooth.

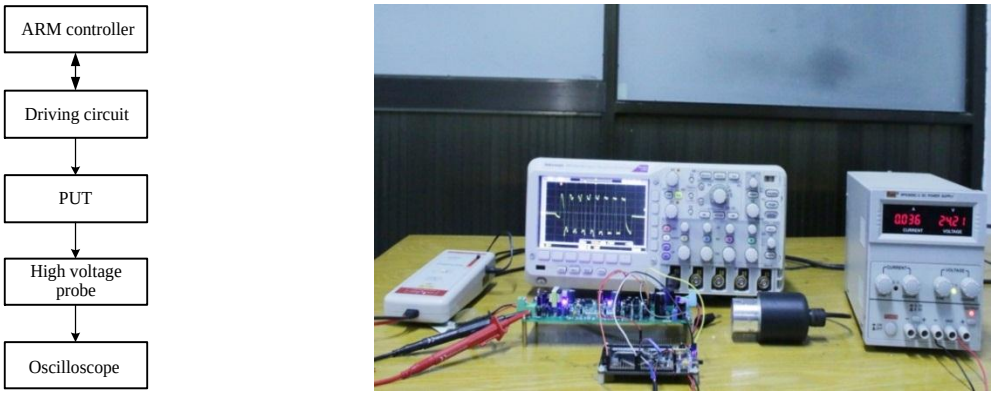

(a) (b)

Fig. 5-11 Test platform of single piezoelectric ultrasonic transducer, (a) test platform connection diagram, (b) physical test platform

The spectrum amplitude and PSD at the resonance frequency point are significantly higher than those of the traditional driver. Secondly, according to Fig. 5-12, the peak-to-peak value of the output voltage of the driver, the frequency spectrum amplitude, and PSD corresponding to the resonance frequency of the PUT have been obtained and listed in Tab. 5-2. In Tab. 5-2, V_{m}, A_{m} and PSD_{m} indicate the peak-to-peak value of output voltage, frequency spectrum amplitude, and Δ_1 denotes the relative error.

Tab. 5-2 Measured results of peak-to-peak, frequency spectrum amplitude and PSD of the output voltage

Parameters	V_{m} (V)	A_{m}	PSD_{m} (dB)
The conventional driver	1630	121.18	41.67
The proposed driver	1400	161.01	44.64
Δ_1(%)	14.11	32.87	7.13

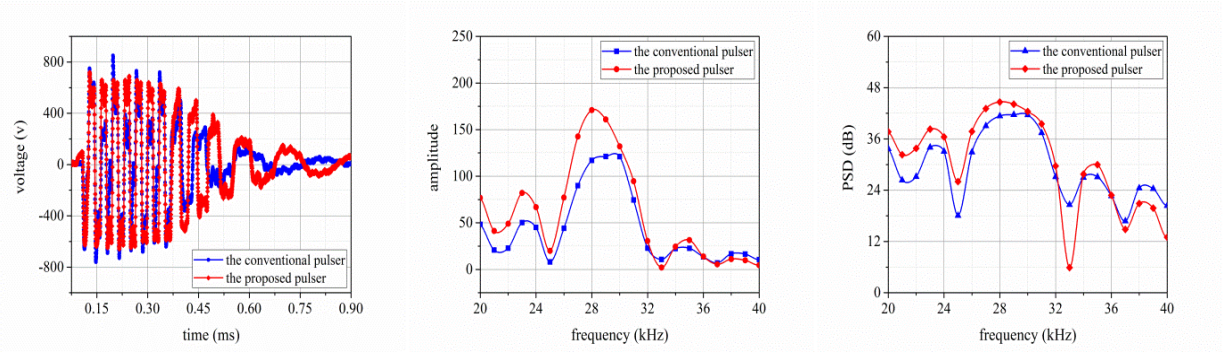

(a) (b) (c)

Fig. 5-12 The comparison of the conventional pulser and the designed pulser, (a) the output voltage, (b) frequency spectrum, (c) PSD

According to Tab. 5-2, compared with the conventional driver, the proposed driver makes peak-to-peak decrease 14.11% while it makes frequency spectrum amplitude and PSD increase 32.87% and 7.13%, respectively. This reflects that the energy of the excitation signal generated by the proposed driver is more concentrated.

5.3.2 The Received Voltage Comparison of PUTs

To further compare the performance of the proposed pulser, a test platform of the pitch-catch setup has been built as shown in Fig. 5-13. It consists of PUTs, an ARM controlled board, a driving circuit board, a filter amplifier, and a waveform recorder. The waveform recorder is mainly responsible for the recording of waveform data for its posterior analysis. The excitation signal loaded by the PUT is a 24-cycle square wave pulse signal with a central frequency of 29.29 kHz, and the DC bus voltage remains unchanged. The test railway line is a railway reserve line in Hancheng County, Shaanxi Province, the rail is CHN60 type, and the test distances are 50 m and 500 m, respectively.

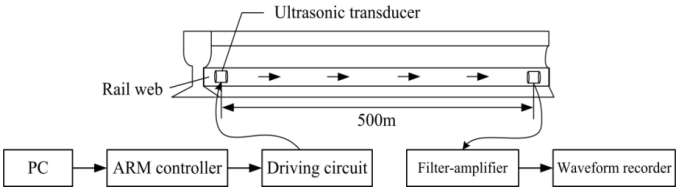

(a)

(a) (c)

Fig. 5-13 Test platform of a pitch-catch setup, (a) test platform connection diagram, (b) transmitting end, (c) receiving end

The received voltage signals are analyzed under different test distances in time and frequency domains. The frequency analysis mainly includes Fourier analysis and PSD analysis, to compare the performance differences between the two drivers. The specific analysis results

of the received voltage signals at two different test distances are shown in Fig. 5-14 and Fig. 5-15. From Fig. 5-14 and Fig. 5-15, the peak-to-peak, frequency spectrum amplitude and PSD of the received voltage at the test distance of 50 m and 500 m are listed in Tab. 5-3 and Tab. 5-4. In these Tables, V_{m1}, A_{m1} and PSD_{m1}, V_{m2}, A_{m2} and PSD_{m2} indicate the peak-to-peak value of output voltage, frequency spectrum amplitude and PSD, while Δ_2 and Δ_3 denote the relative error.

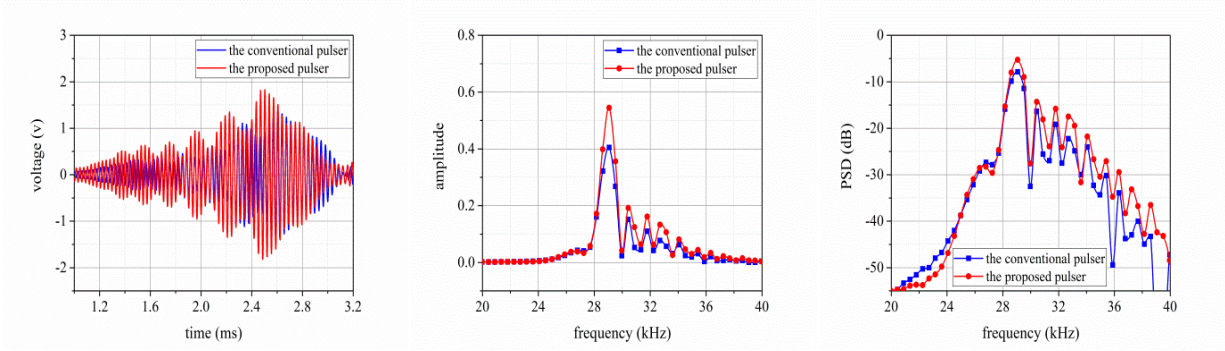

(a) (b) (c)

Fig. 5-14 The comparison of the conventional pulser and the proposed pulser at 50 m test distance, (a) the received voltage, (b) frequency spectrum, (c) PSD

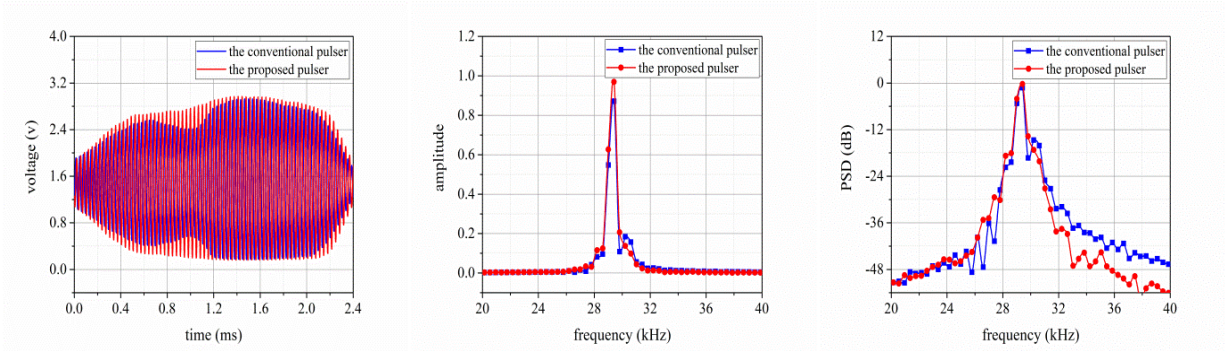

(a) (b) (c)

Fig. 5-15 The comparison of the conventional pulser and the proposed pulser at 500 m test distance, (a) the received voltage, (b) frequency spectrum, (c) PSD

Tab. 5-3 The measured results of peak-to-peak, frequency spectrum amplitude and PSD of the receiving voltage at 50 m test distance

Parameters	V_{m1} (V)	A_{m1}	PSD_{m1} (dB)
The conventional driver	2.77	0.41	-7.72
The proposed driver	3.65	0.55	-5.18
Δ_2(%)	31.8	34.1	32.9

Tab. 5-4 The measured results of peak-to-peak, frequency spectrum amplitude and PSD of the receiving voltage at 500 m test distance

Parameters	V_{m2} (V)	A_{m1}	PSD_{m2} (dB)
The conventional driver	2.76	0.89	-0.62
The proposed driver	2.81	0.98	-0.11
Δ_3(%)	1.8	10.1	82.3

According to Tab. 5-3, it can be found that compared to the conventional driver, the proposed

driver makes peak-to-peak, frequency spectrum amplitude and PSD for the receiving voltage increase 31.8%, 34.1%, and 32.9%, respectively. In the light of Tab. 5-4, it is shown that comparing the conventional pulser with the designed pulser, the latter makes peak-to-peak, frequency spectrum amplitude and PSD for the receiving voltage increase 1.8%, 10.1%, and 82.3%, respectively. In addition, it can be found that with the increase of the test distance, the designed driver makes the peak-to-peak amplitude of the received voltage signal decrease and the frequency spectrum amplitude decreases, but the PSD value is greatly improved. This is mainly because with the increase of the test distance, the dispersion effect and attenuation of the ultrasonic guided waves in the rail are strengthened.

5.4 Research on the Effect of Snubber and Matching Circuits on Driving Circuits

Through the analysis in Section 5.3, it is found that the proposed driver has better performance than the traditional driver. To improve the performance of the proposed driver, this section focuses on the effect of absorption circuits and EIM on the driving circuit.

5.4.1 The Suppression of Turn-off Overshoot and Oscillation

The RC turn-off snubber circuit is designed to decrease the turn-off overshoot and switching losses of the power MOSFETs. From equations (5-9) and (5-10), the parameters of the RC snubber circuit are $C_{sn}=10$ nF and $R_{sn}=2.2\ \Omega$. Owing to the existing PSpice model of power MOSFET IRLU3410 without considering parasitic parameters, the modified PSpice model used in the simulation is shown in Fig. 5-16.

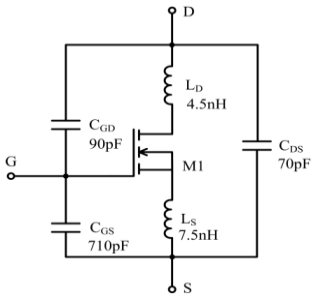

Fig. 5-16 Power MOSFET IRLU3410 model circuit used in the simulation

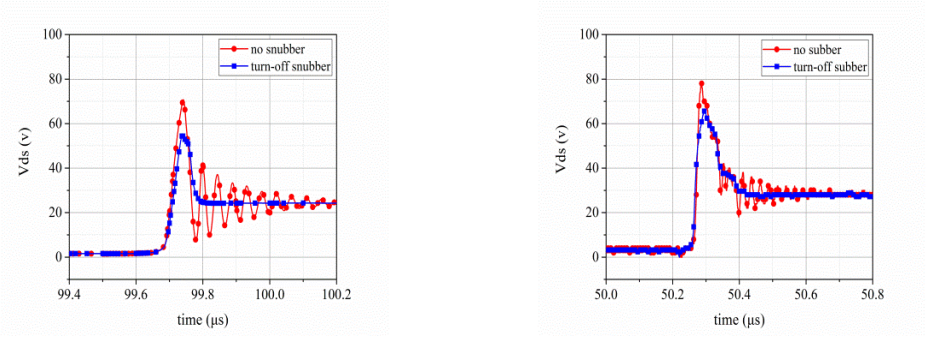

(a) (b)

Fig. 5-17 The turn-off snubber circuit for the effect on the drain-to-source voltage, (a) the simulated result, (b) the measured result

Then the simulation is performed by PSpice (OrCAD PSpice A/D 16.5) and the specific simulated and measured results are shown in Fig. 5-17. According to Fig. 5-17, it can be seen that the turn-off snubber circuit can efficiently reduce the drain-source voltage overshoot and attenuate the long-lasting ringing and the simulated results have good agreement with the measured ones. Therefore, the validity and correctness of the RC snubber circuit are verified.

5.4.2 The Effect of Impedance Matching and Snubber Circuits on the Output Voltage

To further improve power transmission efficiency and tailing absorption for SPUTs, the EIM network and snubber circuit are considered. The effect of the EIM network and snubber circuit on output voltage is conducted with comparative analyses in time and frequency domains by the following situations: no matching with absorbing, matching, absorbing, and matching with absorbing. The driving signal is an 8 cycle square wave pulse with a central frequency of 29.29 kHz, the DC bus voltage VDD1 is 24 V, and the duty cycle is 49%. The detailed analysis results are illustrated in Fig. 5-18.

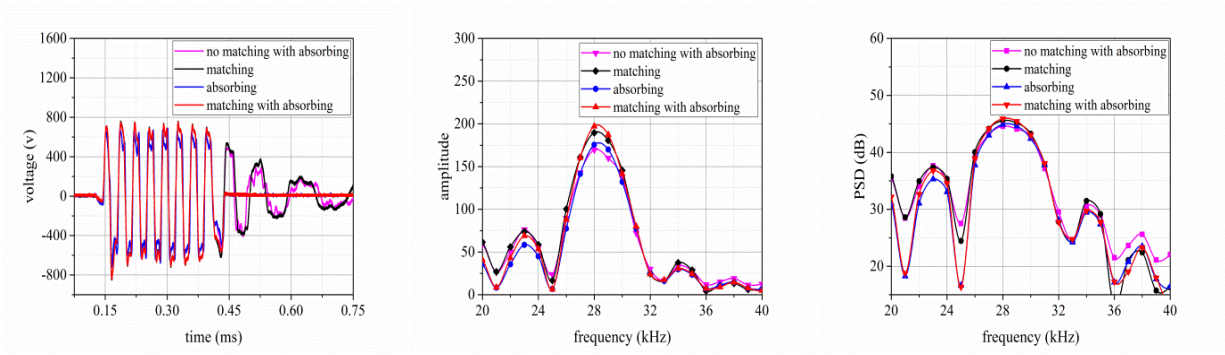

(a) (b) (c)

Fig. 5-18 The effect of EIM network and snubber circuit on the output voltage of the designed pulser, (a) voltage waveform, (b) frequency spectrum, (c) PSD

From Fig. 5-18, the tailing snubber circuit can eliminate the tailing oscillation of the voltage waveform. Under the combined effect of snubber and matching, the voltage waveform is smooth without tailing and the frequency spectrum amplitude and PSD at the resonance frequency are the largest. The peak-to-peak value, frequency spectrum amplitude and PSD of the output voltage are listed in Tab. 5-5. In Tab. 5-5, V_{m3}, A_{m3} and PSD_{m3} are the measured values of the above-mentioned parameters, respectively. Δ_4, Δ_5 and Δ_6 denote the relative error.

Tab. 5-5 The measured results of peak-to-peak value, frequency spectrum amplitude and PSD of the output voltage

Parameters	V_{m3} (V)	A_{m3}	PSD_{m3} (dB)
No matching with absorption	1400	169.51	44.58
Only matching	1610	189.67	45.56
Only absorption	1410	175.47	44.88
Matching with absorption	1590	197.16	45.89
Δ_4(%)	15.00	11.89	2.20
Δ_5(%)	0.71	3.52	0.67
Δ_6(%)	13.57	16.31	2.94

From Tab. 5-5, it can be seen that when EIM network is added, the peak-to-peak, value

frequency spectrum amplitude and PSD are increased 15%, 11.89%, and 2.20%, respectively; when snubber circuit is connected, the mentioned-above parameters are increased 0.71%, 3.52%, and 0.67%, respectively; when EIM network and snubber circuit are used, the above-mentioned parameters are promoted to 13.57%, 16.31%, and 2.94%, respectively. Compared with the first two cases, the third case makes the above parameters more substantially increase.

5.4.3 The Effect of Impedance Matching and Snubber Circuits on the Received Voltage

More tests have been done to further verify the effect of the matching network and the trailing snubber circuit on the improvement of the power transmission efficiency of the PUT, for the same four cases of no matching without absorption, matching without absorption, absorption without matching and absorption with matching. The effects of the matching network and the tailing absorption circuit on the voltage signal received by the receiving transducer are studied in the time domain and frequency domain. The excitation signal loaded by the PUT is consistent with Section 5.4.2 and the specific analysis results are shown in Fig. 5-19.

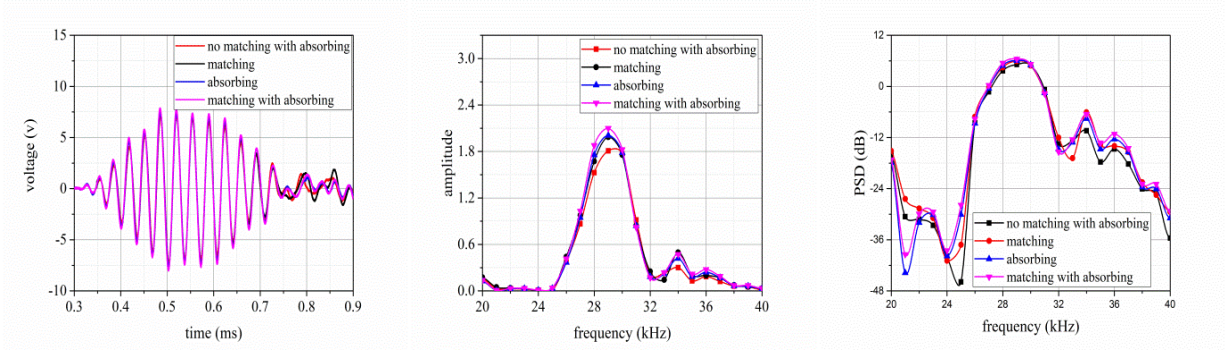

(a) (b) (c)

Fig. 5-19 The effect of EIM network and snubber circuit on the received voltage of SPUTs, (a) voltage waveform, (b) frequency spectrum, (c) PSD

From Fig. 5-19, the peak-to-peak value, frequency spectrum amplitude and PSD of the received voltage signal in the above four cases can be obtained and are listed in Tab. 5-6. In Tab. 5-6, V_{m4}, A_{m4} and PSD_{m4} are the measured values of the above-mentioned parameters, respectively. Δ_7, Δ_8 and Δ_9 denote the relative error.

Tab. 5-6 The measured results of peak-to-peak value, frequency spectrum amplitude and PSD of the received voltage

Parameters	V_{m4} (V)	A_{m4}	PSD_{m4} (dB)
No matching with absorption	14.48	1.81	5.14
Only matching	15.28	1.99	5.96
Only absorption	15.20	2.01	6.05
Matching with absorption	15.92	2.10	6.44
Δ_7(%)	5.52	9.94	15.95
Δ_8(%)	4.97	11.05	17.70
Δ_9(%)	9.94	16.02	25.29

According to Tab. 5-6, it can be found that when an EIM network is added, the peak-to-peak value, frequency spectrum amplitude and PSD are raised 5.52%, 9.94%, and 15.95%, respectively; when snubber circuit is connected, the above parameters are increased 4.97%, 11.05%, and 17.70%, respectively; and when EIM network and snubber circuit are used, the parameters mentioned above are improved 9.94%, 16.02%, and 25.29%, respectively. It can be concluded that the EIM network and the snubber circuit can efficiently improve the power transmission efficiency.

5.5 Conclusion

To improve the energy conversion efficiency of PUTs, this chapter optimizes their driving circuit. The design of the driving circuit is based on the full-bridge topology, which does not require a high DC-voltage. And, consequently, the DC bus voltage is only 34 V~36 V, which is safe and reliable. Besides, the design also considers the suppression of the overshoot and oscillation of the drain-source voltage signal when the power MOSFET is turned off. At the same time, the excitation signal tailing absorption and impedance matching of the PUT are also considered. Through indoor and outdoor test experiments, it is found that the combination of impedance matching and snubber circuits significantly improves the energy conversion efficiency of PUTs. However, with the increase of the test distance, the dispersion effect and attenuation of UGW in the rail become more serious. At the same time, the resonance frequency of the PT will shift due to the influence of the acoustic load. Therefore, there are still many shortcomings in the design of the full-bridge driver. At present, the resonance frequency tracking and dynamic matching of the PUT have not been considered.

6 Research on the Optimization of Excitation Signals for PUTs

In the application of PUTs, especially in the detection of long-distance structural damage, to improve the detection efficiency and accuracy, the amplitude of UGW signals received by PUTs at the receiving end is expected to be as large as possible. This is more conducive to signal feature extraction, as well as judgment and estimation of structural damages. Therefore, it is particularly important to optimize the excitation signal of PUTs. Therefore, this paper will optimize the excitation signal of PUTs from the aspects of excitation frequency and code excitation.

6.1 Research on Optimal Excitation Frequency Tracking of PUTs

During the application of PUTs, due to self-heating, the changes in input power, in acoustic load conditions, and in ambient temperature [152] will cause shifts in the resonance frequency. Fig. 6-1 shows the impedance analysis results of the SPUT. From Fig. 6-1(b), it can be seen that when the PUT is mounted at the rail web of 1 meter CHN60 rail, the resonance frequency and anti-resonance frequency become larger.

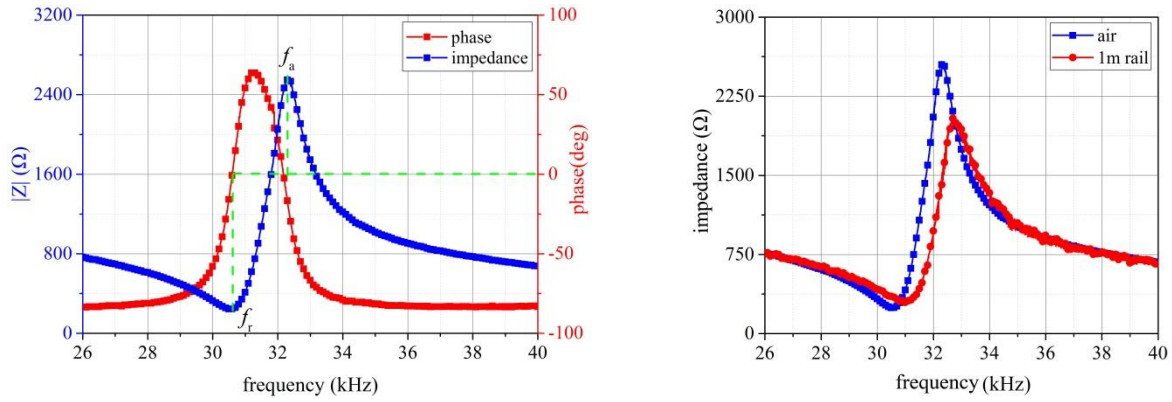

(a) (b)

Fig. 6-1 Impedance analysis of piezoelectric transducers, (a) no-load, (b) a PUT mounted in rail web

If the PUT is operated at a non-resonant frequency, this will cause the mechanical vibration amplitude to be greatly reduced and the power conversion efficiency to be reduced accordingly. Therefore, to maintain the high conversion efficiency of PUTs in the application process, the operating frequency of PUTs must be automatically adjusted to be consistent with the changed resonance frequency. This paper intends to track the optimal excitation frequency of the PUT from the receiving end. To achieve the effective reception of the received signal and filter out the interference signal, a filter with adjustable center frequency, that is, a tracking filter is essential. The implementation of the tracking filter will be introduced in subsection 6.1.1 below.

6.1.1 Tracking Filter

At present, infinite impulse response (IIR) digital filter is usually designed based on the mature theory and design methods of analog filters. The specific design process is given as: firstly, design an analog filter $H_a(s)$ according to the technical specifications of the digital filter; secondly, convert $H_a(s)$ into the system function $H(z)$ of the digital filter according to a certain conversion relationship. It is obvious that the key of the design is to seek this conversion relationship, converting $H_a(s)$ in the s-plane to $H(z)$ in the *z*-plane. To make the system function $H(z)$ stable and meet the design requirements, there are two requirements for the conversion relationship [151]. The first one is that the transform should be such type that the left half of the *s*-plane is mapped into the unit circle of the *z*-plane. And the second is that the frequency response of the digital filter is consistent with the frequency response of the analog filter, so the imaginary axis of the *s*-plane is mapped to the unit circle of the *z*-plane, and the corresponding frequencies are linearly related. Note that there are many methods to convert the system function $H(z)$ from *s*-plane to *z*-plane, but the impulse response invariant method and bilinear transform method are widely used in the engineering applications. The biggest disadvantage of the impulse response invariant method is that it will produce spectrum aliasing, which will cause the frequency response of the digital filter to deviate from the frequency response characteristics of the analog filter.

To overcome this problem, non-linear frequency compression is used to compress the entire frequency axis between $\pm\pi/T$, followed by using $z=e^{sT}$ conversion to the z-plane. Supposing $H_a(s)$, $s=j\Omega$, after nonlinear frequency compression it can be expressed as $\hat{H}_a(s_1)$, $s_1=j\Omega_1$. The frequency compression is achieved by a tangent transform, which is expressed as:

$$\Omega=\frac{2}{T}\tan(\frac{1}{2}\Omega_1 T) \tag{6-1}$$

where T represents the sampling interval. When Ω_1 changes from $-\pi/T$ to π/T, Ω changes from $-\infty$ to $+\infty$. Thus, the conversion between the entire imaginary axis in the *s*-plane is fully compressed to the imaginary axis $\pm\pi/T$ in the *s*1-plane. Equation (6-1) can be expressed as:

$$j\Omega=\frac{2}{T}\frac{e^{j\Omega_1 T/2}-e^{-j\Omega_1 T/2}}{e^{j\Omega_1 T/2}+e^{-j\Omega_1 T/2}}=\frac{2}{T}\frac{1-e^{-j\Omega_1 T}}{1+e^{-j\Omega_1 T}} \tag{6-2}$$

Substituting $s=j\Omega$ and $s_1=j\Omega_1$ into equation (6-2), we can obtain:

$$s=\frac{2}{T}\frac{1-e^{-s_1 T}}{1+e^{-s_1 T}} \tag{6-3}$$

Then, substituting $z=e^{s_1 T}$ into equation (6-3), it can be derived:

$$s=\frac{2}{T}\frac{1-z^{-1}}{1+z^{-1}} \tag{6-4}$$

Equation (6-4) is called bilinear transform. Letting $s=j\Omega$, $z=e^{j\omega}$ and substituting them into equation (6-4), the relationship between analog frequency and digital frequency can be

expressed as

$$j\Omega = \frac{2}{T}\frac{1-e^{-j\omega}}{1+e^{-j\omega}} \Rightarrow \Omega = \frac{2}{T}\tan(\frac{1}{2}\omega) \tag{6-5}$$

To track the frequency variation of the receiving signals derived from SPUTs, a digital bandpass tracking filter (DBTF) is designed based on the bilinear transformation method. Then the standard transfer function of second-order analog bandpass filter can be expressed as

$$H(s) = H_{OBP}\frac{\frac{\Omega_0}{Q}s}{s^2 + \frac{\Omega_0}{Q}s + \omega_0^2} \tag{6-6}$$

where $f_0 = \Omega_0/2\pi$ is the center frequency of the bandpass filter, Q is the quality factor and H_{OBP} represents the bandpass output gain at $\Omega = \Omega_0$. Note that the bandpass output gain $H_{OBP} = 1$ at $\Omega = \Omega_0$. Substituting equation (6-5) into equation (6-6), the transfer function of the digital two-order bandpass filter can be obtained as:

$$H(z) = c\frac{1-z^{-2}}{1+a_1z^{-1}+a_2z^{-2}} \tag{6-7}$$

Due to the bilinear transform with frequency distortion, a pre-correction must be carried out. Then the coefficients from equation (6-7) are given as:

$$c = \frac{\tan(\frac{\omega_0 T}{2})}{Q + \tan(\frac{\omega_0 T}{2}) + Q\tan^2(\frac{\omega_0 T}{2})} \tag{6-8}$$

$$a_1 = \frac{2Q\tan^2(\frac{\omega_0 T}{2}) - 2Q}{Q + \tan(\frac{\omega_0 T}{2}) + Q\tan^2(\frac{\omega_0 T}{2})} \tag{6-9}$$

$$a_2 = \frac{Q - \tan(\frac{\omega_0 T}{2}) + Q\tan^2(\frac{\omega_0 T}{2})}{Q + \tan(\frac{\omega_0 T}{2}) + Q\tan^2(\frac{\omega_0 T}{2})} \tag{6-10}$$

According to the filter design parameters, the filter center angle frequency Ω_0, quality factor Q, and signal sampling interval T can be set to obtain different filter performance, as shown in Fig. 6-2. From Fig. 6-2(a), it can be found that the designed filter has good frequency response characteristics with no lag in the filter phase; the filter bandwidth gets narrower as the quality factor increases. In the light of Fig. 6-2(b), it can be seen that the filter phase change is steeper near the filter center frequency as the quality factor increases. For ease of programming, the transfer function from equation (6-10) can be rewritten as

$$H(z) = c\frac{1-z^{-2}}{1+a_1z^{-1}+a_2z^{-2}} = \frac{Y(z)}{U(z)} \tag{6-11}$$

where $U(z)$ and $Y(z)$ indicate the output and input for the digital bandpass filter, respectively. Letting $U(z)=U(k)$ and $Y(z)=Y(k)$, we can obtain

$$Y(k)+a_1z^{-1}Y(k)+a_2z^{-2}Y(k)=cU(k)-cz^{-2}U(k) \tag{6-12}$$

Considering the equation (6-13), equation (6-12) can be arranged as indicated in (6-17)

$$z^{-n}x(k)=x(k-n) \tag{6-13}$$

$$Y(k)=c\left[U(k)-U(k-2)\right]-a_1Y(k-1)-a_2Y(k-2) \tag{6-14}$$

where n denotes the shift length and $n=\pm1,\ \pm2,\ \pm3\cdots$. According to equation (6-14), the frequency of the received signal is tracked only by adjusting the filter center frequency, quality factor, and sampling interval. For signals in a certain frequency range, the sampling rate can be selected with a large value, so the main adjustment of the center frequency and quality factor can meet the filtering requirements of different frequency signals.

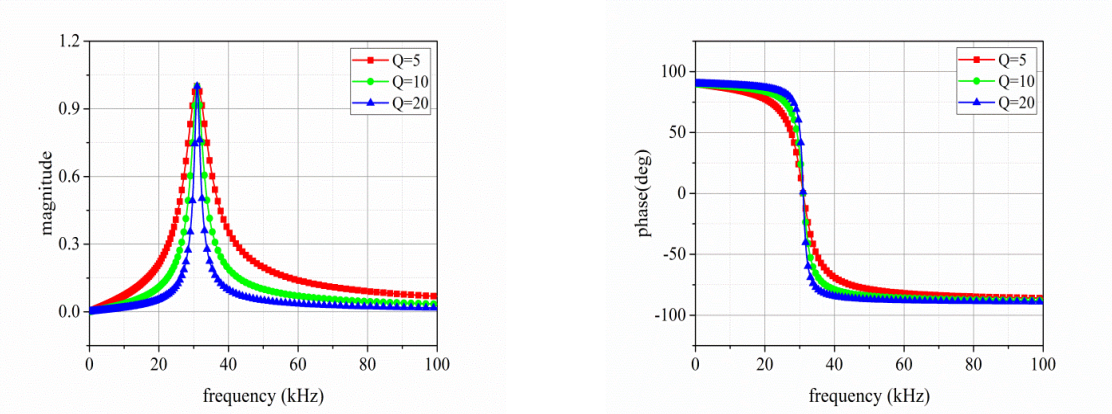

(a) (b)

Fig. 6-2 The frequency response of digital tracking filters at f = 31 kHz , (a) magnitude, (b) phase

Based on the above-mentioned DBTF design method, a bandpass filter with a sampling interval of 2 μs, a quality factor of 18 and a center frequency of 32 kHz and 34 kHz was designed, respectively. The performance of the designed filter is tested using the UGW signals from the actual rails, and the results are shown in Fig. 6-3. The digital bandpass filter is designed to effectively filter out the DC component and the stray signal component. The filter is designed with superior frequency characteristics in the bandwidth. Overall, the digital bandpass filter is designed to meet the filtering needs of the UGW in the rail.

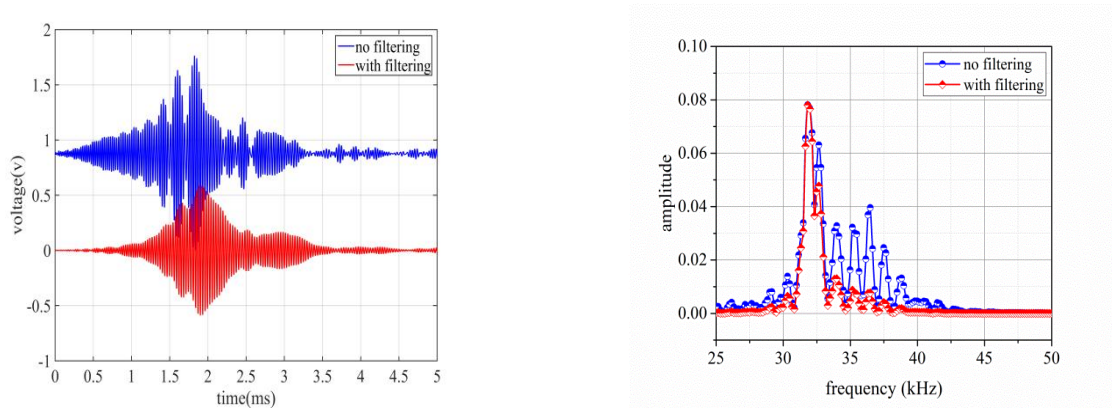

(a) (b)

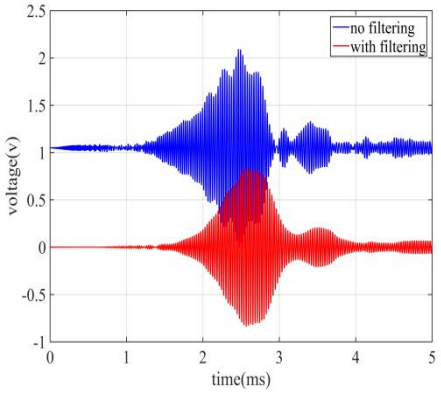

(c)

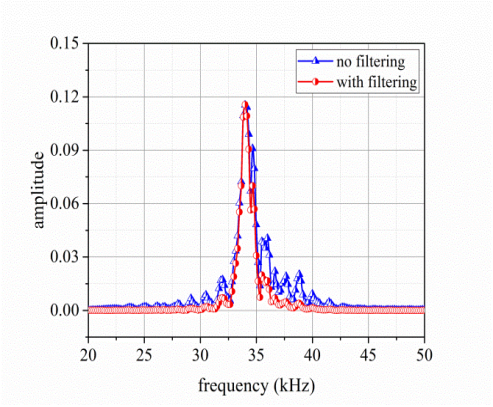

(d)

Fig. 6-3 The performance analysis of the designed DBTF, (a) the receiving signal at 31.91 kHz, (b) frequency spectrum, and (c) the receiving signal at 33.92 kHz, (d) frequency spectrum

6.1.2 The Implementation of Optimal Excitation Frequency Tracking

To obtain the maximum received signal amplitude, the excitation frequency of PUTs is generally selected between the series resonant frequency and parallel resonant frequency. The relationship between the series resonance frequency f_s, parallel resonance frequency f_p, resonance frequency f_r, and anti-resonance frequency f_a of PUTs can be given as:

$$f_a > f_p > f_s > f_r \tag{6-15}$$

The series resonance frequency and parallel resonance frequency can be derived using the impedance analyzer. To obtain the optimal excitation frequency, the frequency sweep range uses a wide to narrow mechanism, consisting of two main frequency ranges. It can be defined as :

$$(f_s - \Delta f) < f_{range} < (f_p + \Delta f) \tag{6-16}$$

$$(f_{op1} - \Delta f_1) < f_{range1} < (f_{op1} + \Delta f_1) \tag{6-17}$$

where Δf and Δf_1 represent the frequency increment, f_{op1} is the roughly selected optimal excitation frequency. The frequency increment mentioned above is decided by the bandwidth of the PUTs. The bandwidth can be expressed as:

$$BW = \frac{f_s}{Q_m} \tag{6-18}$$

where Q_m denotes the mechanical quality factor of PUTs and it can be obtained by measurement using the impedance analyzer.

Then the frequency tracking process is divided into two stages. Based on the wide sweep frequency range from equation (6-16), the first stage is mainly responsible for the search of the excitation frequency f_{op1} by a larger step Δf_2, as shown in Fig. 6-4. The second stage is used for finding the optimal excitation frequency f_{op2} by a smaller step Δf_3 based on the narrow sweep frequency range from equation (6-17). It is pointed out that the second stage utilizes the same search process as the first stage. Note that Δf_2 and Δf_3 are set according to the SPUT bandwidth. Also, the optimal excitation frequency search basis is the maximum value of the

amplitude and FFT amplitude for the receiving signal when SPUTs are excited at the selected frequency point.

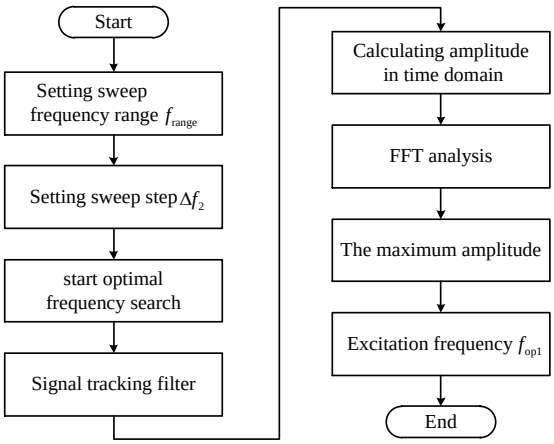

Fig. 6-4 Tracking flow of automatic optimal excitation frequency

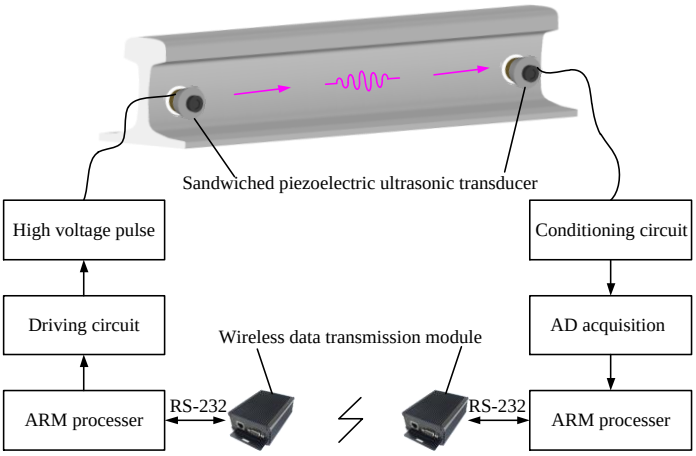

Fig. 6-5 The structure of DBTF-based OEFT system

Based on the pitch-catch mechanism, the DBTF-based optimal excitation frequency tracking (OEFT) system is built as shown in Fig. 6-5. The OEFT system mainly consists of a transmitting end, a receiving end, and a wireless data transmission module (WDTM). The transmitting end primarily includes the SPUT driving circuit used to excite the SPUT mounted in the rail web producing ultrasonic waves. The receiving end is composed of the SPUT used to receive the ultrasonic wave signal, the signal conditioning circuits, and data acquisition circuits. Here, it is noticed that a 433 MHz WDTM is used to achieve communication between the transmitting end and the receiving one. The optimal excitation frequency information is sent to the transmitting end from the receiving end using the WDTM. The chips STM32F103VET6 and STM32F407VET6 (STMicroelectronics Inc.) are selected as the microprocessors of the transmitting and receiving ends, respectively.

6.1.3 Experimental Verification and Results Analysis

To achieve these parameters including the series resonance and parallel resonance frequencies and the mechanical quality factor, the impedance analysis for SPUTs is carried out using an impedance analyzer PV520A (BEIJING BAND ERA Corp., LTD, Beijing, China) as

shown in Fig. 6-6(a). According to Fig. 6-6(b), the series resonance and parallel resonance frequencies are obtained and listed in Tab. 6-1.

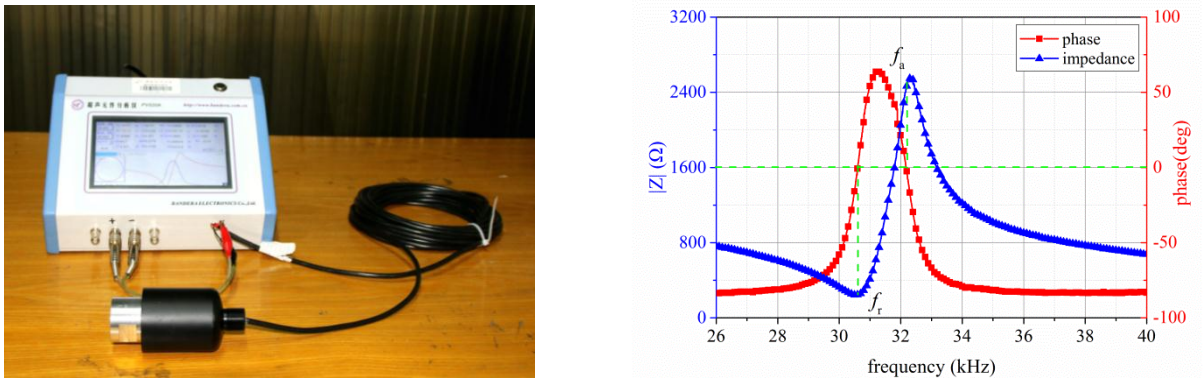

(a) (b)

Fig. 6-6 Impedance test of piezoelectric transducers, (a) experimental platform, (b) impedance test results

According to Tab. 6-1 and equation (6-18), the bandwidth of the SPUT can be derived as 0.625 kHz, so the corresponding frequency increments are given as

$$\Delta f = 8 \cdot BW = 5 \text{ kHz}, \ \Delta f_1 = 2 \cdot BW = 1.25 \text{ kHz} \tag{6-19}$$

$$\Delta f_2 = 2 \cdot BW = 1.25 \text{ kHz}, \ \Delta f_3 = 0.4 \cdot BW = 0.25 \text{ kHz} \tag{6-20}$$

Tab. 6-1 Parameters of piezoelectric ultrasonic transducers used in the long rail detection

Parameters	Values
Series resonance frequency f_s(kHz)	33.97
Parallel resonance frequency f_p(kHz)	35.46
Mechanical quality factor Q_m	54.31

For validating the application and accuracy of the proposed OEFT method, the field test platform is established as shown in Fig. 6-7 utilizing the pitch-catch mechanism. The specific test process is based on Fig. 6-5. The PUT installed on the rail web meets the relevant specifications of railway equipment installation and does not affect the normal operation of the train. It is pointed out that the tested CHN60 rail length L takes 50 m, 100 m, and 150 m, respectively. Through the test of different distances, the reliability and correctness of the proposed OEFT method can be better reflected. To ensure that the PUT is in close contact with the rail web, white petrolatum is used as the acoustic coupling agent. From Fig. 6-7(b), the waveform recorder MR8875-30 (HIOKI E.E. CORPORATION) is used to save the receiving signal data to facilitate subsequent analysis and judgment. The power supply of the transmitter and receiver are DC 24 V, which are provided by two 12 V batteries in series. The excitation signal of the PUT is a 30-cycle square wave pulse and the final excitation pulse voltage is as high as 1800 V.

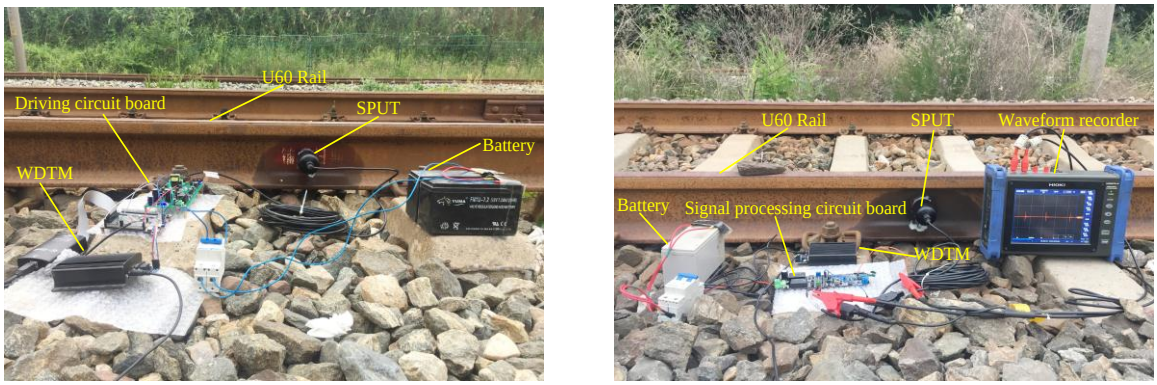

(a) (b)

Fig. 6-7 Experimental platform of the field test, (a) transmitting end, (b) receiving end

To improve the reliability of the OEFT method, the received signal mainly analyzes and judges from the time and frequency domains. The time-domain analyzes the peak-to-peak value of the received signal, and the frequency domain mainly analyzes the signal frequency spectrum and PSD, as shown in Fig. 6-8, Fig. 6-9 and Fig. 6-10. According to these Figures, it is found that, compared with the PUT working at a fixed frequency 33.97 kHz under different test distances, when the PUT works at the optimal excitation frequency, the peak-to-peak received signal, frequency spectrum amplitude and PSD are greatly increased. This fully proves the effectiveness and correctness of the OEFT method. Besides, the optimal excitation frequency value and the maximum amplitude value of the first wave under different test distances are listed in Tab. 6-2 and Tab. 6-3, respectively. The relative errors of the change of the resonance frequency and the change of the arrival time of the maximum amplitude of the first wave are defined as follows:

$$\Delta_{10} = (f_{op} - f_s)/f_s \tag{6-21}$$

$$\Delta_{11} = \left|t_{op} - t_s\right|/t_s \tag{6-22}$$

where f_{op} and f_s represent the optimal excitation frequency and series resonance frequency, t_{op} and t_s denote the arrival time of the maximum amplitude of the first wave under the PUT operating the optimal excitation frequency and series resonance frequency, respectively.

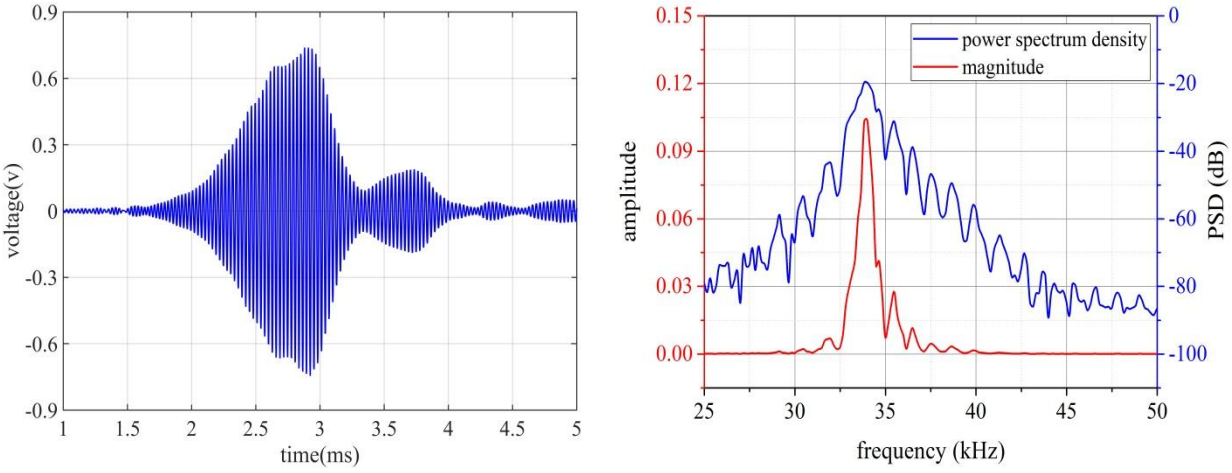

(a) (b)

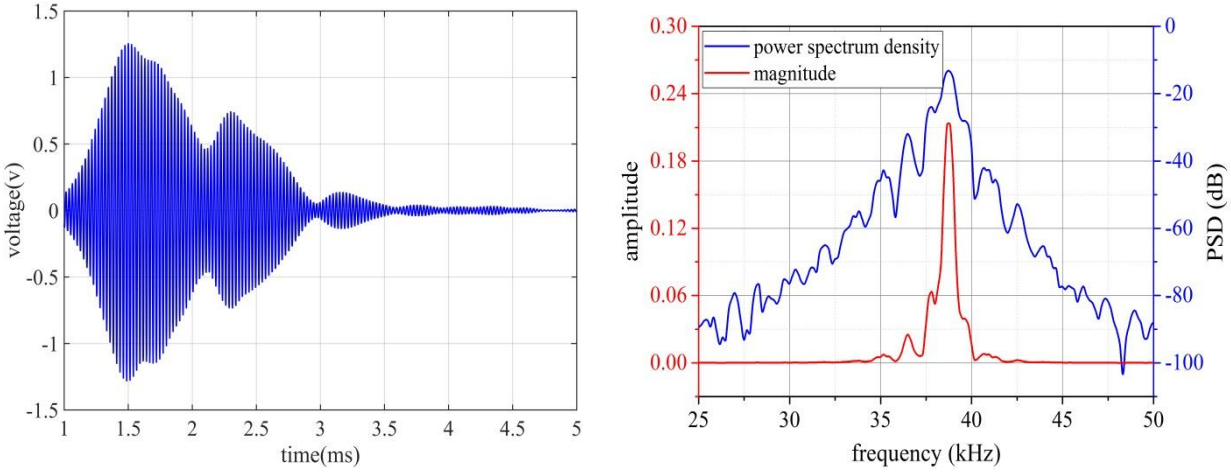

(c) (d)

Fig. 6-8 The analyzed results of the receiving signal under L = 50 m, (a) the receiving signal waveform at f = 33.97 kHz, (b) FFT amplitude and PSD at f = 33.97 kHz, and (c) the receiving signal waveform at the optimal excitation frequency, (d) FFT amplitude and PSD at the optimal excitation frequency

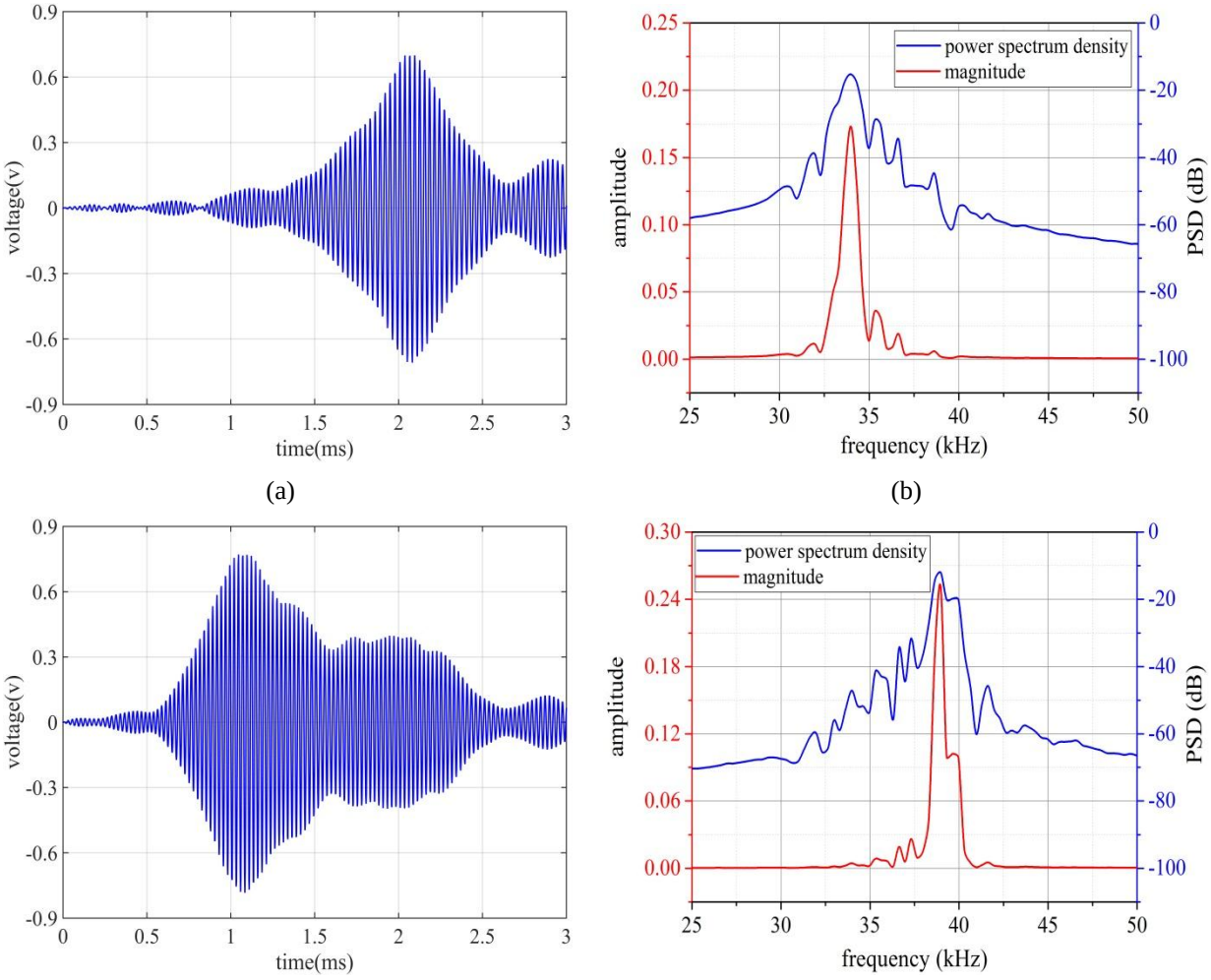

(a) (b)

(c) (d)

Fig. 6-9 The analyzed results of the receiving signal under L = 100 m, (a) the receiving signal waveform at f = 33.97 kHz, (b) FFT amplitude and PSD at f = 33.97 kHz, and (c) the receiving signal waveform at the optimal excitation frequency, (d) FFT amplitude and PSD at the optimal excitation frequency

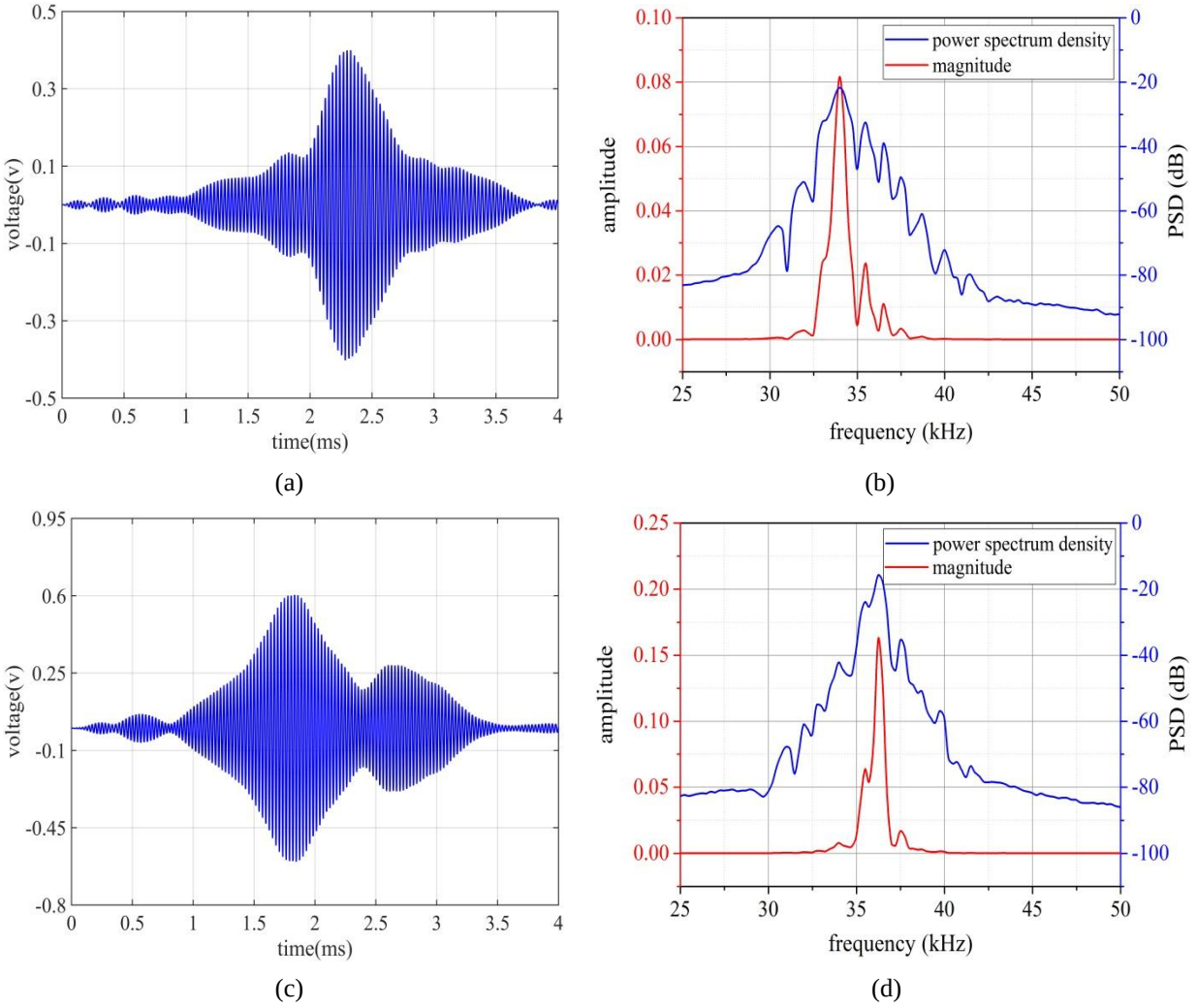

Fig. 6-10 The analyzed results of the receiving signal under L = 150 m, (a) the receiving signal waveform at f = 33.97 kHz, (b) FFT amplitude and PSD at f = 33.97 kHz, and (c) the receiving signal waveform at the optimal excitation frequency, (d) FFT amplitude and PSD at the optimal excitation frequency

From Tab. 6-2, it is obvious that the optimal excitation frequencies under different test distances are larger than the series resonance frequency and it is closer to the parallel resonance frequency. But it can be found that the shift of the series resonance frequency is the largest when the test distance is 100 m, while the shift of the series resonance frequency is the smallest when the test distance is 150 m. As for the frequency error mentioned in Tab. 6-2, several factors can well explain this problem. Firstly, the entire rail with the receiving SPUTs mounted in rail web acts as an acoustic load of the transmitting SPUTs. Secondly, PTs are designed based on the half-wavelength vibrator. Hence, if the length of the detected structure and the half-wavelength meet some relationship, the series resonance frequency has small shift, otherwise, it has relatively large shift. From Tab. 6-3, it can be easily found that compared with SPUTs being actuated at fixed f = 33.97 kHz, the time corresponding to the first wave maximum amplitude is smaller when SPUTs are excited at the optimal excitation frequency under different test distances. It is pointed out that the time difference is the smallest when test distance L = 150 m. As for the time error derived from Tab. 6-3, the following factors can well interpret this problem. First of all, the UGW dispersion characteristic is closely related to the length and shape of the detected structures, the excitation frequencies used to actuate PUTs.

And the phase velocity and group velocity are a function of the frequency and the determined excitation frequency corresponds to multiple vibration modes. Finally, the difference of the optimal excitation frequency and the series resonance frequency is small, so the propagation velocity has less difference.

Tab. 6-2 The comparison of the resonance frequency and the optimal excitation frequency under different test distances

Parameters	50m	100m	150m
f_{op}(kHz)	38.73	38.97	36.25
f_s(kHz)	33.97	33.97	33.97
Δ_{10}%	14.01	14.72	6.71

Tab. 6-3 The comparison of the times corresponding to the first wave maximum amplitude under different excitation frequencies

Parameters	50m	100m	150m
t_{op}(ms)	1.5	1.05	1.83
t_s(ms)	2.88	2.1	2.33
Δ_{11}%	47.91	50	21.46

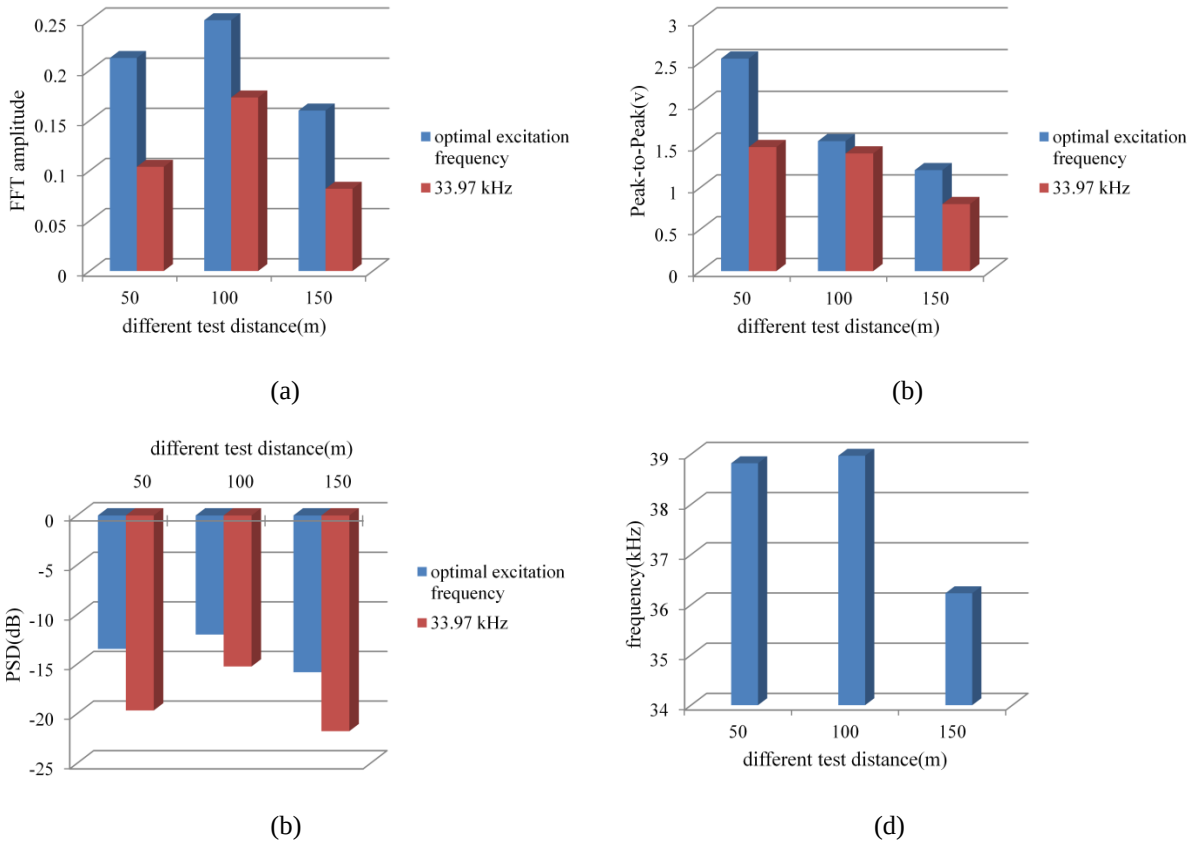

Fig. 6-11 The analyzed results of the receiving signal under different test distances and excitation frequencies, (a) FFT amplitude, (b) Peak-to-Peak, (c) PSD, (d) optimal excitation frequency

Besides, according to Fig. 6-8, Fig. 6-9 and Fig. 6-10, the analyzed results of the receiving

signal under different test distances and excitation frequencies are shown in Fig. 6-11. From Fig. 6-11, it can be easily observed that compared with SPUTs excited at a fixed 33.97 kHz, the frequency spectrum amplitude, PSD and Peak-to-Peak can achieve the largest increase by 104.42%, 31.54%, 71.36%, respectively, when SPUTs are excited at the optimal excitation frequency and the test distance is 50 m. In particular, compared with the SPUT excited at a fixed 33.97 kHz, the above parameters of the receiving signal can obtain the smallest increase when the test distance is 100 m.

UGW signals have typical non-stationary signal characteristics. Thus, in addition to FFT and PSD, PWVD (Pseudo Wigner-Ville Distribution) time-frequency analysis method is used. Based on WVD (Wigner-Ville distribution), the PWVD is proposed to reduce the impact of cross terms. Its expression can be given as:

$$W(t, f) = \int_{-\infty}^{+\infty} h(\tau)x(t+\frac{\tau}{2})x^*(t-\frac{\tau}{2})e^{-jf\tau}d\tau \tag{6-23}$$

where $h(\tau)$ denotes the window function, $x^*(t-\tau/2)$ is the complex conjugate of $x(t-\tau/2)$. The specific analyzed results are shown in Fig. 6-12. In light of Fig. 6-12, it can be seen that compared with SPUTs actuated at fixed f = 33.97 kHz, the area corresponding to the maximum energy value under SPUTs excited at the optimal excitation frequency is decreased. Nevertheless, it exactly illustrates that the maximum time-frequency energy becomes more concentrated. In summary, it can be drawn as a conclusion that the proposed OEFT method can efficiently capture the optimal excitation frequency.

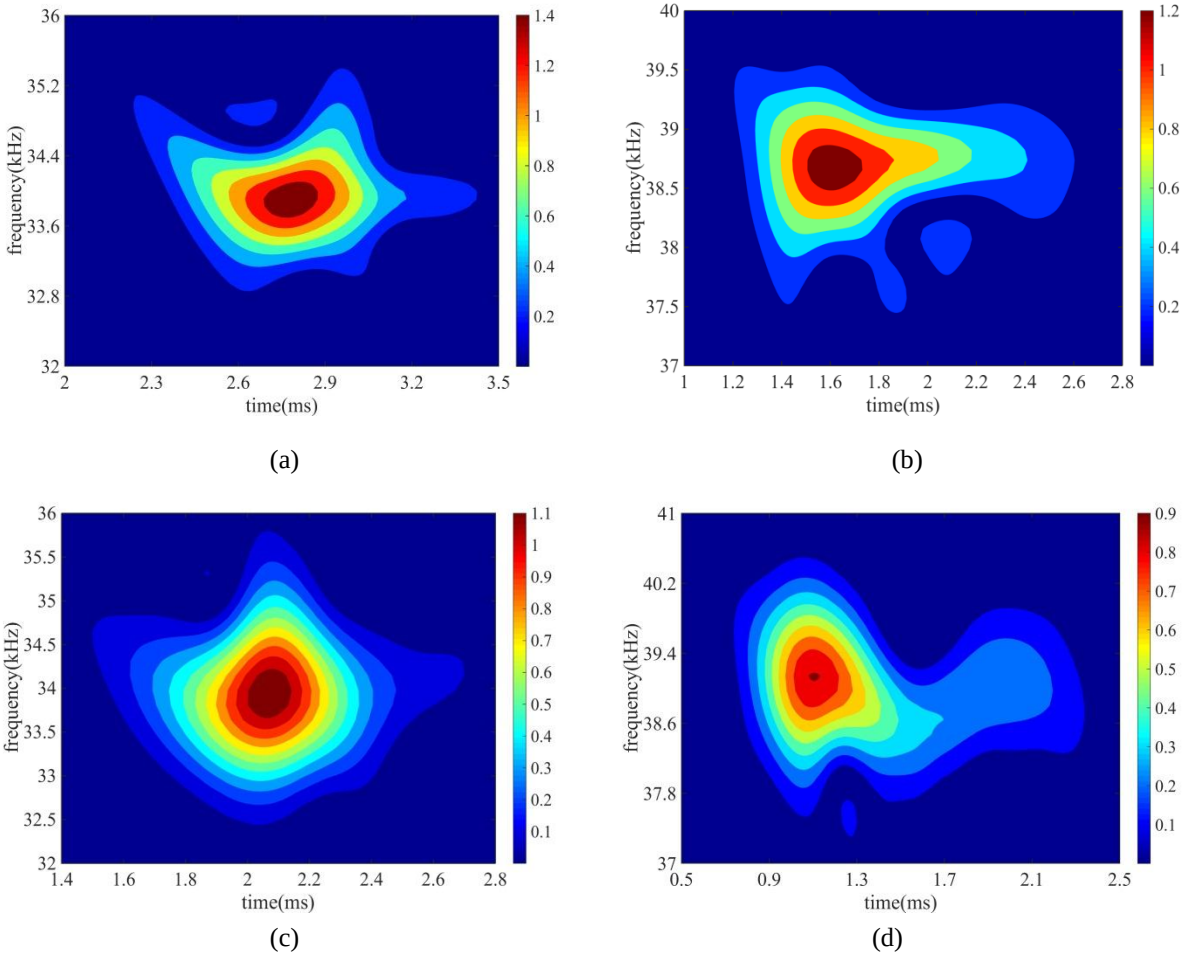

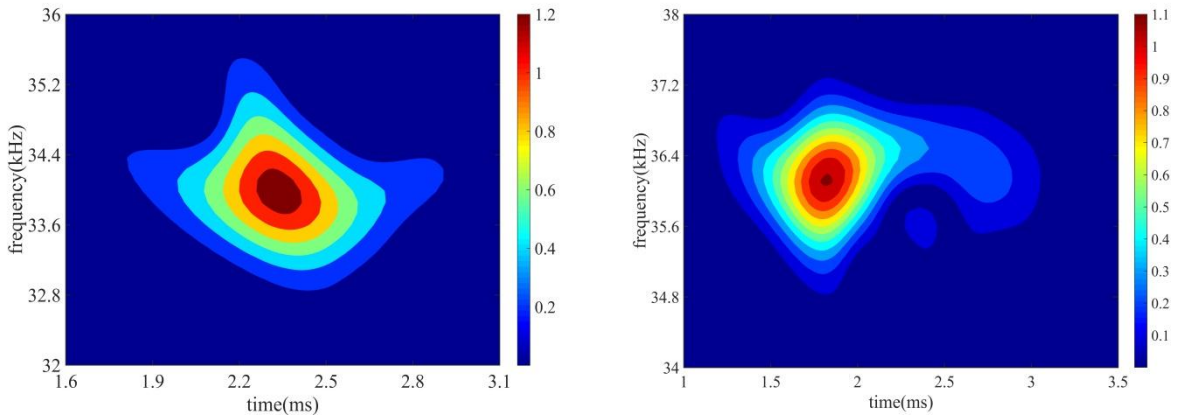

(e) (f)

Fig. 6-12 The time-frequency analysis results of the receiving signal under different test distances, (a) f = 33.97 kHz and L = 50 m, (b) the optimal excitation frequency and L = 50 m, and (c) f = 33.97 kHz and L = 100 m, (d) the optimal excitation frequency and L = 100 m, and (e) f = 33.97 kHz and L = 150 m, (f) the optimal excitation frequency and L = 150 m

6.2 Research on the Coded Excitation

The improvement of the energy transmission of PUTs is often achieved by raising the excitation voltage or increasing the number of excitation pulse cycles. But due to the limitation of the limit voltage parameter of the PUT, the increase of the excitation voltage is also limited. However, the coding excitation technology can overcome the above limitation and it can effectively increase the duration of the excitation pulse and compress the signal at the receiving end, thereby improving the SNR of the signal. Currently, common codes mainly include Barker codes, Golay complementary codes, linear frequency modulation, nonlinear frequency modulation, P4 Polyphase codes, Kasami sequences, LS codes, etc. Among them, except the linear frequency modulation and the nonlinear frequency modulation which belong to the frequency modulation code, the rest belong to the phase modulation codes. Compared to FM codes, phase-modulating codes require less hardware. In addition, in all two-phase coding, the autocorrelation distance sidelobe of the Barker code is the smallest and only requires a single transmission. Thus, considering some factors such as ease of implementation and cost, this section designs the excitation pulse based on the Barker code to improve the SNR of the received UGW signal.

6.2.1 Barker Code and Pulse Compression

For better using the pulse compression technology, it is usually required that the encoded signal has good autocorrelation characteristics because that is very conducive to the correlation peak identification at the receiving end. Essentially, Barker code is a kind of binary sequences that can be expressed as

$$B[N]=[c_0,c_1,\cdots,c_{N-1}],\quad c_i\in\{-1,+1\} \tag{6-24}$$

Its auto-correlation function can be given as

$$\Psi_{AA}[n]=\begin{cases}N, & n=0\\ 0\ or\ \pm1, & n\neq 0\end{cases} \tag{6-25}$$

According to equation (6-25), it is found that the peak of the autocorrelation is the length in bits of the Barker code, and the sidelobe level (SLL) falls between +1 and -1. The length of Barker code can take values of 2, 3, 4, 5, 7, 11, and 13, and cannot be greater than 13 in practice. The Barker codes of different lengths are listed in Tab. 6-4.

Tab. 6-4 Barker codes of different bits

Number of bits	Barker codes
2	+1, -1 or -1, +1
3	+1, +1, -1
4	+1, +1, +1, -1 or +1, +1, -1, +1
5	+1, +1, +1, -1, +1
7	+1, +1, +1, -1, -1, +1, -1
11	+1, +1, +1, -1, -1, -1, +1, -1, -1, +1, -1
13	+1, +1, +1, +1, +1, -1, -1, +1, +1, -1, +1, -1, +1

The received signal of the broken rail detection system based on UGW can be expressed as:

$$y(t)=e(t)*h(t)+n(t) \tag{6-26}$$

where $*$ denotes convolution operator, $e(t)$ is the excitation pulse, $h(t)$ represents the system transfer function, and $n(t)$ is the noise. To better illustrate the process of encoding and decoding of Barker code, a block diagram of the pitch-catch setup is shown in Fig. 6-13.

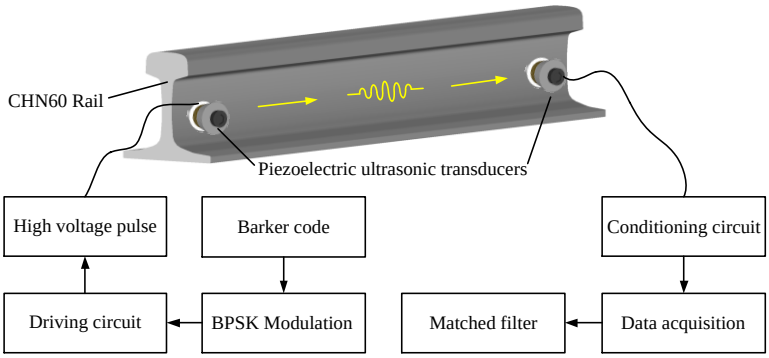

Fig. 6-13 Schematic diagram of the pitch-catch setup based on Barker code

Barker code cannot be used directly to excite a SPUT, since its baseband spectrum does not match with the bandwidth of SPUTs. Hence, it is modulated with a square carrier using the BPSK modulation technique. The transmitted signal $e[n]$ can be obtained as

$$e[n]=v[n]*c[n] \tag{6-27}$$

where $v[n]$ represents the sample sequence of the carrier denoted as $v(t)$, and $c[n]$ is the oversampled Barker code frequency expressed by

$$c[n]=\sum_{k=0}^{N-1}c_k\delta[n-kT_N f_s] \tag{6-28}$$

where $\{c_k = \pm 1,\ k = 0,\ 1,\ \ldots,\ N-1\}$ is the original Barker code sequence before oversampling, $T_N = N_c / f_0$ is the chip duration of the Barker code, N_c indicates cycles of the selected carrier, and f_s is the system sample frequency. The total duration of the Barker coded sequence is $T = NT_N$. Taking a 13-bit Barker code with $N_c = 1$ as an example, the encoding process is shown in Fig. 6-14.

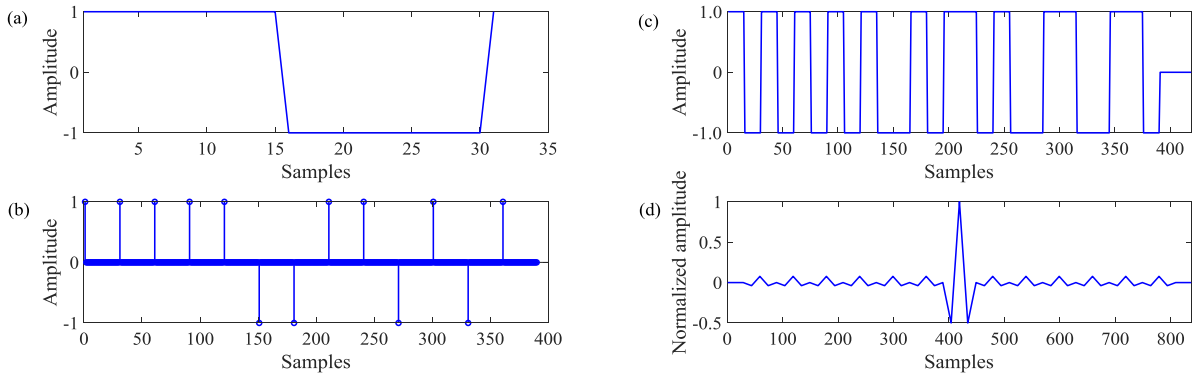

Fig. 6-14 The Barker code encoding process, (a) sampled square wave pulse, (b) oversampled 13-bit Barker code, (c) modulated Barker code, and (d) its autocorrelation curve

Long-range rail detection is different from small range inspection such as long bone detection since it aims at obtaining SNR as high as possible. Currently, the typical methods of pulse compression include matched filter and mismatched filter. The mismatched filter can achieve lower SLLs at the cost of reducing SNR. For the case of a matched filter, its transfer function $H_1(\omega)$ can be obtained as

$$H_1(\omega) = k_1 E^*(\omega) \exp(-j\omega t_0) \tag{6-29}$$

where k_1 is the normalized amplitude constant and $E^*(\omega)$ is the complex conjugate of $E(\omega)$. Through the inverse Fourier transform, the following equations can be achieved:

$$h_1(t) = k_1 \mathrm{e}(t_0 - t) \tag{6-30}$$

According to equation (6-30), it is found that the impulse response function $h_1(t)$ of the matched filter is obtained by shifting t_0 the flipped version $e(-t)$ of the excitation signal $e(t)$. Thus, the pulse compression signal $d(t)$ can be given as:

$$d(t) = y(t) * h_1(t) \tag{6-31}$$

For the performance evaluation of encoding transmission, two metrics are used which include mainlobe width (MLW) and peak sidelobes level (PSL). The PSL formula in decibels can be given as:

$$PSL = 10 \log \left[\frac{\max(A_{sidelobe})}{\max(A_{mainlobe})} \right] \tag{6-32}$$

Here, $A_{sidelobe}$ and $A_{mainlobe}$ represent peak values of sidelobes and mainlobes in correlation results, respectively. On the other hand, MLW can be defined as:

$$MLW = t_2 - t_1 \tag{6-33}$$

Here, $[t_1, t_2]$ denotes the mainlobe width. In practice, MLW determines the inspection resolution. The wider the mainlobe width, the lower the detection accuracy, and vice-versa.

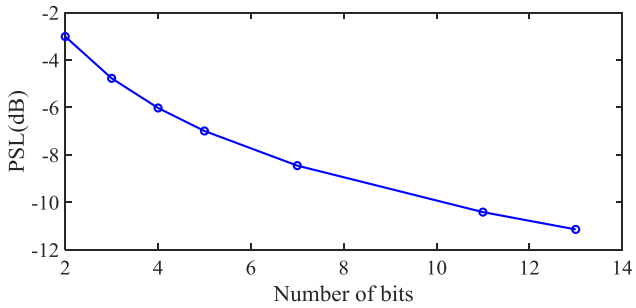

Fig. 6-15 The corresponding PSL values of Barker codes of different bits

According to Tab. 6-4 and equation (6-33), the corresponding PSL values are obtained and shown in Fig. 6-15. From Fig.6-15, it is shown that the 13-bit Barker code has the lowest PSL. This indicates that it has the best suppression effect of pulse compression sidelobes and high SNR. Therefore, the 13-bit Barker code is used to encode the carrier signal in this work.

6.2.2 The Analysis of Barker Code Excitation

To verify the feasibility and superiority of Barker code excitation to generate UGW, a comparison of single-pulse excitation (8 cycles square wave pulse) and Barker coded excitation is performed by experiments based on 1 m CHN60 rail in the lab. The excitation voltage is 20 V and the number of carrier cycles is 8 for Barker coded excitation. The comparative result of the two excitations is shown in Fig. 6-16. From Fig. 6-16, it is found that the amplitude of the received signal is larger when Barker coded excitation is used. The amplitude values of single-pulse excitation and Barker coded excitation are 0.55 V and 1.75 V, respectively. The definition of SNR is given as:

$$SNR = 10 \cdot \log_{10}(\frac{A_s}{A_n}) \tag{6-34}$$

where A_s is the signal amplitude and $A_n = 0.01\,\mathrm{V}$ is the noise amplitude. From equation (6-34), the SNR of the received signal can be calculated. Compared with the single pulse excitation, the SNR of the received signal can be increased by 5 dB when Barker coded excitation is used.

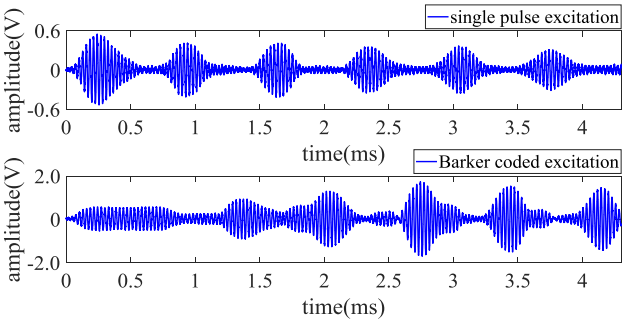

Fig. 6-16 The comparison of the received signals for single pulse excitation and Barker coded excitation

It is well-known that the usual way to excite an ultrasonic inspection system is by using sinusoidal signals. To reduce the dispersion effect and ensure mode purity, the Hanning windowed sinusoidal signal is often used as an excitation waveform. In our study, the sinusoidal wave $v(t)$, square wave $v_1(t)$, and Hanning windowed sinusoidal signal $v_2(t)$ will be the candidates of carrier waveform for Barker encoding. They can be expressed as:

$$v(t) = \sin(2\pi f_0 t), \quad 0 \le t \le T_N \tag{6-35}$$

$$v_1(t) = \frac{4}{\pi}\left[\sin(2\pi f_0 t) + \frac{1}{3}\sin(6\pi f_0 t) + \cdots + \frac{1}{n_1}\sin(2n_1\pi f_0 t) + \cdots\right], \quad 0 \le t \le T_N \tag{6-36}$$

$$v_2(t) = \frac{1}{2}(1-\cos(\frac{2\pi f_0 t}{N_1}))\sin(2\pi f_0 t), \quad 0 \le t \le T_N \tag{6-37}$$

where $N_1 = T_N f_0$ represents the number of carrier cycles. It should be noted that equation (6-36) only contains odd harmonic components, that is, $n_1 = 1, 3, 5, \ldots$.

Firstly, the frequency spectrums of the aforementioned carrier waveforms, in this case with six cycles, are analyzed by using FFT, as shown in Fig. 6-17. The frequency and amplitude of the excitation signals are 35 kHz and 1 V, respectively. From Fig. 6-17, it is obvious that the frequency spectrum value of the square wave at the excitation frequency is larger than the other carrier signals. The Fourier series of the square wave signal equation (6-36) can well explain it. Besides, the frequency spectrum value at the excitation frequency and the spectrum leakage of the Hanning windowed sinusoidal signal is smallest.

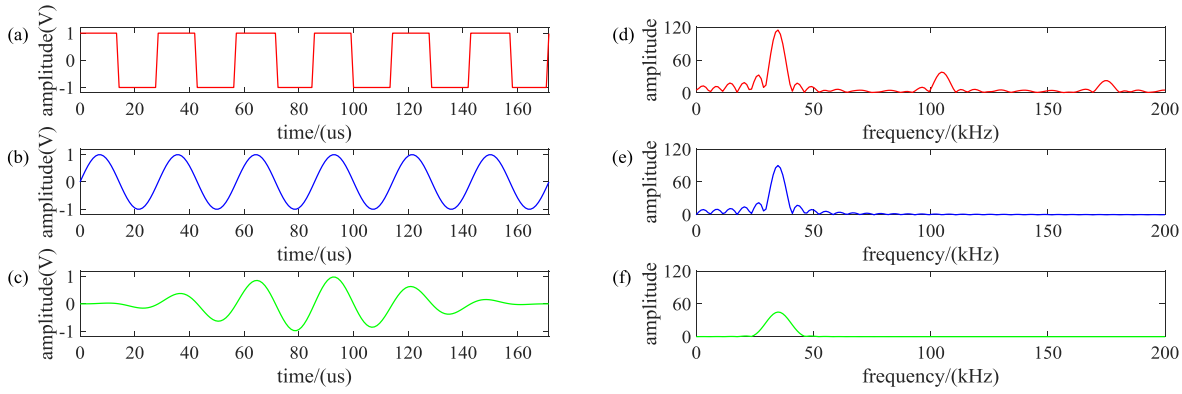

Fig. 6-17 The frequency spectrum analysis for different carrier waveforms, (a) square wave, (b) sinusoidal wave, (c) Hanning windowed sinusoidal signal, and (d), (e), (f) the corresponding frequency spectrum

Next, for the three carrier waveforms, the six carrier cycles per bit are used for the 13 bit Barker code. Then the autocorrelation functions of the Barker encoding signals using three carrier waveforms are calculated and the calculated results are illustrated in Fig. 6-18. Comparing Fig. 6-18(d), Fig. 6-18 (e) and Fig. 6-18 (f), the autocorrelation function curves corresponding to the three carrier waveforms are almost the same because of the very low bandwidth of the system, which acts as a bandpass filter. It can be concluded that the autocorrelation curve is mainly determined by the number of carrier cycles and the number of Barker code bit. To further analyze the effect of the carrier waveforms on pulse compression results, the PUTs are attached to the CHN60 rail web. The length of CHN60 rail is 1 m and the

number of carrier cycles is unchanged. The frequency and amplitude of the carrier signal are 35 kHz, 10 V, respectively. Then the cross-correlation function curves are obtained by correlating the received signal with the excitation signal, as shown in Fig. 6-19. It should be noted that the data of the y-axis from Fig. 6-19(d), Fig. 6-19(e) and Fig. 6-19(f) is scaled by dividing by 10^4. Fig. 6-19(a), Fig. 6-19(b) and Fig. 6-19(c) are the received signals corresponding to the square wave, sinusoidal wave, and the Hanning windowed sinusoidal signal as the carrier waveform, respectively. Comparing Fig. 6-19(d), Fig. 6-19(e) and Fig. 6-19(f), the peak of the cross-correlation curve corresponding to the square wave is the largest.

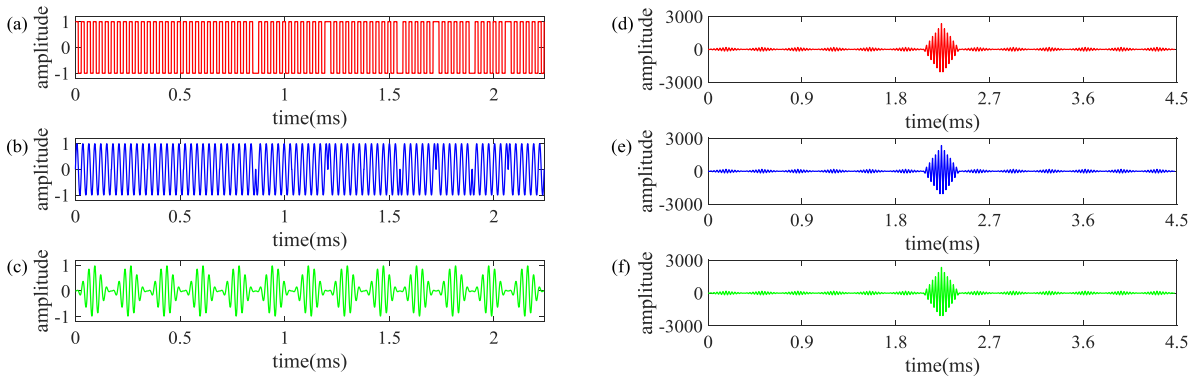

Fig. 6-18 The autocorrelation functions of the Barker encoding signals using different carrier waveforms, (a) square wave, (b) sinusoidal wave, (c) Hanning windowed sinusoidal signal, and (d), (e), (f) the corresponding autocorrelation function curves

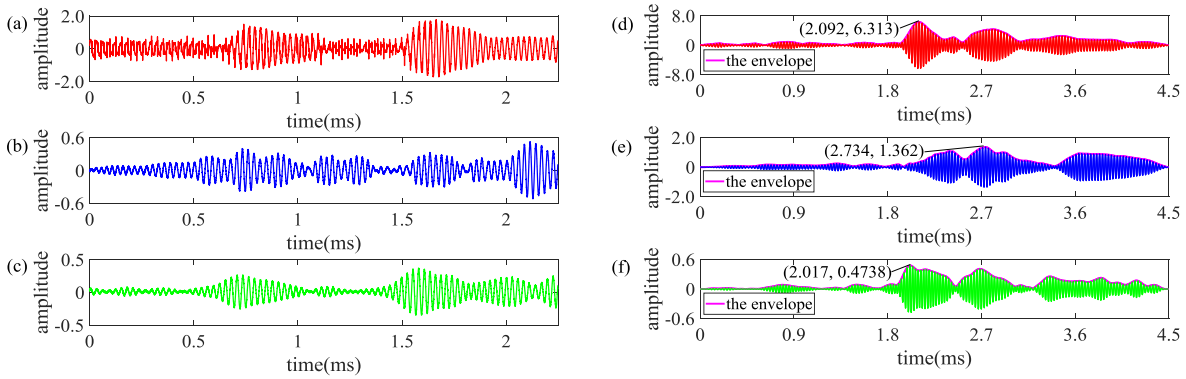

Fig. 6-19 The cross-correlation functions of the Barker encoding signals using different carrier waveforms, (a) square wave, (b) sinusoidal wave, (c) Hanning windowed sinusoidal signal, and (d), (e), (f) the corresponding cross-correlation function curves

To ensure that the amplitude of the received signal is large enough, the excitation voltage of PUTs in long-rail detection is up to kilovolts. If the sinusoidal pulse signal and the Hanning window modulated sinusoidal pulse signal are used to achieve a high voltage, the driving circuit is very complicated, and the detection cost is greatly increased. However, the square wave pulse signal can be easily boosted to a kilovolt by the bridge circuit and the pulse transformer, and the circuit structure is relatively simple. Therefore, the square wave pulse signal is used as the carrier signal of the Barker code in this work. Generally, the BVD model is used to simulate the PUT working around the resonance frequency. To choose the number of carrier cycles, the bandwidth of the PUT must be considered. The parameters of the BVD model of the PUT used

in this article are listed in Tab. 6-5. According to the BVD model parameters in Tab. 6-5, the frequency response analysis of the PUT is analyzed using the circuit analysis software PSpice16.5. Then it is compared with the spectrum analysis results of the Barker coded signals under different cycles, as shown in Fig. 6-20. It can be seen that from Fig. 6-20, the bandwidth of the PUT used is very narrow. As the number of cycles of the excitation signal increases, the frequency spectrum of the excitation signal is gradually narrowed and approaches the response of the PUT.

Tab. 6-5 The parameters of BVD equivalent circuit model of the used SPUT

Parameters	R_0	C_0	C_m	R_m	L_m
Values	186.35 kΩ	6.28 nF	0.46 nF	163.30 Ω	44.80 mH

Additionally, the envelopes of the autocorrelation function curves under different carrier cycles are calculated and the y-axis data is scaled by dividing by 10^3, as shown in Fig. 6-21(a). From Fig. 6-21(a), the peak values are gradually increasing with the increment of carrier cycles. Similarly, the peak value is the highest when the carrier cycle is 10. To investigate the MLW and PSL, the envelopes of autocorrelation function curves are normalized and the threshold is set to 0.3, as shown in Fig. 6-21(b). Then the curves of MLW and PSL can be obtained, as shown in Fig. 6-21(c). In light of Fig. 6-21(c), it is evident that with the increase of carrier cycles, the MLW improves linearly while the absolute value of PSL is almost unchanged.

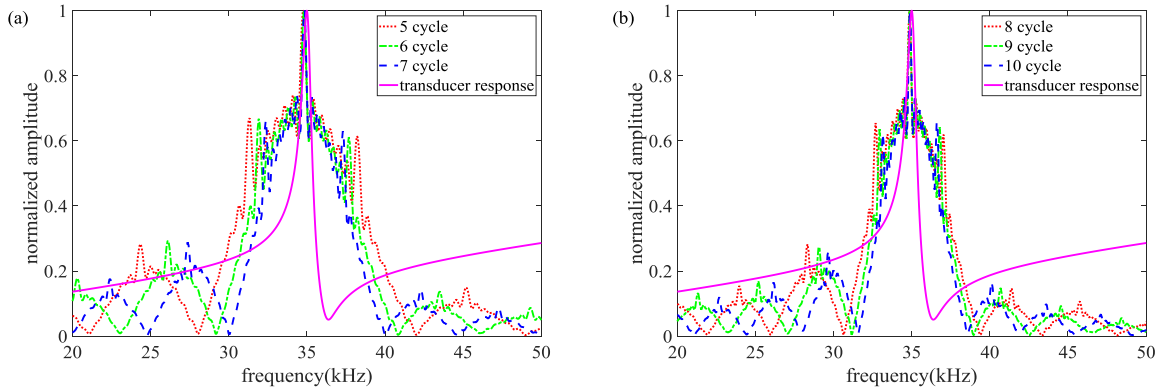

Fig. 6-20 Comparison of the frequency spectrum of PUTs and the frequency spectrum of excitation signals under different carrier cycles, (a) 5, 6 and 7 cycles, (b) 8, 9 and 10 cycles

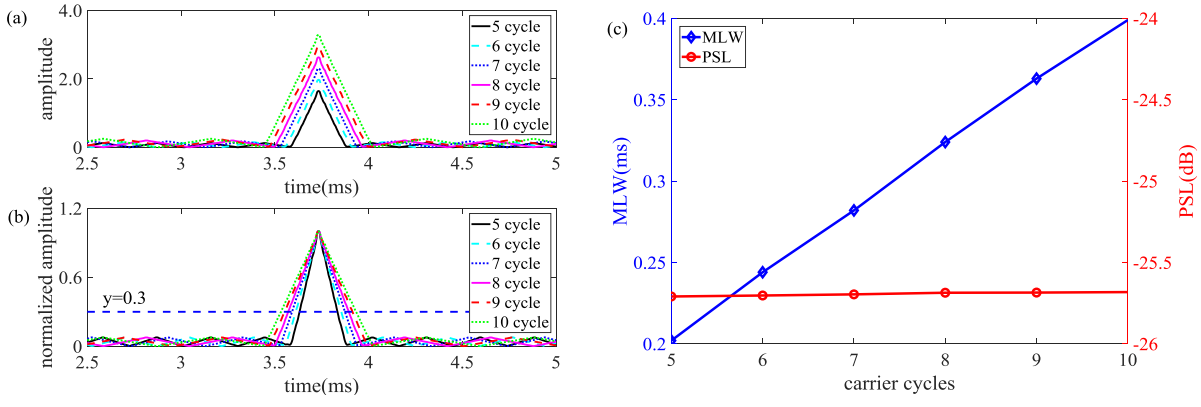

Fig. 6-21 The analysis of the autocorrelation functions under different carrier cycles, (a) the envelopes of autocorrelation curves, (b) the normalized envelopes of autocorrelation curves, (c) MLW and PSL

According to the PSpice model of the pitch-catch setup established in Chapter 3, the effect of different carrier cycles on the pulse compression results is analyzed. The transmission medium rail in the simulation model is modeled using a lossy transmission line. The relevant parameters of the rail are listed in Tab. 6-6.

Tab. 6-6 The material parameters of CHN60 rail used in the simulation

Parameters	A (cm^2)	ρ (kg/m^3)	v_t (m/s)	Q_m
Values	77.45	7850	5790	100

A pitch-catch experimental platform is established in Fig. 6-22, which consists of SPUTs, batteries, CHN60 Rail, driving circuit board, and waveform recorder MR8875-30 (HIOKI E.E. CORPORATION). Here, the driving circuit board is used to excite SPUTs, which is designed based on the full-bridge topology. The waveform recorder saves the data from received signals. In Fig. 6-22(a), TR1 represents transmitters and REi (i=1, 2, 3, 4) denotes receivers. The test distances include 50 m, 100 m, 200 m, and 500 m.

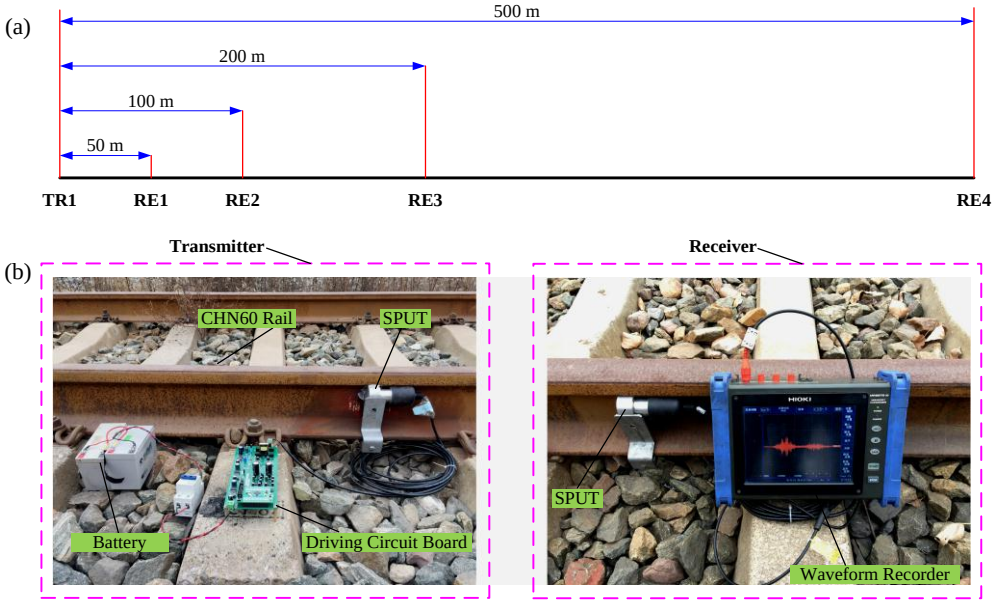

Fig. 6-22 The field test platform based on the pitch-catch, (a) test distance diagram, (b) experimental platform

According to the conclusion of the selection and analysis of the number of carrier cycles in the first half of this subsection, the simulation and experimental research are carried out for 10 and 20 cycles in the carrier. The propagation distance is 50m and the excitation frequency is 35 kHz. Fig. 6-23(a) and Fig. 6-23(b) present the simulated and measured pulsed compression results, respectively, for 10 and 20 carrier cycles. The main lobe peak is greatly increased with 20 cycles compared with the case of using only 10 cycles. Fig. 6-23(c) and Fig. 6-23(d) show the corresponding normalized envelopes. It is seen that the larger number of carrier cycles, the larger MLW and the lower PSL. It is also shown that the simulated results are in agreement with the measured ones. Note that a small MLW and low PSL are required to guarantee good range resolution and high SNR in practice. If carrier cycles keep increasing, MLW and the duration of the received signal will be increased, which leads to taking more time to process the received signal and decreasing range resolution. Therefore, the number of carrier cycles will take 20 in this study.

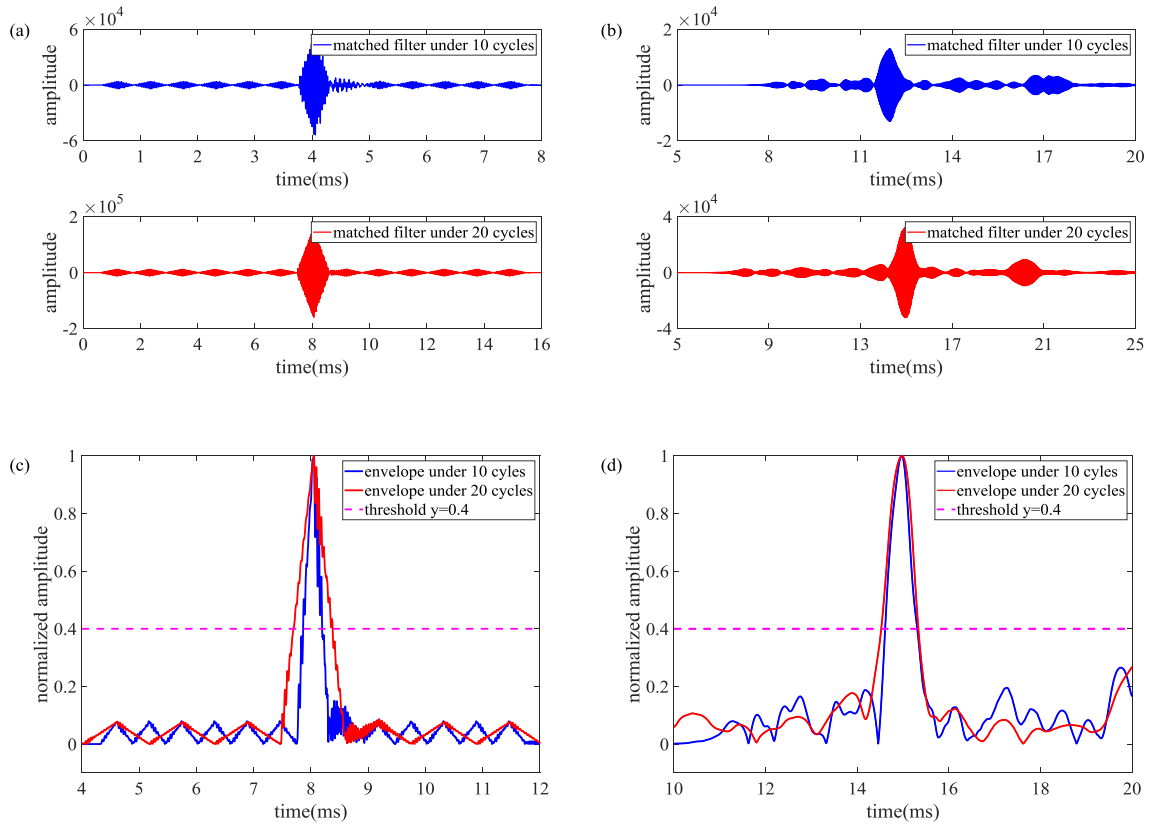

Fig. 6-23 The comparison of simulated and measured results, (a), (b) matched filtering under 10 and 20 cycles, (c), (d) normalized envelopes comparison under 10 and 20 cycles

The detection equipment of broken rails is often in a high noise environment. In general, high SNR is required in the detection. Hence, the analysis of the performance of the Barker code with noise is necessary. The test distance used is 50 m and the number of carrier cycles is 20. Gaussian noises with SNR=-10 dB and -20 dB are added to the measured received signals. In this situation, the received signals cannot be distinguished in the received transmissions, as can be seen in Fig. 6-24. Nevertheless, after matched filtering, the correct correlation peak can still be found. It is concluded that the 13-bit Barker code has a strong immunity to noise, which can well satisfy the requirements of the broken rail detection system.

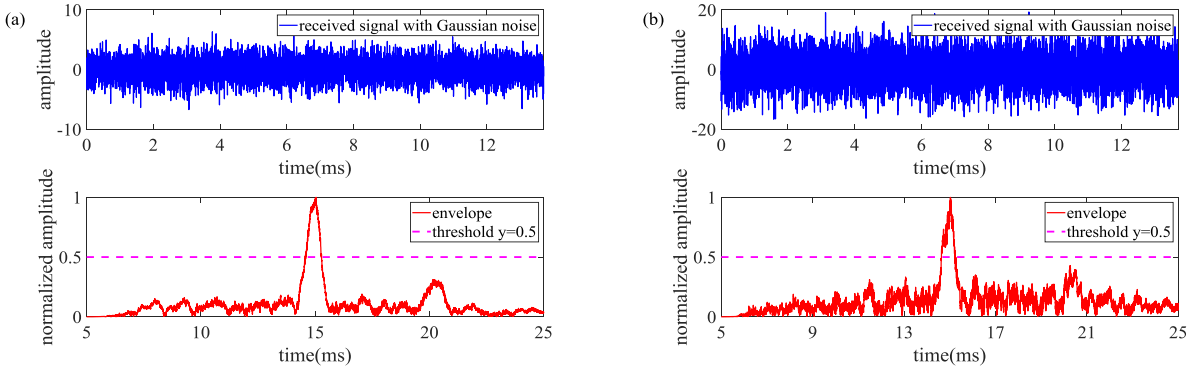

Fig. 6-24 The analysis of noise performance of Barker code, (a) SNR=-10 dB, (b) SNR=-20 dB

The dispersion and multimode transmission of UGW are closely related to the geometry shape of structures and the propagation distances. For this reason, the analysis of the effect of

the propagation distance on the pulse compression is carried out. The number of carrier cycles is 20 and the test distances are 50 m, 100 m, 200 m, and 500 m, respectively. The corresponding normalized envelopes are extracted in Fig. 6-25(a) and the MLW and PSL are calculated and presented in Fig. 6-25(b), to conveniently compare pulse compression results under different propagation distances. According to Fig. 6-25, with the increase of propagation distances, MLW increases linearly while PSL is almost unchanged.

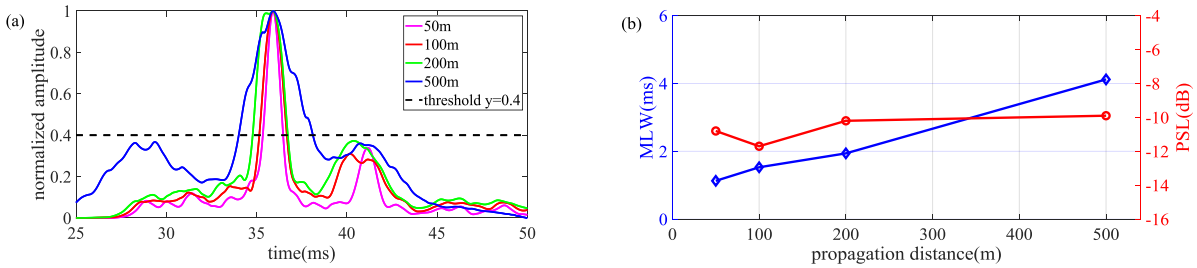

Fig. 6-25 The comparison of pulse compression results under different propagation distances, (a) normalized envelopes comparison, (b) MLW and PSL

The reason is that the dispersion of UGW can cause the wave-packets to spread out in space and time as it propagates through structures. Additionally, the duration of the wave-packet increases linearly with the propagation distance. All that limits the range resolution that can be obtained in a long-range detection system based on UGW.

6.3 Research on the Adaptive Peak Detection

To accurately determine whether there is a rail breakage in the detection interval, the feature extraction of the UGW signal transmitted in the rail is very important. However, with the change of track conditions and environmental factors, the feature of the UGW signal in the rail will change, which will make the UGW feature extraction more difficult. Hence, this work uses coded excitation and pulse compression technology to effectively improve the SNR of the UGW signal, at the same time the detection of the transmitted UGW signal is converted into the detection of the envelope peak. Due to the influence of UGW dispersion, modulation technology, bandwidth limitation, multipath, and noises in the rail, the result after pulse compression is not ideal and often contains some undesirable sidelobes. Currently, the method of setting the amplitude threshold is often used to detect the peak of the envelope to ensure the accuracy of peak detection. For changing UGW signals, the amplitude threshold will have to be updated in real-time. Therefore, to solve the above problems, it is very necessary to study an adaptive peak detection algorithm without any amplitude threshold.

6.3.1 Peak Detection Algorithm

As we all know, the HT is widely used to analyze the instantaneous amplitude and frequency of a signal, and it is used to quickly extract the signal envelope. Its physical meaning is actually an all-pass network that lags the phase by $\pi/2$. According to the physical meaning of HT, it is easy to find that after the envelope signal through HT, and its peak value just corresponds to the positive zero-crossing of the transformed signal. Thence, the envelope signal peak detection can be converted into positive zero-crossing detection. The change of the envelope signal peak value will not affect the positive zero-crossing detection and does not

require any amplitude threshold. Then the HT definition of a real signal $x(t)$ can be given as

$$\hat{x}(t) = H\left[x(t)\right] = \frac{1}{\pi t} * x(t) = \frac{1}{\pi}\int_{-\infty}^{\infty} \frac{x(\tau)}{t-\tau} d\tau \tag{6-38}$$

From equation (6-38), it can be found that the HT in the time domain is obtained by performing the convolution between the signal $x(t)$ and $1/\pi t$. In the frequency domain, the HT can be expressed as

$$\hat{X}(f) = F\left[\frac{1}{\pi t}\right] \cdot F\left[x(t)\right] = -j\,\mathrm{sgn}(f)X(f) \tag{6-39}$$

where $X(f)$ is the Fourier transform of the signal $x(t)$. Then the HT of the signal $x(t)$ can be calculated as

$$\hat{x}(t) = IFT\left[\hat{X}(f)\right] \text{ where } \begin{cases} \hat{X}(f) = jX(f), & f < 0 \\ \hat{X}(f) = -jX(f), & f > 0 \end{cases} \tag{6-40}$$

Here, *IFT* denotes the inverse Fourier transform.

To illustrate the peak finding logic using HT, an even Gaussian function is taken as an envelope model. If HT is applied to the Gaussian function the resulting process is shown in Fig. 6-26. It can be observed that the HT generates a positive zero crossing point in the transformed signal corresponding to a peak of the signal. Hence, by detecting positive zero-crossing points without any amplitude threshold, the peak of the signal can be identified accurately.

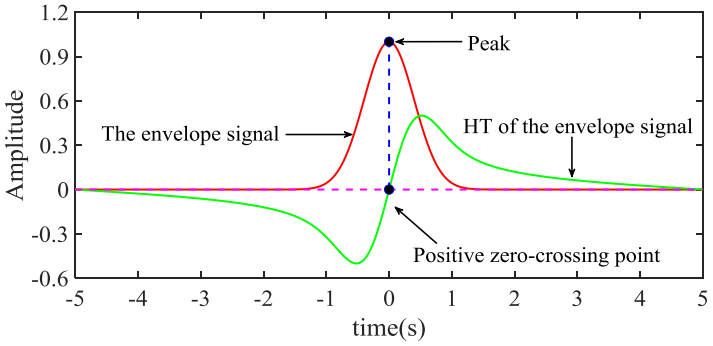

Fig. 6-26 Illustration of peak detection logic by positive zero crossing point

The extraction of the smooth unipolar envelope is to obtain unique positive zero-crossing point in the transformed signal by HT. If the extracted envelope is not smooth because it has many spikes, this will result in generating extra positive zero-crossing points in the transformed signal. To extract a smooth unipolar envelope signal, firstly, the pulse-compressed signal needs to be filtered; secondly, a nonlinear transformation needs to be used to enhance the peak value of the pulse-compressed signal. Based on the fact that it is easy to program and reduce the hardware cost, the received UGW signal $y[n]$ is through the matched-filter to obtain the signal $d[n]$. According to equations (6-41) and (6-42), the above signal are band-pass filtered and first-order forward differential filtering. Note that the band-pass filter used here is a digital band-pass tracking filter, which has been introduced in subsection 6.1.1 and will not be repeated here. Then, to simplify the calculation, the filtered signal $t[n]$ is amplitude normalized according to (6-43).

$$b[n] = c\left[d[n] - d[n-2]\right] - a_1 b[n-1] - a_2 b[n-2] \tag{6-41}$$

$$t[n] = b[n+1] - b[n] \tag{6-42}$$

$$a[n]=norm(t[n])=\frac{t[n]}{\max(|t[n]|)} \tag{6-43}$$

where $b[n]$ indicates the output of the DBTF, $a[n]$ represents the normalized signal, $t[n]$ is the output of the first-order forward differential filter and it is a bipolar signal so a rectification is required to simplify the process of peak identification.

To enhance the mainlobe peak of output results of the matched filter and make the bipolar signal convert to unipolar, a nonlinear transform is required. Squaring transform (ST) and Shannon energy transform (SET) can be a better choice. Their mathematical formulations are given as

$$\text{ST}: \quad s[n]=a[n]\cdot a[n] \tag{6-44}$$

$$\text{SET}: \quad s[n]=-(a[n])^2\log((a[n])^2) \tag{6-45}$$

With the aim of choosing a suitable nonlinear transform, the signal $s[n]$ is calculated for ST and SET in Fig. 6-27(a). In Fig. 6-27(a), it can be observed that ST gives a weighted exponential response to the high-intensity components while SET emphasizes medium intensity components. In addition, Fig. 6-27(b) shows the result of applying ST and SET to a real measured signal through a matched filter. From Fig. 6-27(b), ST greatly enhances the mainlobe peak and decreases sidelobe level compared with SET. Hence, ST is chosen as a nonlinear transform in this work.

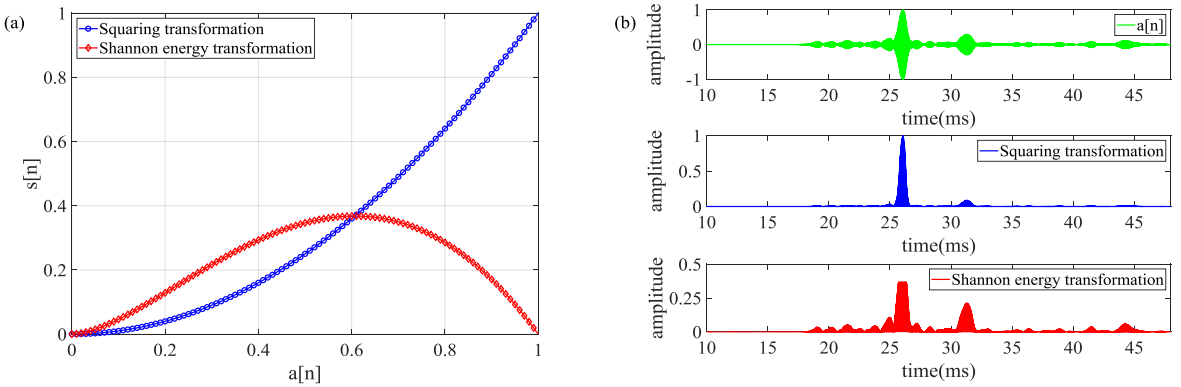

Fig. 6-27 The comparison of ST and SET, (a) comparison of energy values, (b) comparison of signal s[n]

After ST, the transformed signal $s[n]$ passes through a triangle filter to obtain a smooth envelope. The triangle filter consists of two cascaded MA filters. The MA filter acts as a low pass filter, essentially, it is a window-based averaging filter and easy to achieve by programming. The mathematical formulation of the MA filter is given as

$$m[n]=\frac{1}{N_{\text{w}}}\left[s(n-(N_{\text{w}}-1))+s(n-(N_{\text{w}}-2))+\cdots+s(n)\right] \tag{6-46}$$

where N_{w} represents the window width. According to equation (6-46), the impulse response of the triangle filter can be expressed as

$$t_{\text{f}}[n]=m[n]*m[n] \tag{6-47}$$

Additionally, the amplitude normalization, ST, and MA filtering from (6-48), (6-49), (6-50), are used for the filtered signal $t_f[n]$ to smoothen the envelope extraction.

$$a_1[n] = norm(t_f[n]) = \frac{t_f[n]}{\max(|t_f[n]|)} \tag{6-48}$$

$$s_1[n] = a_1[n] \cdot a_1[n] \tag{6-49}$$

$$m_1[n] = \frac{1}{N_w}[s_1(n-(N_w-1)) + s_1(n-(N_w-2)) + \cdots + s_1(n)] \tag{6-50}$$

To sum up, an adaptive peak detection algorithm is proposed and the specific process flow is shown in Fig. 6-28. It is composed of three main stages, namely, the pre-processing, the smooth squaring transform (ST) envelope extraction, and the peak identification. The preprocessing stage mainly involves matched filtering, bandpass filtering, first-order forward difference, and amplitude normalization, the smooth envelope extraction stage involves ST, triangular filter, amplitude normalization and moving average (MA) filtering, and the peak identification stage involves HT and positive zero-crossing point detection.

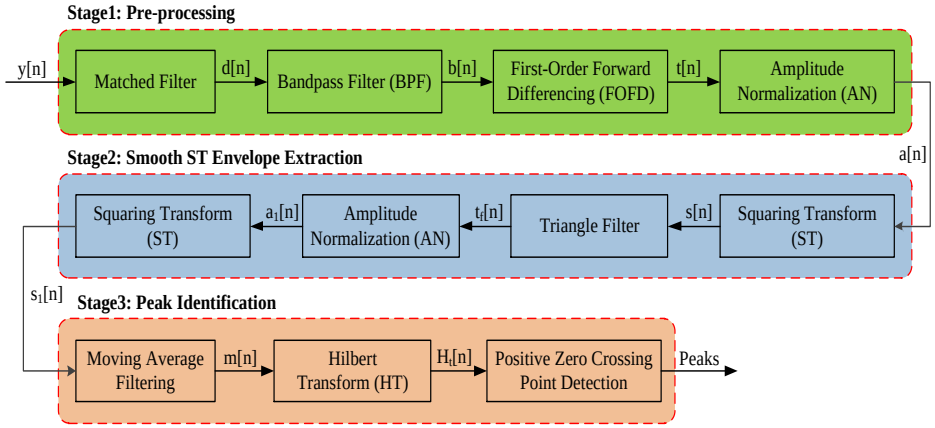

Fig. 6-28 The processing flow of the proposed peak detection algorithm

6.3.2 The Verification of Peak Detection Algorithm

The smooth envelope is crucial for the achievement of positive zero-crossing points by using HT. However, the selection of the window length of the moving average filter has a great influence on the envelope extraction. Generally, the length of this window is equal to the width of the mainlobe of the signal envelope after matched filtering. The analysis of the effect of the window length N_w of the MA filter on peak detection is conducted, for the case of 20 carrier cycles and a test distance of 500 m. In this case, the mainlobe width of the pulse compression result is around 2.4 ms and the sampling frequency is 500 kHz, so the mainlobe width, in samples, is 1200. Consequently, the window lengths considered are $N_w = 100,\ 1200,\ 2000$ samples, respectively. Fig. 6-29 presents the peak detection results under these different window lengths. Fig. 6-29(a) shows that the signal after the triangle filter generates multi-peaks when the window length is $N_w = 100$ samples. This leads to the appearance of unexpected positive zero-crossing points.

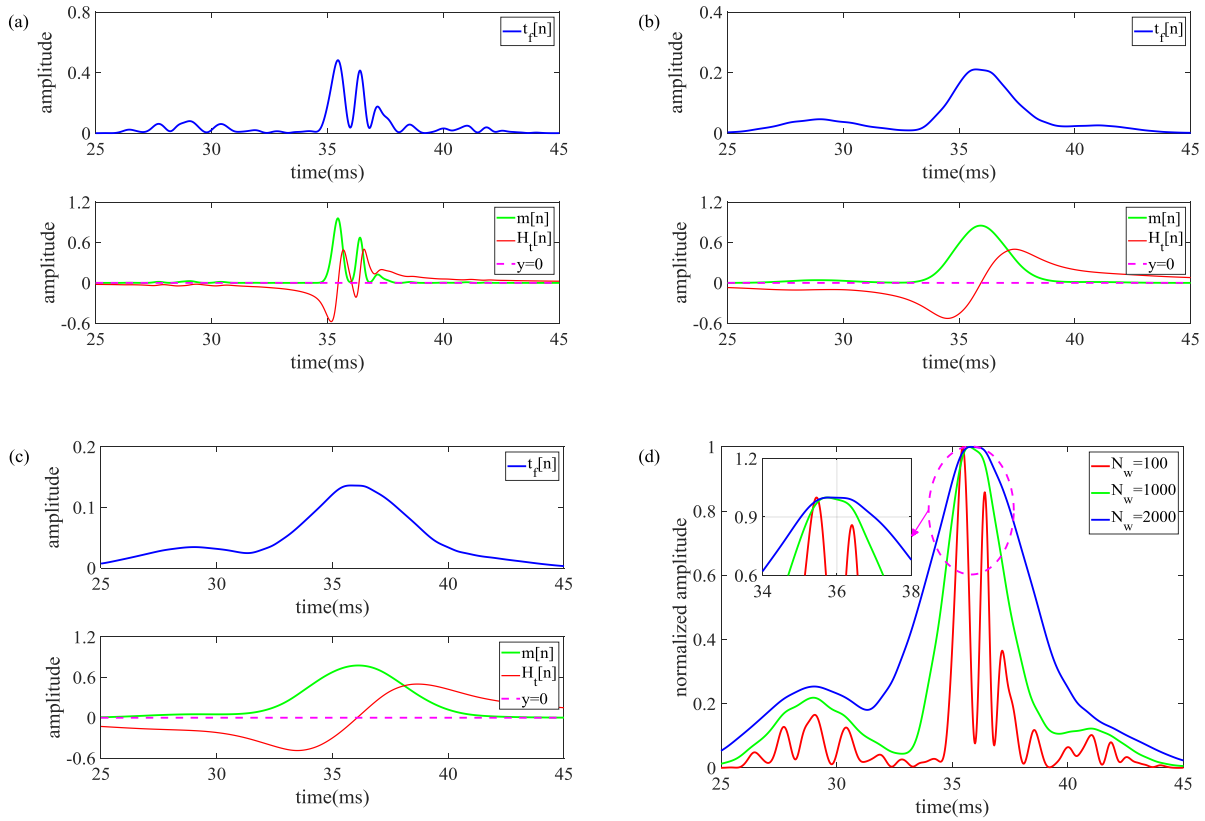

Fig. 6-29 The analysis of the effect of the window length of the Moving averaging filter on the peak detection, (a) *N*w =100, (b) *N*w =1200, (c) *N*w =2000, (d) comparison of normalized envelopes

Besides, it can be observed that if the peak value of the filtered signal $t_{\mathrm{f}}[n]$ is small, the positive zero-crossing point cannot appear by using HT. Considering also the results of Fig. 6-29(b) and Fig. 6-29(c), only one positive zero-crossing point is obtained when the window length is $N_{\mathrm{w}}=1200,\ 2000$ samples. Besides, the normalized envelopes of the filtered signal $t_{\mathrm{f}}[n]$ under the three window lengths are compared in Fig. 6-29(d). It is shown that, compared to 1200 samples, the peak of the envelope will generate a larger shift if $N_{\mathrm{w}}=2000$ samples. This leads to some time difference in identifying the received transmissions. Hence, the window length of the MA filter selected is normally equal to the mainlobe width of the pulse compression results.

Then the performance of the proposed peak detection method for different distances is analyzed. Note that the number of carrier cycles is unchanged and the test distances considered are 50 m, 100 m, 200 m, and 500 m, respectively. It can be seen from Fig. 6-30, as the propagation distance increases, the length of the time domain of the received signal increases, but the proposed adaptive peak detection algorithm can obtain the corresponding positive zero crossing point, thereby effectively identifying the peak point of the signal. It is also shown that small peaks in the filtered signal have no influence on the extraction of positive zero-crossing points. These results can well demonstrate that the proposed method for the detection of peaks has strong robustness.

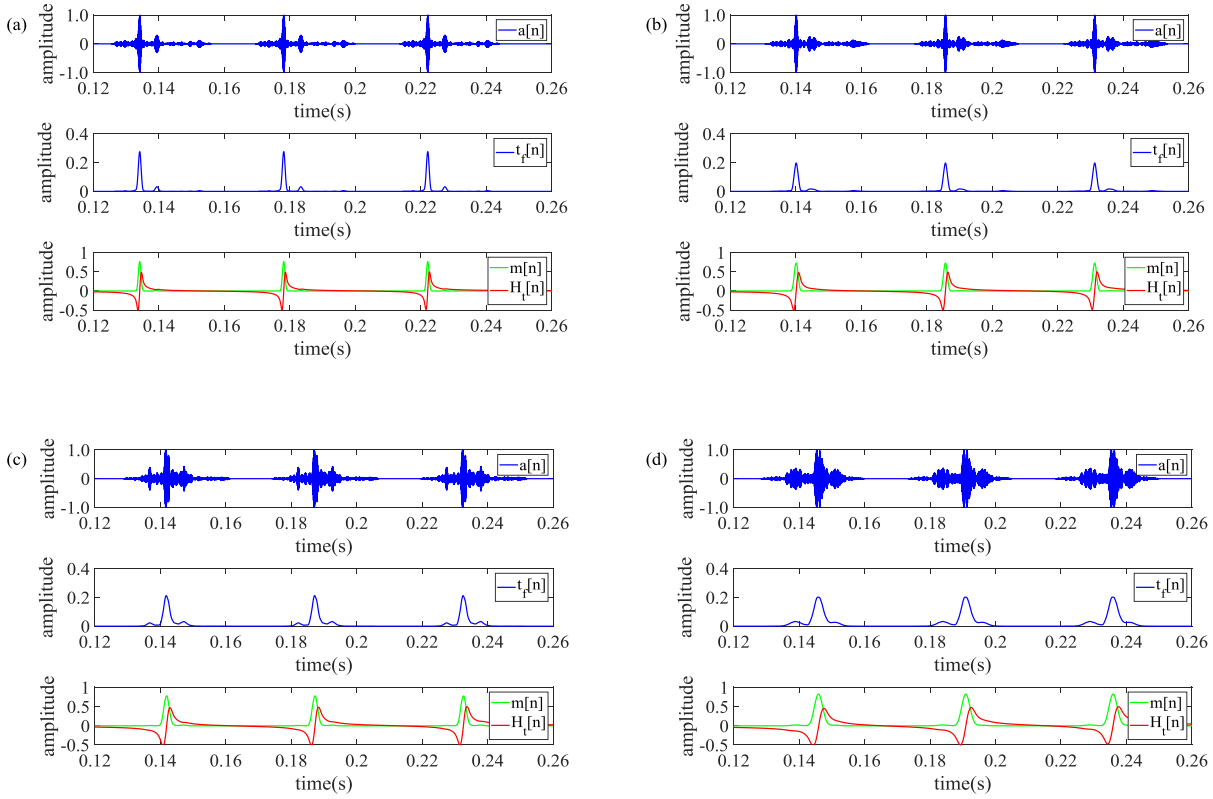

Fig. 6-30 The peaks detection under different test distances, (a) 50 m, (b) 100 m, (c) 200 m, (d) 500 m

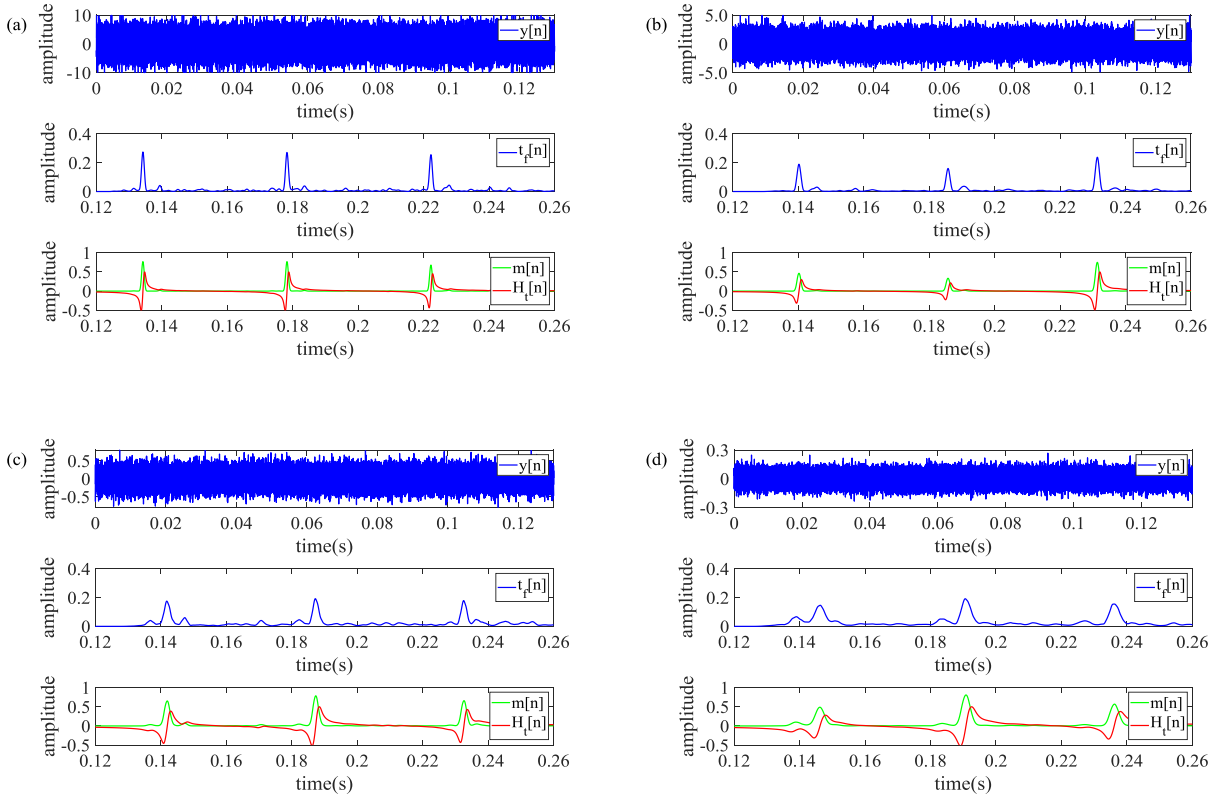

Fig. 6-31 The analysis of peak detection results under Gaussian noise with SNR=-20dB, (a) 50 m, (b) 100 m, (c) 200 m, (d) 500 m

Strong immunity to noise is required for a real-time broken rail detection system, especially in the detection of breakages for long rails in service. Gaussian noises with SNR=-20 dB are added in the received signals of different test distances. As can be seen in Fig. 6-31, after the proposed processing, including filtering, envelope extraction, and HT, the positive zero-crossing points corresponding to the main peaks are obtained under the different test distances. It is shown that the proposed peak detection algorithm has strong anti-noise performance. With the increase of the propagation distance, the influence of the dispersion of UGW on MLW is gradually increasing. It is noted that the lower the MLW, the higher the range resolution.

6.3.3 The Performance Comparison of Peak detection algorithms

To verify the superiority of the proposed peak detection method, the comparison of the proposed peak detection algorithm and the novel adaptive peak detection method proposed in [132] is performed. This peak detection method is mainly based on the discrete wavelet transform (DWT), on a moving average filter, as well as on the HT. Generally, the selection of appropriate wavelet has a great influence on the performance of signal processing algorithms based on the wavelet transform. It should be noted that the choice of wavelet is only application dependent. In this work, the db1 wavelet is used to decompose into four levels. According to Nyquist's rule (($f_{s1} \geq 2 f_m$) where f_{s1} represents the sample rate and f_m is the highest frequency of the signal), the frequency components of the Barker coded UGW signal will be in the range of 0 Hz~250 kHz. A specific description of the frequency range of each level is presented in Fig. 6-32. The frequency of Barker coded excitation is 35 kHz, from Fig. 6-32, the detail coefficients of D3 and D4 can capture this frequency information. Then the reconstruction operation is performed by D3 and D4.

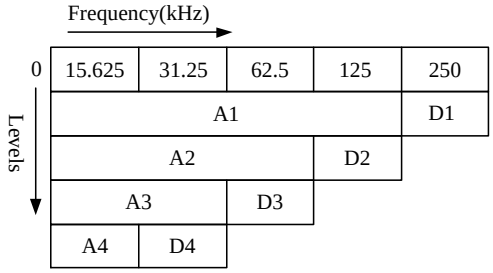

Fig. 6-32 The scheme of DWT decomposition of the UGW signal

By using the measurement signal when the carrier cycle is 20 and the propagation distance is 50 m, the proposed peak detection algorithm is compared with the peak detection algorithm based on DWT, as shown in Fig. 6-33 and Fig. 6-34. From Fig. 6-33 and Fig. 6-34, it is obvious that the two peak detection algorithms can accurately identify the peaks. In addition, compared to the peak detection method based on DWT [132], the signal amplitude through the MA filter is larger for the proposed peak detection algorithm. The total processing time for two peak detection methods and the processing time of DWT and DBTF are calculated by using the following platform:

- Processer and RAM: Inter (R) Core (TM) i7-5500U CPU @ 2.4 GHz, 8 GB;
- Operation system: 64-bit Windows 7;
- Analysis software: MATLAB 9.7.

In addition to the total processing time of the two peak detection methods, Tab. 6-7 also lists the processing time based on DWT and DBTF, respectively. It can be seen from Tab. 6-7 that the peak detection algorithm proposed in this paper requires shorter time than the peak

detection algorithm based on DWT, regardless of the total processing time or filtering processing time.

Tab. 6-7 The comparison of the processing time for the proposed peak detection algorithm and the peak detection algorithm based on discrete wavelet transform

Parameters	Total time	DWT	DBTF
The peak detection method [132]	0.405s	0.122s	-
This work	0.325s	-	0.008s

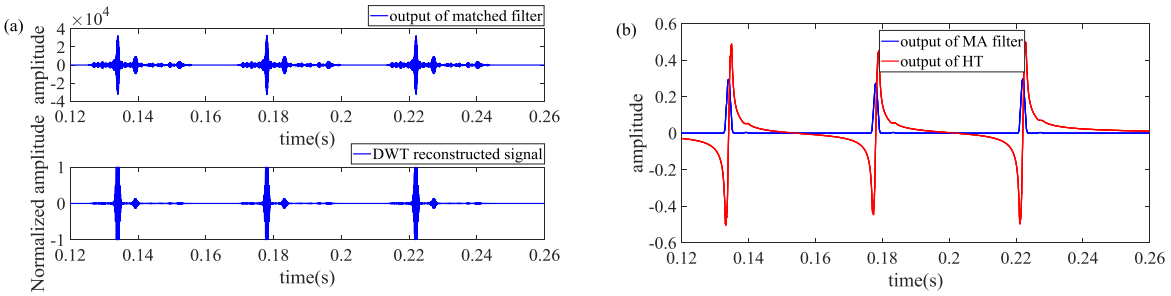

Fig. 6-33 The analysis of peak detection algorithm based DWT for the case of 20 carrier cycles and a test distance of 50 m, (a) DWT reconstructed signal, (b) peak detection results by HT

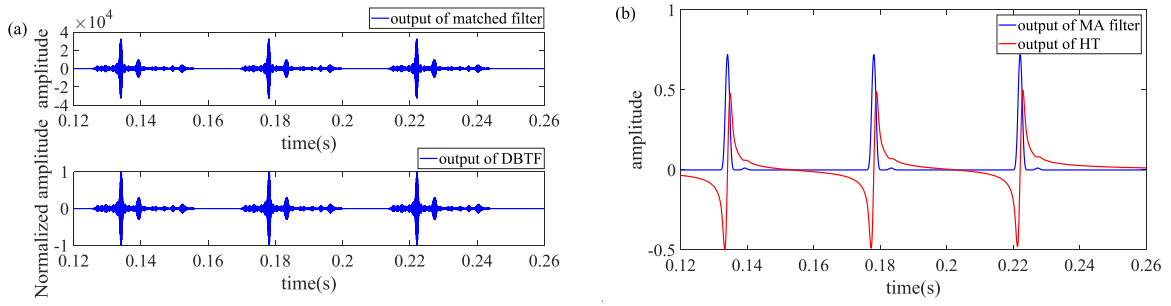

Fig. 6-34 The analysis of peak detection algorithm based DBTF for the case of 20 carrier cycles and a test distance of 50 m, (a) filtered signal by using DBTF, (b) peak detection results by HT

To perform further comparison for two peak detection methods, four performance factors [131] namely, sensitivity (Se), positive predictivity (+P), error rate (Er), and accuracy (Acc) are used in this work. The definition of these factors is given as:

$$Se = \frac{TP}{TP + FN} \tag{6-51}$$

$$+P = \frac{TP}{TP + FP} \tag{6-52}$$

$$Er = \frac{FP + FN}{TP} \tag{6-53}$$

$$Acc = \frac{TP}{TP + FN + FP} \tag{6-54}$$

Here, TP is the number of correctly detected peaks, FN is the number of missed peaks, and FP is the number of false peaks. The Gaussian noise with SNR =-20 dB is added in the received signals under the test distances of 100 m, 200 m, and 500 m. For each of the above cases, TP, FN, and FP are counted for 10 times peak detection results. The performance comparisons of

two peak detection methods for every case are listed in Tab. 6-8, Tab. 6-9, and Tab. 6-10.

Tab. 6-8 The performance comparison of the peak detection method based on discrete wavelet transform and this work for the case of test distance of 100 m

Parameters	TP	FP	FN	Se (%)	+P (%)	Er (%)	Acc (%)
The peak detection method [132]	30	4	0	100	88.24	13.33	88.24
This work	30	1	0	100	96.77	3.33	96.77

Tab. 6-9 The performance comparison of the peak detection method based on discrete wavelet transform and this work for the case of test distance of 200 m

Parameters	TP	FP	FN	Se (%)	+P (%)	Er (%)	Acc (%)
The peak detection method [132]	30	6	0	100	83.33	20	83.33
This work	30	4	0	100	88.24	13.33	88.24

Tab. 6-10 The performance comparison of the peak detection method based on discrete wavelet transform and this work for the case of test distance of 500 m

Parameters	TP	FP	FN	Se (%)	+P (%)	Er (%)	Acc (%)
The peak detection method [132]	30	7	0	100	81.08	23.33	81.08
This work	30	4	0	100	88.24	13.33	88.24

According to Tab. 6-8, Tab. 6-9, and Tab. 6-10, it is found that if the propagation distance increases the accuracy of the two peak detection algorithms decreases. To sum up, the performance of the proposed peak detection algorithm is superior. In general, the power of a broken rail detection system based on UGW is supplied by using solar energy. Hence, the processing algorithm should be as simple and as fast as possible which is conducive to saving energy. In summary, compared to the previous works, the proposed peak detection algorithm has the following advantages:

- Not requiring any amplitude threshold;
- Less time cost;
- It is suitable for other encoding transmissions;
- It is easy to accomplish by programming;
- It is easy to integrate into a real-time detection system;

6.4 Conclusion

Since the PUT will produce a resonance frequency shift under load, resulting in a reduction in the transmission efficiency of the PUT, this chapter proposes an optimal frequency tracking method based on the DBTF. This method is easy to accomplish by programming, which can effectively guarantee the efficient transmission of PUTs. Because the broken rail detection system based on UGW is subjected to the influence of field environmental factors, UGW dispersion and multimodal, the amplitude and SNR of the received UGW signal is relatively small. To solve this problem, this chapter firstly proposes an excitation method based on Barker code and then the receiver uses pulse compression technology to achieve effective

reception and judgment of the transmitted signal. Secondly, because of the undesired peak sidelobes generated by the signal after pulse compression due to the effects of bandwidth, multipath and noise, based on the DBTF, triangle filter, ST and HT, an adaptive peak detection algorithm without any amplitude threshold is proposed.

7 Summary and Future Works

7.1 Summary

As an important part of rail transportation in China, the integrity of the railway lines is directly affected by the operation safety of the train. If the rail generates breakages, this will seriously threaten the train's safety. Therefore, the real-time monitoring of the in-service rail status has great practical significance for ensuring the safe operation of the train. Currently, it is found that the received signal is unstable in some detection intervals and even cannot be received on rainy days when the developed real-time broken rail detection system based on UGW is applied on a large scale. To overcome the above problems, the research on the characteristics optimization of PUTs is of great significance to improve the propagation efficiency of UGW in the rail.

7.1.1 Main Contributions

UGW technology has the advantages of low detection frequency, long detection distance, strong anti-electromagnetic interference ability, and large coverage. Hence, it has potential advantages in real-time detection of broken rails. PUT is a key component in the detection of UGW broken rail, and its electromechanical properties have an important influence on the propagation characteristics of UGW. In this thesis, the characteristics of PUTs in long-distance broken rail detection are systematically optimized, and the main research work is as follows:

1. To deeply study the electromechanical characteristics of SPUTs in the longitudinal vibration, the PSpice equivalent circuit model of SPUTs in the longitudinal vibration and the PSpice equivalent circuit model of the pitch-catch setup are established based on the one-dimensional wave and transmission line theories. The experimental results of comparative impedance analysis and the theoretical values of the vibration speed ratio of the front and back masses are verified from two aspects. It is shown that the established PSpice model is convenient for studying the electromechanical characteristics of the piezoelectric ultrasonic transducer and has strong scalability.

2. To solve the impedance mismatch between the PUT, the driving circuit, and the surface of the rail, the effects of EIM on the electromechanical characteristics of PUTs are studied from the electrical and acoustic ends, respectively. It is found that from the view of electrical ends, in the two LC impedance matching networks, the EIM network formed by the series inductance and the parallel capacitance is better. Considering from the acoustic end, when the epoxy resin is doped with tungsten powder with the ratio of Rv2=10% and an AIM layer with a thickness of 8 mm is applied, the matching effect is the best.

3. To improve the energy conversion efficiency of PUTs, a high-voltage pulse driving circuit based on full-bridge topology. The proposed driving circuit fully considers the absorption of overshoot and oscillation generated when the power MOSFET is turned off, as well as the impedance matching of the PUT and the tailing absorption of the excitation signal. It is shown that compared with the traditional driving circuit, the proposed high-voltage pulse driving circuit can effectively improve the peak-to-peak voltage of the PUT. Compared with the

case of no impedance matching and absorption circuit, the use of impedance matching and absorption can increase the peak amplitude of the received voltage, and the frequency spectrum amplitude and power spectrum density at the resonance frequency point are 9.94%, 16.02%, and 25.29%, respectively.

4. The excitation signal of PUTs is optimized from the aspects of excitation signal frequency and excitation coding. To solve the problem of the resonance frequency shift of PUTs after loading, an OEFT method based on DBTF is proposed and its correctness and reliability are verified by field experiments. To improve the SNR of the UGW signal, it is proposed to apply the Barker code excitation method to the broken rail detection. An adaptive peak detection method based on the combination of a digital band-pass tracking filter, a triangular filter, and HT is proposed. It is shown that compared with the PUT operating at the resonant frequency when it works at the optimal excitation frequency and the test distance is 50 m, the peak-to-peak values of the received signal, spectrum amplitude and power spectrum density are increased by 71.36%, 104.42%, and 31.54%, respectively; Compared with single-pulse excitation, Barker-coded excitation can effectively improve the SNR of the received UGW signal by 5 dB; Compared with the existing peak detection algorithm, the proposed peak detection algorithm has shorter processing time and stronger robustness, and the processing time is only 0.325 s.

7.1.2 Innovations

In this work, impedance matching of PUTs, driving circuit optimization, excitation signal optimization, and signal processing are performed to optimize the characteristics of PUTs and improve the propagation efficiency of UGW in the rail. The aforementioned works involve the following innovations:

1. The PSpice equivalent circuit model of SPUTs in the longitudinal vibration and the PSpice equivalent circuit model of the pitch-catch setup are established based on the one-dimensional wave and transmission line theories. The proposed PSpice equivalent circuit model of SPUTs in the longitudinal vibration is very convenient to study the electromechanical characteristics of PUTs, the parameters extraction such as impedance, phase, electroacoustic gain ratio, and other parameters.

2. The high-voltage pulse driving circuit of PUTs based on full-bridge topology is proposed. The proposed driving circuit considers the EIM of PUTs and the tailing absorption of the excitation signal, while the absorption circuit is designed to suppress the overshoot and oscillation when the power MOSFETs are turned off.

3. An optimal excitation frequency tracking method for PUTs is proposed. The proposed frequency tracking method is accomplished based on a digital band-pass filter at the receiving end. It is easy to be programmed to ensure the high energy conversion efficiency of PUTs and improve the SNR of the received UGW signal.

4. A Barker code-based excitation approach and an adaptive peak detection algorithm are proposed in this work. The proposed peak detection algorithm is based on the DBTF, triangle filters, and HT without any amplitude threshold to improve detection efficiency and detection accuracy. Besides, it is easy to program and also suitable for other applications using coded excitation and peak detection.

7.2 Future Works

To address the signal identification and detection problems in UGW-based broken-rail detection systems, the follow-up research will be carried out in the following aspects:

1. At present, the data communication of the broken rail detection system based on UGW depends on the GPRS module and wireless data transmission module, which results in a higher communication cost. To solve this problem, the combination of data communication and rail damage detection will be the focus of follow-up research work. Therefore, for the sake of simulating different detection and data communication situations, it is very necessary to establish a basic model of the UGW channel of the rail, which will speed up the research progress and greatly reduce the experimental cost.

2. In view of the fact that PUTs will produce resonance frequency shifts and EIM under detection applications must be based on the resonance frequency, the combination of the OEFT of PUTs and online EIM will be investigated.

3. Although the SNR of the received signal after pulse compression is greatly improved by using coded excitation, as the propagation distance increases, the dispersion effect of UGW in the rail becomes more severe, and the width of the envelope mainlobe of the pulse compression result is gradually wider, which in turn leads to reduced resolution of the detected distance. Therefore, the combination of different coding excitations and ultrasonic guided wave dispersion compensation in long-distance rails is also a research focus in the subsequent research work.

4. Currently, PUTs are installed on the rail web, and there is a difference in acoustic impedance between the contact surfaces of the two, which causes most of the incident wave energy to be reflected. To overcome this problem, epoxy resin is usually used as the material of the acoustic impedance matching layer, but the effect is not very good. The electromagnetic ultrasonic transducer does not need to be in contact with the rail when it is used for rail detection. Therefore, the application research of electromagnetic ultrasonic transducers in the broken rail detection system based on UGW is another research focus in subsequent research work.

References

[1] Hao Z, Xiao T Z. Transportation infrastructure quality and economic growth: evidence from speed-up of Chinese railways [J]. The Journal of World Economy, 2012(1):78-97.

[2] Jia W G. Development history and prospect of China's high-speed railway [J]. Economig Research Guide, 2014(17):31-32.

[3] Zhong M Y. Research on road network planning of China's high-speed railway [J]. Railway Economics Research, 2010(6):4-7.

[4] Ono S, Numakura A, Odaka T. High-speed track inspection technologies [J]. Jr East Technical Review, 2003.

[5] Chuang S L, Hsu A, Young E. Fiber optical sensors for high-speed rail applications[J]. High-Speed Rail IDEA Program Project Final Report, 2003.

[6] Wilson J W, Tian G Y. 3D magnetic field sensing for magnetic flux leakage defect characterization [J]. Insight - Non-Destructive Testing and Condition Monitoring, 2006, 48(6):357-359.

[7] Yong L, Wilson J, Gui Y T. Experiment and simulation study of 3D magnetic field sensing for magnetic flux leakage defect characterization [J]. NDT & E International, 2007, 40(2):179-184.

[8] Mandayam S, Udpa L, Udpa S S, et al. Invariance transformations for magnetic flux leakage signals [J]. Magnetics IEEE Transactions on, 1996, 32(3):1577-1580.

[9] Yong L, Gui Y T, Ward S. Numerical simulation on magnetic flux leakage evaluation at high speed [J]. NDT & E International, 2006, 39(5):367-373.

[10] Song Z, Yamada T, Shitara H, et al. Detection of damage and crack in railhead by using eddy current testing [J]. Journal of Electromagnetic Analysis & Applications, 2011, 3(12):546-550.

[11] Thomas H, Dey A, Heyder R. Eddy current test method for early detection of rolling contact fatigue (RCF) in rails [J]. Insight - Non-Destructive Testing and Condition Monitoring, 2010, 52(52):361-365.

[12] Chen L, Liang Y, Wang K. Inspection of rail surface defect based on machine vision system [C] International Conference on Information Science and Engineering. IEEE, 2011:3793-3796.

[13] Min Y, Xiao B, Dang J, et al. Real time detection system for rail surface defects based on machine vision[J]. Eurasip Journal on Image & Video Processing, 2018, 2018(1):3.

[14] Ze L, Wei W, Ping W. Design of machine vision system for inspection of rail surface defects [J]. Journal of Electronic Measurement and Instrumentation, 2010, 24(11):1012-1017.

[15] Sebko V P, Suchkov G M, Malakhov A V. Ultrasonic testing of railheads using the electromagnetic-acoustic method [J]. Russian Journal of Nondestructive Testing, 2004, 40(7):442-448.

[16] Ribichini R, Cegla F, Nagy P B, et al. Study and comparison of different EMAT configurations for SH wave inspection [J]. IEEE Transactions on Ultrasonics Ferroelectrics & Frequency Control, 2011, 58(12):2571-81.

[17] Huang S, Wei Z, Zhao W, et al. A new omni-directional EMAT for ultrasonic Lamb wave tomography imaging of metallic plate defects [J]. Sensors, 2014, 14(2):3458-3476.
[18] Guo F Z, Kai C W, Wu J M, et al. An electromagnetic ultrasonic technology rail defect detection method and device. China: 2008101398410 [P]. 2009.
[19] Reverdy F, Hopkins D. Inspection of spot welds using a portable ultrasonic phased-array system [C]. Review of Progress in Quantitative Nondestructive Evaluation. American Institute of Physics, 2005, 1212-1219.
[20] Garcia G, Zhang J. Application of ultrasonic phased arrays for rail flaw inspection [J]. Nondestructive Tests, 2006.
[21] Alnazer L, Raslear T, Welander L R. Rail Integrity Application of Ultrasonic Phased Arrays for Rail Flaw Sizing [J]. Maintenance of Way, 2014.
[22] Lao J J, Lu C. Application of portable ultrasonic phased array instrument for rail welds ultrasonic inspection [J]. Advanced Materials Research, 2013, 717:384-389.
[23] Garcia G. Update on laser-based ultrasonic technology for rail-flaw detection [J]. Railway Track & Structures, 2005, 101.
[24] Zhao Y, Jia Z Q, Rui G, et al. A novel Laser-EMAT system for noncontact testing metal materials [J]. Applied Mechanics & Materials, 2013, 281:422-425.
[25] Zhao Y, Jia Z Q, Rui G, et al. The application of Laser-EMAT technique used to testing defect in rail [J]. Advanced Materials Research, 2014, 875-877(875-877):574-577.
[26] Ji H S, Yang Z, Gang Y , et al. Research on the rail waist defect testing with laser—EMAT ultrasonic and signal processing [J]. Laser Journal, 2017(12):22-25.
[27] Rayleigh J W S B, Lindsay R B. The theory of sound [M]. Dover Publications, 1945, ISBN: 9781108032216.
[28] Horace Lamb F R S. On waves in an elastic plate [J]. Proceedings of the Royal Society of London, 1917, 93(648):114-128.
[29] Ghosh J. Longitudinal vibrations of a hollow cylinder [J]. Bulletin Calcutta Mathematical Society, 1923, 14: 31-40.
[30] Naghdi P M, Cooper R M. Propagation of elastic waves in cylindrical shells, including the effects of transverse shear and rotatory inertia [J]. Journal of the Acoustical Society of America, 1956, 28(1):56-63.
[31] Silk M G, Bainton K F. The propagation in metal tubing of ultrasonic wave modes equivalent to Lamb waves [J]. Ultrasonic, 1979, 17(1): 11-19.
[32] Vogt T, Lowe M J S, Cawley P. The scattering of ultrasonic guided waves in partly embedded cylindrical structures [C]. AIP Conference Proceedings. 2003, 657(22): 221-228.
[33] Zhen Q L. Ultrasonic guided waves in pipes [J]. Nondestructive Testing, 1999(12):560-562.
[34] Zhen Q L. Guided waves in ultrasonic nondestructive testing [J]. Nondestructive Testing, 1999, 21(8): 367-369.
[35] Zhen Q L, Xiao L. Development of ultrasonic nondestructive testing techniques [J]. NDT, 2000, 22(9):403-405.
[36] De A T, Zhen Q L. Relationship between the dispersion characteristics of ultrasonic guided waves and the inner diameter-to-thickness ratio of pipes [J]. Journal of Fudan

University (Natural Science), 2003, 42(1):7-13.

[37] Li J Y, Lin L Z, Song W G. The propagation characteristics of ultrasonic guided waves in steel pipes [J]. Nondestructive Testing Technology, 2011, 35(1): 9-12.

[38] L. Gavrić. Computation of propagative waves in free rail using a finite element technique [J]. Journal of Sound & Vibration, 1995, 185(3):531–543.

[39] Pavlakovic B, Lowe M, Alleyne D, et al. Disperse: A General Purpose Program for Creating Dispersion Curves [C]. Review of Progress in Quantitative Nondestructive Evaluation. 1997:185-192.

[40] Hayashi T, Song W J, Rose J L. Guided wave dispersion curves for a bar with an arbitrary cross-section, a rod and rail example [J]. Ultrasonics, 2003, 41(3):175-183.

[41] Bartoli I, Marzani A, Scalea F L D, et al. Modeling wave propagation in damped waveguides of arbitrary cross-section [J]. Journal of Sound & Vibration, 2006, 295(3):685-707.

[42] Gravenkamp H, Bause F, Song C. On the computation of dispersion curves for axisymmetric elastic waveguides using the Scaled Boundary Finite Element Method [J]. Computers & Structures, 2014, 131(2):46-55.

[43] Gravenkamp H, Birk C, Song C. The computation of dispersion relations for axisymmetric waveguides using the Scaled Boundary Finite Element Method [J]. Ultrasonics, 2014, 54(5):1373-1385.

[44] Cun F H, Qin Q L, Jin P J, et al. Propagation characteristics of ultrasonic guided wave in rails based on vibration modal analysis [J]. Journal of Vibration and Shock, 2014, 33(3):9-13.

[45] Rose J L, Avioli M J, Song W J. Application and potential of guided wave rail inspection [J]. Insight - Non-Destructive Testing and Condition Monitoring, 2002, 44(6):353-358.

[46] Rose J L, Avioli M J, Mudge P, et al. Guided wave inspection potential of defects in rail [J]. NDT & E International, 2004, 37(2): 153-161.

[47] Schwartz K, District B A R T. Development of an acoustic broken rail detection system [J]. Final Report for High-Speed Rail IDEA Project, 2004, 42.

[48] Hayashi T, Miyazaki Y, Murase M, et al. Guided wave inspection for bottom edge of rails [C]. Aip Conference. American Institute of Physics, 2007:169-176.

[49] Fan Y, Dixon S, Edwards R S, et al. Ultrasonic surface wave propagation and interaction with surface defects on rail track head [J]. NDT & E International, 2007, 40(6): 471-477.

[50] Coccia S, Bartoli I, Marzani A, et al. Numerical and experimental study of guided waves for detection of defects in the rail head [J]. NDT & E International, 2011, 44(1):93-100.

[51] Bartoli I, Phillips R, Coccia S, et al. Stress dependence of ultrasonic guided waves in rails [J]. Transportation Research Record: Journal of the Transportation Research Board, 2010, 2159(1):91-97.

[52] Ryue J, Thompson D J, White P R, et al. Investigations of propagating wave types in railway tracks at high frequencies [J]. Journal of Sound and Vibration, 2008, 315(1):157-175.

[53] You P Z, Yuan R. Research on real-time detection method for broken rail based on

ultrasonic guided waves [J]. Journal of Railway Engineering Society, 2010, 27(11):47-51.

[54] Chao L, Chen L, Jun J C. E on guided wave detection technology for rail bottom vertical vibration mode [J]. Journal of Experimental Mechanics, 2012, 27(005): 593-600.

[55] Chao L, Hua J S, Kai S, et al. Ultrasonic guided wave scattering characteristics of rail base oblique cracks [J]. Nondestructive Testing, 2016, 38(5):18-22.

[56] Xi N X. The basic research on on-line monitoring of stress in continuously welded rails based on ultrasonic guided waves [D]. Doctoral thesis, Beijing Jiaotong University 2013.

[57] Li Q Z, Xi N X, Zu J Y, et al. Study on the railway integrity monitoring method based on ultrasonic guided waves [J]. Chinese Journal of Scientific Instrument, 2016, 37(7):1603-1609.

[58] Jun J C, Yuan Y L, Guang Y L. Air coupled ultrasonic guided wave detection of shallow surface defects of rail head [J]. Nondestructive Testing, 2018, 40(3).

[59] Cawley P. et al. Long range inspection of rail using guided wave-field experience [C]. Proceedings of the 16th World Conference on Non-Destructive Testing, 2004, 1-7.

[60] Miki M, Ogata M. Phased array ultrasonic testing methods for welds in bogie frames of railway vehicles [J]. Insight, 2015, 57(7):382-388.

[61] Mariani S, Nguyen T V, Zhu X, et al. Non-contact ultrasonic guided wave inspection of rails: field test results and updates [C]. ASME 2013 International Mechanical Engineering Congress and Exposition. 2013:539-548.

[62] Jian H H, Zhi F T, Jin Z J, et al. Research on guided wave detection technology for defects of turnout rail bottom [J]. China Railway Science, 2014, 35(3):34-40.

[63] Dixon S, Edwards R S, Jian X. Inspection of rail track head surfaces using electromagnetic acoustic transducers (EMATs) [J]. Or Insight, 2004, 46(6):326-330.

[64] Han H, Lu G, Cong P, et al. Development of novel rail non-destructive inspection technologies [J]. Sensors & Transducers, 2014, 179(9):121.

[65] Chahbaz A. Development of a mobile inspection system for rail integrity assessment [J]. Journal of the Society of Naval Architects of Japan, 2000, 188:351-358.

[66] Hay T, Jayaraman S, Hay R. Ultrasonic guided wave inspection of rail defects under shelling [C]. Joint Rail Conference. 2009:47-50.

[67] Yu Q, Ji X, Kai C W, et al. Online rail flaw detection device based on electromagnetic acoustic surface wave [J]. Nondestructive Testing, 2013, 35(5):43-46.

[68] Burger F A. A practical continuous operating rail break detection system using guided waves [C]. 18th World Conference on Non-destructive Testing, 16-20 April 2012, Durban, South Africa.

[69] Burger F A, Loveday P W, Long C S. Large scale implementation of guided wave based broken rail monitoring [C]. Review of Progress in Quantitative Nondestructive Evaluation: Volume. American Institute of Physics, 2015:771-776.

[70] Wei X, Yang Y, Yu N. Research on broken rail real-time detection system for ultrasonic guided wave [C]. International Conference on Electromagnetics in Advanced Applications. 2017:906-909.

[71] Loveday P W. Development of piezoelectric transducers for a railway integrity monitoring system [J]. Proceedings of SPIE - The International Society for Optical Engineering, 2000, 3988.

[72] Ramatlo D A, Wilke D N, Loveday P W. Optimal design of a piezoelectric transducer for exciting guided wave ultrasound in rails [C]. Review of Progress in Quantitative Nondestructive Evaluation. 43rd Review of Progress in Quantitative Nondestructive Evaluation, 2016:030007.

[73] Ramatlo D A, Wilke D N, Loveday P W. Development of an optimal piezoelectric transducer to excite guided waves in a rail web [J]. NDT & E International, 2018, 95.

[74] Kijanka P, Packo P, Zhu X, et al. Three-dimensional temperature effect modelling of piezoceramic transducers used for Lamb wave based damage detection [J]. Smart Materials and Structures, 2015, 24(6):065005.

[75] Xiaoyuan W, Yuan Y, Wenqing Y, et al. PSpice modeling of a sandwich piezoelectric ceramic ultrasonic transducer in longitudinal vibration [J]. Sensors, 2017, 17(10):2253.

[76] Yuan Y, Xiaoyuan W, Lei Z, et al. The effect of electrical impedance matching on the electromechanical characteristics of sandwiched piezoelectric ultrasonic transducers [J]. Sensors, 2017, 17(12):2832.

[77] Roy S, Ladpli P, Chang F K. Load monitoring and compensation strategies for guided-waves based structural health monitoring using piezoelectric transducers [J]. Journal of Sound and Vibration, 2015, 351:206-220.

[78] Bullis D C, Budak A. Response of ultrasonic motional bridge circuits under resistive and reactive loads [J]. IEEE Transactions on Sonics and Ultrasonics, 1982, 29(2):92-98.

[79] Ramos-Fernandez A, Gallego-Juarez J A, Montoya-Vitini F. Automatic system for dynamic control of resonance in high power and high Q ultrasonic transducers [J]. Ultrasonics, 1985, 23(4):151-156.

[80] Pons J L, Ochoa P, Villegas M, et al. Self-tuned driving of piezoelectric actuators: The case of ultrasonic motors [J]. Journal of the European Ceramic Society, 2007, 27(13):4163-4167.

[81] Dong H J, Wu J, Zhang G Y, et al. An improved phase-locked loop method for automatic resonance frequency tracing based on static capacitance broadband compensation for a high-power ultrasonic transducer [J]. IEEE Transactions on Ultrasonics Ferroelectrics & Frequency Control, 2012, 59(2):205-210.

[82] Kuang Y, Jin Y, Cochran S, et al. Resonance tracking and vibration stablilization for high power ultrasonic transducers [J]. Ultrasonics, 2014, 54(1):187-194.

[83] Jittakort J, Sangswang A, Naetiladdanon S, et al. Full Bridge Resonant Inverter Using Asymmetrical Control with Resonant-frequency Tracking for Ultrasonic Cleaning Applications [J]. Journal of Power Electronics, 2017, 17:1150-1159.

[84] Mortimer B, Bruyn T D, Davies J, et al. High power resonant tracking amplifier using admittance locking [J]. Ultrasonics, 2001, 39(4):257-261.

[85] Cheng L, Kang Y, Chen C. A Resonance-Frequency-Tracing Method for a Current-Fed Piezoelectric Transducer [J]. IEEE Transactions on Industrial Electronics, 2014, 61(11):6031-6040.

[86] Di S, Fan W, Li H. Parallel resonant frequency tracking based on the static capacitance

online measuring for a piezoelectric transducer [J]. Sensors and Actuators A: Physical, 2018, 270:18-24.

[87] Zhang H, Wang F, Zhang D, et al. A new automatic resonance frequency tracking method for piezoelectric ultrasonic transducers used in thermosonic wire bonding [J]. Sensors and Actuators A Physical, 2015, 235:140-150.

[88] Liu X, Colli-Menchi A, Gilbert J, et al. An Automatic Resonance Tracking Scheme With Maximum Power Transfer for Piezoelectric Transducers [J]. IEEE Transactions on Industrial Electronics, 2015, 62(11): 7136 - 7145.

[89] Garcia-Rodriguez M, Garcia-Alvarez J, Yaez Y, et al. Low cost matching network for ultrasonic transducers [J]. Physics Procedia, 2010, 3(1):1025-1031.

[90] An J, Zhang S. A new method of designing electrical impedance matching network for piezoelectric ultrasound transducer [J]. Journal of engineering science & technology review, 2014, 7(1):71-75.

[91] An J, Song K, Zhang S, et al. Design of a Broadband Electrical Impedance Matching Network for Piezoelectric Ultrasound Transducers Based on a Genetic Algorithm [J]. Sensors, 2014, 14(4):6828-6843.

[92] Huang H, Paramo D. Broadband electrical impedance matching for piezoelectric ultrasound transducers [J]. IEEE Transactions on Ultrasonics Ferroelectrics & Frequency Control, 2011, 58(12):2699-707.

[93] Lockwood G R, Foster F S. Modeling and optimization of high-frequency ultrasound transducers [J]. IEEE Transactions on Ultrasonics, Ferroelectrics, and Frequency Control, 1994, 41(2):225-230.

[94] Moon, J Y, Lee, J, Jin, H C. Electrical impedance matching networks based on filter structures for high frequency ultrasound transducers [J]. Sensors and Actuators, A. Physical, 2016, 251:225–233.

[95] Kim, M G, Yoon, S, Kim, H H. Impedance matching network for high frequency ultrasonic transducer for cellular applications [J]. Ultrasonics, 2016, 65:258–267.

[96] Lin S. Study on the Parallel Electric Matching of High Power Piezoelectric Transducers [J]. Acta Acustica united with Acustica, 2017, 103(3):385-391.

[97] Kim Y B, Roh Y. New design of matching layers for high power and wide band ultrasonic transducers [J]. Sensors & Actuators A, 1998, 71(1-2):116-122.

[98] GERLACH R, KRAUS O, FRICKE, et al. Modified SiO_2 aerogels as acoustic impedance matching layers in ultrasonic devices [J]. Journal of Non Crystalline Solids, 1992, 145:227-232.

[99] Lamberti N, Espinosa F M D, Giosu è Caliano, et al. A new technique for the design of acoustic matching layers for piezocomposite transducers [C]. International Conference on Theoretical And Computational Acoustics, Beijing, China, May. 2001, 505-515.

[100] Zhou Q, Cha J , Huang Y, et al. Alumina/epoxy nanocomposite matching layers for high-frequency ultrasound transducer application [J]. IEEE Transactions on Ultrasonics Ferroelectrics & Frequency Control, 2009, 56(1):213-219.

[101] Troge A, O'Leary, Richard L, Hayward G, et al. Properties of photocured epoxy resin materials for application in piezoelectric ultrasonic transducer matching layers [J]. Journal of the Acoustical Society of America, 2010, 128(5):2704.

[102] Ha S, Chang F K. Adhesive interface layer effects in PZT-induced Lamb wave propagation [J]. Smart Materials & Structures, 2010, 19(2):025006.
[103] Peng B L. Study on the acoustic matching properties of high frequency medical ultrasound transducers materials [J]. Piezoelectrics & Acoustooptics, 2016, 38(3):450-453.
[104] Fang H J, Chen Y, Wong C M, et al. Anodic aluminum oxide–epoxy composite acoustic matching layers for ultrasonic transducer application [J]. Ultrasonics, 2016, 70:29-33.
[105] Zhang L, Yang Y, Yang X, et al. Grease-like Coupling Agent Based on Metal Ionization Method for Low-Frequency Ultrasonic NDT [J]. Results in Physics, 2019, 12:1770-1776.
[106] Salazar J, Turo A, Chavez J A, et al. High-power high-resolution pulser for air-coupled ultrasonic NDE applications [J]. IEEE Transactions on Instrumentation and Measurement, 2003, 52(6):1792-1798.
[107] Gammell P M, Harris G R. IGBT-based kilovoltage pulsers for ultrasound measurement applications [J]. IEEE Transactions on Ultrasonics Ferroelectrics & Frequency Control, 2003, 50(12):1722-1728.
[108] Zhang H, Zhang S Y, Zheng K. Electrode effects on general modes in high-overtone bulk acoustic resonators [J]. Ultrasonics, 2007, 44(8):737-740.
[109] Wu J X, Du Y C, Lin C H, et al. A novel bipolar pulse generator for high-frequency ultrasound system[C]. 2013 IEEE International Ultrasonics Symposium (IUS), Prague, 2013, 1571-1574.
[110] Cowell D M J, Freear S. Quinary excitation method for pulse compression ultrasound measurements [J]. Ultrasonics, 2008, 48(2):98-108.
[111] Aydın EA, Güler I. Design of pic-controlled pulsed ultrasonic transmitter for measuring gingiva thickness [J]. Instrumentation Science & Technology, 2010, 38(6):411-420.
[112] Jonny J, Jerker D. Microelectronics mounted on a piezoelectric transducer: method, simulations, and measurements [J]. Ultrasonics, 2006, 44(1):1-11.
[113] Xu X, Yen J T, Shung K K. A low-cost bipolar pulse generator for high-frequency ultrasound applications [J]. IEEE Transactions on Ultrasonics, Ferroelectrics, and Frequency Control, 2007, 54:443-447.
[114] Qiu W, Yu Y, Tsang F K, et al. A multifunctional, reconfigurable pulse generator for high-frequency ultrasound imaging [J]. IEEE Transactions on Ultrasonics, Ferroelectrics and Frequency Control, 2012, 59(7):1558-1567.
[115] Svilainis L, Chaziachmetovas A, Dumbrava V. Half bridge topology 500V pulser for ultrasonic transducer excitation [J]. Ultrasonics, 2015, 59:79-85.
[116] Svilainis L, Chaziachmetovas A, Dumbrava V. Efficient high voltage pulser for piezoelectric air coupled transducer [J]. Ultrasonics, 2013, 53(1):225-231.
[117] Seyed K, Sina F, Lu G, et.al. Split-spectrum processing technique for SNR enhancement of ultrasonic guided wave [J]. Ultrasonics, 2018, 83(1):48-59.
[118] Lei Z，Yuan Y, Wen T L, et al. A novel ultrasonic guided wave signal wavelet threshold denoising method [J]. Journal of Xi'an University of Technology，2015，31(3):322-327.
[119] Wilcox P D. A rapid signal processing technique to remove the effect of dispersion from guided wave signals [J]. IEEE Transactions on Ultrasonics, Ferroelectrics, and

Frequency Control, 2003, 50(4):419-427.
[120] Xu C B, Yang Z B, Chen X F, et al. A guided wave dispersion compensation method based on compressed sensing [J]. Mechanical Systems and Signal Processing, 2018, 103:89-104.
[121] Zhang H, Wu S, Ta D, et al. Coded excitation of ultrasonic guided waves in long bone fracture assessment [J]. Ultrasonics, 2014, 54(5):1203-1209.
[122] Fu J, Wei G, Huang Q, et al. Barker coded excitation with linear frequency modulated carrier for ultrasonic imaging [J]. Biomedical Signal Processing & Control, 2014, 13:306-312.
[123] Yucel M, Fateri S, Legg M, et al. Coded Waveform Excitation for High Resolution Ultrasonic Guided Wave Response [J]. IEEE Transactions on Industrial Informatics, 2016, 12(1):257-266.
[124] Li H, Zhou Z. Application of P4 Polyphase codes pulse compression method to air-coupled ultrasonic testing systems [J]. Ultrasonics, 2017, 78:57-69.
[125] Yuan, Lei, Yang, et al. Improvement of high-voltage impulses in track circuits with Kasami and LS codes [J]. International Journal of Circuit Theory & Applications, 2018, 46(4):926-941.
[126] Hill, R. J. Optimal construction of synchronizable coding for railway track circuit data transmission [J]. IEEE Transactions on Vehicular Technology, 1990, 39(4):390-399.
[127] Filippone F, Mariscotti A, Pozzobon P. The Internal Impedance of Traction Rails for DC Railways in the 1–100 kHz Frequency Range [J]. 1616 IEEE Transactions on Instrumentation and Measurement, 2006, 55(5):1616-1619.
[128] Escudero R, Hernandez A, Perez M C, et al. Local maximum detection for active sensory systems based on encoding and correlation techniques[C]. IEEE Instrumentation & Measurement Technology Conference, Graz, Austria, May 2012, 1697-1702.
[129] Gutierrez-Rivas R, Garcia J J, Marnane W P, et al. Novel real-time low-complexity QRS complex detector based on adaptive threshold [J]. IEEE Sensors Journal, 2015, 15(10):6036-6043.
[130] Manikandan M S, Soman K P. A novel method for detecting R-peaks in electrocardiogram (ECG) signal [J]. Biomedical Signal Processing and Control, 2012, 7(2):118-128.
[131] Rakshit M, Das S. An effcient wavelet-based automated R-peaks detection method using Hilbert transform [J]. Biocybern. Biomed. Eng., 2017, 37(3):566-577.
[132] Lei Y, Yuan Y, Alvaro H, et al. Novel Adaptive Peak Detection Method for Track Circuits based on Encoded Transmissions [J]. IEEE Sensors Journal, 2018, 18(15):6224-6234.
[133] Hui D. Computational ultrasound: sound field analysis and application [M]. Beijing, China：Science Press, 2010, ISBN: 9787030279378.
[134] Shuyu L. The principle and design of ultrasonic transducer [M]. Beijing, China: Science Press, 2004, ISBN: 9787030134196.
[135] Xiaofeng M. ABAQUS 6.11 Chinese version of finite element analysis from entry to mastery [M]. Tsinghua University Press, 2013, ISBN: 9787302310778.

[136] Mason, W P. Electromechanical Transducers and Wave Filters[M]. 2nd ed., Van Nostrand: Princeton, NJ, USA, 1948, ISBN 9780442051648.
[137] Redwood, M. Transient Performance of a Piezoelectric Transducer[J]. Journal of the Acoustical Society of America, 1961, 33(4):527.
[138] Krimholtz R, Leedom D A, Matthaei G L. New equivalent circuits for elementary piezoelectric transducers[J]. Electronics Letters, 1970, 6(13):398.
[139] Leach W M. Controlled-source analogous circuits and SPICE models for piezoelectric transducers[J]. IEEE Transactions on Ultrasonics, Ferroelectrics, and Frequency Control, 1994, 41(1):60-66.
[140] Chunan A, Zhao L H, Jian L, et al. Research of electric impedance matching method of piezoelectric ultrasonic transducer based on extended BVD model [J]. Science Technology and Engineering, 2015(5):41-45.
[141] Puttmer A, Hauptmann P. SPICE model for lossy piezoceramic transducers [J]. IEEE Transactions on Ultrasonics Ferroelectrics & Frequency Control, 1997, 44(1):60-66.
[142] Collin R E. Theory and Design of Wide-Band Multisection Quarter-Wave Transformers[J]. Proceedings of the IRE, 2007, 43(2):179-185.
[143] Desilets C S, Fraser J D, Kino G S. The design of efficient broad-band piezoelectric transducers[J]. IEEE Transactions on Sonics & Ultrasonics, 2005, 25(3):115-125.
[144] Gandole, Y. B. Computer modeling and simulation of ultrasonic signal processing and measurements [J]. Physics Research International, 2012, 2012:1-12.
[145] Galloy L, Berquez L, Baudoin F, et al. PSpice modeling of the pulsed electro-acoustic signal[J]. IEEE Transactions on Dielectrics & Electrical Insulation, 2014, 21(3):1143-1153.
[146] Dennis, F. Analog Design and Simulation Using OrCAD Capture and PSpice (First Edition) [M]. Newnes: Oxford, UK, 2011, pp. 217 – 218, ISBN: 9780080970950.
[147] Zhang H, Wang F, Tian Y, et al. Electrical matching of low power piezoelectric ultrasonic transducers for microelectronic bonding [J]. Sensors and Actuators A Physical, 2013, 199(6):241-249.
[148] Jindan N. The study of design method and acoustic properties of acoustic matching layer for ultrasonic transducer [D]. Master thesis, Harbin Institute of Technology, China, 2014.
[149] Huiting Z, Jun B L, Rui W. New method of eliminating ultrasonic tailing efficiently [J]. Chinese Journal of Scientific Instrument, 2007, 28(6):1075-1079.
[150] Bendik Nybakk Torsæter, Tiwari S, Lund R, et al. Experimental evaluation of switching characteristics, switching losses and snubber design for a full SiC half-bridge power module[C] IEEE International Symposium on Power Electronics for Distributed Generation Systems. IEEE, 2016.
[151] Xianfeng H, Xiang Y C. High-voltage pulse generating circuit with tail flicking function [J]. Science Technology and Engineering, 2016, 16(21):251-254.
[152] Roy, Surajit, Ladpli, Purim, Chang, Fu-Kuo. Load monitoring and compensation strategies for guided-waves based structural health monitoring using piezoelectric transducers [J]. Journal of Sound & Vibration, 2015, 351:206-220.
[153] Xiquan G. Digital Signal Processing (Third Edition) [M]. Xi'an, China: XIDIAN

UNIVERSITY PRESS, 2008, ISBN: 9787560609225.

Achievement during the Period of Ph.D

1. **Xiaoyuan Wei**, Yuan Yang, Wenqing Yao, et al. PSpice Modeling of a Sandwich Piezoelectric Ceramic Ultrasonic Transducer in Longitudinal Vibration [J]. Sensors, 2017, 17(10):2253. (SCI index: 000414931500095, **Q1**)
2. Yuan Yang, **Xiaoyuan Wei**, Lei Zhang, et al. The Effect of Electrical Impedance Matching on the Electromechanical Characteristics of Sandwiched Piezoelectric Ultrasonic Transducers [J]. Sensors, 2017, 17(12):2832. (SCI index: 000423285800132, **Q1**)
3. **Xiaoyuan Wei**, Yuan Yang, Wenqing Yao, et al. An automatic optimal excitation frequency tracking method based on digital tracking filters for sandwiched piezoelectric transducers used in broken rail detection [J]. Measurement, 2019, 135:294-305. (SCI index: 000468747300030, **Q1**)
4. **Xiaoyuan Wei**, Yuan Yang, Wenqing Yao, et al. Design of full bridge high voltage pulser for sandwiched piezoelectric ultrasonic transducers used in long rail detection [J]. Applied acoustics, 2019, 149:15-24. (SCI index: 000462108100002, **Q1**)
5. **Xiaoyuan Wei**, Yuan Yang, Jesús Ureña Ureña, et al. An adaptive peak detection method for inspection of breakages in long rails by using barker coded UGW [J]. IEEE Access, 2020, 8(1):48529-48542. (SCI index: 000524719700007, **Q1**)
6. **Xiaoyuan Wei**, Yuan Yang, Lei Yuan, et al. The effect of acoustical load on the electromechanical characteristics of sandwiched piezoelectric ultrasonic transducers used in broken rail detection [J]. Applied acoustics, 2020. (SCI, **Q1**, Under review)
7. **Xiaoyuan Wei**, Yuan Yang, Yang Wang. Design of Driving Circuit in Ultrasonic Transducer for Long Rail Detection [J]. Chinese Journal: Piezoelectrics & Acoustooptic, 2017, 39(6):939-944.
8. **Xiaoyuan Wei**, Yang Yuan, Yu Ningmei. Research on broken rail real-time detection system for ultrasonic guided wave [C]. Proceedings of the 2017 19th International Conference on Electromagnetics in Advanced Applications, ICEAA 2017, Verona, Italy, Sep. 11-15, 906-909, 2017. (EI index: 20174804472128)
9. **Xiaoyuan Wei**, Yuan Yang. Study the effect of acoustic load on the performance for sandwiched piezoelectric ultrasonic transducers [C]. 2018 Far East NDT Forum New Technology&Application, Xiamen, China, Jul. 5-8, 2018. (EI index: 20191806846001)
10. **Xiaoyuan Wei**, Yuan Yang, Jesús Ureña Ureña. A novel real-time detection system of breakages in the rail based on ultrasonic guided waves [C]. 2020 IEEE International Instrumentation & Measurement Technology Conference, Dubrovnic, Croatia, May 25-28, 2020.
11. Yuan Yang, **XiaoyuanWei**, Kai Zhao. Ultrasonic sensor driving circuit for long track detection [P]. Chinese Patent, ZL201520438206.2